POLISH ACADEMY OF SCIENCES
COMMITTEE OF METALLURGY
INSTITUTE OF METALLURGY
AND MATERIALS SCIENCE

ARCHIVES OF METALLURGY AND MATERIALS

QUARTERLY

Volume 49 · Issue 4

This issue is devoted to presentations during the workshop "Thermoelastic and magnetoelastic intelligent materials" in Niedzica between 10—13 October, 2004 (papers 1 to 15), papers 16 and 17 are presentations during Calphad XXXIII in Kraków May 30 to June 4, 2004, while papers 18 to 22 are the regular research papers.

WARSZAWA — KRAKÓW 2004

The Archives of Metallurgy and Materials is covered in the following Institute for Scientific Information® products: SciSearch (the Science Citation Index® — Expanded), Research Alert®, Materials Science Citation Index®, and Current Contents® / Engineering, Computing and Technology. Articles published in the Archives of Metallurgy and Materials are also indexed or abstracted by Cambridge Scientific Abstracts.

EDITORIAL ADDRESS
M. Bitner al. Mickiewicza 30, AGH, paw. A-4, III p., pok. 312b
30-059 Kraków, Poland
Tel. +48 (12) 6173425
e-mail: archives@imim-pan.krakow.pl

Skład, łamanie druk i oprawa: Warszawska Drukarnia Naukowa PAN
Warszawa, ul. Śniadeckich 8, tel./fax 628-87-77

Ark. wyd. 21,5 Ark. druk. 17,25
Nakład: 220 egz.
Druk ukończono w marcu 2005 r.

Editorial

The special issue of *Archives of Metallurgy and Materials* contain invited papers presented during the workshop „**Thermoelastic and magnetoelastic intelligent materials**" organized in the frame of the Center of Excellence *Nano and Microscale Characterization and Development of Advanced Materials* at the Institute of Metallurgy and Materials Science of the Polish Academy of Sciences. The Workshop took place in Niedzica between 10—13 October 2004 and it gathered 54 participants from 11 countries like: Belgium, Czech Republic, Finland, France, Italy, Poland, Russia, Spain, Switzerland, Ukraine and USA.

The objective of this Workshop was to spread the existing knowledge in the field of shape memory, superelastic and magnetoelastic materials among researchers and employees of research units and small enterprises. It provided a forum for presenting recent developments in processing, characterization, and application of recently developed intelligent materials. The lectures were given by scientists from several universities, research institutes, and companies from Europe and USA. Special attention was given to linking fundamental knowledge to the engineering practice in order to identify possible routes to solving problems, and to promote application of magnetoelastic and shape memory materials. Representatives of two companies from Finland and USA shared their experience in production and development of conventional shape memory and magnetoelastic materials with special attention to the recent market requirements. In the field of structure analysis the special attention was given to methods of structural and microstructural studies applying analytical, conventional, in-situ and high- resolution electron microscopy. The Workshop was especially dedicated to young researchers, PhD students and university graduates to introduce them to this new field of intelligent materials, their characterization using latest research techniques, and to the recent applications. Participants had the opportunity to present their research results in short oral communications and to discuss them with leading specialists in the field of intelligent materials. Furthermore, the workshop stimulated cooperation between scientists from research centers, universities and industry in Central and Western Europe and hopefully it will generate mutual joint research projects.

The workshop was located in Niedzica near Castle Niedzica situated on a rocky mountain. The castle was constructed in the XIVth century by the Hungarian family Berzevicy. From 1410, the castle was under Polish rule with other surrounding towns. In 1601, the new owner Jerzy Horwath rebuilt the castle to its presents state. The location is picturesque at the foothills of the Pieniny Mountains, in the community of Niedzica on Czorsztyn Lake (surface of 12.5 square kilometers) developed in the course of construction of the dam of the Dunajec river, in the period 1975—1997. It created a rare possibility of visting this part of Poland by foreign participants.

All of the invited and contributed papers were reviewed to be published in the journal Archives of Metallurgy and Materials and will constitute useful publication covering recent developments in such an expanding field like intelligent materials.

Professor Jan Dutkiewicz
Chairman of the Workshop

A R C H I V E S O F M E T A L L U R G Y A N D M A T E R I A L S
Volume 49 2004 Issue 4

STEFAN WOJCIECHOWSKI *, ANNA BOCZKOWSKA*

INTELLIGENT MATERIALS 2004

MATERIAŁY INTELIGENTNE 2004

Synthetic overview of the state of knowledge in the field of intelligent materials will be made. Interest in intelligent materials has been growing rapidly from the late 1980 ties of the XX c. One can state that they have currently become an individual group of materials. In the English language literature the terminology varies, two terms coexist: "intelligent materials" and "smart materials", however sometimes they are also called "adaptive materials".

On a basis of literature survey, as the most important intelligent materials, shape memory alloys, ceramic piezoelectric materials, magnetostrictive materials, rheological fluids, intelligent polymers and its composites have been selected.

Interest in exhibiting intelligent behavior of polymers appeared much latter than it was in the case of metallic or ceramic intelligent materials. Within last two decades the role of intelligent polymers grew rapidly due to the promising results of research proving that some polymers show properties useful for practical applications. Available scientific data indicates that current level of knowledge on intelligent polymers varies substantially and very basic reports appear parallel to much matured and advanced developments, which are ready for implementations.

The second part of the paper brings brief analysis of the scope of the Smart Structures / NDE Joint SPIE Conference, held at San Diego in March 2004.

Keywords: intelligent materials, smart materials, smart structures, shape memory, piezoelectricity, magnetostrictive materials, rheological fluids, intelligent polymers

W artykule przedstawiono w sposób syntetyczny stan wiedzy w obszarze materiałów inteligentnych. Zainteresowanie materiałami inteligentnymi wzrosło gwałtownie w końcu lat 80-tych XX wieku. Można uznać, że aktualnie stanowią one indywidualną klasę materiałów. W publikacjach w języku angielskim terminologia nie jest jednolita i współistnieją dwie nazwy: „intelligent materials" i „smart materials", a czasami nawet są one określane jako „adaptive materials".

Na podstawie przeglądu literatury uznać można, że materiałami inteligentnymi o największym znaczeniu są: stopy z pamięcią kształtu, ceramiczne materiały piezoelektryczne, materiały magnetostrykcyjne, ciecze reologiczne oraz inteligentne polimery i ich kompozyty.

* WARSAW UNIVERSITY OF TECHNOLOGY, FACULTY OF MATERIALS SCIENCE AND ENGINEERING, WOŁOSKA 141, 02-507 WARSAW, POLAND

Zainteresowanie polimerami inteligentnymi pojawiło się znacznie później niż materiałami ceramicznymi i metalowymi. W ciągu ostatnich dwóch dekad znaczenie inteligentnych polimerów gwałtownie wzrosło w wyniku obiecujących możliwości ich praktycznego zastosowania. Dostępne wyniki badań wskazują, że stopień zaawansowania wiedzy dotyczącej inteligentnych materiałów polimerowych jest zróżnicowany. Istnieją wyniki badań podstawowych, a jednocześnie wyniki wskazujące na możliwość już zaawansowanego wykorzystania.

W części drugiej artykułu przedstawiono syntetyczny przegląd materiałów z konferencji „Smart Structures and Materials 2004 and Nondestructive Evaluation for Health Monitoring and Diagnostics 2004", która odbyła się w San Diego w Marcu 2004.

1. Introduction

Intelligent materials are today considered to be a new group of materials nevertheless some of them were known for many years, e.g. shape memory alloys (SMA) or ceramic piezoelectric materials. Interest in intelligent materials has been growing rapidly from the late 1980 – ties of the XX c. and one can state they have currently become an individual group of materials. In the English language literature the terminology varies, two terms coexist: "intelligent materials" and "smart materials", however sometimes they are also called "adaptive materials". Currently does not exist commonly accepted definition characterizing intelligent materials, which leads to ambiguities in classifying different materials as intelligent. An interesting approach to solving this problem has been suggested by Takagi. According to him one can call the material intelligent when it plays a role of a sensor, processor and transferring signal device (actuator), accompanied by simultaneous feedback [1]. A similar approach is given in Fig. 1 [2].

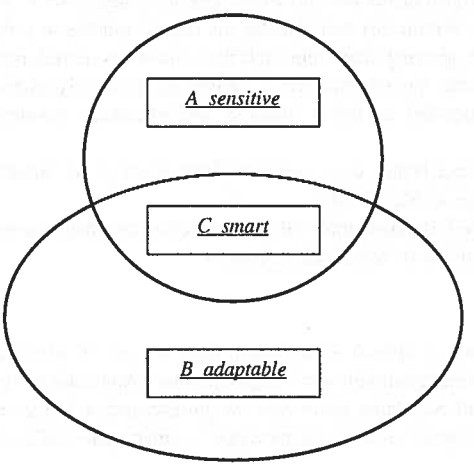

Fig. 1. Scheme of the intelligent materials functions

When a new field in materials science arises there is usually some confusion about formal definitions and terminology. An interesting discussion about the idea of intelligent materials could be find in [3]. It was concluded that smart materials and structures are different from existing materials and structures because they have the means to sense their

surrounding environment, process the sensory information, and through commands to actuators act in a beneficial and controlled way to respond to the changing environment. Smart structures should be lighter in weight, consume less energy to manufacture and operate, and achieve higher performance levels than existing structures. Smart structures and materials are important because they have the ability to take advantage of the new advancing computer technologies and integrated sensor/actuators, and thereby contain some sense of intelligence which enables better structural performance capabilities". [3].

The last decade was a period of intensive research activity and many interesting findings were presented in scientific journals, mainly in the *Journal of Intelligent Materials and Structures, or Smart Materials and Structures*. The first encyclopedia on smart materials was published two years ago [4].

The International Society for the Optical Engineering (SPIE) is organizing Annual International Symposiums on Smart Structures and Materials, and NDE for Health Monitoring and Diagnostics. The scope of these two simultaneous events comprises all important aspects of the field and they are worldwide forum. As cosponsors are serving important organizations, e.g. American Society of Mechanical Engineering, Society for Experimental Mechanics, National Science Foundation, DARPA – Defence Advanced Research Projects Agency, Intelligent Materials Forum (Japan), Boeing Co.

The goal of this short presentation is to make the synthetical overview of the state of the art – in the field of the most important intelligent materials. The attention will be given to:

- shape memory alloys,
- ceramic piezoelectric materials,
- magnetostrictive materials,
- application of rheological fluids,
- intelligent (smart) polymers and polymer matrix composites.

The second part of the paper brings brief analysis of the scope of the Smart Structures / NDE Joint SPIE Conference, held at San Diego (USA), March 2004.

Synthetic overview of the most important groups of intelligent materials

Shape memory alloys (SMA)

The ability of returning a deformed piece of alloy to its initial shape under certain circumstances was discovered in 1962 but the practical applications of this property in engineering or medicine came much later. Basic studies on reversible martensic transformation make possible to find Ni-Ti, Cu-Al-Zn and Cu-Al-Ni candidate alloys for applications in such areas as automatics, safety, medical devices and many domestic appliances. Since shape change of SMA is caused by martensic transformation activated by temperature change, the working frequency of SMA is limited to 10^2 Hz.

Currently the most important appears to be research on magnetic shape memory materials and high temperature SMA. The classic SMA exploit phase transformation on thermal affect but this mechanism is slow for many applications. In magnetic SMA the memory shape effect is activated magnetically and the process is much faster. Currently Ni_2MnGa alloy (Huesler alloy) is one of prime candidates both in film and bulk forms.

Ceramic piezoelectric materials

The piezoelectric effect in some materials was discovered in 1880 but first piezoelectric ceramic materials, useful for applications, arrived 60–70 years later. The main advantage of piezoelectric materials is the ability to exhibite dimensions change in the presence of electric field. That effect is reversible and therefore a change of pressure (deformation) could be sensored. Among the variety of ceramic piezoelectric material the most important appear to be lead zirconate titanate (called PZT) and less useful barium titanate ($BaTiO_3$). Substantial drawback for many applications of piezoelectric ceramics is their brittleness. Important research goal is development of lead free materials, which can exhibit properties similar to the PZT ceramics (lead content in PZT is more than 60 percent Pb).
Piezoelectric polymers have been known for more than 40 years but many properties of those polymers are very different from those of ceramic materials and therefore they have own good established area for technical applications.
Ceramic piezoelectric materials find applications in many modern disciplines such as: automatics, micromanipulation, measuring techniques, medical diagnostic and many others.

Magnetostrictive materials

The magnetostrictive effect was first observed in 1842 for iron and later it was found in nickel, cobalt and their alloys. Magnetostrictive materials convert reversibly magnetic energy into energy of elastic deformation. Modern type of magnetostrictive materials, exhibiting effect of giant magnetostriction (giant magnetostriction materials – GMM), was proposed in 1963. The best known is Terfenol-D, not cheap because of costly alloying elements (Tb and Dy) and expensive production techniques. Currently investigations focused on cheaper alloys are performed, e.g. on gallium – iron alloys (galfenol). Areas where it could provide advantages will be identified. Potential application areas of magnetostrictive materials are generally related to their use as sensors and actuators. Magnetostrictive materials find applications in sonar devices, seismic sensors, geological tomography, hydraulic valves, sensors of motion, force and magnetic field, and many others.

Application of rheological fluids

The rheological fluids are suspension of very fine dielectric particles suspended in an insulating medium exhibiting rheological properties that change in the presence of applied electric or magnetic field. Typically the particles are 5–50 micrometers in diameter. When electric or magnetic field is applied to the fluid the particles form ordered chains. Physically the rheological fluid changes from the state of viscous oil to an almost solid gel [5]. The application of electric or magnetic field results very quickly in a significant change of the physical properties of rheological fluid. That means that electric or magnetic signals can easily change their properties.

Magnetic field has practical advantage in many applications over electric field because the generation of the field does not need very strong source (e.g. 24 V DC could be enough). For the same reason on interaction in other equipment or instruments is rather small.
Magnetorheological fluids have been used commercially since mid 1990's. Current application comprises vibration control devices (dampers) in automotive, aircraft and domestic applications. A new investigated field is application in structural monitoring and impact energy absorption, e.g. in aircraft landing gears.

Intelligent polymers

Interest in exhibiting intelligent behavior in polymers appeared much later than in the case of metallic or ceramic intelligent materials. Within last two decades the role of intelligent polymers grew rapidly due to the promising results of research proving that some polymers show properties useful for practical applications. Available scientific data indicates that current level of knowledge on various intelligent polymers differs substantially and basic reports appear parallel to matured and advanced developments, which are ready for implementations. Special focus is put on piezoelectric polymers, shape memory polymers, electroactive polymers (conductive polymers and polymer ionic gels) and stimuli-responsive polymers. As the use of intelligent materials grows, it becomes increasingly important for scientist and engineers in fields ranging from materials science to electronics and biomedicine to understand the properties and potential of intelligent polymers. The examples of intelligent polymers application in sensors and actuators, in aerospace, architecture, marine industry and medicine are also reported.

Shape-memory polymers

Polymers showing thermally induced shape-memory effect have found growing interest and have been studied intensively. The relatively easy manufacturing of shape-memory polymers (SMP) makes these materials a cheap and efficient alternative to well established metallic alloys. SMP are also distinguished by low density. They have the capacity to recover large strain imposed by mechanical loading. The unconstrained recoverable strain limits in SMP are on the order of 100%, in sharp contrast to shape memory metals. Very broad spectrum of possible application for shape-memory polymers covers the area from not invasive surgery to technical devices. The shape-memory effect results from the polymers structure that could be gained in the proper production techniques. Shape-memory behaviour can be observed for miscellaneous polymers that may differ significantly in their chemical composition. Shape-memory effect is observed in multiblok copolymers, mainly polyurethanes. The mechanism of the thermally induced shape-memory effect of linear block copolymers is based on the formation of a phase-separated morphology with one phase acting as molecular switch. As shown in Fig. 2, if the temperature is higher than the transition temperature T_{trans} (e.g. glass transition T_g or melting point T_m) of the switching segments, these segments become flexible and the polymer can be easily deformed elastically. The temporary shape is fixed by cooling down below T_{trans}. If the polymer is heated up again, the permanent shape is recovered [6].

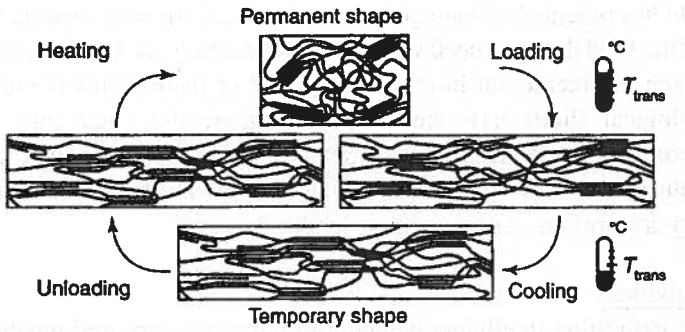

Fig. 2. Schematic illustration of the thermally induced shape-memory effect for a multiblock copolymer

Piezoelectric polymers

Piezoelectric polymers have been known for more than 40 years, but in recent years they have gained repute as a valuable class of intelligent materials. The properties of those polymers are very different from those of ceramic materials, and they are uniquely qualified to fill niche areas where ceramics cannot perform as effectively. The piezoelectric strain constant (d_{31}) for the polymer is lower than that of the ceramic. However, piezoelectric polymers have much higher piezoelectric stress constant (g_{31}) which indicates that they are much better sensors than ceramics. Piezoelectric polymeric sensors and actuators offer the advantage of processing flexibility because they are lightweight, tough, readily manufactured in large areas, can be cut and formed into complex shapes. They also exhibit high strength and impact resistance. Other notable features of piezoelectric polymers are low dielectric constant, low elastic stiffness, and low density, which result in high voltage sensitivity (excellent sensor characteristics) and low acoustic and mechanical impedance (crucial for medical and underwater applications). Polymers also typically posses high dielectric breakdown and high operating field strength, which means that they can withstand much higher driving fields than ceramics. Based on these features, piezoelectric polymers posses their own established area for technical application and useful device configurations [7].

Among the existing piezoelectric / ferroelectric polymers, PVDF – poly(vinylidene fluoride) and its copolymers P(VDF-TrFE) – poly(vinylidene fluoride-trifluoroethylene) and P(VDF-TFE) – poly(vinylidene fluoride-tetrafluoroethylene) exhibit the best electromechanical performance. The copolymer P(VDF-TrFE) containing 50–80 mol% VDF has been attracted lots of attention because the materials can be easily prepared to have ferroelectric phase, which exhibits piezo- and pyro-electricity [8]. The electromechanical characteristic of PVDF-based polymers originates from the crystalline regions in the material. The morphology of such polymers consists of crystallites dispersed within amorphous regions, as shown in Fig. 3. The structure of the crystalline regions is non-polar. To convert the structure from non-polar to polar phase with a large strain response the apply of external electric field is needed. The polarization can remain constant for many years if it is not degraded by moisture uptake or elevated temperatures. These semicrystalline fluoropolymers are currently the only commercial piezoelectric polymers.

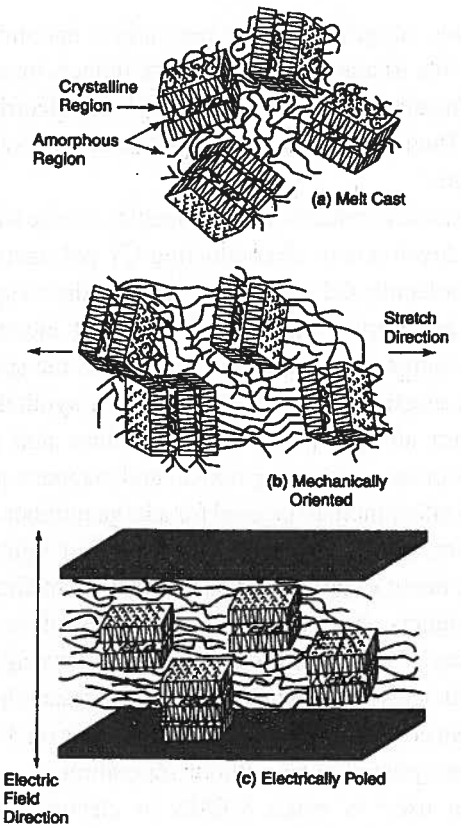

Fig. 3. Schematic illlustration of random stacks of amorphous and crystal lamellae in PVDF polymer

Other semicrystalline polymers including odd-numbered polyamides, polyureas, liquid crystalline polymers, biopolymers are still in the stage of studies.

Typical applications of piezoelectric polymers are sensing and actuating devices in medical instrumentation, robotics, optics, computers and also ultrasonic, underwater and electroacoustic transducers [7].

Electroactive polymers

Electroactive polymers (EAP) are one the most important and promising group of intelligent polymers. They respond to electrical stimulation with a significant shape or size change. They are lightweight and easy to control. EAP materials can be easily formed in various shapes, their properties can be engineered, and they can potentially be integrated with micro sensors to produce actuators.

The available EAP materials can be divided into two distinct groups: electronic (driven by electric field or Coulomb forces) and ionic (involving mobility or diffusion of ions) [9]. The first group includes such polymers as electrostrictive, dielectric, ferroelectric and liquid crystals. The second, among others includes conductive polymers, ionic gels and also

polymer-carbon nanotubes composites. Polymer-carbon nanotubes based nanoactuators and robotic systems are able to manipulate nano-size objects in a controlled, reproducible and reversible manner. The electronic EAP are driven by an electrical field and they require high activation voltage. The ionic EAP are involved with the mobility or diffusion of ions and require lower voltage.

The discovery of electrical conductivity in molecular charge transfer (CT) complexes in the 1950s promoted the development of conducting CT polymers. In 1980 was found the superconductivity with molecular CT complexes. The conductivity in CT complexes arises from the formation of appropriate segregated stacks of electron donor and acceptor molecules and a certain degree of charge transfer between the stacks. Various conjugated polymers with excellent electrical properties have been synthesized during the past 25 years. The most common are polypyrolles, polyanilines and polythiophenes. Certain conjugated polymers also posses interesting optical and magnetic properties. These unusual optoelectronic properties allow them to be used for a large number of applications including sensing devices, actuators, non-linear optical devices and light emitting displays [10]. Various applications are being explored for such fields as medical, aerospace, entertainment and consumer products. The recent development of sensor arrays (conducting polymer electronic "noses", DNA chips, etc.) is revolutionizing the way in which many chemical and biomedical tests are performed in both research and clinical diagnostic laboratories. Sensor arrays consist of many different sensors on a single chip and enable to identify complex mixture systems even without separation.

EAP have also been used to make MEMS or electrochemomechanical actuators – exploited as "artificial muscles". Actuators based on conjugated conducting polymers are capable of producing at least 10 times more force per unit cross-sectional area than biological muscle, with strain typically between 1 and 10%. The high force-generation capabilities, high work densities per cycle and low operation voltages make conducting polymer actuators very attractive for use in robotics, prosthetics and microelectrochemomechanical systems and many others, in place of conventional electrostatic and piezoelectric actuators. However, before the commercialisation some of the major problems must be solved, including the limitations of the cycle life, energy conversion efficiency and their relatively slow speed.

Dielectric elastomers are of particular interest for the present application due to their high actuation speed and very large strains. The dielectric elastomer actuator is a three-component system consisting of a soft dielectric elastomer between two compliant electrodes, as shown in Fig. 4A. Application of an electric field polarizes the elastomer, generating a "state of stress" within the dielectric medium called the Maxwell stress. Coulomb forces arise between the oppositely charged electrodes, and the actuator stretches in the directions perpendicular to the force and thins in the direction parallel to the force (Fig. 4B) [11].

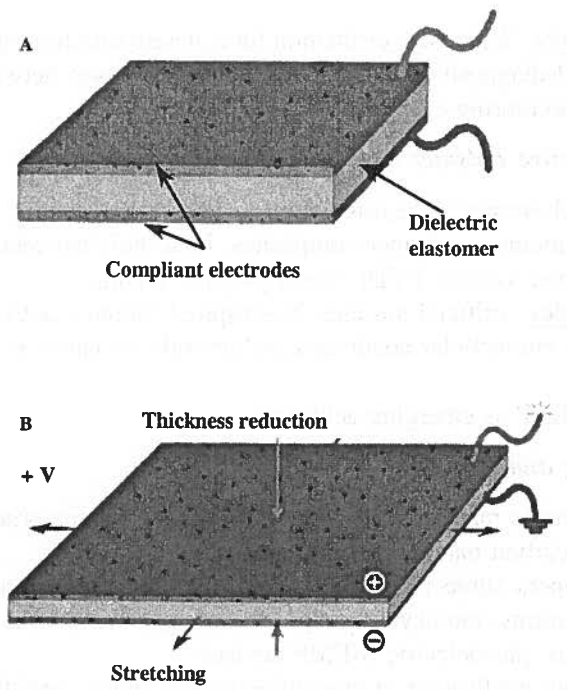

Fig. 4. Dielectric elastomer actuator

State of the art – in the year 2004

The International Society for Optical Engineers (SPIE) is sponsoring annual Smart Structures / NDE Joint Conferences. The last conference "Smart Structures and Materials 2004 and Nondestructive Evaluation for Health Monitoring and Diagnostics 2004", held in San Diego in March 2004, is giving a very good insight in the field of smart structures and materials. The conference proceedings [12] contain about 800 papers, 90 percent of them directly out of the field of smart structures and materials. The scope of the proceedings brings following information:

Topic 1: Modelling, Signal Processing, and Control

Materials: piezoceramic (PZT), shape memory alloys, ferroelectric materials, magneto-strictive materials, ionic polymers.
Research areas: applications, optimisation, control design.
Important notice: advanced mathematical approach (e.g. Finite Elements Method, modelling), no PZT substitutes considered.

Topic 2: Smart Sensor Technology and Measurement Systems

Sensors (materials): fiber optic sensors, fiber grating sensors (e.g. Bragg grating sensors), electrical and acoustic sensors, piezoceramic sensors, photonic crystal fibers.

Application examples: 'KDamage evaluation for concrete structures using fiber-reinforced composites as self-diagnosis", "Wireless intelligent sensor network for autonomous structural health monitoring".

Topic 3: Electroactive Polymer Actuators and Devices (EAPAD)

Materials: electroelastomers, electrostrictive polymers, conducting polymers, dielectric elastomers, shape memory polymer composites, ionic polymer-metal composites, novel electroactive polymer system: PVDF-based polymer blends.
Application examples: artificial muscles, bio-inspired robotics, active pump applications, sensor to monitore intracellular conditions, polypyrolle actuators as valves for controlled drug delivery.
Important notice: EAP as emerging actuators.

Topic 4: Damping and Isolation

Materials: piezoelectric materials, shape memory alloys, magnetorheological fluids, hard ceramic coatings, carbon nanotubes (in composites).
Applications: dampers subjected to impact loading (e.g. on aircraft landing gears, in wheeled vehicles, trains, motocycle, suspended mass), vibration isolation and damping, seismic applications, piezoelectric MEMS devices.
Important notice: no application of electrorheological fluids considered.

Topic 5: Active Materials: Behavior and Mechanics

Materials: ionic polymers, carbon nanotubes – polymer composites, piezoelectric materials, ferromagnetic shape memory alloys, single crystal and polycrystalline magnetic shape memory effect alloys (e.g. Ni-Mn-Ga), iron-gallium single-crystals, Cu-Al-Ni single crystals, Fe-Mn-Si, piezoceramics (PZT and lead magnesium niobate), magnetic materials Gal – fenol, Fe-Ga, Fe-Ga-Al, Terfenol-D.
Applications: mechanical and medical application, microvalves..
Important notice: multifuncional composites considered, research concentrated on magnetic shape memory effect alloys.

Topic 6: Industrial and Commercial Applications of Smart Structures Technologies

Materials: shape-memory alloys and polymers, magnetostrictive materials, magnetorheological fluids, fiber Bragg grating (sensors).
Application examples: adaptive aerostructures (e.g. adaptive wing structures), reduction of aerodynamic vibrations, dampers, space application, in microlithography.

Topic 7: Smart Electronics, MEMS, BioMEMS, and Nanotechnology

Materials: polymer and ferroelectric thin film, ceramic thick film, piezoelectric materials, smart materials based on carbon nanotubes, metallic closed cellular materials containing organic materials, funcionalized nanomaterials (electroceramic, protein/polymer, tin oxide/carbon), electroactive polymers, carbon black-polymer composites, resistive nanomaterials.

Applications: MEMS, BioMEMS, micro-, bio- sensors, actuators, fuel cells, power devices.
Examples: "Fabrication of cell structures for bionanobattery", "Electrochemical reconstitution of biomolecules for applications as electrocatalysts for the bionanofuel cell".

Topic 8: Smart Structures and Integrated Systems

Materials: piezoelectric materials (piezoceramics PZT), active fiber composites, Terfenol-D, magnetorheological fluids, dielectric elastomers, shape memory polymer, electroactive smart polymers, ferromagnetic shape memory alloy composites, fiber Bragg grating.
Applications: actuators (ex.: shape memory polymer actuators), sensors (ex.: fiber optic sensors, fiber Bragg grating sensors), MR fluid brake, pumps, vibration reduction, variable shape systems, control of smart structures (ex.: "Numerical simulation of actuation behavior of acctive fiber composites in helicopter rotor blade application"), flow control (and actuation).

Topic 9: Sensor and Smart Structures Technologies for Civil, Mechanical, and Aerospace Systems

Materials: piezoelectric materials, optical fibers, fiber optic cables, magnetorheological fluids, dielectrostriction effect polymeric materials, fiber Bragg grating.
Applications: sensors (piezoelectric active sensors, fiber grating sensors, fiber Bragg grating sensors, optical fiber sensors), MEMS, degradation and damage detection (ex.: "Bolt loosening detection using vibration characteristic of thin plate with piezoelectric elements", "Embedded MEMS for health monitoring and management of civil infrastructure"), structural health monitoring (bridges, composite elements).

Topic 10: Testing, Reliability, and Application of Micro- and Nano-material. Nondestructive Evaluation and Health Monitoring of Aerospace Materials and Composites, Structural and Biological System

Advanced research: Techniques: X-ray, reflection topography, computer tomography,, atomic force microscopy, position annihilation spectroscopy, acoustic emmision diagnostics, Barkhausen noise and eddy current microscopy, scanning probe (image) microscopy, ultrasonic characterization, eddy current sensors, MEMS and NEMS sensors.
Applications: degradation and damage location in aerospace (aircraft) structures, civil engineering structures, biological and medical applications.

Summary

The scope of proceedings allows formulation of general conclusions:

- The field of smart structures and materials is growing rapidly, the research teams are great in number and experience.
- All papers are reporting results of basic research oriented on application or R and D projects. Present day advanced research techniques and mathematical approach were applied.

– A great number of papers apply to important or novel smart materials, i.e. magnetic shape memory alloys, magnetorheological fluids, smart polymers and polymer composites or piezoelectric ceramics.

REFERENCES

[1] T. Takagi, J. Intel. Mat. Systems and Struc. **10**, 575-581 (1999).
[2] P-F. Gabin, G. Guenin, M. Marin, M. Salvia, J. Tatibonet, J. Intel. Mat. Systems and Struc. **7**, 353-357 (1996).
[3] W.B. Spillman, J.S. Sirkis, P.T. Gardiner, Smart Mater. Struct. **5**, 247-254 (1996).
[4] Encyclopedia of Smart Materials, edited by Mel Schwartz, Wiley & Sons, (2002).
[5] H.S. Tzou, G.L. Anderson, Intelligent Structural Systems, Kluwer Academic Publishers, p. 1-8 (1992).
[6] Encyclopedia of Polymer Science and Technology, vol. 4, Wiley & Sons, **125-136**, 510-532 (2003).
[7] Encyclopedia of Smart Materials, edited by Mel Schwartz, **2**, Wiley & Sons, 860-873 (2002).
[8] Z. Li, M.D. Arbatti, Z.Y. Cheng, Proceedings of SPIE **5385**, 99-107 (2004).
[9] Y. Bar-Cohen, Proceedings of SPIE **5385**, 10-16 (2004).
[10] L. Dai, Intelligent Macromolecules for Smart Devices; Springer **41-72**, 406-423 (2004).
[11] N. Goulbourne, M. Frecker, E. Mockenstrum, Proceedings of SPIE **5385**, 122-133 (2004).
[12] Proceedings of SPIE **5383-5395** (2004).

Received: 3 November 2004.

A R C H I V E S O F M E T A L L U R G Y A N D M A T E R I A L S
Volume 49 2004 Issue 4

J. VAN HUMBEECK *

SHAPE MEMORY ALLOYS: MULTI-PURPOSE FUNCTIONAL MATERIALS

STOPY Z PAMIĘCIĄ KSZTAŁTU: WIELOZADANIOWE MATERIAŁY FUNKCJONALNE

Shape memory alloys (SMA) are not exclusively derived from intermetallic compounds. Also solid solutions based on an element having allotropic phases or specific Fe-based alloys with a $\gamma \leftrightarrow \varepsilon$ transition or certain alloys showing a cubic to tetragonal phase have clearly revealed similar functional properties as some definite intermetallic solid solutions with a bcc-parent phase.

However so far only the intermetallic structures became successful industrial alloys. The first condition for good shape memory effects (SME) is the occurrence of a reversible (thermo-elastic) martensitic transformation. Other important factors for successful SME is the ability of matrix strengthening by ordering, precipitation or cold deformation. The combination of those requirements are excellently fulfilled by the NiTi intermetallic compound, being presently the far most applied system. Also β-Hume-Rothery phases such as the β Cu-, Ag-, Au-based alloys, or intermetallic phases such as β Cu-Zr and β Ni-Al are very much investigated. This paper will describe and compare those important intermetallic SMA and the alloys derived there of.

Stopy z pamięcią kształtu (SMA) nie są wyłącznie związkami międzymetalicznymi. Także roztwory stałe, bazujące na pierwiastkach występujących w postaci faz alotropowych, lub niektóre stopy na bazie Fe, podlegające przemianie $\gamma \leftrightarrow \varepsilon$ i z przemianą fazy regularnej w tetragonalną mają podobne własności funkcjonalne jak określone roztwory stałe, z fazą macierzystą o strukturze bcc.

Jednakże, jak dotychczas, jedynie związki międzymetaliczne znalazły zastosowanie jako stopy przemysłowe. Podstawowym warunkiem dla uzyskania dobrego efektu pamieci kształtu (SME) jest występowanie odwracalnej (termosprężystej) przemiany martenzytycznej. Inny ważny warunek uzyskania dobrego efektu pamieci kształtu to możliwość umocnienia fazy macierzystej poprzez uporządkowanie atomowe, wydzieleniowe lub poprzez przeróbkę plastyczną na zimno.

Związek międzymetaliczny NiTi, mający obecnie największe zastosowanie, wykazuje doskonałą kombinację powyższych wymagań. Intensywnie badane są także stopy na bazie β Cu-, Ag- i Au, należące do faz β- Hume – Rothery'ego i fazy miedzymetaliczne takie jak β Cu-Zr i β Ni-Al. W artykule przedstawiono i porównano ważne związki międzymetaliczne wykazujące efekt pamięci kształtu i stopy pochodne.

* KASTEELPARK ARENBERG 44, B-3001 LEUVEN, BELGIUM

1. Introduction

The functional properties of shape memory alloys (SMA) are related to a (diffusionless) martensitic transformation. For most SMA this martensitic transformation is thermoelastic but also some Fe-based shape memory alloys exhibiting a non-thermoelastic transformation have been developed. The principles of a martensitic transformation are very well explained by C o h e n et al. [1].

TABLE 1

Classification of the Nonferrous Martensites [2]

Group	Alloy System
Termina Solid Solutions based on an element having allotropic phases	Cobalt and its alloys Rare earth metals and their alloys Titanium, Zirconium and their alloys Alkali metals and their alloys and Thallium Others as Pu, Ur, Hg and alloys
Intermetallic solid solutions with a bcc-parent phase	β-Hume-Rothery phases of the Cu-, Ag-, Au-based alloys β-Ni-Al alloys Ni-Ti-X alloys
Alloys showing cubic to tetragonal trans. (incl. quasi-martensite)	Indium-based alloys Manganese based alloys (paramagn. ↔ antiferromagn.) A15-compounds Others: Ru-Ta, Ru-Nb, Y-Cu, LaCd, $LaAg_x$-In_{1-x}

Many systems exhibit a martensitic transformation. Generally they are subdivided in ferrous and non-ferrous martensites. A classification of the Nonferrous Martensites was first given by D e l a e y et al. [2], Table 1, while ferrous alloys exhibiting a shape memory effect were first reviewed by T. M a k i and T. T a m u r a [3], Table 2.

TABLE 2

Ferrous alloys which exhibit a complete or nearly complete shape memory effect [3]

Alloy	Composition	Crystal structure of martensite	Nature of transformation*
Fe-Pt	≈ 25at%Pt	bct (α')	T.E.
	≈ 25at%Pt	fct	T.E.
Fe-Pd	≈ 30at%Pd	fct	T.E.
Fe-Ni-Co-Ti	23%Ni-10%Co-4%Ti	bct (α')	–
	33%Ni-10%Co-4%Ti	bct (α')	T.E.
Fe-Ni-C	31%Ni-0.4%C	bct (α')	Non-T.E.
Fe-Mn-Si	30%Mn-1%Si	hcp (ε)	Non-T.E.
	28~33%Mn-4~6%Si	hcp (ε)	Non-T.E.

* T.E.: Thermoelastic martensite, Non-T.E.: Non thermoelastic martensite

From all systems mentioned in both tables, only the intermetallic solid solutions with a (ordered) bcc parent phase delivered interesting potential commercial systems. From these, in fact, only one major system became industrial successful: NiTi(X,Y) in which X,Y are elements replacing Ni or Ti. Besides the NiTi system a lot of attention has been given in earlier times to Cu-based alloys [4] and to Fe-Mn-Si-based alloys [5]. Furthermore, during recent years special attention has been given to high temperature shape memory alloys (HTSMA), based on ternary NiTi alloys, CuAlNi or CuZr alloys [6].
In this paper we will describe short the functional properties, the most important and interesting intermetallic alloy systems, exhibiting those functional properties and a short view on applications.

2. Functional properties of shape memory alloys

Shape memory alloys show different functional properties and can be used in different ways. For most of those properties a shape change is at the origin of the property. This shape change is a consequence of the shearing component of the martensitic variants during martensitic transformation. The so called "cold shape" is thus related to the martensite phase, while the material has its "hot shape" when in the austenitic phase.

These properties are described in general terms below. Quantitative data refer to Ni-Ti alloys unless otherwise stated.

2.1. One way shape memory effect

A shape memory element can be easily deformed to almost any "cold shape". The basic restriction is that the deformations may not exceed a certain limit, typically 8% for NiTi somewhat lower for Cu-based and Fe-based shape memory alloys. These apparent plastic deformations can be recovered completely during heating, resulting in the original "hot shape". This strain and shape recovery during heating is called the *one way shape memory effect* since only the hot shape is memorised.

2.2. Two way shape memory effect and training

The two way memory effect refers to the memorisation of two shapes. A cold shape is obtained spontaneously during cooling from the hot shape, that had been obtained by the former thermo-mechanical processing. Different from the one way memory effect, no external forces are required to obtain the "memorised" cold shape. During subsequent heating the original hot shape is restored. The maximum strains are in general substantially smaller than in the case of the one way memory effect. A strain limit of about 2% has been mentioned although higher TWME strains have been found in specific cases.

The microstructural asymmetry and the resulting TWME are not inherent characteristics of shape memory alloys, as the one way effect, but can only be induced after particular thermomechanical procedures. These thermomechanical procedures are in general based on the repetition of thermomechanical cycles through the transformation region [8, 7, 9], i.e. transformation cycles from the parent phase to preferentially oriented martensite. The goal of these repetitive procedures is to acquire the cold shape and therefore these procedures are referred to as "training". Some examples of such training procedures are temperature cycling at a constant strain or at a constant stress, and superelastic cycling. It can be easily understood that many combinations and variants of these procedures can also be applied.

2.3. Superelasticity

The shape memory effects described above require temperature changes. In contrast, the superelastic effect, also indicated as pseudoelastic effect, is isothermal in nature [10, 11]. A superelastic specimen exhibits normal elastic behaviour until a critical stress is reached. With further stressing, the specimen elongates substantially as if it were plastically deformed. However when the stress is removed, the specimen contracts to its original dimension and the apparent plastic strain is recovered.

Superelasticity can be considered as the mechanical analogue of the thermal shape memory effect. Isothermal loading at a temperature above A_f results in a stress induced martensitic transformation which starts at a critical stress σ_{Ms}. Further straining occurs at a nearly constant stress level until the transformation finishes at σ_{Mf}. The apparent plastic strain is thus caused by the shape strain accompanying the stress induced formation of preferentially oriented martensite. During subsequent unloading, the reverse transformation occurs at a lower stress level between σ_{As} and σ_{Af} and the apparent plastic strains are recovered. Large reversible deformations of up to 10% can be obtained, to be compared to 0.2%-0.5% elastic strain in most other metallic alloys. Further straining at stress levels above σ_{Mf} results in elastic straining of the stress induced martensite, followed at σ_y by plastic yielding of martensite.

The stress induced transformation shows a stress hysteresis, revealed by the different stress levels for the forward and reverse transformation. This hysteresis is typically 150-300 MPa in NiTi and results in the dissipation of energy during superelastic cycling. The energy dissipated per cycle is given by the area enclosed between the upper and lower curve. Superelasticity also involves the storage of potential energy. This elastic energy storage capacity can be as high as 10 J/g. All above mentioned superelastic characteristics are strongly affected by processing and composition [12, 13].

The critical transformation stresses (σ_{Ms}, σ_{Mf}, σ_{As} and σ_{Af}) increase in a first approximation linearly with temperature starting from zero at the corresponding transformation temperature, as described by the Clausius-Clapeyron equation:

$$\frac{d\sigma}{dT} = \frac{\Delta S}{\epsilon_{max}}$$

in which σ is the stress at which martensite is induced, T the temperature, ΔS the entropy change during transformation and ε_{max} the maximum strain due to transformation. It follows that at a temperature, denoted as M_d, the stress for plastic yielding becomes equal to the stress for martensite formation. Superelasticity occurs thus only over a relatively narrow temperature window between the temperatures A_f and M_d. This temperature range of typically 20-100 K is too small for applications in most industrial and consumer fields. The strong temperature dependence of the mechanical behaviour, described by the Clausius-Clapeyron equation, is a further impediment to the general use of superelasticity [14].

The temperature dependence and small temperature range are no barrier to the use in mammalian bodies where the temperature is constant. Moreover, the superelastic effect results in a unique combination of deduced properties. No other material or technology can offer the combination of high strength, high stiffness, high pliability and a high kink resistance. NiTi with a proper surface treatment shows an excellent biocompatibility. Also the concept of a metallic material with an extreme elasticity and with nearly constant stress levels over a large strain area is something that can be tackled easier by designers than the concepts related with temperature activated shape memory effects [Me94]. Accordingly, the largest commercial successes of SMAs in recent years are linked with the use of superelasticity in biomedical applications [14, 15, 16]. Other advantages related to superelasticity and relevant for medical applications have been described in detail by Duerig et al. [14].

2.4. Generation of recovery stresses

When an external constraint prevents the SMA-element from returning to the hot shape on heating, high recovery stresses are gradually generated during heating. Stresses up to 700 MPa can be obtained [17].

Similar to the one way and two way memory effect, the generation of recovery stresses starts from a macroscopic deformation in the martensitic state. During subsequent heating free recovery occurs until a temperature T_c at which contact is made with an external mechanical obstacle. The recovery of the remaining deformation, characterized by the contact strain e_c, is impeded by this obstacle. Therefore, from the temperature T_c recovery stresses are generated at a nearly constant stress rate $d\sigma_r/dT$, often described by a Clausius-Clapeyron equation. This shape memory property is the basis of some very successful shape memory applications, especially in earlier years for couplings [18, 19].

The recent substantial efforts in the development of hybrid composites with embedded shape memory elements have resulted in an increasing interest in the understanding of the generation of recovery stresses [20, 21, 17, 22]. In these smart composites, thin SMA-wires or other SMA-elements are embedded into advanced structural materials, without losing the structural integrity of the matrix material. Most functional properties of such adaptive

composites are directly related to the following mechanism on the level of the SMA-elements. Prestrained martensitic SMA-elements operate during heating against he elastic stiffness of the host matrix, biasing the strain recovery and the reverse transformation of the SMA-elements. The result is that recovery stresses are generated gradually by the SMA-elements in the composite during heating, and the strain recovery and reverse transformation of the SMA-elements is delayed. After overcoming a temperature hysteresis, the reverse process occurs during cooling. A crucial difference with earlier applications using the generation of recovery stresses is that these hybrid composites are activated repeatedly, i.e. recovery stresses are generated cyclically.

2.5. Work output

The one and two way memory effect can be used for free recovery applications in which the single function of the SMA-element is to cause motions without any biasing stress. At constant strains, shape memory elements can generate substantial recovery stresses. Between these two extremes of free recovery and completely constrained recovery, shape memory components can yield a wide variety of combinations of strains and stresses. The shape memory element can be deformed with a low force in the martensitic condition or during the forward transformation, and can exert a substantially higher force as it reverts to the hot shape on heating. So, work is done on heating, up to 5 J/g. This concept can be used in thermal actuators in which the SMA-element is activated by an increase in the environmental temperature, or in electrical actuators in which the SMA-element is in general activated by direct Joules heating. The work needed to deform the SMA-element is much lower than the work that can be obtained during heating. This has been the basis of many prototypes of heat engines which could convert heat into useful work (see e.g. [23].

SMA-actuato rs offer distinct advantages with respect to other types of actuators [24]. The main advantage is that SMA-actuators offer by far the highest work and power to weight ratios from all available actuating technologies at low levels of weight [25]. These high work and power densities enable a whole class of applications (e.g. in the field of micro-actuation) which are simply impossible to realise with other actuation technologies. SMA-actuators can mostly be reduced to a single SMA-element without auxiliary parts, resulting in a simple compact and reliable device.

Several important drawbacks which limit the use of SMA-actuators to specific niches, should also be considered. The conversion of heat into mechanical energy via SMA-actuators has been studied extensively 15 to 25 years ago. Simple thermodynamic calculations have shown that the maximum theoretical efficiency of an SMA-actuator is below 10% [26]. In practice, the conversion of heat into mechanical work occurs less efficient with the result that the real efficiency is even one order of magnitude smaller than the theoretical value. Another drawback is that the SMA-actuator has to be heated and cooled. Especially the low cooling rate limits the use of SMA-actuators to relatively low frequency applications.

2.6. High damping capacity

SMA-elements have a high damping capacity in the austenitic and martensitic condition. Shape memory alloys show in the martensitic condition a strong amplitude dependent internal friction. For impact loads, the specific damping capacity can be as high as 90%. Starting from the austenitic condition, energy is dissipated during superelastic cycling as a result of the stress hysteresis between superelastic loading and unloading, as explained before. A detailed analysis can be found in [27].

3. Intermetallic sma-alloy systems

3.1. Cu-based systems [4, 28]

Copper based shape memory alloys are derived from Cu-Zn, Cu-Al and Cu-Sn systems. The composition range of these alloys corresponds to that of the well-known β Hume Rothery phase. In most shape memory alloys, this phase has a disordered bcc structure at high temperatures but orders to a B2, $D0_3$ or $L2_1$ form at lower temperatures. The shear elastic constant of the β phase exhibits an anomalous behaviour with decreasing temperature, i.e. it is lowered till the lattice instability with respect to $\{110\}\langle 1\bar{1}0\rangle$ shears at some temperature transforms β to martensite. The elastic anisotropy of the β phase is much higher compared to normal metals and alloys and increases further as the martensitic transformation is approached.

Cu-Zn and Cu-Al martensites are of three types α', β' or γ' with subscript 1, 2 or 3 added to indicate the ordering schemes in β, viz. B2 (2) or $D0_3$ (1) or $L2_1$ (3). Some conversion from one martensite structure to another, e.g. $\beta' \rightarrow \gamma'$ may also take place. The net result is a coalescence of plates within a self-accommodating group and even coalescence of groups. Heating this deformed martensite microstructure transforms it to the β phase with the shape memory effect accompanying the structural change.

The transformation temperatures are apart from the composition strongly influenced by other chemical and non-chemical factors, such as the degree of order of the parent phase, the stabilisation of the martensite phase, the presence of precipitates, impurities, grain size, lattice defects, ...

So the global thermomechanical processing will have an influence on the final transformation temperatures.

In order to obtain good functional properties, the parent phase has to be retained at low temperatures by fast cooling (quenching) in order to avoid the growth of alfa- or gamma-phase which are thermodynamically more stable at low temperatures.

This makes that the functional properties can only be obtained at low temperatures where diffusion is (almost) not occurring, limiting the martensitic transformation temperatures below 100°C.

TABLE 3

Actual industrial Cu-based alloys

Base alloy	Composition Wt %	Ms (°C)	Hyst. (°C)	Other alloying elements in solution (%)	Current grain refining elements producing precipitates	Remarks on the base alloy
Cu-Zn-Al	5-30 Zn 4-8 Al	-190- + 100	10 (β')	Ni -5%) Mn (-12%)	Co (CoAl)); B (AlB_2); Zr (?); B, Cr (Cr_xB_y)	– good ductibility and reproducibility – prone to martensite stabilisation – poor β-stability (T > 200°C)
Cu-Al-Ni	11-14.5 Al 3-5 Ni	-140- + 200	10 (β') 40 (γ')	Mn (-5%)	Ti ($(Cu, Ni)_2$ TiAl); B (AlB_{12}); Zr (?)	– low ductility – low mar. stabilisation – good β-stability
Cu-Al-Be	9-12 Al 0.4-1 Be	-80- + 80	6 (β')	Ni (-5%)	B (AlB_2 or AlB_{12}) Ti (Cu_2TiAl)	– poor reproducibility – excellent β-stability (T > 200°C)

But transformation temperatures are in generally not only restricted because of atom diffusion. A second important factor is that the yield stress, either of martensite either of the parent phase decreases with increasing temperatures. In order to obtain good functional properties, plastic deformation has to be avoided in all circumstances. As a consequence initial strengthening of the parent phase can be a good solution to increase the temperature of applications.
Table 3 summarizes some Cu-based alloys that enjoy a (limited) industrial interest.

3.2. Ni-Ti alloys

$Ni_{80}Ti_{50}$ is the best explored system of all shape memory alloys and occupies almost the whole market of SMA. $Ni_{80}Ti_{50}$ is an intermetallic phase that has some solubility at higher temperatures.

The science and technology of Ni-Ti is overwhelmingly documented. The influence of composition and thermomechanical processing on the functional properties is well understood and described in literature. Therefore we refer only to some very interesting and relevant publications such as [29-32].

The basic concept of processing Ni-Ti alloys is that in order to avoid plastic deformation during shape memory or during pseudoelastic loading, the martensitic and the β-phase have to be strengthened. This occurs by classic methods: strain hardening during cold deformation, solution hardening, precipitation hardening. Ni-Ti alloys have the significant advantage that these techniques can be easily applied due to an excellent ductility and a very interesting but complicated precipitation process of metastable and stable neighbouring intermetallic phases [33].

The compositions of the Ni-Ti-SME alloys are approximately between 48 and 52 at % Ni and the transformation temperatures of the B2 structure to the martensitic phase with a monoclinic B19' structure, are very sensitive to the nickel-content (a decrease of about 150 degrees for an increase of 1 at % Ni). The transformation temperatures can be chosen between −40°C and +100°C.
Ni-Ti alloys show the best shape memory behaviour of all SMA. Even in polycrystalline state 8% shape recovery is possible and 8% pseudo-elastic strain is completely reversible above A_f, while the recovery stress is of the order of 800 MPa.

In some cases the martensitic transformation is preceded by the so-called R-phase transition. The R-transition is a B2 ↔ rombohedral transformation that has also second-order characteristics [34].

The most specific characteristics of this R-phase transition is that it shows a clear one- and two-way memory effect in the order of 1% recoverable strain and that the hysteresis of the transformation is very small, only a few degrees which creates possibilities for accurately regulating devices.

It should be noted that further cooling transforms the R-phase into B19' martensite. During heating only the reverse martensitic transformation will be observed. To observe the reverse R-phase transition cooling should be stopped above M_s.

It has been shown that the appearance of the *R*-phase depends on composition, alloying elements and thermomechanical processing [32]. In fact the major common point is that all effects depressing the martensitic forward transformation below room temperature will favour the appearance of the R-phase transition which is quite stable near 30°C.

3.3. Ternary Ni-Ti alloy systems

Addition of third elements opens even more possibilities for adapting binary Ni-Ti alloys toward more specific needs of applications. Adding a third element implies a relative replacement of Ni and/or Ti. Therefore it must be always very well indicated which atom Ni or Ti or both is replaced by the third element.

Alloying third elements will influence not only the transformation temperatures but will also have an effect on hysteresis, strength, ductility, shape memory characteristics and also on the B2→(R)→B19' sequence. The influence of several elements has been already described in [35-38].

More application oriented, one can distinguish four purposes to add third elements:
1. to decrease (Cu) or increase (Nb) the hysteresis,
2. to lower the transformation temperatures (Fe, Cr, Co, Al),
3. to increase the transformation temperatures (Hf, Zr, Pd, Pt, Au),
4. to strengthen the matrix (Mo, W, O, C).

Some of the ternary alloys have been developed for large-scale applications. We will only summarise the two most well developed: NiTiCu and NiTiNb and the Ni(Ti,X) with X=Hf, Zr which are under investigation as High Temperature Shape Memory Alloys (HTSMA).

Ti-Ni-Cu

Ternary Ti-Ni-Cu alloys in which mainly Ni is substituted by Cu are certainly as important as binary TiNi. Increasing Cu-content decreases the deformation stress for the martensite state and decreases also the pseudoelastic hysteresis without affecting significantly the M_s-temperature [39]. However, more than 10% Cu addition embrittles the alloys, hampering the formability.

It should also be remembered that while TiNi transforms from a B2 into a monoclinic phase, Ti-Ni-Cu exceeding 15 at % Cu transforms from a B2 into an orthorhombic phase. Ti-Ni-Cu with less than 15 at % Cu transforms in two stages [32].

A disadvantage of most Ti-Ni-Cu alloys is that the transformation temperatures do not decrease below room temperature. In order to obtain pseudoelastic alloys at room temperature but with small hysteresis Cr or Fe can be alloyed. This way an $Ni_{39.8}$ $Ti_{49.8}$ Cu_{10}

$Cr_{0.4}$ alloy has been developed with a small hysteresis (130 Mpa), one fourth compared with Ni50 Ti50 and Ms below room temperature [40].

Ti-Ni-Nb [41, 42]

The inherent transformation hysteresis of NiTiNb is larger than for binary Ni-Ti alloys. By the presence of a large dispersed volume fraction of deformable β-Nb particles, the hysteresis can be further widened by an over-deformation of stress-induced martensite, generally between Ms and Md. Originally NiTiNb (more specifically $Ni_{47}Ti_{94}Nb_9$) was developed by Raychem Corp. for clamping devices. The large shift of the reverse transformation temperatures from below to above room temperature by deformation, allows room storage for open couplings.

Recently, also pseudoelastic Ni-Ti-Nb alloys have been developed with three significant differences relative to binary alloys [42]

- stress rate is much lower
- the $\sigma^{P\text{-}M}$ stresses are much higher
- the superelastic window is much larger

Ni(Ti-X), X = Hf,Zr

Those alloy systems have been investigated quite significantly, mainly because of the much lower price for the raw materials as compared with the alloys which will be described in the next part and are based on noble metals (Au, Pd, Pt). Very detailed studies can be found in [43, 44] and several patents have been issued [45, 46]. Other relevant literature that can be helpful to come to a complete literature survey can be found in [47, 48].

Figure 1 [46] summarises the behaviour of the transformation temperatures. A_p is the temperature at the calorimetric peak (endothermic) position during the reverse transformation and is thus situated between A_s and A_f. M_p can be analogously defined during cooling and is thus situated between M_s and M_f. The most important characteristics of this type of alloys, based on the above mentioned literature can be summarised as follows:

- the addition of Hf and Zr increases the stress for reorientation which can lead to increased plasticity during deformation at higher temperatures.
- the materials become harder and less ductile.
- only one-way shape memory effect has been observed so far. Complete recovery is limited to a few percent.
- the best shape memory behaviour is obtained when the material is deformed just above M_s. This leads to the optimal variant formation, avoiding reorientation.
- The hysteresis of the martensitic transformation becomes larger.
- Lowering of transformation temperatures during cycling or ageing a high temperature.

According to [43] the advantages of one system relative to the other can be summarised as follows.

Advantages of Ni-Ti-Zr over Ni-Ti-Hf:
- the slightly smaller hysteresis for alloys with the same transformation temperatures
- the lower price of Zr as compared to Hf

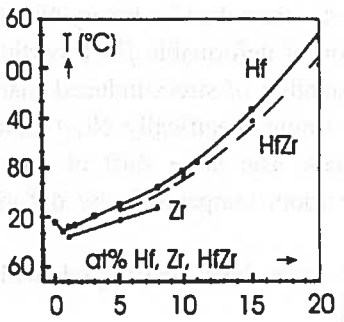

(a)

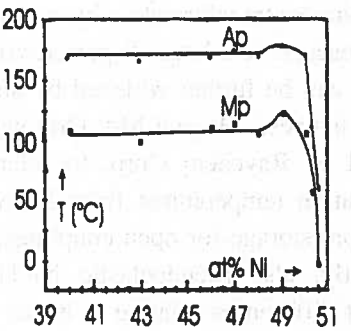

(b)

Fig. 1a: Ap as a function of Hf + Zr, Zr or Hf content for $Ni_{49}Ti_{51-x}Zr_{0.5x}Hf_{0.5x}$ and $Ni_{49}Ti_{51-x}Hf_x$ [46]
Fig. 1b: Mp and Ap as a function of Ni content for Ni_{40+y} Ti_{50-y} Hf_{10} alloys, as melted [46]. Ap and Mp are respectively the calorimetric peak-position on the temperature scale during the reverse and the forward reaction

Advantages of Ni-Ti-Hf over Ni-Ti-Zr are:
- the higher transformation temperatures for the same third element content
- the lower oxygen content of commercially available Hf as compared to Zr
- the lower affinity for O of Hf as compared to Zr
- a larger temperature range for hot working due to the slightly higher peritectic and melting point.

$(Ni\text{-}X)_{50}$ Ti_{50} alloys (X = Pt, Pd, Au, Rh)

Similar to NiTi alloys of compositions near AuTi, PdTi, PtTi have an ordered CsCL-type structure (B2), that transforms into a B19-martensite. The main difference between NiTi and the other alloys is that the latter show this martensitic transformation at very high temperatures. This was first explored by Donkersloot and Van Vucht [49]. The high transformation temperatures do not allow.
NiTi on one hand and TiAu, TiPt, TiPd and TiRh on the other hand are mutually soluble. Fig. 2 gives the Ms-temperature as function of the atomic fraction Pd, Pt or Au for a $(Ni\text{-}X)_{50}Ti_{50}$ alloys. The continuous curve is calculated based on the model from Huisman-Kleinherenbrink while the dots are experimental values [50].

It must be observed that replacement of Pd, Pt or Au leads initially to a lowering of the transformation temperatures. According to the definition given in the introduction, more

than 20 at% is required to obtain a significant raise of the transformation temperatures. As a consequence, those materials become very expensive.

Most attention has so far been given to the TiNi-TiPd system, the microstructure has been studied in detail, attempts have been given to improve the ductility by B-addition. From the result presented by G o l b e r g et al. [51], it can be concluded that $Ti_{50}Pd_{50-x}$ alloys might become interesting candidates as HTSMA. Conditions to obtain full recovery of 2% deformation could be obtained and also the recovery rates for higher strains are very good. However, significant information on long term stability, cycling effects, two way-memory effect, pseudoelasticity is still missing. Moreover, further research can also include the investigation of alloys in which the Ti content deviates (slightly) from 50 at%.

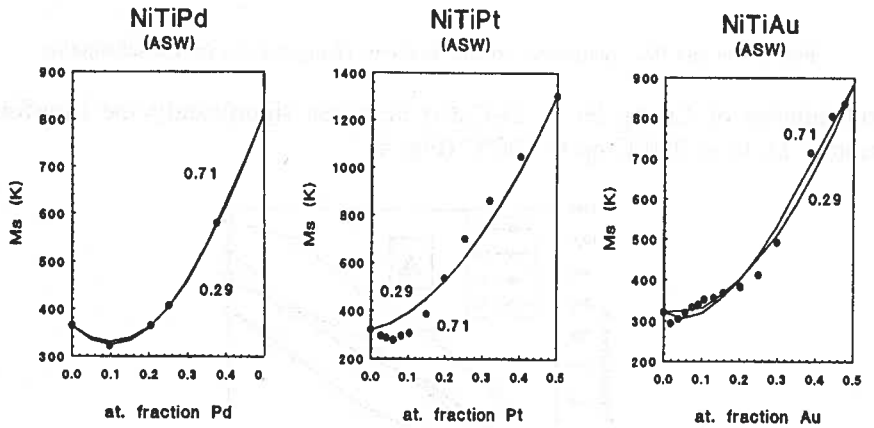

Fig. 2. Fits of calculated Ms-X curves on emperical data for (Ni-X)TiX alloys [50]

3.4. Zr-based intermetallic

CuZr, Zr_2CuCO, Zr_2CuNi have received recently the attention as potential high temperature shape memory alloys.

While the binary intermetallic CuZr alloy (Ms = 170°C, As = 250°C) is very brittle and with changing transformation temperatures during cycling through the martensitic transformation, a slight improvement in ductility could be obtained by adding Ti or Ni [52, 53, 54].

More promising, however, are the Zr_2CuCo and Zr_2CuNi intermetallic alloys [55]. The martensitic transformation in Zr_2CuCo is considered as thermoelastic and allows full shape memory recovery for small applied strains, while Zr_2CuNi transforms in a non-thermoelastic martensite.

Substituting Co for Ni leads to a mixture of thermo-elastic and non-thermoelastic martensite (Fig. 3), hampering the full recovery of the applied strain by shape memory effect. However, a recovery rate of more than 80 % can still be obtained.

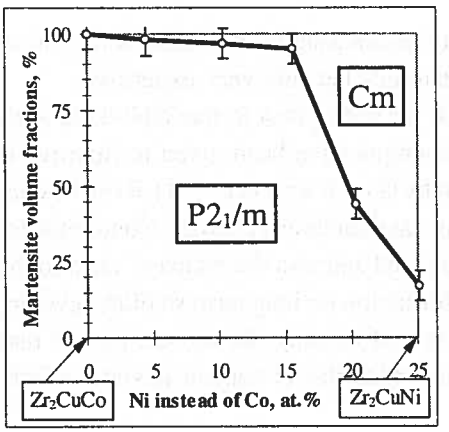

Fig. 3. Cm and $P2_{1/m}$ martensite volume fractions changes vs Ni for Co substitution

The substitution of Cu by Ni in Zr_2CuCo increases significantly the transformation temperature M_s from 250°C up to 800°C (Fig. 4).

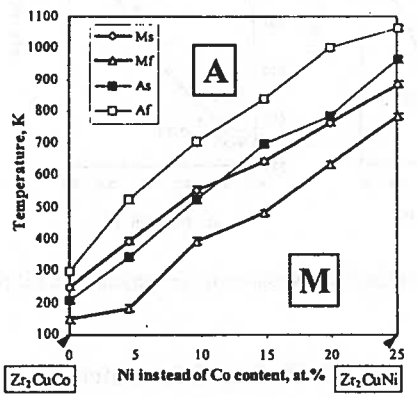

Fig. 4. Martensitic transformation temperatures as a function of the Ni content for the Zr_2CuNi-Zr_2CuCo quasibinary cross-section [55]

4. Applications of shape memory alloys

The diversity of (potential) shape memory applications using shape memory alloys becomes quite large. Success for applications can only be realised in so far those materials offer also a price-competitive advantage relative to other functional materials or mechanical designs.

In spite of the hearty welcome to shape memory alloys, it took about 25 years before SMA , a discovery of the 1960s, became a well-known and established functional material. The real breakthrough could be realised by functional applications into medical technology.

But also on the non-medical sector a wide variety of types of applications exist at present. In this paragraph we will only review very briefly those applications. More detailed information can be found in the given references.

Medical applications [56, 57]

A first big advantage is that NiTi is very biocompatible in spite of the high Ni-content. The reason for this property is a stable Ti_2O layer at the outer surface.

The property most applied is the superelastic effect. This effect results in a unique combinations of high strength, high stiffness and high pliability. No other material can offer this combination of properties. The temperature dependent character of the superelastic effect, which is disadvantageous in many other application areas, is of less importance in the biomedical field because of the stable temperature of the human body. The concept of a biocompatible metallic material with an extreme elasticity and nearly constant stress levels over a large strain area offers therefore many possibilities in different medical areas such a orthodontic devices (archwires, compression and tension springs, brackets,), stents for intravascular scaffolding (especially selfexpandable stents from a catheter so that balloon dilatation is not required,..), rods for scoliosis treatments, miniature bone anchors, endoscopic instruments for minimal invasive surgery (scissors, graspers,), guidewires,
Apart from the superelastic effect , also the shape meory effect is used in constained condition or as actuator, i.e. in orthodontics (root implants), orthopaedics (intramedullary fixation nails, locking rings for the fixation of liners in the cups of hip prostheses, osteosynthesis bone staples, external distraction devices) or in devices such as self-locking instruments that can not be reused without sterelisation, microactuators for Braille systems or implantable microvalves, vena cava filters to filter embolized blood clots in the vena cava vein,.
SMA have really offered unique opportunities in medical technology. As a consequence the medical applications gain far more interest than the non-medical applications.

Non-medical application [58]

The variety of SMA non-medical applications is quite large. In the area of Fashion, decoration and gadgets one can find some of the most successful applications: eye glass frames, frames for brassires and antennas for potable cellular telephones. All tree applications use the superelastic effect. Minor quantities are used in shoes, clothing, lamp shades, toys and even artistic (dynamic) sculptures.

In a more industrial environment couplings and fasteners play an important role. In those applications one makes use of the force created by a deformed SMA element (ring, wire, torsion bar,..) during constrained recovery. Special cases can be found in the aerospace industry for locking-unlocking mechanisms for antennas, satellites or other parts.

Since SMA can also perform work, the area of actuators is quite explored. Nevertheless it is now evident now that SMA can be mainly if not only successful for micro-actuators due

to their high work per weight (or volume) output, but with a very low thermal efficiency (less than 1%).

A new field of application can be found in adaptive materials and hybrid composites (smart materials). In those hybrid composites the SMA play the role of sensor or actuator through a control system.

The high damping capacity receives a lot of attention in machinery, sports equipment and especially in civil engineering where devices are developed in order to protect buildings or bridges against seismic activity.

Finally an increasing interest exist for wear applications. It has been shown that NiTi are extremely wear-resistant. The main problem is the price of the material and the difficulty in welding or cladding this material to other construction materials.

5. Conclusions

Some intermetallic B2-ordered materials have created a new field of functional materials with exceptional properties. The specific temperature and strain response of those materials related to a thermoelastic martensitic transformation created a market with a present value of several billion dollar which is strongly increasing. It is a challenge for material scientist to identify new systems or improved systems and for designers to make optimal use of the thermal and mechanical response of those materials.

Acknowledgements

The author acknowledges the FWO-Vlaanderen (Fund for Scientific Research Flanders) for its financial support by project nr. G.0387.98

REFERENCES

[1] M. Cohen, G. B. Olson, P. C. Clapp, Proceedings of ICOMAT-79, Edit. Office: Dep. Mat. Science & Eng. MIT, Cambridge, p. 1.

[2] L. Delaey, M. Chandrasekaran, M. Andrade, J. Van Humbeeck, Proceedings of the International Conference on Solid-Solid Phase Transformation, Publ. by Met. Society of AIME, ISBN 0-89520-452-5, p. 1429.

[3] T. Maki, T. Tamura, Proceedings ICOMAT-86, Ed. Japanese Institute of Metals, 936 (1986).

[4] J. Van Humbeeck, M. Chandrasekaran, R. Stalmans, Proceedings ICOMAT-92, Ed. Monterey Institute of Advanced studies, Monterey, CA, USA, 1015, 1993.

[5] Q. Gu, J. Van Humbeeck, L. Delaey, Journal de Physique IV Col. C3 4 C3-135 (1994).

[6] J. Van Humbeeck, Transactions ASME **121**, 98 (1999).

[7] J. Perkins, D. Hodgson, The two-way shape memory effect, in: T. W. Duerig, K. N. Melton, D. Stöckel, C. M. Wayman (Eds.), Engineering aspects of shape memory alloys, Butterworth-Heinemann Ltd, London, 195-206 (1990).

[8] J. Perkins, R. O. Sponholz, Met. Trans A **15**, 313 (1984).

[9] G. Guénin, The two way memory effect in relation to the nucleation and growth of martensite, in: E. Hornbogen, N. Jost (Eds.), The martensitic transformation in science and technology, DGM Informationsgesellschaft, Oberursel, 39-52 (1989).

[10] K. Otsuka, K. Shimizu, International Metals Reviews **31**, 93 (1986).
[11] T. W. Duerig, R. Zadno, An engineer's perspective of pseudoelasticity, in: T. W. Duerig, K. N. Melton, D. Stöckel, C. M. Wayman (Eds.), Engineering aspects of shape memory alloys, Butterworth-Heinemann Ltd, London, 369-393, 1990.
[12] S. M. Russell, D. E. Hodgson, F. Basin, Proceedings of the Second International Conference on Shape Memory and Superelastic Technologies, SMST, Santa Clara, 429, 1997.
[13] C. S. Zhang, Y. Q. Wang, J. X. Cheng, C. L. Zhao, Proceedings of the First International Conference on Shape Memory and Superelastic Technologies, MIAS, Monterey, 383 1994.
[14] T. W. Duerig, A. R. Pelton, D. Stöckel, Metall **50**, 569 (1996).
[15] K. N. Melton, in: C. Yougi, T. Hailing (Eds.), Shape Memory Materials '94, International Academic Publishers, Beijing, China, 523-529 1994.
[16] Chapter: Superelastic technology and devices, Proceedings of the First International Conference on Shape Memory and Superelastic Technologies, MIAS, Monterey, 341, 1994.
[17] P. Sittner, D. Vokoun, G. N. Dayananda, R. Stalmans, Mat. Sci. Eng. **286**, 298 (2000).
[18] J. L. Proft, T. W. Duerig, The mechanical aspects of constrained recovery, in: T. W. Duerig, K. N. Melton, D. Stöckel, C. M. Wayman (Eds.), Engineering Aspects of Shape Memory Alloys, Butterworth-Heinemann Ltd, London, 115-129 1990.
[19] M. Kapgan, K. N. Melton, Shape memory alloy tube and pipe coupling in: T. W. Duerig, K. N. Melton, D. Stöckel, C. M. Wayman (Eds.), Engineering Aspects of Shape Memory Alloys, Butterworth-Heinemann Ltd, London, 137-148 1990.
[20] R. Stalmans, L. Delaey, J. Van Humbeeck, Proceedings Mat. Res. Soc. Symp, E. P. George, R. Gotthardt, K. Otsuka, S. Trolier-McKinstry, M. Wun-Fogle (Eds.), **459**: Materials for Smart Systems II, Materials Research Society, Pittsburgh, 119 1987.
[21] D. Vokoun, R. Stalmans, SPIE 3667, 825 (1999).
[22] Y. Zheng, L. Cui, D. Zhu, D. Yang, Materials Letters **43**, 91 (2000).
[23] R. M. Banks, M. C. Fleming, Journal de Physique Col. C-4 833 (1982).
[24] J. Van Humbeeck, R. Stalmans, P. A. Besselink, Shape memory alloys, in: J. Helsen, H. Breme (Eds.), Metals as biomaterials, John Wiley & Sons, 73-100 1998.
[25] K. Ikuta, Proceedings of the IEEE Workshop, 2156 1990.
[26] P. Wollants, M. De Bonte, L. Delaey, J. Roos, Z. Metallk. **74**, 146 (1979).
[27] J. Van Humbeeck, Mat. Sci. Eng. A **273-275**, 134 (1999).
[28] T. Tadaki, Cu-based shape memory alloys, in: K. Otsuka and C. M. Wayman (Eds.), Shape Memory Materials, Chapter 3, Cambridge Univ. Press, 284 pp., ISBN 052144487 (1998).
[29] T. Saburi, Ti-Ni shape memory alloys, in: K. Otsuka and C. M. Wayman (Eds.), Shape Memory Materials, Chapter 3, Cambridge Univ. Press, 1998.
[30] D. Treppman, E. Hornbogen, D. Wurzel, Proceedings ICOMAT-95, R. Gotthardt, J. Van Humbeeck (Eds.), Journal de Physique IV, Colloque C8, Suppl. au Journal de Physique III, **5**, 569 1995.
[31] C. M. Wayman, MRS Int'l. Mtg. on Adv. Mats. **9**, MRS, 63 (1989).
[32] T. Todoriki, H. Tamura, Trans. of the Jap. Inst. of Metals **28**, 83 (1987).
[33] M. Nishida, C. M. Wayman, T. Honma, Met. Trans. **17A**, 1505 (1986).
[34] C. M. Wayman, Proceedings Int. Conf. On Mart. Transf., The Japanese Institute of Metals (Ed.), 645 (1986).
[35] K. H. Eckelmeyer, Scripta Met. **10** 667 (1976).
[36] T. Honma, M. Matsumoto, Y. Shugo, I. Yamazaki, Proceedings ICOMAT-79, p. 259.
[37] V. N. Kachin, Revue Phys. Appl. **24**, 733 (1989).
[38] V. N. Kachin, V. P. Voronin, V. P. Sivokha, V. G. Pushin, Proceedings ICOMAT-95, Part I and II, Lausanne, Gotthardt R. and Van Humbeeck J. (Eds.), Editions de Physique, Journal de Physique IV 5 (8), France, 707 1995.
[39] T. Saburi, T. Takagaki, S. Nenno, K. Koshino, MRS Int'l. Mtg. on Adv. Mats. 9, 147 (1989).
[40] H. Horikawa, T. Ueki, Trans. Mat. Res. Soc. Jpn. **18B**, 1113 (1993).
[41] K. N. Melton, J. L. Proft, T. W. Duerig, MRS Int'l Mtg. on Adv. Mats. **9**, 165 (1989).

[42] J. H. Yang, J. W. Simpson, Proceedings ICOMAT-95, Part I and II, Lausanne, R. Gotthardt, J. Van Humbeeck (Eds.), Editions de Physique, Journal de Physique IV 5 (8), France, 771 1995.
[43] J. H. Mulder, "Investigation of high temperature shape memory alloys from the Ni-Ti-Zr and Ni-Ti-Hf Systems", Ph. D. thesis, Univ. Twente, 1995.
[44] P. Olier, "Influence du mode de fabrication, de la teneur en oxygne et de lajout de zirconium ou dhafnium sur les caracteristiques mtallurgiques et les proprits mechaniques, des alliages mmoire de forme de base NiTi", Ph. D. Thesis, Univ. de Paris-sud, U.F.R. Sc. D'Orsay, 1995.
[45] Krupp GmbH, Fried., Essen, Patenschrift DE-4006076C1, 1990.
[46] D. N. AbuJudom, P. E. Thoma, M. Y. Kao, D. R. Angst, US Patent 5.114.504, 1992.
[47] D. R. Angst, P. E. Thoma, M. Y. Kao, Journ. de Physique IV Col. C8, Suppl. Journ. de Physique III 5 (1995) 8-747.
[48] Proceedings of SMST-94, A. Pelton, D. Hodgson, T. Duerig (Eds.), Edition Mias, ISBN O-9645943-9-7, p. 43 1995.
[49] H. C. Donkersloot, J. H. N. Van Vucht, Journal of Less-Common Metals 83.
[50] P. Huisman-Kleinherenbrink, "On the Martensitic transformation temperatures of NiTi and their dependence on alloying elements", Ph. D. Thesis, Univ. Twente (NL), 1991.
[51] D. Goldberg, Ya Xu, U. Murakami, K. Otsuka, T. Ueki, H. Horikawa, Mat. Letters **22**, 241 (1995).
[52] W. Y. Jang, J. Van Humbeeck, L. Delaey, Yu N. Koval, G. S. Firstov, Trans. Mat. Res. Soc. Jpn. 18b, Elsevier, 1109 1994.
[53] Yu N. Koval, G.S. Firstov, J. Van Humbeeck, L. Delaey, Scripta Met. et Mat. **31**, 799 (1994).
[54] Yu N. Koval, G.S. Firstov, J. Van Humbeeck, L. Delaey, W.Y. Jang, Journ. de Physique IV Col. C8, Suppl. Journ. de Physique 111 5 (1995) C8-1103.
[55] G. S. Firstov, Yu N. Koval, J. Van Humbeeck, Proceedings ESOMAT-1997, Ed. de Physique IV, Suppl. Journ. de Phys. III, 549 1997.
[56] J. Van Humbeeck, Chapter 3: Shape Memory Alloys, in: Jef. A. Helsen, H. Jrgen Breme (Eds.), Metals as Biomaterials, John Wiley and Sons, 73-100 1998.
[57] T. Duerig, A. Pelton, D. Stöckel, Mat. Science and Engineering A273-275, 149 (1999).
[58] J. Van Humbeeck, Mat. Science and Engineering A273-275, 134 (1999).

Received: 3 November 2004.

A R C H I V E S O F M E T A L L U R G Y A N D M A T E R I A L S
Volume 49 2004 Issue 4

P. OCHIN*

PROCESSING AND SYNTHESIS OF SHAPE MEMORY ALLOYS

WYTWARZANIE I SYNTEZA STOPÓW WYKAZUJĄCYCH EFEKT PAMIĘCI KSZTAŁTU

A survey of the main preparation and processing routes of shape memory alloys is presented. Some of the basic requirements for SMA's synthesis are declined and different methods and techniques are described, namely: melting and casting of SMA' ingots; how they have to be thermo-mechanically processed to be shaped in final products demonstrating adequate functional shape memory or superelastic properties, single crystal growing, the powder metallurgy route, synthesis of thin films, and eventually rapid solidification techniques to produce semi-finite products directly from the melt. Each synthesis method is developed with respect to peculiarities of each technique (describing difficulties and limits) and as-prepared materials.

Keywords: processing, casting, shape memory alloys, thin films, single crystal, rapid solidification, powder metallurgy.

Praca zawiera przegląd głównych metod przygotowania i wytwarzania stopów wykazujących efekt pamięci kształtu. Przedstawiono podstawowe wymagania dla przeprowadzenia syntezy powyższych stopów oraz metody ich wytwarzania. Szerzej omówiono sposób przetapiania i odlewania wlewków ze stopów z pamięcią kształtu, wskazując na procesy cieplno-mechaniczne które powinny być zastosowane w celu nadania finalnego kształtu produktom wykazującym odpowiednie funkcjonalne własności związane zarówno z efektem pamięci kształtu jak i super sprężystością. Omówiono również metody hodowania monokryształów, metalurgii proszków, syntezy cienkich warstw oraz niektóre techniki szybkiego chłodzenia pozwalające na wytwarzanie półwyrobów bezpośrednio z cieczy. Metody syntezy stopów z pamięcią kształtu opisano w odniesieniu do specyfiki ich wytwarzania (przedstawiono trudności i ograniczenia) jak również postaci uzyskanego materiału.

1. Introduction

Shape Memory Alloys are materials and consequently they can be prepared as any other metallic alloys, solidified from the liquid state at different cooling rates

* CENTRE D'ETUDES DE CHIMIE METALLURGIQUE, CNRS UPR 2801, 15 RUE GEORGES URBAIN, 94407 VITRY SUR SEINE, FRANCE

(conventional casting and fast quenching), by pressing and sintering powders, or by thin film physical or chemical vapour deposition. Meanwhile due to their structural characteristics, including the possible formation of thermally induced thermal martensitic transformations, special attention has to be paid to the control of the process. Adequate and precise transformation temperatures, chemical homogeneity of the master ingot, microstructural features compatible with suitable mechanical characteristics, and a good surface quality are the key-issues to reach the commercial production.

Transformation temperatures and functional properties are sensitive on the one hand to the extremely small variation of the chemical composition, and on the other hand to the thermal history and microstructure of the as-received products [1]. Consequently, there are still some technological challenges in the melting and processing with regard to the precise control of the chemical composition, and the choice of thermo-mechanical treatments (hot & cold-working). For instance 1% Ni shift (in Nitinol) results in about 100K changes in martensite (Ms) temperature. Shifts from the nominal composition come from contaminant elements in raw materials, highly reactive components of the alloy (such Ti, Zr, Hf, Mn..), the melting process itself by contamination from the crucible materials such as graphite, alumina, magnesia, also the surrounding atmosphere-oxygen, and finally the presence of chemical heterogeneities (precipitations). Thermal and mechanical post-treatments are indispensable to overcome the poor ductility of as-cast materials and to recover the superelasticity and SM effects. In conclusion the main preparation requirements are:

- Accurate chemical composition (±0.1%)
- Chemical homogeneity of the ingot section
- Atmosphere control (specially with Ti containing alloys)
- To avoid chemical contamination of the melt: inert crucible, protective coating, water-cooled earth or jacket...
- Relatively high cooling rate to avoid large chemical segregations

2. Melting and casting of ingots

The following principal technological methods to produce SMA's ingots are:

- Arc remelting (consumable electrode) – Vacuum Arc Remelting (VAR): Vacuum arc remelting with a cooled copper crucible, Vacuum arc skull remelting, with a mould (graphite, copper) and consumable /non-consumable electrode.
- Induction melting: Vacuum induction melting (VIM) with a graphite or calcia (CaO) mould, Vacuum induction melting with a copper water-cooled mould.
- Other techniques also used at experimental scale: Electron beam melting (EBM), Plasma melting with a cooled copper hearth, Electric furnace (SiC resistance for example) with graphite mould, Continuous casting with a electric furnace (SiC-Kanthal), Ohno Continuing Casting process.

Graphite or calcia crucibles for NiTi based alloys are preferred because alumina and magnesia contaminate the melt with oxygen. Meanwhile it is worth to notice that VIM in graphite crucibles can cause the contamination of the melt with carbon. Consequently, when using a graphite crucible, a precise control of the temperature is necessary (1450°C for NiTi) in order to avoid the formation of carbides, which leads to only 200 to 500 ppm of C in the ingot [2].

VAR requires multiple melting stages to achieve acceptable homogeneity, because a small molten volume is formed at one time inside the "skull", added to the solidifying layer causing a heterogeneity of the ingot. On the contrary VIM allows to easily produce more homogeneous ingots. For instance Mateks C° (Russia) can melt 60 kg in VIM furnaces with high density graphite moulds, under 10^{-3} Torr vacuum, in one melting stage; oxygen content is $\leqslant$ 0.08% -H 0.04% - N 0.01% - C 0.035% (wt%) [3].

Copper based SMA's can easily be melted in graphite mould under an inert atmosphere (nitrogen or argon) by induction melting, arc melting or in an electrical furnace [4]. Continuous casting has also been tried out to produce, at a speed of 1to 2 mm/s, rods or sheets of Cu-Al-Ni based SMA's with a electrical furnace (SiC-Kanthal heating elements). EBM, at the laboratory scale (350g alloy melted), has been employed as an alternative process for the production of NiTi SMA's, using a water-cooled copper hearth, which eliminates contamination problems by oxygen (vacuum better than 10^{-2} Pa) and carbon [5]. Homogenization treatment of ingots are carried out under vacuum or inert atmosphere for several hours.

3. Thermo-mechanical processing

As-cast SMA's ingots show rather poor mechanical characteristics with regard to forming (lack of ductility, fatigue resistance). They often do not exhibit superelastic and shape memory effects. The microstructure has to be refined by additional cold and hot deformation processes for instance: Hot forging→deformation of cast alloy→wrought structure [2,3,6]. Plastic deformation ensures the shape of semi-products, such as extrusion (hydroextrusion between 850-950°C for NiTi), thereafter hot rolling: rolling mill with grooved rollers or helical rolling (pressure treatment under conditions of Hydrostatic Pressing), which allows round shaped semi- products, bars of different diameters. Shaping by Injection moulding has also been performed from NiTi sintered prealloyed powders mixed with an organic binder [7].

Temperature of hot working has to be determined precisely: for instance tensile strength of NiTi alloy Nitinol decreases above 600°C, and optimal temperature has been determined close to 1073 K. The formation of the product structure with adequate superelastic or SME properties often requires final treatment stages, combination of cold working with annealing and ageing at specific temperatures, according to the alloy composition and researched functional properties: for instance drawing (obtaining of wires, tubes) over a deformable or non-deformable mandrel, rotation forging. Semi-products as bars ⌀ 1.5 to 15 mm, wires ⌀ 0.15 to 2.5 mm (NiTi) can be processed

like this. It is worth to notice that they are more difficult stages because of the work hardening of the alloys. A last annealing will enable to remove the internal stress produced during hot/cold working.

The semi-products and products have to finally be cleaned, removing the oxide layer by grinding, acid pickling or electropolishing to improve corrosion resistance or biocompatibility. Moreover electropolishing removes micro-cracks and the heated affected zone. In conclusion thermo-mechanical stages are decisive for obtaining the SM or/and superelastic response for the special application.

4. Single crystals growth

Fundamental investigations require the making of single crystals. For instance the measurement of the elastic constant of alloys demonstrating a martensitic transformation is of great importance in providing information to help to understand the nucleation and growth processes of martensite phases, and data for modelling. Moreover, single crystal materials demonstrate, when choosing the optimal crystallographic orientation, larger strain and stress values, and subsequently they can be used to create new SM actuators generating large forces and torques [8].

The good knowledge of the equilibrium phase diagram of the system is desirable for the right choice of the method. A single-phase domain and congruent melting at the chosen composition are favourable conditions for growing from the melt.

Preparation of the ingot is regularly performed by arc or induction melting of the components followed by casting in a copper water-cooled mould. A subsequent annealing to finalize the chemical homogeneity of the polycrystal is carried on with additional thermo-mechanical treatment when necessary, such as forging which has been used for NiTi (hot-forged at 850°C) [9].

The Bridgman technique is the most commonly used method to produce single crystals of Ni-Ti and Ni-Mn-Ga alloys [9,10,11]. The master ingot, contained in a non-reactive crucible, is placed into a specially designed furnace (induction melting or graphite resistance). The growing of a single grain is obtained by translation of the melting zone into a temperature gradient at a control velocity. The crucible is chosen the less chemically reactive with the molten alloy at the desired temperature, and is made from a refractory material such as alumina, calcia, magnesia or graphite, boron nitride. The crucible is shaped to generate a single grain at its bottom or to place a seed when available. Cu-Al- Mn bicrystals have successfully been prepared by using a specially designed two compartments crucible to generate two grains [12].

A containerless method, the vertical Floating Zone method, using an Image Furnace or induction heating with a specially designed coil, has been employed to grow Fe_3Pt and Fe-31.2Pd (at%) single crystals [13].

The encountered difficulties are the reactivity of the melt, side reactions with the crucible, high vapour tension of the melt, not getting a full or near congruent melting at the chosen composition. The main parameters are the choice of the crucible, the melt

temperature control, the translation speed control, and the choice of the atmosphere (vacuum, argon...).

Control and orientation of the single crystal grains are thereafter carried on by Laue Back Reflection method.

5. Powder metallurgy (PM)

Near net shape fabrication routes, on an industrial scale, have gained considerable interest throughout the last decade because an easier achievement of complex shapes, with minimal post- machining treatments can be reached and in consequence cost saving is possible. The other main reason is, as we mentioned above, that most of SMA's suffer from poor workability. PM routes avoid difficulties associated with casting like segregations of alloying elements and extensive grain growth. Other advantages include a precise control of the chemical composition and permit introduction of second phases (hard particles which can increase stiffness for instance) to form a composite. It can sometimes decrease the density of the resultant material.

Pre-alloyed powders or mixture of elemental powders are prepared by gas atomization (giving the best quality-size distribution) or other techniques such the electro-explosion of wire (EEW) process. This latest technique results in a high quenching rate and the synthesis of nano-sized particles [14]. Blending (for instance in a turbular mixer) for several hours is the second and quite sensitive step. The mixtures are filled in stainless steel cans. In the case of NiTi alloys a Nickel foil can be added to avoid a side reaction and evacuated before welding the top of the can.

Pre-compaction by uniaxial pressing or Cold Isostatic Pressing (CIP) of powders is carried out to reach a partial density (around 65%), followed by sintering of the green powder.

Hot Isostatic Pressing (HIP) has also been employed to prepare NiTi alloys [7,15], on the one hand from elemental powders without pre-compaction, at 195 MPa, and 900°C during 5 hours, or on the other hand from pre-alloyed powders directly in evacuated and welded stainless steel cans ($\varnothing 18 \times 100$ mm) in the range 915-1065°C, according to the Ni content, at 100 MPa for 3 hours [7]. Johansen et al have also synthesized NiTi composites from pre-alloyed 70 μm average size NiTi and 10-15 μm TiC particles, in steel cans (Ni foil cladded), first mechanically pressed (uniaxial compressive stress 14 MPa) prior to welding, and then HIPing at 102 Mpa and 1065°C for 3 hours. An increase of Oxygen content (max 1400 ppm) and a small reduction Ni/Ti ratio due to solid reactions have been noticed. A good distribution of the particles TiC in the matrix has been observed [15].

One can conclude from different studies that the performances of PM applied to SMA's match those of alloys produced by the conventional ingot metallurgy processing routes.

6. Thin films

The development of SMA's thin films, especially TiNi base alloys, has been mainly proposed in the field of micromachines. Some results show that classical micromachines processing are applicable for making microstructures with silicon substrates and Ti-Ni thin films. Several types of techniques have been applied to make films with thickness less than 10 μm such Sputter deposition, Vacuum vapour deposition, Laser ablation etc. [16,17].

PVD sputtering is the major method used to achieve, since the 90's, perfect SME in thin films such as Ni-Ti, Ni-Ti-x (x = Cu, Pd, Hf) alloys. One great advantage, compared to bulk material, is the easier removal of heat that increases the response of SMA's. Fabrication methods have to improve the quality of sputter-deposited films that contain micro-defects, and others defaults such as oxygen and hydrogen content responsible for the brittleness.

Films SM characteristics depend on the alloys composition, the annealing temperature, the ageing temperature and time, and obviously the sputtering conditions. Radio frequency (r.f.) conventional diode or magnetron sputtering methods are commonly employed to produce films 0.5 to 10 μm thick demonstrating SME. The general process consists in argon ions that are accelerated into a target to sputter atoms (Ni, Ti...) which are deposited onto a substrate (made of copper or silicon for instance) to form the film. Depending on the sputtering yield (number of atoms sputtered per Ar ion) for each element, pure elemental chips, as complementary targets, have to be used to control the content of each component of the alloy.

Several parameters are in control of the process, typically the distance between the substrate and the target (30 to 50 mm), the r.f. power (typically 600 W)-self-bias voltage, the argon gas pressure, the substrate temperature, the alloy composition of the target, the substrate material (coated or not glass, silicon, copper..), and the substrate surface roughness.

A too low Ar pressure is responsible for a featureless structure. On the contrary a high Ar pressure favours a columnar structure (porous film). The inclination angle of targets is another parameter which has been found to be responsible of the brittleness or toughness of heat-treated NiTi films [18]. As-sputtered Ni-Ti films are amorphous if the substrate is not heated. After removal of the film from the substrate, a heat treatment under inert atmosphere (500° or 700°C for NiTi) is carried out to recover SM properties [18].

T. Lehnert et al have prepared Ni-Ti films based on sputter-deposited multilayers which consisted of individual Ni and Ti layers, that demonstrate a martensitic transformation and SME [19]. For this experiment they used an automated Leybold Z600 sputtering system with a DC magnetron, with pure Ar at 0.13 Pa and ∅ 50 cm substrates (glass covered with a photoresist or Si). After thermal treatments, the grain structure of the film is relatively homogeneous with some regions richer in precipitates (Ti_2Ni type), which transform at different temperatures.

7. Rapid solidification

Technologies producing near net shaped alloys receive a lot of attention because with such direct preparation methods, it is not only possible to make savings in reducing the number of further processing stages, but also to obtain new material properties. Such methods indeed create a unique opportunity for manufacturing small-sized actuators, micro-switches or implants for the human body. This can be achieved directly from the molten state, with a higher rate of solidification (cooling rates going from 10^3 to 10^7 K/s) than in conventional ingot casting. Rapid solidification techniques are means to enlarge the range of applications of SMA's. Rapid solidification introduces structural and microstructural differences as compared to the bulk material, the best-known example is the reduction of grain size, which can decrease brittleness, but also has been found to lower the transformation temperatures. According to the alloy composition, the as spun-ribbons can be in a fully or partially amorphous state. That leads to a more ductile material and facilitates the forming in the undercooled region (Tx-Tg, with Tg the vitreous transition and Tx the crystallization onset temperature) [20]. Then appropriate thermal treatments allow the recovering of SM properties. High cooling rates also reduce chemical segregation and an important precision on the chemical composition can be reached (±0.1 at%), as well as an improvement of the chemical homogeneity of the product. The possibility of obtaining nano-sized grains and a disordered state can largely affect characteristics of alloys demonstrating a double ferro-magnetic/ SM effect [21].

Rapid Solidification techniques (RS) applied to SMA's, due to the numerous operational parameters of the processes, the structural and microstructural complexity of the resulting materials, still require more fundamental investigations. Only a narrow set of values for these parameters (which have to be determined for each specie of alloys), allows to obtain suitable products for potential applications. We present here the Planar Flow Casting technique, a variant of the Chill Block Melt Spinning (CBMS) technique, which permits to produce thin ribbons (20-80 μm thick), that has generated numerous works. We also introduce two other methods allowing the preparation of thin sheets of SMA' (Twin Roll Casting TRC) and a more uncommon one, the In Rotating Water Melt Spinning technique (INROWASP), which allowed us to prepare round thin wires (⌀100-200 μm) of Cu based SMA's, directly from the melt.

7.1. Planar Flow Casting

Rapid solidification on a rotating drum proceeds through a liquid puddle on the hard surface, that is next dragged away forming a stationary liquid-solid interface at the origin of a thin tape, a few tenths micrometers thick, fully solidified at a very high cooling rate (10^5 to 10^6 Ks^{-1}). In this method, the small gap between the wheel and crucible is maintained so that the upper surface of the melt puddle is constrained by the nozzle; the stability of the flow is higher due to this small gap (< 1 mm). A master alloy ingot is placed in a nozzle and induction-melted. Nozzles (made of

quartz or boron nitride) with a narrow slit allow the solidification of ribbons with a larger width than in CBMS. The nozzle is pressurised with argon and the melt ejected on the rotating substrate. Some authors, in the case of Fe-Pd SMA's, have used electromagnetic levitation to induction- melt the ingots, to avoid any contact with a container [22]. In this case, the ingot is a rotating feeding rod that is translated at a adjusted speed into a special conic coil to melt the tip. The molten tip regularly wets the rotating substrate forming a puddle that solidifies. Linear speed, according to the wheel diameter varies from 5 to 50 m/s. Numerous variables of the process, responsible for the heat transfer on the substrate, influence the structure, microstructure and surface quality of ribbons: the wheel velocity, the viscosity of the melt (depending on the superheating of the melt), the melt flow (directly related to the nozzle slot width and the ejection overpressure). Secondary parameters also participate in the achievement of the most appropriate casting conditions. Some are related to the adhesion of the solidified tape on the rotating substrate to provide the best heat removal and to improve the surface quality of the ribbon. They depend on the wheel (material, diameter, surface roughness), the distance between the nozzle tip and the substrate, the surrounding atmosphere (secondary cooling) [23].

Another important structural feature of rapidly quenched tapes is their texture. It exhibits a certain degree of tilting between the crystallographic direction in columnar grains and the ribbon's normal against or toward the spinning direction [24].There are numerous publications that concern rapidly solidified ribbons of Cu-based alloys and less devoted to Ni-Ti based alloys. The main references can be found in [23]. Some recent examples on the relation between the quenching rate, the resulting microstructure and SME, are described in [25] on Cu base alloys, [26,27] on Ni-Ti-Hf based alloys, [28,29] on Ni-Ti-Cu based alloys, [21] on Ni-Mn-Ga, and [30] on Ni-Al alloys. SMA ribbons can find application in numerous fields as thermosensitive devices [31].

7.2. Twin Roll Casting (TRC)

TRC combines solidification of a liquid layer on the rotating substrates (copper rolls) and hot rolling of the solidified shell into a single operation producing a thin metal strip directly coilable. Hard to roll materials as Cu-based and Ni-Ti-Hf SMA's, are good candidates for this method of preparation of semi-finite products. $Cu_{86-x}Ni_xAl_{13}Ti_1$ (wt%, x = 4.5-5.5), $Cu_{82}Al_{13.4}Ni_4Ti_{0.4}Cr_{0.2}$ (wt%), NiTi, $Ni_{25}Cu_{25}Ti_{50}$, $Ni_{50}Ti_{42}Hf_8$ (at%) strips (250-500 μm thick) have been prepared like that [32,33]. The foil formation is complex and controlled by the interaction of both fluid and heat flows. The casting speed, which is equal to the tangential velocity of the rotating drums, was chosen in the range 0.5- 0.9 m/s. It is worth to notice that this value is much higher than a conventional casting speed (0.017- 0.03 m/s). The "solidification end point" corresponding to the lower limit of the solid-liquid interface in the nip between the two rolls, has been observed as a determinant parameter of the process, controlling the rolling ratio. Heterogeneity of the microstructure has been observed along the width but also in the thickness of the stripes. Each half-part of the sheets present an

ingot-like solidification microstructure with a wide "basaltic" zone. The transformation temperatures are close to the bulk corresponding material [34]. This complicate microstructure has particularly been investigated in Ni-Ti-Hf thin sheets, showing the chemical and structural homogeneity of the strips along their length but not along their width [35]. Twin rolled casting produces materials with reproducible SM properties, and mechanical properties which are still under investigation.

7.3. Production of round thin wires directly from the melt

Thin cylindrical (⌀100-250μm) have been prepared, directly from the liquid state, using the In Rotating Water Melt Spinning technique (INROWASP). Promising results have been obtained for Cu-Al-Ni and Cu-Al-Ni-(Ti-Cr) SM alloys. As for other RS techniques, only a narrow set of values of the process parameters permitted the synthesis of "no-defects wires". Acoustoplastic post- treatment has been applied to the as-cast wires reducing the surface irregularities [36]. As for RS ribbons, transformation temperatures are depressed compared to the bulk material, but ageing at moderate temperature (250°C) reduces the temperature shift. The wires exhibit superelasticity as well as SM properties for uniaxial elongation and bending[37]. Microstructural investigations of the thin wires (TEM) are in progress.

8. Concluding remarks

Shape memory materials are not very different regarding preparation methods from other intermetallic alloys. Their relative lack of ductility and the high dependence of the transformation temperatures on the chemical composition, impose strict requirements as it concerns a choice of the methods and care in processing. Carefully design thermo-mechanical and surface post-treatments are necessary to obtain shape memory effect in required strain and temperature range.

REFERENCES

[1] K. Otsuka, X. Ren, Mat. Sci. Forum **394-395**, 177-184 (2002), Trans. Tech. Publications.
[2] M.H. Wu, Mat. Sci. Forum **394-395**, 285-292 (2002), Trans. Tech. Publications.
[3] A.B. Bondarev, V.A. Andrey, Mat. Sci. Forum **394-395**, 301-304 (2002), Trans. Tech. Publications.
[4] H. Xu, Mat. Sci. Forum **394-395**, 375-382 (2002), Trans. Tech. Publications.
[5] J. Otubo, O.D. Rigo, C. Moura Neto, M.J. Kaufman, P.R. Mei, J. Phys. IV France **112**, 873-876 (2003).
[6] L.M. Wang, L.H. Liu, H. Yang, L.Y. Wang, G.Q. Xiu, Mat. Sci. Forum **394-395**, 297-300 (2002), Trans. Tech. Publications.
[7] E. Schüller, M. Bram, H.P. Buchkremer, D. Stöver, Mat. Sci. Eng. A **378**, 165-169 (2004).

[8] I. Vahhi, S. Pulnev, A. Priadko, J. Phys. IV France **112**, 1181-1184 (2003).
[9] O. Mercier, K.N. Melton, G. Gremaud, J. Hägi, J. Appl. Phys. **51**(3), 22 1833 (1980).
[10] S.J. Murray, M. Marioni, S.M. Allen, R.C. O'Handley, T.A. Lograsso, Appl. Phys. Lett. **77**, 6, 886-888 (2000).
[11] F. Takei, T. Miura, S. Miyazaki, S. Kimura, K. Otsuka, Y. Suzuki, Scripta Met. **17**, 987-992 (1983).
[12] H. Kato, S. Miura, Mat. Sci. Forum **394-395**, 205-208 (2002), Trans. Tech. Publications.
[13] T. Kakeshita, T. Fukuda, Mat. Sci. Forum **394-395**, 531-536 (2002), Trans. Tech. Publications.
[14] Y. Fu, C. Shearwood, Script. Mat. **50**, 319-323 (2004).
[15] K. Johansen, H. Voggenreiter, G. Eggeler, Mat. Sci. Eng. A **273-275**, 410-414 (1999).
[16] S. Miyazaki, A. Ishida, Mat. Sci. Eng. A **273-275**, 106-133 (1999).
[17] A. Isalgue, V. Torra, J-L. Seguin, M. Bendahan, J.M. Amigo, V. Esteve-Cano, Mat. Sci. Eng. A **273-275**, 717-721 (1999).
[18] T. Yamamoto, S. Miyazaki, J. Phys. IV France **112**, 869-872 (2003).
[19] T. Lehnert, S. Tixier, P. Böni, R. Gotthardt, Mat. Sci. Eng. A **273-275**, 713-716 (1999).
[20] A. Sezonenko, V. Kolomytsev, M. Babanly, A. Pasko, P. Ochin, R. Portier, Ph. Vermaut, J. Phys. IV France **112**, 889-892 (2003).
[21] V. Chernenko, C. Segui, J. Pons, E. Cesari, P. Ochin, R. Portier, Proc. of the Int. Conf. On Solid Phase Transf. '99 (JIMIC-3), edt. M. Koiwa, K. Otsuka, T. Miyazaki (the Japan Inst. of Metals 1999).
[22] Y. Furuya, N.W. Hagood, H. Timura, T. Watanabe, Mat. Trans. JIM **39-12**, 1248-1254 (1998).
[23] P. Ochin, A. Dezellus, Ph. Plaindoux, F. Dalle, C. Elgoyhen, Ph. Vermaut, R. Portier, Metallofizika I Noveishie Tekhnologii **23**, 93-99 (2001).
[24] T. Goryczka, H. Morawiec, P. Ochin (2004) to be published.
[25] W.Y. Jang, Y.S. Lee, K.K. Jee, E.G. Lee, Mat. Sci. Forum **394-395**, 507-510 (2002). Trans. Tech. Publications.
[26] F. Dalle, A. Paslo, Ph. Vermaut, V. Kolomytsev, P. Ochin, R. Portier, Script. Mater. **43-4**, 331-335 (2000).
[27] R. Santamarta, A. Pasko, J. Pons, E. Cesari, P. Ochin, Mat. Trans.(JIM) to be published.
[28] L. Litynska, Ph. Vermaut, J. Morgiel, J. Dutkiewicz, P. Ochin, R. Portier, J. Phys. IV France **11** Pr8-357-361 (2001).
[29] T. Goryczka, M. Karolus, P. Ochin, H. Morawiec, J. Phys. IV France **11**, Pr8-345-349 (2001).
[30] P.L. Potapov, P. Ochin, J. Pons, D. Schryvers, Acta Mater. **48**, 3833-3845 (2000).
[31] A.V. Shelyakov, S.G. Larin, V.P. Ivanov, V.V. Sokolovski, J. Phys. IV France **112**, 1169-1172 (2003).
[32] C. Elgoyhen, M. Larnicol, P. Ochin, R. Portier, J. Phys. IV France **10**, Pr6-21-26 (2000).

[33] Ph. Vermaut, P. Ochin, A. Dezellus, Ph. Plaindoux, F. Dalle, Ph. Muguerra, R. Portier, Mat. Sci. Forum **394-395**, 483-486 (2002), Trans. Tech. Publications.
[34] P. Ochin, A. Dezellus, Ph. Plaindoux, Ph. Vermaut, F. Dalle, R. Portier, J. Phys. IV France **112**, 881-884 (2003).
[35] F. Dalle, G. Despert, Ph. Vermaut, R. Portier, A. Dezellus, Ph. Plaindoux, P. Ochin, Mat. Sci. Eng. A346320-327 (2003).
[36] P. Ochin, A. Dezellus, Ph. Plaindoux, R. Portier, J. Pons, E. Cesari, A. Kozlov, Mat. Sci. Forum **394-395**, 503-506 (2002), Trans. Tech. Publications.
[37] A. Dezellus, Ph. Plaindoux, P. Ochin, J. Pons, R. Portier, E. Cesari, J. Phys. IV France **112**, 567-570 (2003).

Received: 3 November 2004.

A R C H I V E S O F M E T A L L U R G Y A N D M A T E R I A L S
Volume 49 2004 Issue 4

H. PETRYK*, S. STUPKIEWICZ*

MICROMECHANICAL MODELLING OF STRESS-INDUCED PHASE TRANSITION IN SHAPE MEMORY ALLOYS

MICRO-MECHANICZNY MODEL PRZEMIANY MARTENZYTYCZNEJ AKTYWOWANEJ NAPRĘŻENIEM W STOPACH WYKAZUJĄCYCH EFEKT PAMIĘCI KSZTAŁTU

A micro-mechanical model of stress-induced martensitic transformation in shape memory alloys is presented. A laminated microstructure of austenite and martensite phases is assumed along with a time-independent thermodynamic criterion for phase transformation. In numerical examples, the pseudoelastic behaviour of single crystals of CuZnAl and CuAlNi shape memory alloys is investigated. Several aspects are examined, including the effects of the loading direction, external constraints, detwinning, and instability of macroscopically uniform transformation.

W pracy przedstawiono mikro-mechaniczny model przemiany martenzytycznej aktywowanej naprężeniem w stopach z pamięcią kształtu. Mikrostruktura faz austenitu i martenzytu posiada płytkowy charakter zgodnie z niezależnym od czasu kryterium termodynamicznym przemiany fazowej. Na przykładzie numerycznych obliczeń przedstawiono analizę zjawiska pseudosprężystości monokryształów ze stopów CuZnAl i CuAlNi wykazujących efekt pamięci kształtu. Zbadano kilka aspektów zjawiska zawierających m.in. efekty kierunku obciążenia, ekstremalnych ograniczeń, zanikanie bliźniaków i niestabilność makroskopowo jednorodnej przemiany.

1. Introduction

Shape memory alloys at a temperature high enough to ensure stability of the austenitic phase at zero stress, upon loading undergo stress-induced martensitic transformation. As commonly observed in experiments, the transformation proceeds by the formation and growth of martensitic plates within the austenite matrix. Upon unloading, the martensite is transformed back to austenite, which corresponds to pseudoelastic (or

* INSTITUTE OF FUNDAMENTAL TECHNOLOGICAL RESEARCH, POLISH ACADEMY OF SCIENCES, ŚWIĘTOKRZYSKA 21, 00-049 WARSAW, POLAND

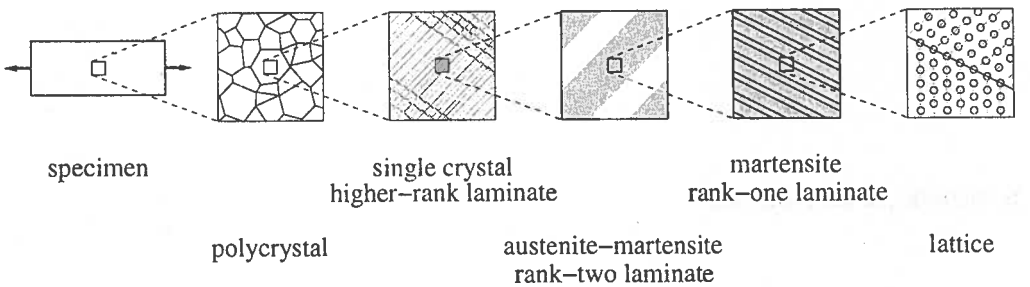

Fig. 1. An example of a multi-scale modeling scheme

superelastic) behaviour of the material with a characteristic hysteresis loop on the stress-strain diagram, cf. e.g., [6].

In this paper, a micromechanical model is presented which provides a link between the structure and mechanical properties of shape memory materials at different scales of observation. One of the main objectives of micromechanics is to predict and explain the macroscopic behaviour in terms of the material microstructure and properties at a micro-scale where physical mechanisms of deformation are better recognized. It is natural to apply such approach to shape memory alloys in which the basic microstructural changes are related to crystal lattice rearrangements. The transition from transformations of the atomic structure to the behavior of a polycrystalline specimen is, however, not straightforward and requires consideration of intermediate levels. This leads to hierarchical, multi-scale micromechanical modeling that involves sequential transition between more than two different spatial (and also temporal) scales, Fig. 1.

A representative volume element of a polycrystalline material is used to describe overall properties of the material at the highest level. The transition to a still larger scale of a specimen can generally be accompanied by temperature nonuniformity and instability phenomena influenced by the specimen shape, dimensions and boundary conditions. Experiments show (e.g. [12, 18]) that the phase transformation process in polycrystalline specimens can proceed nonuniformly by propagation of transformation zones. In consequence, mechanical characteristics of the specimen can significantly differ from those of the material. The respective transition is not discussed in this paper being restricted to the modeling of the material itself.

The overall isothermal response of a polycrystalline aggregate can be simulated by using one of the known averaging methods. Several crystal-to-polycrystal transition schemes, not restricted to uniaxial models, have been applied to shape memory alloys, e.g. a self-consistent model [7], a layered model for textured polycrystals [14], a uniform strain model, and finite element discretization [19], to mention just a few examples. It is beyond the scope of this paper to discuss polycrystal models in more detail. For the present work it is only essential that effective methods exist for simulating a

macroscopic response of a polycrystalline material starting from a model of a single crystal behavior.

This paper deals with the micromechanical modeling of a *single* crystal of a shape memory alloy undergoing stress-induced martensitic transformation at a given temperature. The analysis is restricted here to the multi-scale transition between the last three (or sometimes four) levels indicated in Fig. 1, starting from the crystallographic lattice transformations. The main assumption is that of a *laminated microstructure* within the crystal when the martensitic transformation is stress-induced; a similar concept has appeared earlier, e.g. in [10]. This assumption is motivated by the existing experimental evidence and simplifies considerably the description of mechanical interactions between the phases. The basic step of the analysis reduces to the micro-macro transition for a rank-one laminate, described in detail in [16], with due account for moving interfaces and differences in elastic anisotropy of the constituents. In this paper, some novel applications of the model developed by the authors in [16] are presented.

2. Micro-macro transition for evolving microstructures

2.1. Preliminaries

For simplicity, the considerations below are limited to the small deformation theory, although extensions to finite deformations are possible, cf. [8]. The macroscopic strain and stress in a volume V, distinguished from a local strain $\boldsymbol{\varepsilon}$ and stress $\boldsymbol{\sigma}$ by a superimposed bar, are given by the standard formulas

$$\bar{\boldsymbol{\varepsilon}} = \langle \boldsymbol{\varepsilon} \rangle , \qquad \bar{\boldsymbol{\sigma}} = \langle \boldsymbol{\sigma} \rangle , \qquad \langle \cdot \rangle \equiv \frac{1}{V} \int (\cdot)\, dV . \tag{1}$$

Analogously, $\bar{\phi} = \langle \phi \rangle$ is the macroscopic counterpart to the local Helmholtz free energy per unit volume, assuming temperature uniformity and no interface energy.

Sudden formation of a thin transformed layer within V corresponds to small changes in $\bar{\boldsymbol{\varepsilon}}$ and/or $\bar{\boldsymbol{\sigma}}$ accompanied by a substantial jump $\Delta\boldsymbol{\varepsilon}$ in *local* strain, and possibly also by a jump $\Delta\boldsymbol{\sigma}$ in local stress. When the process of phase transformation is smoothed out in time then small changes in $\bar{\boldsymbol{\varepsilon}}$ and $\bar{\boldsymbol{\sigma}}$, divided by a small time increment, are interpreted as *forward* rates, $\dot{\bar{\boldsymbol{\varepsilon}}}$ and $\dot{\bar{\boldsymbol{\sigma}}}$. Similarly, the transformed layer thickness is represented by its forward rate $\dot{s} \geqslant 0$ interpreted as the speed of a *regularized* transformation front. The local jumps $\Delta(\cdot) = (\cdot)^- - (\cdot)^+$ from the parent (+) to product (−) phases do not admit such a rate representation. Moreover, their distribution within an internally laminated plate is not smooth. Due to the existing irregularities, $\dot{\bar{\boldsymbol{\varepsilon}}}$ and $\dot{\bar{\boldsymbol{\sigma}}}$ are to be calculated by applying the transport theorem in an *extended* form [8], which yields

$$\dot{\bar{\boldsymbol{\varepsilon}}} = \langle \dot{\boldsymbol{\varepsilon}} \rangle + \frac{1}{V} \int_S \Delta\boldsymbol{\varepsilon}\, \dot{s}\, dS , \qquad \dot{\bar{\boldsymbol{\sigma}}} = \langle \dot{\boldsymbol{\sigma}} \rangle + \frac{1}{V} \int_S \Delta\boldsymbol{\sigma}\, \dot{s}\, dS . \tag{2}$$

Here, S denotes the set of all interfaces, and the prefix Δ denotes the forward jump with respect to *time* in a local variable on S, averaged over the layer thickness. Note that at an initial instant of phase transformation, spatial jumps are not yet present.

The continuity of displacements and equilibrium of stresses, assumed throughout the paper, imply

$$\Delta\varepsilon = \tfrac{1}{2}(\mathbf{c}\otimes\mathbf{n} + \mathbf{n}\otimes\mathbf{c}), \qquad \Delta\sigma\,\mathbf{n} = \mathbf{0}, \tag{3}$$

where $\otimes$ denotes the tensor product, $\mathbf{n}$ is a unit normal to S and $\mathbf{c}$ is a vector such that $\dot{s}\mathbf{c}$ is the velocity jump across S. The local *thermodynamic driving force*, per unit area of the phase transformation front, has the familiar form

$$f = \sigma\cdot\Delta\varepsilon - \Delta\phi, \tag{4}$$

where the stress σ can be taken from any side of the front. Accordingly, the intrinsic dissipation rate due to the transformation is expressed by

$$\dot{\mathcal{D}}^{\mathrm{t}} = \int_S \dot{\mathcal{D}}^{\mathrm{t}}\,dS, \qquad \dot{\mathcal{D}}^{\mathrm{t}} = f\,\dot{s} \geqslant 0. \tag{5}$$

2.2. Basic microstructure

In accord with experimental observations, the stress-induced martensitic transformation in a single crystal of a shape memory alloy proceeds by the formation of parallel martensitic plates within an austenite matrix. Typically, a martensite plate can either involve only one crystallographic variant of martensite (usually with internal stacking faults) or be a fine mixture of two twin-related martensite variants. The corresponding microstructure is thus a rank-one laminate in the former case and a rank-two laminate in the later case.

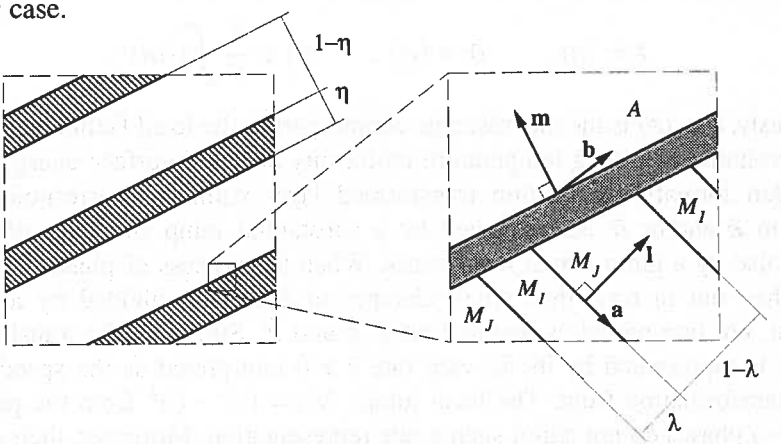

Fig. 2. A schematic view of a periodic microstructure formed by internally twinned martensite plates within austenite matrix (A – austenite, M_I, M_J – martensite variants)

A single crystal of austenite may transform to several variants of martensite, indexed by I, with known transformation strain $\varepsilon_I^{\mathrm{t}}$. Following [16], consider the microstructure associated with the formation of internally twinned martensite plates as

shown in Fig. 2. The microstructural parameters can be determined, in the first approximation, from the crystallographic theory of martensitic transformation [20, 1], which can be adopted in the geometrically linear framework for small strains [2]. In this theory, compatibility between the *homogenized* phases is assumed to hold at zero stress. In the small strain format, this leads to the twinning equation

$$\boldsymbol{\varepsilon}_I^{\mathrm{t}} - \boldsymbol{\varepsilon}_J^{\mathrm{t}} = \tfrac{1}{2}(\mathbf{a} \otimes \mathbf{l} + \mathbf{l} \otimes \mathbf{a}) \tag{6}$$

with the unit vector $\mathbf{l}$ normal to the twin interface and a non-zero vector $\mathbf{a}$ as the unknowns, and the habit plane equation

$$\boldsymbol{\varepsilon}^{\mathrm{t}} = \tfrac{1}{2}(\mathbf{b} \otimes \mathbf{m} + \mathbf{m} \otimes \mathbf{b}) \tag{7}$$

with the unknowns $\mathbf{m}$ and $\mathbf{b}$ denoting, respectively, the unit vector normal to the austenite-martensite interface and a non-zero vector (shape strain). The *effective* transformation strain $\boldsymbol{\varepsilon}^{\mathrm{t}}$ in an internally twinned martensitic plate reads

$$\boldsymbol{\varepsilon}^{\mathrm{t}} = \lambda \boldsymbol{\varepsilon}_I^{\mathrm{t}} + (1 - \lambda)\boldsymbol{\varepsilon}_J^{\mathrm{t}} \tag{8}$$

where λ denotes the (unknown) volume fraction of variant I in the plate. In turn, for an untwinned plate of martensite variant I with internal faults, where equation (6) does not apply, we have

$$\boldsymbol{\varepsilon}^{\mathrm{t}} = \boldsymbol{\varepsilon}_I^{\mathrm{t}} + k_{\mathrm{sf}} \frac{1}{2}(\mathbf{s}_I \otimes \mathbf{n}_I + \mathbf{n}_I \otimes \mathbf{s}_I) \tag{9}$$

where k_{sf} is the (unknown) magnitude of shear due to stacking faults, and $\mathbf{n}_I$ and $\mathbf{s}_I$ are known unit vectors normal to the shear plane and parallel to the shear direction, respectively.

By solving the above algebraic equations with respect to the unknowns, we obtain geometric characteristics of N distinct martensitic plates, indexed by $\alpha = 1, \ldots, N$. Subsequently, depending on the loading program, the preferred martensitic plates are selected by applying the transformation criterion, to be discussed in subsection 2.4. However, if detwinning within the twinned martensite plates *during* stress-induced transformation is accounted for then the twin fraction λ is not constant and transformation strain compatibility (7) no longer holds at zero stress. Consequences of this are indicated in subsection (3.2) and examined in more detail in [17].

Mechanical properties of each constituent at the micro-level are defined by the free energy functions for austenite (ϕ_{a}) and for I-th martensite variant (ϕ_I), assumed in the form

$$\phi_{\mathrm{a}} = \phi_0 + \tfrac{1}{2}\boldsymbol{\varepsilon} \cdot \mathbf{L}_{\mathrm{a}}\boldsymbol{\varepsilon}, \quad \phi_I = \phi_0 + \Delta^{\mathrm{am}}\phi_0 + \tfrac{1}{2}(\boldsymbol{\varepsilon} - \boldsymbol{\varepsilon}_I^{\mathrm{t}}) \cdot \mathbf{L}_I(\boldsymbol{\varepsilon} - \boldsymbol{\varepsilon}_I^{\mathrm{t}}), \tag{10}$$

where ϕ_0 is the Helmholtz free energy density for austenite at zero stress at a given temperature, $\Delta^{\mathrm{am}}\phi_0$ is the temperature-dependent free energy jump due to martensitic transformation, taken at zero stress, while the quadratic terms represent the elastic energy due to non-zero local stresses in the phases.

2.3. Constitutive micro-macro transition for laminates

Laminated microstructures in shape memory alloys are particularly convenient from the point of view of micromechanical modelling since the micro-macro relationships can be derived analytically for these microstructures. The complete set of equations for two-phase rank-one laminates at small deformation can be found in [16]; for higher-rank laminates of separable scales the equations can be used sequentially. The derived expression for the bulk contribution to the overall Helmholtz free energy per unit representative volume of the austenite/martensite laminate as shown in Fig. 2 is

$$\bar{\phi} = \phi_0 + \eta\Delta^{\mathrm{am}}\phi_0 + \tfrac{1}{2}\bar{\boldsymbol{\sigma}} \cdot \tilde{\mathbf{M}}\bar{\boldsymbol{\sigma}} + \tfrac{1}{2}\eta(1-\eta)\boldsymbol{\varepsilon}^{\mathrm{t}} \cdot \mathbf{Q}\boldsymbol{\varepsilon}^{\mathrm{t}}, \tag{11}$$

where η is the total volume fraction of martensite and $\tilde{\mathbf{M}}$ is the effective elastic compliance tensor for the laminate. Interfacial energy effects are disregarded here. Under the assumption (7) of an invariant habit plane at zero stress, the product $\boldsymbol{\varepsilon}^{\mathrm{t}} \cdot \mathbf{Q}\boldsymbol{\varepsilon}^{\mathrm{t}}$ in (11) vanishes. In this case, the related thermodynamic driving force (4) corresponding to increasing η has been transformed to

$$f = -\partial\bar{\phi}/\partial\eta = \bar{\boldsymbol{\sigma}} \cdot \bar{\boldsymbol{\varepsilon}}^{\mathrm{t}} - \tfrac{1}{2}\bar{\boldsymbol{\sigma}} \cdot \mathbf{B}_{\mathrm{a}}^{T}(\mathbf{M}_{\mathrm{a}} - \mathbf{M}_{\mathrm{m}})\mathbf{B}_{\mathrm{m}}\bar{\boldsymbol{\sigma}} - \Delta^{\mathrm{am}}\phi_0, \tag{12}$$

with the first right-hand side term known as the Schmid factor and the second term, quadratic in $\boldsymbol{\sigma}$, being proportional to the difference between the elastic compliance tensor $\mathbf{M}_{\mathrm{a}}$ for austenite and the effective one $\mathbf{M}_{\mathrm{m}}$ for a martensite plate. Analytic expressions for $\mathbf{Q}, \tilde{\mathbf{M}}, \mathbf{M}_{\mathrm{m}}, \mathbf{B}_{\mathrm{a}}, \mathbf{B}_{\mathrm{m}}$ and further details are available in [16].

The averaged rates of stress and strain in a rank-one laminate are related by

$$\langle\dot{\boldsymbol{\sigma}}\rangle = \tilde{\mathbf{L}}\langle\dot{\boldsymbol{\varepsilon}}\rangle, \qquad \langle\dot{\boldsymbol{\varepsilon}}\rangle = \tilde{\mathbf{M}}\langle\dot{\boldsymbol{\sigma}}\rangle, \qquad \tilde{\mathbf{M}} = \tilde{\mathbf{L}}^{-1}. \tag{13}$$

provided no transformation occurs *inside* the layers.

Evolution of the layered microstructure can most simply be described when the transformation proceeds only between a fixed ordered pair of (+) and (−) phases treated as homogeneous. Then, equations (2) reduce to

$$\dot{\bar{\boldsymbol{\varepsilon}}} = \langle\dot{\boldsymbol{\varepsilon}}\rangle + \dot{\eta}^{-}\Delta\boldsymbol{\varepsilon}, \qquad \dot{\bar{\boldsymbol{\sigma}}} = \langle\dot{\boldsymbol{\sigma}}\rangle + \dot{\eta}^{-}\Delta\boldsymbol{\sigma}, \tag{14}$$

where η^{-} is the volume fraction of the product phase, and the jumps $\Delta\boldsymbol{\varepsilon}$ and $\Delta\boldsymbol{\sigma}$ are determined locally by solving (3) on moving interfaces. From (14) and (13) the plasticity-like macroscopic constitutive rate equations are obtained for a specified (+) → (−) transformation:

$$\dot{\bar{\boldsymbol{\varepsilon}}} = \tilde{\mathbf{M}}\dot{\bar{\boldsymbol{\sigma}}} + \dot{\eta}^{-}\boldsymbol{\mu}, \qquad \dot{\bar{\boldsymbol{\sigma}}} = \tilde{\mathbf{L}}\dot{\bar{\boldsymbol{\varepsilon}}} - \dot{\eta}^{-}\boldsymbol{\lambda}, \tag{15}$$

where

$$\boldsymbol{\lambda} = \tilde{\mathbf{L}}\Delta\boldsymbol{\varepsilon} - \Delta\boldsymbol{\sigma} = \tilde{\mathbf{L}}\boldsymbol{\mu}. \tag{16}$$

Equations (15) with (16) are valid for a rank-one laminated microstructure independently of the adopted criterion of phase transformation.

2.4. Criterion of phase transformation

The value of $\dot{\eta}^-$ is to be determined from a criterion of phase transition. Neglecting time-dependence effects, the local criterion for martensitic phase transformation is assumed in the form (cf. [9])

$$f - f_c \leqslant 0, \qquad (f - f_c)\dot{s} = 0, \qquad f_c \geqslant 0, \tag{17}$$

where f is the thermodynamic driving force (4) and f_c is a threshold value related to the width of a hysteresis loop in a transformation cycle. In the following we take f_c = const, which is the simplest assumption.

A remarkable consequence [16] is that in the absence of dissipation due to reorientation of martensite variants, the intrinsic dissipation $\bar{\mathcal{D}}^t$ due to any transformation in a volume V^t is

$$\bar{\mathcal{D}}^t = V^t f_c \tag{18}$$

separately for forward and reverse transformation. It follows that for a closed transformation cycle in a given volume V^t, the area of a hysteresis loop does not depend on the loading program (e.g. tension or compression, loading direction, etc.).

By using the criterion (17), for a given loading program the preferred martensite plate is selected for which the respective transformation condition $f - f_c = 0$ is satisfied first. This defines the parameters of the (+) → (−) transformation that is followed in subsequent calculations as long as another transformation is preferred by the criterion (17).

From (17) with f_c = const after certain rearrangements the following *macroscopic* criterion for a specified (+) → (−) transformation is obtained [8, 16]

$$\begin{aligned} \dot{\eta}^- &= \frac{1}{g}\boldsymbol{\lambda}\cdot\dot{\bar{\boldsymbol{\varepsilon}}} > 0 \quad \text{if } \eta^- < 1 \text{ and } f = f_c \text{ and } \boldsymbol{\lambda}\cdot\dot{\bar{\boldsymbol{\varepsilon}}} > 0, \\ \dot{\eta}^- &= 0 \qquad\qquad \text{otherwise}. \end{aligned} \tag{19}$$

In consequence, an increment in the volume fraction η^- of the product phase is explicitly related to an increment in the overall strain $\bar{\boldsymbol{\varepsilon}}$, with the help of two quantities, $\boldsymbol{\lambda}$ defined by (16) and g defined by

$$g = \Delta\boldsymbol{\varepsilon}\cdot\tilde{\mathbf{L}}\Delta\boldsymbol{\varepsilon}, \tag{20}$$

with $g > 0$ if the laminate is *elastically* stable.

Substitution of (19) into (15) yields

$$\dot{\bar{\boldsymbol{\sigma}}} = \tilde{\mathbf{L}}^t\dot{\bar{\boldsymbol{\varepsilon}}}, \qquad \tilde{\mathbf{L}}^t = \tilde{\mathbf{L}} - \frac{1}{g}\boldsymbol{\lambda}\otimes\boldsymbol{\lambda} \qquad \text{if } \dot{\eta}^- > 0 \text{ and } f_c = \text{const}, \tag{21}$$

where $\tilde{\mathbf{L}}^t$ is the overall tangent moduli tensor for a rank-one laminate undergoing martensitic phase transformation. In multiscale modeling, it can be used as a local tangent moduli tensor of a higher-level laminate.

The constitutive framework in the rate form shown above is useful in establishing qualitative properties of the material behavior. Step-by-step calculations can be performed with the help of analytic expressions for the jumps $\Delta\boldsymbol{\varepsilon}$ and $\Delta\boldsymbol{\sigma}$ on interfaces and the effective stiffness and compliance tensors $\tilde{\mathbf{L}}$ and $\tilde{\mathbf{M}}$, given in the matrix form in [16] for arbitrary anisotropic linear elastic materials with eigenstrains. The task is simplified for the transformation between a fixed pair of (+) and (−) phases without elastic unloading or reverse transition since then the value of η^- corresponding to the current $\bar{\boldsymbol{\varepsilon}}$ can be found directly from the algebraic condition $f = f_c$. In general, the volume fractions of the parent and product phases are also dependent on the history of $\bar{\boldsymbol{\varepsilon}}$, which is associated with the appearance of hysteresis loops.

3. Examples

3.1. Untwinned martensite in CuZnAl

As the first example of application of the model outlined above, consider the stress-induced cubic-to-monoclinic transformation in a CuZnAl alloy. In this transformation the cubic austenite of DO_3 structure transforms to the monoclinic martensite of 18R structure (also called 6M structure). The martensite forms untwinned plates in which compatibility at the austenite-martensite interface is provided by random stacking faults (sequence faults) on the basal (101) planes [4, 15].

The material parameters, i.e. the crystallographic lattice parameters and the elastic constants of single-crystalline austenite and martensite, are taken from the available literature. Parameters of $N = 24$ symmetry-related martensitic plates, i.e. the habit plane normal $\mathbf{m}$, shape strain vector $\mathbf{b}$ and shear magnitude due to stacking faults k_{sf} are calcualted from (7) and (9). Numerical values of all these parameters along with the relevant references are given in [15]. The actually preferred plate is selected by using the transformation criterion (17).

Figure 3 shows the isothermal stress-strain diagrams corresponding to loading and unloading under uniaxial tension and compression (with axial strain control) for two loading directions specified by vector $\mathbf{t}$ relative to the cubic basis of austenite as indicated in the figure. The calculations have been performed for the value of chemical energy $\Delta^{am}\phi_0 = 10\,[\mathrm{MJ/m^3}]$ and the critical thermodynamic driving force $f_c = 0.5\,[\mathrm{MJ/m^3}]$. The overall stress-strain diagrams correspond to the formation of a single family of martensite plates in austenite under loading in two crystallographically distinct directions, and to the reverse transformation upon unloading. A strong effect of the crystal anisotropy is visible as the influence of the loading direction on the material response. However, the area of different hysteresis loops is invariant, in accord with the formula (18).

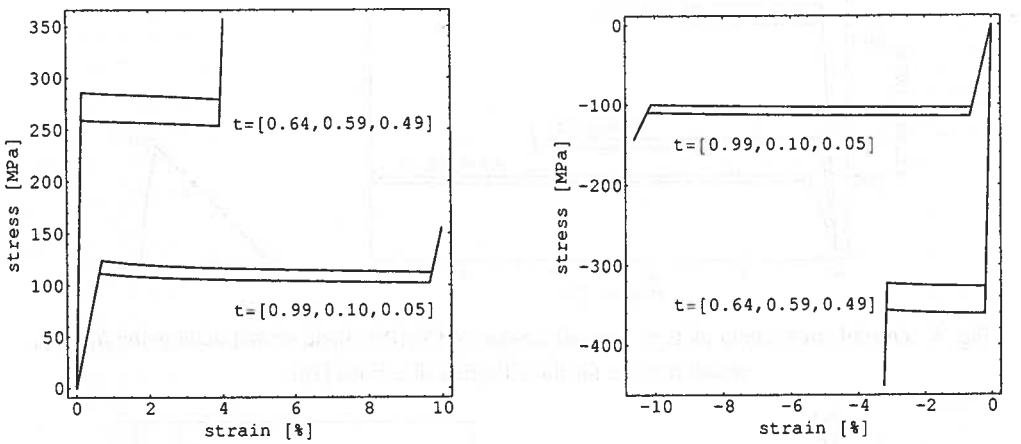

Fig. 3. Overall stress-strain diagrams in uniaxial tension (a) and compression (b) of CuZnAl crystal for two loading directions

3.2. Twinned martensite in CuAlNi

Consider now the case of internally twinned martensite plates. As an example we take isothermal stress-induced cubic (β_1) to orthorhombic (γ_1') transformation in a single crystal of a CuAlNi shape memory alloy. There are 6 crystallographic variants of martensite which, according to the theory outlined above, can form $N = 96$ distinct martensitic plates.

Three parameters of the transformation strain, three elastic constants for austenite and nine for martensite are taken from the literature. The temperature-dependent parameter $\Delta^{\mathrm{am}}\phi_0$ and constant f_c in (17) have been selected to fit the uniaxial stress-strain data for tensile specimen A1T1 in [13]. The numerical values of all these experiment-based parameters and the respective references are provided in [16]; no other material parameters are required to perform the calculations.

Sample results of small-strain calculations for an isothermal uniaxial tension test (under axial strain control) are shown in Fig. 4. Similar graphs were recently obtained in [3] by using another model. The overall stress-strain diagrams correspond to the formation of a single family (selected by using the transformation criterion (17)) of internally twinned martensitic plates in austenite under tension in three crystallographically distinct directions, and to the reverse transformation upon unloading. It must be noted, however, that the assumption of $\beta_1 \to \gamma_1'$ transformation may not correspond to reality since other transformation types are also possible in CuAlNi, cf. [5].

The diagrams presented in Figs. 4 and 3 are similar in character. Due to the difference in elastic properties of the phases, the internal stresses vary as the transformation

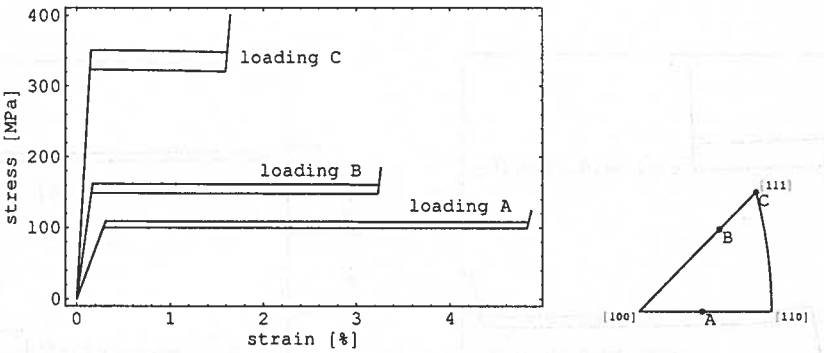

Fig. 4. Overall stress-strain plots in uniaxial tension of CuAlNi single crystal undergoing $\beta_1 \rightarrow \gamma_1'$ transformation for three loading directions [16]

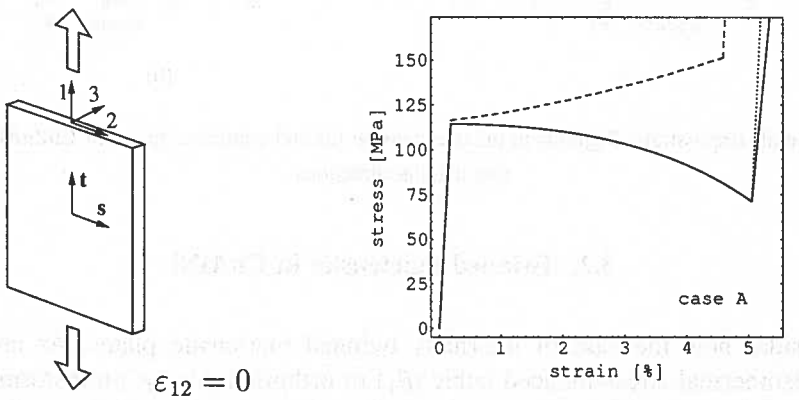

Fig. 5. Constrained tension of CuAlNi single crystal undergoing $\beta_1 \rightarrow \gamma_1'$ transformation for $\mathbf{t} = [0.925, 0.380, 0.]$ and $\mathbf{s} = [-0.380, 0.925, 0.]$. A solid line corresponds to free detwinning and a dashed line to a fixed twin fraction λ

proceeds with an increasing volume fraction of martensite, although the overall stress is almost constant (actually slightly decreasing in absolute value).

The results are significantly different if detwinning, i.e. martensite variant rearrangement by propagation of twinning planes, is taken into account, which was ruled out naturally in untwinned martensite and artificially when calculating the diagrams in Fig. 4. As discussed in [11, 17], detwinning can induce a drop of the overall uniaxial tensile stress even to zero as austenite diappears.

The detwinning effect can be not so strong, but still significant, in the presence of kinematic constraints. In the examples discussed above, a crystal could deform freely under uniaxial loading. This is a highly idealized situation for a grain in a polycrystal, but also for a specimen whose deformation is constrained by grips. The effect of such constraints can be illustrated by the example of a tensile specimen with the superimposed kinematic constraint $\varepsilon_{12} = 0$ (so that $\sigma_{12} \neq 0$) as indicated in Fig. 5; the directions $\mathbf{t}$ and $\mathbf{s}$ are given relative to the cubic basis of austenite. The resulting stress-strain curve in loading is shown in Fig. 5 by a broken line in the case of

prohibited detwinning, and by a solid line in the case of fully mobile twinning planes within martensite plates. Detwinning is *not* completed when austenite diappears at the lowest stress point and is continued with increasing stress. The apparent stiffness of martensite thus differs from the purely elastic behaviour of martensite indicated by a dotted line; cf. [17] for a more detailed discussion.

It must be emphasized that the material response has been calculated under the assumption of a *uniformly* laminated microstructure. However, due to the instability related to the softening behaviour, the transformation pattern of a specimen may be strongly non-uniform macroscopically. This can happen also in the absence of detwinning and irrespective of external boundary constraints, which is examined in the next subsection.

3.3. Instability of macroscopically uniform transformation

Consider the so-called *acoustic tensor* $\mathbf{A} = \mathbf{n}\tilde{\mathbf{L}}^{t}\mathbf{n}$, defined by contracting the tangent stiffness tensor $\tilde{\mathbf{L}}^{t}$ from both sides with some unit vector $\mathbf{n}$. A detailed study of the form of $\tilde{\mathbf{L}}^{t}$ specified by (21), (16) and (20) shows that the lowest eigenvalue of $\mathbf{A}$ for some $\mathbf{n}$ is, as a rule, *negative* (or zero in particular cases). Consequently, the macroscopically uniform transformation process, which at a micro-scale produces a fine rank-one laminate, may be regarded as intrinsically unstable. Even if this conclusion may be mitigated by realizing that an infinitely fine laminate is only an idealization, the tendency to build up more complex patterns, e.g. higher-rank laminated microstructures, may be expected. The idea of relating the formation of complex martensitic microstructures to an intrinsic instability of *macroscopically* uniform transformation is presented here only in outline; a more detailed exposition will be given elsewhere.

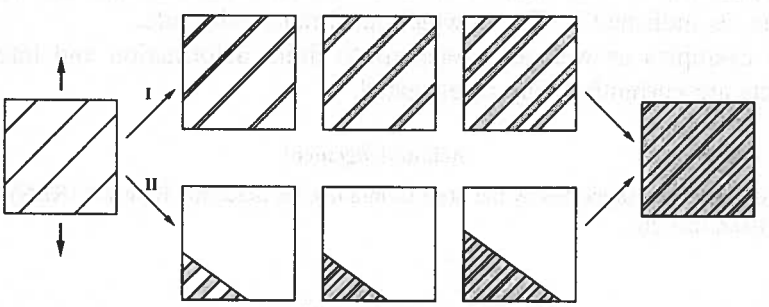

Fig. 6. Bifurcation of the layered transformation pattern: the transformation can proceed quasi-uniformly (upper pattern I) or be completed first within some volume fraction of the material (lower pattern II)

For example, in the tensile test simulation for loading A in Fig. 4 there exists a *bifurcation* of the layered transformation pattern, sketched (not to scale) in Fig. 6. The upper pattern (I) is that assumed earlier to be macroscopically uniform, i.e. to cover the volume fraction $\eta_0 = 1$ of the whole material. However, an alternative solution (II) exists in which the primary (internally twinned) martensitic plates first appear within a certain volume fraction $\eta_0 < 1$ only, while the remaining part of

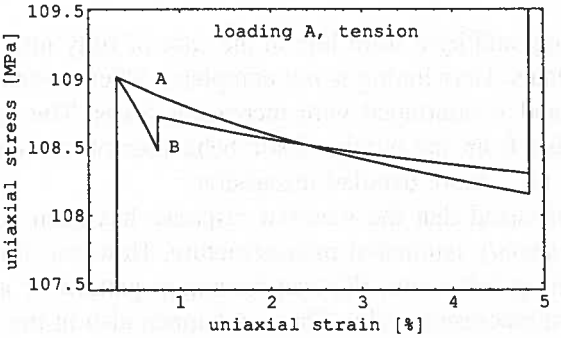

Fig. 7. Overall stress-strain diagrams in uniaxial tension for two solutions corresponding to transformation patterns I and II in Fig. 6, with $\eta_0 = 0.1$ in case II

austenite undergoes unloading. These two regions are separated by parallel planes (only one such plane appears in schematic Fig. 6), forming thus a rank-three laminated microstructure. Across these separation planes, the kinematic and static compatibility conditions analogous to (3) can be satisfied after lower-level averaging. This is found to be the case if the separation planes are orthogonal to the vector **b** that appears in (7).

The corresponding macroscopic stress-strain diagrams are shown in Fig. 7. Compared to the macroscopically uniform pattern (I), the solution with $\eta_0 = 0.1$ is energetically preferable initially. When the transformation within the volume fraction η_0 is completed, a short period of fully elastic straining follows, accompanied by a sharp increase in stress. Next, after reaching the threshold value f_c by the corresponding thermodynamic driving force, the martensite region starts to grow through propagation of the separation planes. In this case, the final microstructure reached on both routes is the same, as indicated in Fig. 6, which need not be the rule.

Other examples as well as extensions to finite deformation and internal length scale effects are currently being investigated.

Acknowledgement

This work has been supported by the State Committee for Scientific Research (KBN), Poland, Grant No. 4 T07A 032 26.

REFERENCES

[1] J.M. Ball, R.D. James. Fine phase mixtures as minimizers of energy. Arch. Ration. Mech. An. **100**, 13-50 (1987).

[2] K. Bhattacharya. Comparison of the geometrically nonlinear and linear theories of martensitic transformation. Continuum Mech. Thermodyn. **5**, 205-242 (1993).

[3] P. Blanc, C. Lexcellent. Micromechanical modelling of CuAlNi shape memory alloy behaviour. Mater. Sci. Eng. A**378**, 465-469 (2004).

[4] K.F. Hane. Bulk and thin film microstructures in untwinned martensites. J. Mech. Phys. Solids. **47**, 1917-1939 (1999).

[5] V. Novák, P. Šittner, J. Van Humbeeck. Martensitic transformations of Cu-Al-Ni single crystals in tension/compression. J. Physique IV **11**, 191-196 (2001).

[6] K. Otsuka, C.M. Wayman, editors. Shape Memory Materials. Cambridge University Press, 1998.

[7] E. Patoor, A. Eberhardt, M. Berveiller. Thermomechanical behaviour of shape memory alloys. Arch. Mech. **40**(5–6), 775-794 (1988).

[8] H. Petryk. Macroscopic rate-variables in solids undergoing phase transformation. J. Mech. Phys. Solids **46**, 873-894 (1998).

[9] J.R. Rice. Continuum mechanics and thermodynamics of plasticity in relation to microscale deformation mechanisms. In A.S. Argon, editor, Constitutive Equations in Plasticity, pages 23–79. MIT Press, Cambridge, Mass., 1975.

[10] A.L. Roytburd, J. Slutsker. Deformation of adaptive materials. Part I. Constrained deformation of polydomain crystals. J. Mech. Phys. Solids **47**, 2299-2329 (1999).

[11] A.L. Roytburd, J. Slutsker. Deformatin of adaptive materials. Part III: Deformation of crystals with polytwin product phases. J. Mech. Phys. Solids **49**, 1795-1822 (2001).

[12] J.A. Shaw, S. Kyriakides. Thermomechanical aspects of NiTi. J. Mech. Phys. Solids **43**, 1243-1281 (1995).

[13] T.W. Shield. Orientation dependence of the pseudoelastic behavior of single crystals of Cu–Al–Ni in tension. J. Mech. Phys. Solids **43**, 869-895 (1995).

[14] Y.C. Shu, K. Bhattacharya. The influence of texture on the shape-memory effect in polycrystals. Acta Mater. **46**(15), 5457-5473 (1998).

[15] S. Stupkiewicz. The effect of stacking fault energy on the formation of stress-induced internally faulted martensite plates. Eur. J. Mech. A/Solids **23**(1), 107-126 (2004).

[16] S. Stupkiewicz, H. Petryk. Modelling of laminated micro-structures in stress-induced martensitic transformation. J. Mech. Phys. Solids **50**, 2303-2331 (2002).

[17] S. Stupkiewicz, H. Petryk. Micromechanical modelling of stress-induced martensitic transformation and detwinning in shape memory alloys. Journal de Physique IV **115**, 141-149 (2004).

[18] Q.-P. Sun, Z.-Q. Li. Phase transformation in superelastic NiTi polycrystalline micro-tubes under tension and torsion–from localization to homogeneous deformation. Int. J. Sol. Struct. **39**, 3797-3809 (2002).

[19] P. Thamburaja, L. Anand. Polycrystalline shape-memory materials: effect of crystallographic texture. J. Mech. Phys. Solids **49**, 709-737 (2001).

[20] M.S. Wechsler, D.S. Lieberman, T.A. Read. On the theory of the formation of martensite. Trans. AIME J. Metals **197**, 1503-1515 (1953).

Received: 3 November 2004.

A R C H I V E S O F M E T A L L U R G Y A N D M A T E R I A L S
Volume 49 2004 Issue 4

E. CESARI*, J. PONS*, R. SANTAMARTA*, C. SEGUI *, V.A. CHERNENKO**

FERROMAGNETIC SHAPE MEMORY ALLOYS: AN OVERVIEW

FERROMAGNETYCZNE STOPY Z PAMIĘCIĄ KSZTAŁTU: PRZEGLĄD

Ferromagnetic shape memory alloys (FSMA) have the unique capability to exhibit the thermoelastic martensitic transformation and rearrangement of martensitic variants by applying a magnetic filed, in addition to temperature and/or stress changes as in conventional shape memory alloys. The different mechanisms which can produce a shape change under a magnetic field and their relation with the magnetocrystalline anisotropy are discussed. The transformation sequences and martensitic structures are reviewed, particularly in Ni-Mn-Ga alloys as the best known system and representative of the martensites appearing in most FSMA systems. Some transformation features of more recently developed FSMA, namely Ni-Co-Al and Co-Ni-Ga, are also considered.

Keywords: martensitic transformation, shape memory alloys, ferromagnetism.

Ferrmomagnetyczne stopy z pamięcią kształtu (FSMA) wykazują unikalną zdolność do termosprężystej przemiany martenzytycznej i reorganizacji wariantów martenzytu w polu magnetycznym, w dodatku do przemian wywołanych zmianami temperatury i/lub naprężeniem, podobnych jak w konwencjonalnych stopach z pamięcią kształtu. W pracy przedyskutowano różne mechanizmy, które mogą wytwarzać zmianę kształtu w polu magnetycznym i ich związek z anizotropią magnetyczną. Przedstawino przegląd sekwencji przemian i struktur martenzytu, w szczególności w stopach Ni-Mn-Ga, jako należących do układu najlepiej znanego i reprezentatywnego dla większości ferrmomagnetycznych stopów z pamięcią kształtu. Pewne cechy charakterystyczne przemiany w ostatnio rozwijanych ferromagnetycznych stopach z pamięcią kształtu Ni-Co-Al i Co-Ni-Ga zostały także przedyskutowane.

1. Introduction

Shape-memory effects are related to a difusionless structural phase transformation (a thermoelastic martensitic transformation, MT) from a high-temperature high-symmetry phase (austenite) to a low-temperature low-symmetry phase (martensite)

* DEPARTAMENT DE FÍSICA, UNIVERSITAT DE LES ILLES BALEARS, E-07122 PALMA DE MALLORCA, SPAIN
** INSTITUTE OF MAGNETISM, VERNADSKY STR. 36B, KIEV 03142, UKRAINE

[1]. In conventional shape memory alloys (SMA) the MT can be induced either by temperature or stress changes or by a combination of both. In the temperature induced MT, in absence on any stress field, the lower symmetry of the martensite results in the formation of several variants, each one with its own associated shape change. The different variants are twin-related, and some variants bring about nearly opposite shape changes, forming the so-called self-accommodated groups of variants. As all the variants have the same free energy, all of them are equally likely to form upon cooling. Once a given martensite variant is formed in a certain region, the surrounding areas are prone to transform to their self-accommodating variants, in order to reduce the total strain energy, thus leading to a minor shape change when thermally transforming from austenite to martensite at the temperature T_M. However, under a biasing stress field, certain variants will be favoured (those whose shape change accommodate or "relax" the applied stress field) and will grow at the expenses of the other variants. This reorientation of (twin) variants by an applied stress is the basis of the *shape memory effect* [1]. Selected variants will also appear when stress-inducing the transformation at $T > T_M$, involving rather large deformations (up to a few % in single crystals). The reversibility of the stress-induced transformation upon unloading leads to the full recovery of the deformation, which constitutes the so-called superelasticity effect, being another interesting property of SMA.

SMA develop the largest strains of the actuator materials available to date. However, a serious drawback of the shape memory actuators is their low working frequency (of the order of Hz) mainly due to the relatively slow temperature changes that can be achieved (specially on cooling). Conventional giant magnetostrictive materials (driven by a magnetic field instead of temperature change) provide higher operating frequencies (order of 10^2 Hz) compared to SMA, but the attainable strains are notably smaller ($\sim$ 0.2%). Magnetic control of the shape memory effect would lead to much faster response of the actuators than the thermal control. The discovery of large magnetically induced strains (MIS) in Ni_2MnGa Heusler alloys [2] and the confirmation that giant magnetostriction or MIS up to a few percent takes place in these alloys associated to the magnetic-field-induced reorientation of martensitic variants [3] has triggered the interest in the ferromagnetic shape memory alloys (FSMA).

The Ni-Mn-Ga alloys close to the stoichiometric Ni_2MnGa are by far the most studied within the FSMA systems, and some of their specific features, representative of the FSMA behaviour, will be discussed below. Ni-Mn-Ga alloys have also been the basis for understanding the conditions and mechanims for ferromagnetic shape memory effect. However, due to the wide field of applications expected for FSMA and relatively poor ductility of Ni-Mn-Ga, there is a large interest in developing new FSMA as for example, Fe-Pd [4], Fe_3Pt [5], Ni_2MnAl [6], Ni_2FeGa [7] and Co-Ni- Ga [8] alloys. Pd and Pt containing alloys are less studied due to, in some cases, low MT temperature and their high cost.

2. Magnetic-field-induced strains

FSMA have the unique possibility to exhibit the thermoelastic martensitic transformation and rearrangement of martensitic variants by applying a magnetic field, in addition to temperature and/or stress changes as in conventional SMA. In the alloys showing large MIS, the transformation usually takes place in a ferromagnetically ordered parent phase, i.e. the Curie temperature $T_C > T_M$. In some cases, both the para-ferro and the martensitic transformations proceed simultaneously, thus a paramagnetic parent phase transforms to a ferromagnetic martensite. However, the main issue is that for materials undergoing a thermoelastic martensitic transformation and being ferromagnetic, the variant structure may also be biased by a magnetic field. It has to be mentioned that the rearrangement of martensite variants is not the only mechanism that can produce a shape change under a magnetic field: applying a magnetic field to the austenite can induce the martensitic transformation. Indeed, if the anisotropy constants of austenite are low (low anisotropy energy) the field will first rotate the magnetization into the direction of the field, which will be accompanied by ordinary magnetostriction. Since the saturation magnetization of martensite is higher than that of austenite, there is a driving force to induce the structural change, so it can be expected that high enough fields will induce the MT. However, large fields are required and the MT is only induced at temperatures very close to the nominal T_M, i.e., the shift in the transformation temperature caused by the magnetic field is small (for instance, a shift of about 6 K has been observed in a Ni-Mn-Ga alloy under an applied field of 12 T [9]). Several models have been proposed to account for the different contributions produced by a magnetic field on the MT. At high fields (much larger than the saturation fields), the Zeeman (magnetostatic) energy term is predominant leading to a Clausius-Clapeyron type relation: $dT/dH = \Delta M/\Delta s$, where ΔM and Δs are the magnetization and entropy changes, respectively, associated to the MT. Under lower fields, the Zeeman energy is no longer predominant, and the magnetoelastic contribution can be even larger [9, 10].

A second mechanism producing a shape change is related to the rotation of the spontaneous magnetization with respect to the crystal lattice, under the action of a magnetic field. This is the mechanism acting in conventional (giant) magnetostrictive materials as Terfenol-D. This commercially available material (composition $Fe_2Dy_{1-x}Tb_x$, $x \sim 0.27$) offers up to 0.17% magnetostrictive strains. In ordinary magnetostrictive materials the magnetic-field- induced strain has a volume component (related to spontaneous magnetization, but not dependent of its orientation) and a shear component (associated to the magnetic anisotropy), both in the range of 10^{-3}% in ferrous materials. The shear magnetostrain is much larger in rare earth-Fe compounds (RFe_2), but they have too large magnetocrystalline energy. In order to obtain large strains at relatively low magnetic fields, the strategy was to design ternary (solid-solution R_1Fe_2 - R_2Fe_2) compounds having opposite sign in magnetocrystalline anisotropy constants, as in the case of Terfenol-D [11]. In this way there is little cost for rotating the magnetization with respect to the crystal lattice.

In the case of FSMA a large magnetic anisotropy is desirable to constrain the spontaneous magnetization along the variant easy axis (in other words, to prevent, in each variant, the rotation of the magnetization with respect to the lattice, and force the lattice to rotate until aligning its easy axis with the field). This constrain is a necesary condition to develop the driving forces (or magnetoelastic energies) needed for the variant rearrangement [3]. Under this condition, the giant MIS will take place provided there is a high mobility of the twin interfaces between variants. In the alloys showing large MIS, the critical stress to reorientate the martensitic variants is usually $\leqslant 5$ MPa. Therefore, in both (giant) conventional magnetostrictive materials and martensitic FSMA the values of strain and magnetization should be always associated (changes in magnetization $\Rightarrow$ changes in strain) which corresponds to the behaviour governed by magnetoelastic energies. In both types of materials (FSMA and ordinary magnetostrictive compounds) the conditions to be fulfilled by the magnetic anisotropy are essential to obtain large magnetic-field-induced strains, although of opposite nature.

Magnetic anisotropy constants (MAC) have been widely studied in relation to recording media, in particular the conditions that promote very high magnetic anisotropy. To summarize, the main finding was that magnetic anisotropy is favored by high crystalline anisotropy, which can be related to anisotropy of crystal structure, anisotropic ordering and fine-scale multilayers. Variants of low-symmetry martensite are also beneficial. Thus several characteristic features of FSMA promoting magnetic anisotropy can be recognized. The magnetic anisotropy energy (MAE) and the easy axis depend on the particular martensite. For the Ni-Mn-Ga alloys, in the so called 5-layered martensite the [001] direction (the short *c*-axis) is the easy axis and the MAE is around $2.0–2.5 \times 10^5$ J/m^3 at room temperature; in the non-modulated tetragonal martensite, [001] is the hard direction and there is an easy plane with MAE of 3.0×10^5 J/m^3 [12–13] (in the 7-layered martensite there are three non-equivalent directions; more details on the martensitic structures are given below), which can be compared to 5×10^4 J/m^3 for Fe-bcc and 4.5×10^5 J/m^3 for Co-hcp.

The effect of magnetic field can be considered equivalent to an additional mechanical applied stress. This is a quite natural assumption, as both the mechanical energy and the magneto- mechanical energy play equivalent roles, for example to the free energy contributions in the L a n d a u model. In the case of simple two-variant twinning geometry, the magnetic-field- induced stress can be found from the twinning transformation strain and specific magnetizations along easy and hard magnetization directions [14]. From the balance between the mechanical and the magnetic stresses, the magneto-strain effect can be calculated and compared to stress-strain behaviour in twinning (de-twinning) between martensite variants. Maximal magnetic-field-induced stresses of 3—5 MPa, in agreement with the experiment, are given by the model. Very recent experimental and theoretical studies of the superelastic behaviour of Ni-Mn-Ga martensite under constant magnetic field have shown that the magnetoelastic stress is responsible for both ordinary magnetostriction and detwinning of the martensite [15]. Moreover, a formerly proposed statistical model of the magnetostrain has been applied to the quantitative description of the superelastic behaviour in a magnetic field:

both experimental and model results show that the field-induced stress is proportional to the square of the magnetization, thus supporting the idea that the magnetoelastic interaction is the fundamental source of the large field-induced strains caused by twin rearrangement. It is worth to notice that despite the equivalence between mechanical and magnetic stresses, the level of magnetoelastic coupling limits the stress that can be produced by a magnetic field.

3. Transformation sequences and martensitic structures

Ni-Mn-Ga alloys, derived from the Ni_2MnGa compound, have the Heusler $L2_1$ ordered crystal structure above T_M and present a large variety of martensitic structures as well as pre- and inter-martensitic transformations, depending on the composition (to which T_M is much more sensitive than T_C), and the relative position of T_M and T_C [16–20]. These alloys were classified into three basic groups [16]: alloys with $T_M < 300\ K < T_C$ (e/a < 7.7, group I) exhibit during cooling a weakly first order premartensitic phase transition (basically a soft mode phonon condensation) from the parent phase to a cubic intermediate phase, prior to the MT itself. The crystal structure of martensite in this group is characterized by the existence of four extra diffraction spots along one of the ⟨110⟩ directions, which involves a five atomic plane periodicity along this direction. This feature gives rise to the generic name of 5-layered for this martensite, although it is also denoted as 10M. Single crystalline alloys of group III ($T_M > T_C$, e/a > 7.7) do not show the premartensitic transformation, but they undergo on cooling a sequence of MT to layered structures with higher periods, like 7 (14M martensite) or 10 (10O martensite) as well as to a non-layered tetragonal martensite with c/a > 1 not showing any extra diffraction spot (denoted in the literature as T, non-modulated, NM, or 2M). In the alloys of group II (e/a ≈ 7.5–7.7, $T_M \approx 300$ K $< T_C$) the above mentioned soft mode condensation is inhibited by the MT taking place before, thus no premartensitic transition is revealed. The 10M and 14M martensites (or a mixture of both) are thermally induced in these alloys. To give an example of the behaviour of the different groups, the characteristic trends of the elastic modulus evolution for the different groups of Ni-Mn-Ga alloys are shown in Fig. 1. Ni-Mn-Ga single crystals exhibit different sequences of stress-induced transformations as well, for example, $L2_1 \rightarrow$ 10M $\rightarrow$ 14M $\rightarrow$ 2M upon compression along ⟨110⟩p or tension along ⟨100⟩p for the nearly stoichiometric compositions [21–22]. These martensites, after unloading, can remain in their own temperature intervals of metastability, leading, on heating, to the sequence of reverse intermartensitic transformations. The superelastic effect has been studied in single crystalline alloys with transformation temperatures around 300 K and above, showing fully recoverable strains of up to 6%, depending on the stress axis orientation and temperature [23, 24]. In the alloys with high transformation temperatures ($T_M > T_C$) the experimental values of transformation strain and temperature dependence of the critical stress to induce the martensitic transformation can only be thermodynamically understood if it is assumed that different

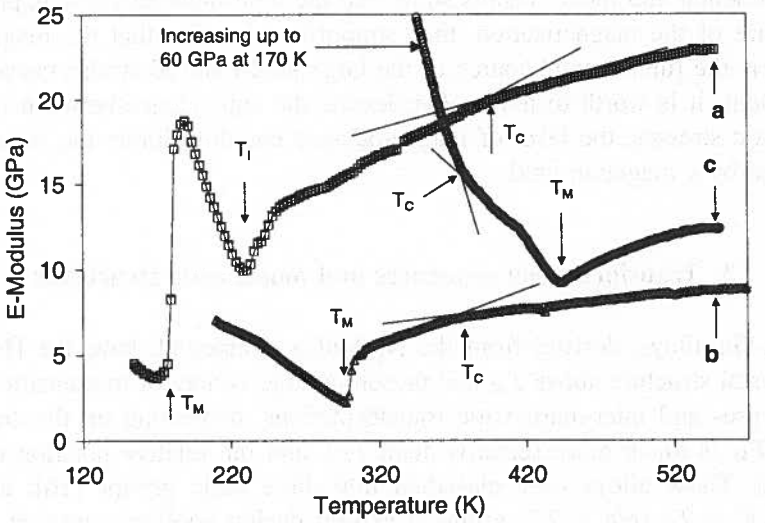

Fig. 1. Elastic modulus vs. temperature curves obtained on cooling Ni-Mn-Ga alloys belonging to group I (curve a), group II (curve b) and group III (curve c). The arrows indicate the temperatures corresponding to the different phase transitions: T_M holds for the martensitic transformation; T_I holds for the premartensitic transformation into the intermediate phase I; T'_M indicates the intermartensitic transformation occurring in the group III alloys, and T_C the Curie temperature

martensitic structures are formed when compressing along different crystallographic directions [24].

The five- and seven-layered structures were firstly studied by Martynov et al. [22]. Using the crystallographic axes derived from ⟨100⟩ directions of the cubic austenite, the unit cells of the 5- and 7-layered martensites deduced from the fundamental spots were reported as body centered tetragonal with c/a < 1 and body centered orthorhombic, respectively. The extra diffraction spots present along one of the ⟨110⟩ directions were interpreted as a periodical shuffling (modulation), in such a way that every 5th or 7th (110) plane remains in its original (non-shifted) position, the modulation being described by a function containing three harmonic terms [22]. More recently [18], this model has been compared with that used for the description of the long period martensites in Ni-Al-type alloys [25–27], i.e., periodic stacking of nearly close packed basal planes derived from {110} planes of austenite, with sequences $(5\,\bar{2})_2$ and $(3\,\bar{2})_2$ in Zhdanov notation, for the 7- and 5- layered martensites, respectively. Following the nomenclature introduced in [28], these structures are denoted as 14M and 10M. The 10-layered martensite was analysed according to this description, the $(5\,\bar{5})$ sequence (10O structure) showing the best fitting with the experimental selected-area electron diffraction patterns [18]. The structures built up by stacking of close packed planes are nano-twinned in nature, the two twin lamellae having thicknesses of 5-2, 3-2 and 5-5 atomic planes, for 14M, 10M and 10O martensites, respectively. It has been shown in [18] that the two structural models (modulation by shuffling or stacking

of basal planes) result in similar atomic positions, being practically indistinguishable due to the limited resolution of the diffraction techniques with photographic recording. Recent results obtained by HRTEM have demonstrated the nano-twinned nature of the 7-layered martensite, although only in very limited areas the two lamellae have the ideal thicknesses of 5-2 planes inherent to the 14M structure (Fig. 2a); in general the

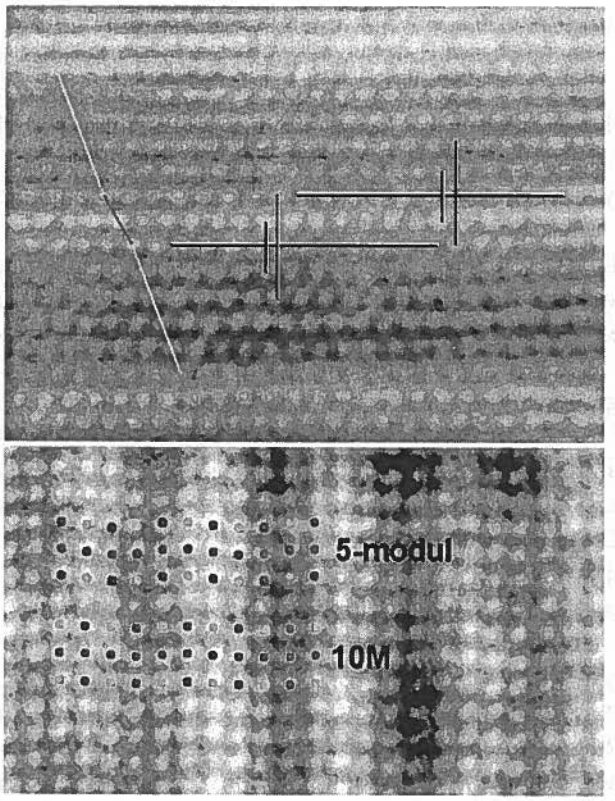

Fig. 2. (a) HRTEM image of the 7-layered martensite showing the (5 $\bar{2}$) stacking sequence. The two lamellae of the nanotwins are marked as well as the twin planes. (b) Experimental HRTEM image of the 5-layered martensite with the superposition of the atomic positions deduced from the two structural models discussed, showing a good agreement in both cases.

sequence of stacking planes is significantly distorted from the ideal (5 $\bar{2}$). On the other hand, for the 5-layered martensite, the two structural models lead to almost identical atomic positions, which can not be distinguished from the HRTEM images (Fig. 2b). Concerning the non-layered martensite, its unit cell can be described as a tetragonal distortion of the cubic austenite, in such a way that the a and b axes shrink by an equal amount, while the *c* axis enlarges, leading to a tetragonal unit cell with $c/a > 1$. It is equivalent to the martensite observed in Ni-Al alloys having the $L1_0$ structure: ordered face centered tetragonal with $c/a < 1$. The difference arises from the choice of the

crystallographic axes and from the type of order exhibited by the austenite (B2 in Ni-Al alloys). In Ni-Mn-Ga with $L2_1$ austenitic structure, the corresponding martensitic lattice would be a "double" $L1_0$ (double c axis).

Other FSMA as Ni-Mn-Al, which have been initially developed as high temperature conventional SMA, to overcome the brittleness of Ni-Al-based alloys through the introduction of the ductile γ phase (fcc disordered A1 structure), present the same martensitic structures as in Ni-Mn-Ga: the tetragonal non modulated (denoted as $L1_0$, for analogy with the martensite of the binary Ni-Al and Ni-Mn systems) and also the layered 14M and 10M phases for compositions not far from the stoichiometric Heusler Ni_2MnAl [27]. The five-layered (10M) and seven-layered (14M) martensitic structures occur as well in Ni-Fe-Ga alloys, which in analogy to Ni-Mn-Al, show improved ductility – as compared to brittle Ni-Mn-Ga alloys – due to the presence of the γ phase [7].

The Fe-Pd alloys containing close to 30 at% Pd undergo a sequence of transformations: a thermoelastic MT from fcc parent to fct structure at temperatures close to room temperature, followed, on further cooling, by a transformation to a bct phase. The fct $\rightarrow$ bct (or the fcc $\rightarrow$ bct , which occurs directly in alloys with lower Pd content) is irreversible. Interesting features are found in the fcc $\rightarrow$ fct transformation, as the tweed microstructure of the parent phase which is a precursor phenomenon in the MT, and the gradual appearance of the tetragonality with decreasing temperature which allows to consider the fcc $\rightarrow$ fct transformation as having nearly second order character [29].

Addition of Co to Ni-Al alloys preserves the MT from the β phase (B2 structure) to the β' ($L1_0$, equivalent to the non modulated tetragonal martensite of Ni-Mn-Ga alloys), at decreasing temperatures as Co content increases. The MT occurs even for alloys containing more than 40 at% Co. As for the Ni-Mn-Al and Ni-Fe-Ga alloys, the presence of γ phase (A1 disordered or $L1_2$ ordered fcc structure) as a second phase increases the ductility of the β phase. Therefore, Ni-Co-Al alloys constitute a new system of FSMA with high ductility at room temperature [30–31]. It has been found that T_C increases with increasing Co content and decreasing Al, while T_M temperatures decrease with an increase in both Co and Al content. As the extrapolated T_C temperatures for the β' are about 85 K higher than those of the β phase for the same composition, there is a composition range for which the paramagnetic β phase transforms into ferromagnetic β' on cooling (for example in the range Ni-(35-37)Co-29Al); at higher Co content $T_C > T_M$, thus leading to a composition range of "classical" FSMA.

In Co-Ni-Ga alloys, a direct transformation from β-para to β'-ferro exists around Co-(23-24)Ni-30Ga [32]. In these alloys, as in Ni-Co-Al, T_C increases and T_M decreases with increasing Co content. It is worth to note that the just mentioned compositions are not far from the stoichiometric Co_2NiGa, which has been claimed to be a new family of Co-based FSMA [8]. Alloys in the composition range $Co_2Ni_{1-x}Ga_{1+x}$ ($0.09 \leqslant x \leqslant 0.15$) show MT from a ferromagnetic parent phase at temperatures in the domain 280—330 K, with a hysteresis of about 30 K [8]. Thermal and stress induced transformations as well as the magnetization behaviour have been studied in a

single crystalline Co-22.0Ni-29.0Ga alloy [33]. This alloy transforms at $T_M \approx 320$ K to the non-modulated tetragonal martensite with c/a > 1 (or $L1_0$ fct structure in other crystallographic axes). When compressed in martensite the alloy shows full shape recovery upon heating, but at temperatures ~ 70 K above the nominal ones. This effect is directly related to the mechanical stabilization of stress induced martensite found in this alloy: The stress-strain curves show a large hysteresis ($\geqslant$ 200 MPa) and the stabilization degree is strain dependent. Such features had been observed in non-magnetic SMA like Ni-Ti or Cu-Al-Ni but they are not typical for other martensites formed in FSMA. For instance, mechanical stabilization has not been observed in Ni-Mn-Ga alloys transforming to the modulated 10M (c/a < 1) structure, but it has been found in Ni-Mn-Ga alloys transforming to the non-modulated tetragonal structure with c/a > 1, although with a much lower stabilization degree than in the Co-Ni-Ga alloy.

Thus, apart from the Fe-Pd or Fe-Pt systems, equivalent austenitic and martensitic phases are formed in all the other ferromagnetic shape memory alloys, the main differences arising from the type of atomic order exhibited by the parent phase (either nearest neighbour ordering -B2 structure- or next-nearest neighbour ordering -Heusler or $L2_1$ structure-, which depends on alloy composition and thermal treatment) and inherited by the martensite. The largest MIS, close to 6% and 10%, have been observed in alloys transforming to the 5-layered (10M) or 7-layered (14M) martensites respectively [34–36], which fulfill the conditions of existence of an easy axis with high magnetic anisotropy energy, together with a very low critical stress to induce the rearrangements of martensitic plates. The non-modulated tetragonal martensite (c/a > 1) is not favourable, as it presents an easy plane for the magnetization instead of an easy axis. Moreover, the critical stress for variant reorientation is considerably higher, altogether inhibiting the large MFIS effect.

Acknowledgements

Partial financial support from DGI (project MAT2002-00319) is acknowledged.

REFERENCES

[1] L. Delaey, Diffusionless Transformations, in "Phase Transformations in Materials", P. Haasen, ed., VCH, Germany, 1991.

[2] K. Ullakko, J.K. Huang, C. Kanter, V.V. Kokorin, R.C. O'Handley, Large magnetic-field-induced strains in Ni_2MnGa single crystals. Appl. Phys. Lett. **69**, 1966-1968 (1996).

[3] R. Tickle, R.D. James, Magnetic and magnetomechanical properties of Ni_2MnGa. J. Magn. Magn. Mat. **195**, 627-638 (1999).

[4] Y. Furuya, N.W. Hagood, H. Kimura, T. Watanabe, Shape memory effect and magnetostriction in rapidly solidified Fe-29.6 at% Pd alloy. Mat. Trans. JIM **39**, 1248-1254 (1998).

[5] T. Kakeshita, T. Takeuchi, T. Fukuda, M. Tsujiguchi, T. Saburi, R. Oshima, S. Muto, Giant magnetostriction in an ordered

Fe_3Pt single crystal exhibiting a martensitic transformation. Appl. Phys. Lett. **77**, 1502-1504 (2000).

[6] A. Fujita, K. Fukamichi, F. Gejima, R. Kainuma, K. Ishida, Magnetic properties and large magnetic-field-induced strains in off-stoichiometric Ni-Mn-Al Heusler alloys. Appl. Phys. Lett. **77**, 3054-3056 (2000).

[7] K. Oikawa, T. Ota, T. Ohmori, Y. Tanaka, H. Morito, A. Fujita, R. Kainuma, K. Fukamichi, K. Ishida, Magnetic and martensitic phase transitions in ferromagnetic Ni-Ga-Fe shape memory alloys. Appl. Phys. Lett. **P81**, 5201-5203 (2002).

[8] M. Wuttig, J. Li, C. Craciunescu, A new ferromagnetic shape memory alloy system. Scripta mater. **44**, 2393-2397 (2001).

[9] V. Chernenko, O. Babil, V. L'vov, P.G. McCormick, Martensitic transformations in Ni-Mn-Ga system affected by external fields, Mat. Sci. Forum **327-328**, 485-488 (2000).

[10] T. Kakeshita, K. Shimizu, M. Ono, M. Date, Magnetic field-induced martensitic transformations in a few ferrous alloys, J. Magn. Mag. Mat. **90-91**, 34-36 (1990).

[11] A.E. Clark, H.S. Belson, Giant room-temperature magnetostrictions in $TBFe_2$ and $DyFe_2$, Phys. Rev. B **5**, 3642-3644 (1972).

[12] R. Tickle, R.D. James, Magnetic and magnetomechanical properties of Ni_2MnGa, J. Magn. Mag. Mat. **195**, 627-638 (1999).

[13] O. Heczko, K. Jurek, K. Ullakko, Magnetic properties and domain structure of magnetic shape memory Ni-Mn-Ga alloy, J. Magn. Mag. Mat. **226-230**, 996-998 (2001).

[14] A. Likhachev, K. Ullakko, The model development and experimental investigation of giant magneto-mechanical effects in Ni-Mn-Ga, J.Magn.Mag.Mat. **226-230**, 1541-1543 (2001).

[15] V.A. Chernenko, V.A. L'vov, P. Müllner, G. Kostorz, T.Takagi, Magnetic-field-induced superelasticity of ferromagnetic thermoelastic martensites: Experiment and modeling, Phys. Rev. B **69**, 134410-1-8 (2004).

[16] V.A. Chernenko, E. Cesari, V.V. Kokorin, I.N. Vitenko, The development of new ferromagnetic shape memory alloys in Ni-Mn-Ga system, Scripta Met. et Mater. **33**, 1239-1244 (1995).

[17] V.A. Chernenko, C. Seguí, E. Cesari, J. Pons, V.V. Kokorin, Sequence of martensitic transformations in Ni-Mn-Ga alloys, Phys. Rev. B **57**, 2659-2662 (1998).

[18] J. Pons, V.A. Chernenko, R. Santamarta, E. Cesari, Crystal structure of martensitic phases in Ni-Mn-Ga shape memory alloys. Acta Mat. **48**, 3027-3038 (2000).

[19] V.A. Chernenko, J. Pons, C. Seguí, E. Cesari, Premartensitic phenomena and other phase transformations in Ni-Mn-Ga alloys studied by dynamical mechanical analysis and electron diffraction, Acta Mat. **50**, 53-60 (2002).

[20] V.V. Kokorin, V.A. Chernenko, J. Pons, C. Seguí, E. Cesari, Acoustic phonon mode condensantion in Ni_2MnGa compound, Solid State Communications, **101**, 7-9 (1997).

[21] V.V. Kokorin, V.V. Martynov, V.A. Chernenko, Stress-induced martensitic transformations in Ni_2MnGa, Scripta Met. Mat. **26**, 175-177 (1992).

[22] V. V. Martynov, V. V. Kokorin, The crystal structure of thermally- and stress-induced martensites in Ni_2MnGa single crystals, J. Phys. III **2**, 739-749 (1992).

[23] V. A. Chernenko, V. V. Kokorin, O. M. Babii, I. K. Zasimchuk, Phase diagrams in the Ni-Mn-Ga system under compression, Intermetallics **6**, 29-34 (1998).

[24] V. A. Chernenko, V. L'vov, J. Pons, E. Cesari, Superelasticity in high-temperature Ni-Mn-Ga alloys, J. Appl. Phys. **93**, 2394-2399 (2003).

[25] V. V. Martynov, K. Enami, L. G. Khandros, S. Nenno, A. V. Tkachenko, Phys. Met. Metall. **55**, 136-143 (1983).

[26] S. Morito, K. Otsuka, Electron microscopy of new martensites with long period stacking order structures in $Ni_{50}Al_xMn_{50-x}$ alloys I. Structures and morphologies, Mat. Sci. & Eng. A **208**, 47-55 (1996).

[27] R. Kainuma, H. Nakano, K. Ishida, Martensitic transformations in NiMnAl β phase alloys, Metall. Mat. Trans. A **27A**, 4153-4162 (1996).

[28] K. Otsuka, T. Ohba, M. Tokonami, C. M. Wayman, New description of long period stacking order structures of martensites in small β-phase alloys, Scripta Met. Mat. **29**, 1359-1364, (1993).

[29] R. Oshima, M. Sugiyama, Martensite transformations in Fe-Pd alloys, J. de Phys. **43**, C4-383-388, (1982).

[30] R. Kainuma, M. Ise, C. C. Jia, H. Ohtami, K. Ishida, Phase equilibria and microstructural control in the Ni-Co-Al system, Intermetallics **4**, S151-S158 (1996).

[31] K. Oikawa, L. Wulff, T. Iijima, F. Gejima, T. Ohmori, A. Fujita, K. Fukamichi, R. Kainuma, K. Ishida, Promising ferromagnetic Ni-Co-Al shape memory alloy system, Appl. Phys. Lett. **79**, 3290-3292 (2001).

[32] K. Oikawa, T. Ota, F. Gejima, T. Ohmori, R. Kainuma, K. Ishida, Phase equilibria and phase transformations in new B2-type ferromagnetic shape memory alloys of Co-Ni-Ga and Co-Ni-Al systems, Mat. Trans. **42**, 2472-2475 (2001).

[33] V. A. Chernenko, J. Pons, E. Cesari, I. K. Zasimchuk, Transformation behaviour and martensite stabilization in the ferromagnetic Co-Ni-Ga Heusler alloy, Scripta Mat. **50**, 225-229 (2004).

[34] S. J. Murray, M. Marioni, S. M. Allen, R. C. O'Handley, T. A. Lograsso, 6% magnetic-field-induced strain by twin-boundary motion in ferromagnetic Ni-Mn-Ga, Appl. Phys. Lett. **77**, 886-888 (2000).

[35] A. Sozinov, A. A. Likhachev, N. Lanska, K. Ullakko, Giant magnetic-field-induced strain in NiMnGa seven-layered martesnitic phase, Appl. Phys. Lett. **80**, 1746-1748 (2002).

[36] P. Müllner, V. A. Chernenko, G. Kostorz, Large cyclic magnetic-field-induced deformation in orthorhombic (14M) Ni-Mn-Ga martensite, J. Appl. Phys. **95**, 1531-1536 (2004).

Received: 3 November 2004.

A R C H I V E S O F M E T A L L U R G Y A N D M A T E R I A L S
Volume 49 2004 Issue 4

V.A. CHERNENKO*, S.P. ZAGORODNYUK**, R.C. O'HANDLEY***, Y. KONO****, V.A. L'VOV**

MAGNETIZATION CURVES FOR TETRAGONAL MARTENSITE: EXPERIMENT AND MODELING

KRZYWE MAGNETYZACJI STOPÓW O STRUKTURZE MARTENZYTU TETRAGONALNEGO: EKSPERYMENT I MODELOWANIE

Magnetization curves of the ferromagnetic tetragonal martensite in Ni-Mn-Ga single crystals are shown experimentally and theoretically to depend on the tetragonality ratio as a source of the magnetocrystalline anisotropy field as well as on the shape anisotropy field which is produced by the magnetic dipole interaction and dependent on the sample geometry. A good agreement between experimental and computed magnetization curves is achieved.
Keywords: magnetization curve, ferromagnetic martensite, tetragonality ratio, Ni-Mn-Ga alloys

Eksperymentalnie i na podstawie teorii pokazano, że krzywe magnetyzacji ferromagnetycznych monokryształów Ni-Mn-Ge o strukturze martenzytu tetragonalnego zależą od współczynnika tetragonalności jako źródła magneto krystalicznego pola anizotropii, jak również od kształtu pola anizotropii wytwarzanego w wyniku oddziaływania dipoli magnetycznych i ostaecznie od geometrii próbki. W pracy pokazano dobrą zgodność pomiędzy krzywymi magnetyzacji eksperymentalnymi i obliczonymi wg przyjętego modelu.

1. Introduction

Ferromagnetic thermoelastic martensites formed as a result of the martensitic transformation in Ni-Mn-Ga alloys represent new multifunctional materials having great potential to be implemented in new actuators and sensors [1-5]. A crystal structure which is mainly composition dependent [6], controls main characteristics of these materials

* INSTITUTE FOR MAGNETISM, VERNADSKY STR. 36-B, 03-142 KYIV, UKRAINE
** DEPARTMENT OF RADIOPHYSICS, TARAS SHEVCHENKO UNIVERSITY, GLUSHKOV STR. 2, 03-022 KYIV, UKRAINE
*** MASSACHUSETTS INSTITUTE OF TECHNOLOGY, CAMBRIDGE, MASSACHUSETTS 02-139, USA
**** TOHOKU GAKUIN UNIVERSITY, FACULTY OF ENGINEERING, TAGAJO 985-8537, JAPAN

such as sign and value of a magnetic anisotropy parameter and the maximum value of magnetostrain effect [7, 8]. Martensite with a tetragonal lattice is especially interesting for applications since it is a subject to much less fatigue than an orthorhombic martensite [9].

Magnetoelastic model of ferromagnetic martensite developed in Refs.[7, 10-12] correlates with the experimental results [8, 13] when stating that the Ni-Mn-Ga tetragonal martensites with tetragonality ratio of $c/a > 1$ exhibit an "easy-plane" magnetic anisotropy, while martensites with $c/a > 1$ are the ferromagnets of the "easy-axis" type.

The magnetization curves provide an important information about both the magnetic anisotropy parameters and the reorientation of martensite under the action of applied magnetic field (see, e.g., [14-16]). A quantitative computation of the magnetization curves is impossible without accounting two basic mechanisms of magnetization processes such as the magnetic moments rotation and 180° domain walls motion [11, 12]. In addition, a magnetization process in Ni-Mn- Ga martensite, which exhibits the giant magnetically induced deformation of the order of few percents, is accompanied by the field-induced twin rearrangements which complicate the computations [15, 16]. Present work is an original experimental and theoretical study of the magnetization curves for the different Ni-Mn-Ga tetragonal martensites which do not show the pronounced magnetically induced structural changes. As a systematic approach, two contributions to magnetization process are varied controllably by proper choice of specimens shape. Both the fundamental and engineering aspect can be deduced from this study. For example, a computation of the magnetization curves can serve as a monitoring tool for the estimations of the volume fractions of different martensite variants (twin components) being function of any preliminary technological treatments.

2. Physical mechanisms of magnetization

The non-isotropic part of the magnetic free energy for j-variant of tetragonal martensite can be expressed according to the magnetoelastic model [10-12] as

$$F = -Am_j^2 + \frac{1}{2}M^2\left[D_1\left(m_x^2 + m_z^2\right) + D_2 m_y^2\right] - \mathbf{mH}M, \qquad (1)$$

where $\mathbf{m} = \mathbf{M(T)}/M(T)$ is a magnetisation vector, $A = 6\delta\mathbf{M}^2(c/a - 1)$ is a parameter of crystallographic magnetic anisotropy and $\delta = \delta_1/M^2$ is a dimensionless magnetoelastic constant. The first term of Eq.(1) describes magnetic anisotropy energy of the crystal lattice with j-axis aligned with [100], [010] or [001] crystallographic directions oriented with Cartesian coordinate axes x, y and z, respectively. The second term presents the magnetostatic energy of the ellipsoidal specimen with the revolution axis aligned with y-direction, $D_1 = D_3$ and D_2 are the diagonal elements of a demagnetizing matrix. The third term is Zeeman energy. In the absence of a magnetic field, $\mathbf{m}$ vector is along

easy-axis. An application of the magnetic field will cause its rotation to some angle Ψ_N so, the magnetization process will proceed through *rotation mechanism* as follows:

$$M(H,T) \equiv M_N^{rot} = M(T)\cos\psi_N, \tag{2}$$

where

$$\cos\psi_N = \begin{cases} H/H_{SN}^{rot}(T), & H < H_{SN}^{rot} \\ 1 & H \geqslant H_{SN}^{rot} \end{cases} \tag{3}$$

N numerates the saturation field values for the different martensitic variants, field directions and correspondent field dependencies of the rotation angle.
The *displacive mechanism* (displacements of 180° domain walls) is represented as:

$$M(H,T) \equiv M_N^{dis} = \begin{cases} H/H_{SN}^{dis}(T), & H < H_{SN}^{dis} \\ 1 & H \geqslant H_{SN}^{dis} \end{cases} \tag{4}$$

A modeling of a magnetization process of tetragonal martensite implies that one has to identify the magnetization mechanisms in each variant and then perform summation over all variants. For the determination of the directions of the spontaneous magnetization we take into account all possible configurations of three variants, two types of the unit cells ($c/a < 1$ or $c/a > 1$), two specimens shapes (platelet or rod), and two magnetic field directions so, totally $2 \times 2 \times 3 \times 2 = 24$ items in a sum are expected. For the definiteness, we assume that the crystallographic axis y is oriented along a normal to a platelet or with the long axis of rod so, the condition $D_1 = D_3$ is fulfilled.

3. Magnetization of the tetragonal martensite with c/a<1

3.1. The "easy direction" for the magnetic vector in zero magnetic field (c/a<1)

In the absence of the magnetic field, we assume that the martensitic state of platelet or rod consists of x-, y-and z-variants with volume fractions of β_x, β_y and β_z, respectively. It is obvious that , for instance, in the case of platelet, the direction of magnetization of x- and z-variants is along their four-fold c-axes. In case of y-variant, there exists a competition between demagnetizing field and anisotropy field so, the magnetization vector is aligned with y-axis when the anisotropy field dominates, i.e., the condition of

$$2A > (D_2 - D_1)M^2 \tag{5}$$

holds. The magnetization vector is equally probable to be aligned with x- or z-axis when

$$0 < 2A < (D_2 - D_1)M^2. \tag{6}$$

In the Table 1, we summarize all the magnetic phases which can obtained by the similar analysis.

TABLE 1
Possible magnetic phases, $(i; j)$, formed in the tetragonal martensite with $c/a < 1$ in zero magnetic field where i is c-axis direction, j is easy direction for magnetization

	x-variant	y-variant	z-variant
Platelet	$(x; x)$	$(y; y)$,	$(z; z)$
$(D_1) < D_2)$		$2A > (D_1 - D_2)M^2$	
		$(y; x)$, $(y; z)$,	
		$0 < 2A < (D_1 - D_2)M^2$	
Rod	$(x; x)$,	$(y; y)$	$(z; z)$,
$(D_1) < D_2)$	$2A > (D_1 - D_2)M^2$		$2A > (D_1 - D_2)M^2$
	$(x; y)$,		$(z; y)$,
	$0 < 2A < (D_1 - D_2)M^2$		$0 < 2A < (D_1 - D_2)M^2$

3.2. Magnetization of the platelet under magnetic field (c/a < 1)

Let us analyze the magnetic behavior of each martensitic variant formed in a platelet under the magnetic field applied in-plane, for instance, along z-axis. A magnetic field rotates the magnetization vector of the x-variant in the xz-plane from the initial state with components of $m_x = 1, m_y = 0, m_z = 0$ to the state characterized by some angle ψ having components of $m_x = \sin\psi, m_y = 0, m_z = \cos\psi$. The substitution of the latter components into Eq.(1) results in

$$F = -A\cos^2\psi + \frac{1}{2}M^2 D_1 - MH_z\cos\psi. \tag{7}$$

The condition of the full magnetization of x-variant is $\psi = 0$ and the value of saturation magnetization field, H_s, can be found by minimizing of Eq.(7):

$$\frac{\partial F}{\partial \psi} = -2A\sin\psi\cos\psi + H_z M\sin\psi = 0 \tag{8}$$

as $H_S = H_z = 2A/M$.
The similar procedure is used to obtain all possible values of the saturating field for the different orientations of the magnetic field which are compiled in the Table 2.

The magnetization process of the whole platelet should be now considered as a summation over all three variants. In the field applied with z direction:

$$M(H,T) = \beta_x M_4^{rot} + \beta_y M_1^{rot} + \beta_z M_1^{dis}, if 2A > (D_2 - D_1)M^2 \tag{9}$$

$$M(H,T) = \beta_x M_4^{rot} + \left(\beta_y + \beta_z\right) M_1^{dis}, if 0 < 2A < (D_2 - D_1)M^2. \tag{10}$$

Using the step-wise Heaviside function $\theta(H_s$ the Eqs. (9) and (10) can be unified as:

$$M(H,T) = \beta_x M_4^{rot} + \beta_y \left[M_1^{rot}\theta\left(H_{S1}^{rot}\right) + M_1^{dis}\theta\left(-H_{S1}^{rot}\right)\right] + \beta_z M_1^{dis} \tag{11}$$

TABLE 2

Saturation fields for the platelet containing different martensitic variante with c/a<1

$-H \parallel z$	H_S^{rot}	H_S^{dis}	Condition
x-variant	$2A/M$	–	–
y- variant	$2A/M - (D_2 - D_1)M$	–	$2A > (D_2 - D_1)M^2$
*	–	D_1M	$0 < 2A < (D_2 - D_1)M^2$
**	0	–	$0 < 2A < (D_2 - D_1)M^2$
z-variant	–	D_1M	–
$H \parallel y$	H_S^{rot}	H_S^{dis}	Condition
x-, z- variant	$2A/M + (D_2 - D_1)M$	–	–
y- variant	–	D_2M	$2A > (D_2 - D_1)M^2$
	$-2A/M + (D_2 - D_1)M$	–	$0 < 2A < (D_2 - D_1)M^2$

* and ** are for (yz) and (yx) initial state, respectively.

Similarly, in the field applied with y direction one can obtain:

$$M(H,T) = (\beta_x + \beta_z) M_2^{rot} + \beta_y \left[M_2^{dis} \theta\left(H_{S1}^{rot}\right) - M_1^{rot} \theta\left(-H_{S1}^{rot}\right) \right] \tag{12}$$

In order to keep valid the Eqs.(5) and (6) for each of two specimens shapes and c/a values, it is of advantage to denote the following expressions:

$$\begin{aligned} H_{S1}^{rot} &= 2|A|/M - |D_1 - D_2|M \\ H_{S2}^{rot} &= 2|A|/M + |D_1 - D_2|M \\ H_{S3}^{rot} &= |D_1 - D_2|M \\ H_{S4}^{rot} &= 2|A|/M \\ H_{S1}^{dis} &= D_1M \\ H_{S2}^{dis} &= D_2M. \end{aligned} \tag{13}$$

3.3. Magnetization of the rod under magnetic field (c/a<1)

Likewise for the platelet, the magnetization behavior of each variant present in the rod and corresponding values of the saturating magnetic fields were analyzed. The results are shown in Table 3.

The magnetization process of the rod can be now analytically expressed by the following formulas: in the field applied with y direction:

$$M(H,T) = \beta_y M_2^{dis} + (\beta_x + \beta_z) \left[M_1^{rot} \theta\left(H_{S1}^{rot}\right) + M_2^{dis} \theta\left(-H_{S1}^{rot}\right) \right] \tag{14}$$

in the field applied with z direction:

$$\begin{aligned} M(H,T) = {} & \beta_y M_2^{rot} + \beta_x \left[M_4^{rot} \theta\left(H_{S1}^{rot}\right) + M_3^{rot} \theta\left(-H_{S1}^{rot}\right) \right] + \\ & + \beta_z \left[M_1^{dis} \theta\left(H_{S1}^{rot}\right) - M_1^{rot} \theta\left(-H_{S1}^{rot}\right) \right]. \end{aligned} \tag{15}$$

TABLE 3

Saturation fields for the rod containing different martensitic variants with c/a<1

$H \parallel y$	H_S^{rot}	H_S^{dis}	Conditions
x-, z-variant	$2A/M - (D_1 - D_2)M$	–	$2A > (D_1 - D_2)M^2$
	–	D_2M	$0 < 2A < (D_1 - D_2)M^2$
y- variant	–	D_2M	–
$H \parallel z$	H_S^{rot}	H_S^{dis}	Conditions
x-variant	$2A/M$	–	$2A > (D_1 - D_2)M^2$
	$(D_1 - ED_2)M$	–	$0 < 2A < (D_1 - D_2)M^2$
y- variant	$2A/M + (D_1 - D_2)M$	–	–
z- variant	–	D_1M	$2A > (D_1 - D_2)M^2$
	$-2A/M + (D_1 - D_2)M$	–	$0 < 2A < (D_2 - D_1)M^2$

4. Magnetization of the tetragonal martensite with c/a>1

The formalism described for the case of c/a<1 is applied in this section for the case of tetragonal unit cell with c/a>1. The essential difference between these two types of the crystal lattices is taken into account. As it is shown below, the difference in both the spatial distribution of magnetization directions and in the mechanisms of magnetization process for these two types lattices gives rise to the different analytical expressions for the magnetization vs magnetic field dependences.

4.1. The "easy direction" for the magnetic vector in zero magnetic field (c/a>1)

Table 4 summarizes all possible magnetic states formed in martesitic variants with c/a>1 in zero magnetic field.

TABLE 4

Possible magnetic phases, $(i; j)$, formed in the tetragonal martensite with $c/a < 1$ in zero magnetic field where i is c-axis direction, j is easy direction for magnetization

	x-variant	y-variant	z-variant
Platelet	$(x; z)$	$(y; x)$, $(y; z)$*	$(z; x)$
$(D_1 < D_2)$			
Rod	$(x; y)$,	$(y; x)$, (y, z)	$(z; y)$,
$(D_1 < D_2)$		$2A < (D_2 - D_1)M^2$	
		$(y; y)$	
		$(D_2 - D_1)M^2 < 2A < 0$	

* For the uniaxial magnetic anisotropy (2-nd order terms), all directions in xz plane of y-variant are equivalent while the forth-order terms distinguish the x and z directions.

4.2. Magnetization of the rod under magnetic field (c/a>1)

The results of the analysis of saturating fields for the different variants of martensite with c/a>1 are shown in the Table 5.

TABLE 5

Saturation fields for the rod containing different martensitic variants with c/a<1

$H \parallel y$	H_S^{rot}	H_S^{dis}	Condition
x-, z-variant	–	D_2M	–
y- variant	$2\lvert A\rvert/M - (D_1 - D_2)M$	–	$2A < (D_2 - D_1)M^2$*
	–	D_2M	$(D_2 - D_1)M^2 < 2A < 0$
$H \parallel z$	H_S^{rot}	H_S^{dis}	Conditions
x-variant	$(D_1 - D_2)M$	–	–
y-variant	0	D_1M	$2A < (D_2 - D_1)M^2$
	$-2\lvert A\rvert/M + (D_1 - D_2)M$	–	$(D_2 - D_1)M^2 < A < 0$*
z- variant	$2\lvert A\rvert/M + (D_1 - D_2)M$	–	–

*It means $H_S^{rot} > 0$.

In the field parallel to the revolution axis y, the field dependence of the magnetization value is

$$M(H,T) = (\beta_x + \beta_z)\, M_2^{dis} + \beta_y \left[M_1^{rot} \theta\left(H_{S1}^{rot}\right) + M_2^{dis} \theta\left(-H_{S1}^{rot}\right) \right], \tag{16}$$

where M_2^{dis} and M_1^{rot} are expressed by Eqs.(13). Compare with the Table 5: when $H_{S1}^{rot} > 0$, a rotational mechanism takes place in the y-variant and a displacive mechanism is inherent in two others variants; when $H_{S1}^{rot} < 0$, the displacive mechanism takes place in all variants. In the field directed perpendicularly to the revolution axis:

$$M(H,T) = \beta_x M_3^{rot} + \beta_y \left[M_1^{dis} \theta\left(H_{S1}^{rot}\right) - M_1^{rot} \theta\left(-H_{S1}^{rot}\right) \right] + \beta_z M_2^{rot}. \tag{17}$$

The magnetic saturation of the specimen takes place when $H = \max\left\{H_{S2}^{rot}, H_{S1}^{dis}\right\}$, because $H_{S2}^{rot} > H_{S3}^{rot} > H_{S4}^{rot}$.

4.3. Magnetization of the platelet under magnetic field (c/a>1)

In the field parallel to the revolution axis y, the magnetization value is

$$M(H,T) = (\beta_x + \beta_z)\, M_3^{rot} + \beta_y M_2^{rot}. \tag{18}$$

In the field directed perpendicularly to the revolution axis (in parallel with z axis) we have:

$$M(H,T) = \left(\beta_x + \beta_y\right) M_1^{dis} + \beta_z M_4^{rot}. \tag{19}$$

TABLE 6

The saturating field values for the different martensitic variants with $c/a > 1$ formed in the platelet

$H \parallel z$	H_S^{rot}	H_S^{dis}	Condition
x- variant	–	$D_1 M$	–
y- variant	0	$D_1 M$	–
z- variant	$2\|A\|/M$	–	–
$H \parallel y$	H_S^{rot}	H_S^{dis}	Conditions
x-, z- variant	$(D_2 - D_1)M$	–	–
y- variant	$2\|A\|/M + (D_2 - D_1)M$	–	–

5. Experimental magnetization curves and results of computations

Two earlier studied [6, 7, 17] Ni-Mn-Ga single crystalline alloys exhibiting tetragonal martensites were chosen in this study. Their main characteristics are presented in Table 7. Two crystallographic oriented samples in the form of platelet and rod (all edges were parallel to < 100 > type directions) were sparkcut from each ingot. The samples labels and dimensions are shown in Table 7.

TABLE 7

Alloy compositions, martensitic transformation temperatures, M_s, Curie temperatures, T_C, tetragonality ratios and sizes and shapes of the samples used for measurement

Alloy composition, at.%	M_s, K	T_C, K	Tetragonality ratio of martensite, c/a	Sample legend	Sample shape and size, mm
$Ni_{51.0}Mn_{27.9}Ga_{21.1}$	314	370	0.94	M1_plate	Platelet, $0.5 \times 5 \times 3.85$
				M1_rod	Rod, $4.95 \times 1 \times 0.5$
$Ni_{53.1}Mn_{26.6}Ga_{20.3}$	363	373	1.2	M2_plate	Platelet, $0.66 \times 4 \times 5$
				M2_rod	Rod, $1.07 \times 0.83 \times 4.35$

The measurements of magnetization curves have been made at room temperature by vibrating sample magnetometer (VSM). The magnetic field was always applied along < 100 > axis. Each sample was measured along two directions. In the case of rod, a magnetic field was applied either in parallel to long edge of a sample or in the perpendicular direction. In the case of a platelet, the field was either with a normal to its plane or in-plane along any of two edges.

The computations of magnetization curves have been performed using Eqs.(11, 12, 15-19). The procedure accounting the dispersed character of the Curie temperature of the martensitic state [12] was incorporated into computations. An equal volume fraction of each of three variants was assumed. A satisfactory fit with the experimental results has been achieved with using the numerical values of -23 and -6 as the magnitudes of the magnetoelastic parameters for c/a<1 and c/a>1 martensitic phases, respectively (e.g., [12]).

Fig. 1 displays the results form martensite with c/a < 1 formed in a platelet. With the given sample dimensions and in accordance to Eq. (9), one can conclude that the magnetocrystalline anisotropy energy is about 1.8 factor larger than shape anisotropy energy. The first kink on the theoretical curve at 1 kOe in Fig. 1 is due to a

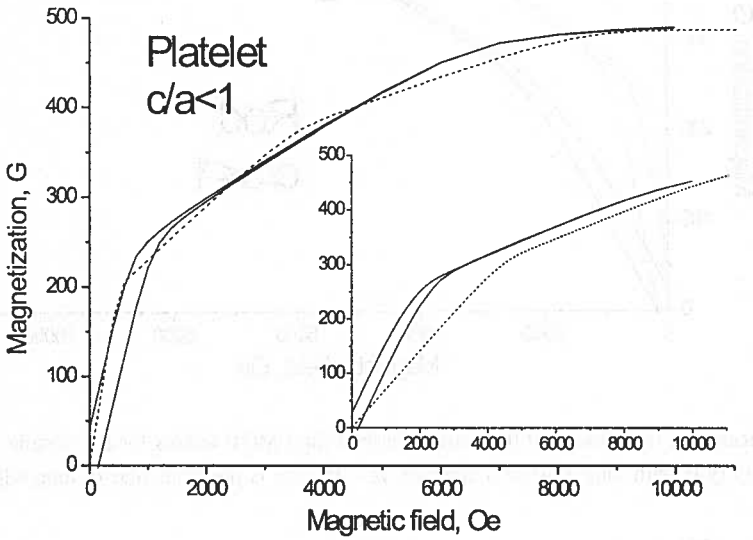

Fig. 1. Experimental (full line) and theoretical (dashed line) M(H) curves for the sample M1_plate: *H//z* (in-plane). Inset: *H//y* (out-of-plane)

completeness of the displacive mechanism of magnetization process in *z*-variants. The second kink at 4 kOe is related to the end of the magnetization process of *y*-variants by rotation. The third kink at 9 kOe is due to the finish of magnetization rotation of the x-variants. Worse results are obtained when a field is perpendicular to the platelet (Inset to Fig. 1). In this case, the calculated value of the saturation field of *y*-variants (about 5.5 kOe) is twice larger than experimental one which can be explained by the imperfections of both the sample and calculation algorithm. The M(H) dependences for the rod-like sample with the same martensite ($c/a < 1$) depicted in Fig. 2 demonstrate a good agreement of the experiment with modeling. The first kink on the curves A is related with the displacive mechanism of the magnetization process for *y*-variant, while second one is explained by the hard magnetization process of *x* and *z*-variants by the rotation. In the case of the curves *B*, three kinks can be identified theoretically: at 2.5 kOe, magnetization is due to the displacive mechanism for *z*-variant; at 6 kOe and 9 kOe, there are limits for the rotation mechanisms in *x*- and *y*-variants, respectively.

Figs 3, 4 show the results for martensite with c/a > 1 for both two sample shapes. In the case of platelet studied under perpendicular magnetic field (Fig. 3), there is a good agreement of the measured and computed curves, while magnetization curve in parallel field presented in the Inset to Fig. 3 does not contain any kinks so, the computed curve is a rough approximation of real behavior, the last one being controlled

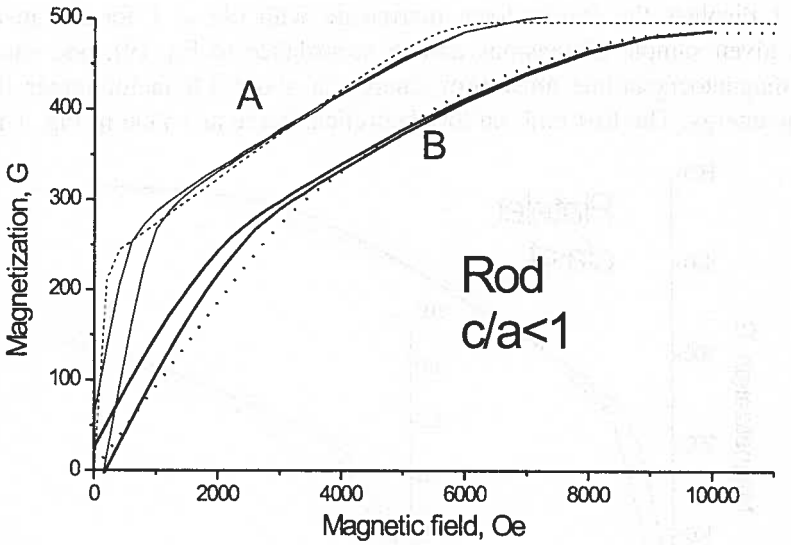

Fig. 2. Experimental (full line) and theoretical (dashed line) M(H) curves for the sample M1_rod: A – *H//y* (*y* is with long edge of a sample); B – *H//y* (*y* is perpendicular to long edge)

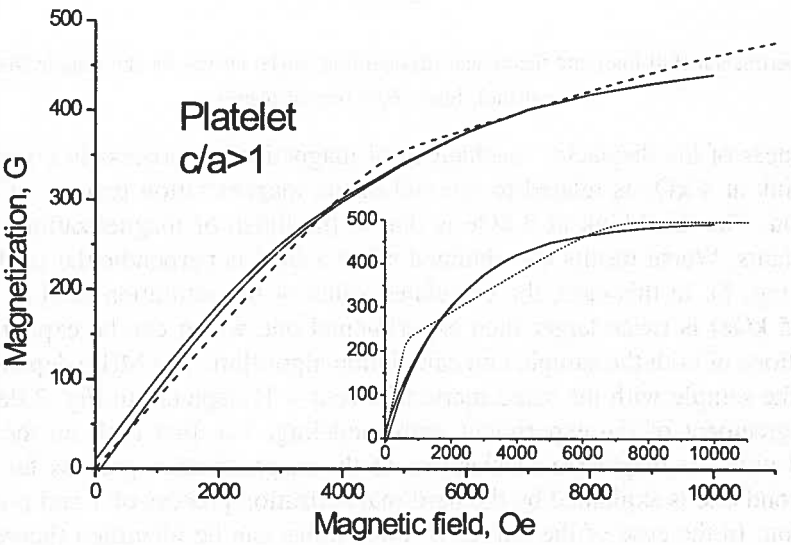

Fig. 3. Experimental (full line) and theoretical (dashed line) M(H) curves for the sample M2_plate: *H//y* (out-of-plane). Inset: *H//z* (in-plane)

by the contributions which are not taken into account in the theory. In the case of rod-like sample a better agreement between experiment and theory is observed for both orientations of the magnetic field (Fig. 4) although again experimental dependences

are too smooth evidencing much complicate magnetization process than modeled one in M2-type alloy.

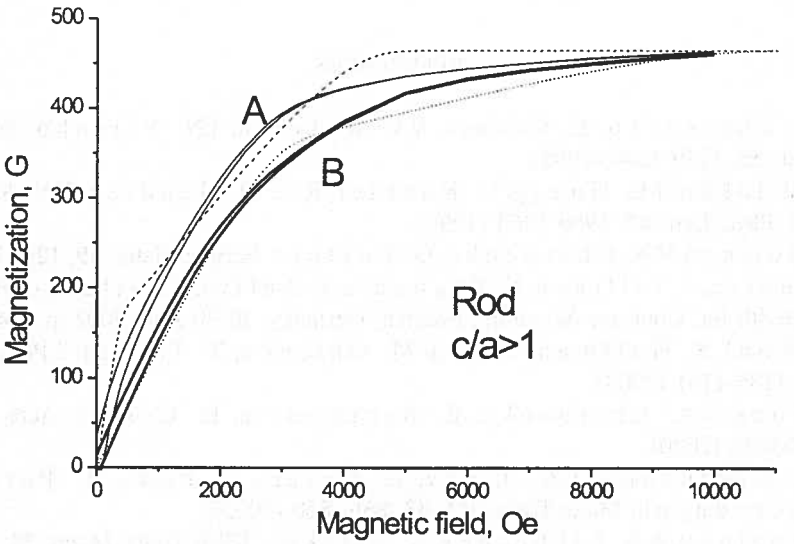

Fig. 4. Experimental (full line) and theoretical (dashed line) M(H) curves for the sample M2_plate: A – $H//y$ (with long edge of a sample); B – $H//z$ (perpendicular to long edge)

6. Conclusions

1. The magnetization curves as a function of the sample shape and direction of the external magnetic field were experimentally studied for two types of the martensites with the tetragonal lattice (c/a<1 and c/a>1) exhibited by two Ni-Mn-Ga single crystals.

2. For the theoretical description of the results one should determine the directions of the spontaneous magnetization for each martensitic variant. Those directions are dependent on the spatial distribution and competitive character of the anisotropy fields produced by both the magnetocrystalline anisotropy governed by the c/a ratio and magnetic anisotropy controlled by the shape of a sample.

3. The magnetization process proceeds either through the rotation mechanism when the "easy" direction of a variant is perpendicular to the magnetic field, or through the displacive mechanism when the "easy" direction of a variant is along the magnetic field.

4. A majority of the computed magnetization curves are in a good agreement with the experimental ones. In some cases the divergence of the experimental and theoretical curves is observed. The divergence may be caused, in particular, by the forth-order anisotropy parameter, whose influence is well pronounced in the case of the tetragonal lattice with the strongly elongated unit cell [14].

Acknowledgements

VAC is grateful to US CRDF for support in framework of Travel Grant Award # TGP-478.

REFERENCES

[1] V.A. Chernenko, E. Cesari, V.V. Kokorin, I.N. Vitenko. Scripta Met. Mater. **33**, 1239-1244 (1995).
[2] K. Ullakko, J.K. Huang, C. Kantner, R.C. O'Handley, V.V. Kokorin. Appl. Phys. Lett. **69**, 1966-1968 (1996).
[3] P. Müllner, V.A. Chernenko, G. Kostorz. Scripta Mater. **49**, 129- 133 (2003).
[4] I. Suorsa, J. Tellinen, E. Pagounis, I. Aaltio, K. Ullakko, Proceedings of the 8th Int. Conf. on Actuators, Bremen, Germany, 10-20 June 2002, p. 158.
[5] M. Kohl, S. Hoffman, Y. Liu, M. Ohtsuka, T. Takagi. J.Phys.IV France **112**, 1185-1191 (2003).
[6] J. Pons, V.A. Chernenko, R. Santamarta, E. Cesari. Acta Mater. **48**, 3027-3038 (2000).
[7] V.A. Chernenko, V.A. L'vov, E. Cesari, J. Pons, R. Portier, S.P. Zagorodnyuk. Mater.Trans.JIM, **43**, 856- 860 (2002).
[8] A. Sozinov, A.A. Likhachev, K. Ullakko. IEEE Trans. Magn. **38**, 2814-2816 (2002).
[9] P. Müllner, V.A. Chernenko, D. Mukherji, G. Kostorz. Mat. Res. Soc. Symp. Proc. **785**, D12.2.1-6 (2004).
[10] V.A. L'vov, E.V. Gomonaj, V.A. Chernenko. J.Phys.: Condens. Mat. **10**, 4587-4596 (1998).
[11] V.A. Chernenko, V.A. L'vov, E. Cesari. JMMM, **196-197**, 859- 860 (1999).
[12] V.A. Chernenko, V.A. L'vov, S.P. Zagorodnyuk, T. Takagi. Phys.Rev. **B67**, 064407 (2003).
[13] R. Tickle, R.D. James. J. Magn. Magn. Mater. **195**, 627-638 (1999).
[14] L. Straka, O. Heczko. J. Appl. Phys. **93**, 8636-8638 (2003).
[15] O. Heczko, A. Sozinov, K. Ullakko. IEEE Trans. Mag., **36**, 3266- 3268 (2000).
[16] M. Pasquale, C.P. Sasso, G. Bertotti, V.A. L'vov, V.A. Chernenko, A. De Simone. J.Appl. Phys. **93**, 8641-8643 (2003).
[17] V.A. Chernenko, P. Müllner, M. Wollgarten, J. Pons, G. Kostorz. J. de Physique IV France, **112**, 951-954 (2003).

Received: 3 November 2004.

A R C H I V E S O F M E T A L L U R G Y A N D M A T E R I A L S
Volume 49 2004 Issue 4

G. KORZNIKOVA*

PHENOMENA OF MAGNETOSTRICTION AND THEIR TECHNICAL APPLICATION

ZJAWISKA MAGNETOSTRYKCJI I ICH TECHNICZNE ZASTOSOWANIA

A brief survey of basic principles and applications of magnetostriction is presented in this work. Related phenomena are considered as well. The advantages and drawbacks of different magnetostrictive materials are demonstrated. Main tendencies of the development of new magnetostrictive materials are examined. materials.

Keywords: Magnetostriction; Magnetoelastic properties; Giant magnetostrictive films.

W pracy przedstawiono krótki przegląd podstawowych zasad i zastosowań magnetostrykcji. Rospatrzono także zjawiska pokrewne. Przedstawiono także zalety i wady różnych materiałów magnetostrykcyjnych i przedyskutowano główne tendencje występujące w rozwoju nowych materiałów o tej własności.

1. Phenomena and application of magnetostriction

The ordered arrangement of magnetic moments in ferromagnetic, antiferromagnetic, ferrimagnetic solids appears below critical temperature T_c. It was found that at the temperatures below and above T_c not only the magnetic properties are different, but other physical properties change as well. The phenomenon of magnetostriction involves the variation of the size and the form of solids as an effect of presence of a longitudinal magnetic field [1]. J.P. Joule discovered this phenomenon in 1842 in pure iron. Later, it was found that the phenomenon of magnetostriction is inherent in all solids. The value of magnetostriction in poorly magnetic materials (dia- and paramagnets) is low $\lambda_s = \Delta l/l \sim 10^{-7} - 10^{-5}$, except some rare earth paramagnets, where $\lambda_s \sim 10^{-4}$. In ferromagnetic metals Fe, Ni, Co, in a number of alloys and ferrites the typical value of magnetostriction is about $10^{-6} - 10^{-4}$. More recent advanced materials such as rare

* INSTITUTE FOR METALS SUPERPLASTICITY PROBLEMS, RUSSIAN ACADEMY OF SCIENCES, KHALTURIN ST. 39, UFA, 450001, RUSSIA

earths and the alloys on the basis of rare earths have magnetostriction as high as 10^{-3} [2-4].

At present, along with ordinary magnetostriction other related phenomena are under the studies, i.e.:

- *Spontaneous magnetostriction*, resulting in the deformation of crystalline lattice upon heating due to variation of spontaneous magnetization. This phenomenon is observed clearly near to the Curie point.
- *Mechanostriction*, i.e. mechanical strains that cause additional elastic deformation which is inherently magnetostrictive. Two types of mechanostriction may be recognized – the mechanostriction in the region of technical magnetization, which is connected with redistribution of the domain structure and magnetization under the effect of elastic strains (tension and pressing) and another in the region of saturation or paraprocess, which causes the change of exchange interaction due to elastic strains. Both these phenomena cause anomalies of elastic modula in magnetics.
- *Magnetoelastic effects*, resulting in the influence of mechanical straining on the magnetization value (*reverse magnetostriction*), due to the affecting elastic properties by magnetic ordering.

All these phenomena have attracted the attention of physicists and engineers: physicists gain information about the dependence of the exchange and magnetocrystalline interactions on crystalline lattice parameters from the analysis of magnetostriction effects and engineers use these phenomena to construct new generations of devices and facilities.

Different mechanisms of magnetostriction are considered in the theory of magnetism [1, 3]:

1. Acting through the changes in dipole-dipole interaction;
2. Acting through spin-orbital interaction;
3. Or involving an interaction between electron cloud of magnetic ion and intercrystalline field ("single-ion" model).

In ferro- and ferrimagnetic solids, in the range of magnetic field, where the shift of domain walls and rotation of the direction of spontaneous magnetization takes place (area of technical magnetization) magnetostriction is anisotropic and manifests itself by the change of the shape of crystal without any change of it's volume (linear magnetostriction):

$$\lambda = \Delta l/l \qquad (H < H_S).$$

In the range of larger magnetic field (area of paraprocess) magnetostriction is isotropic and reveals also in the change of the volume (volume magnetostriction):

$$\omega = \Delta V/V \qquad (H < H_S).$$

Figure 1 shows linear magnetostriction in monocrystalline sample of pure iron along different axis at room temperature. The magnetization of the sample leads to

elongation along direction [100], to shortening along [111] and to elongation in low field and shortening in high magnetic field along [110].

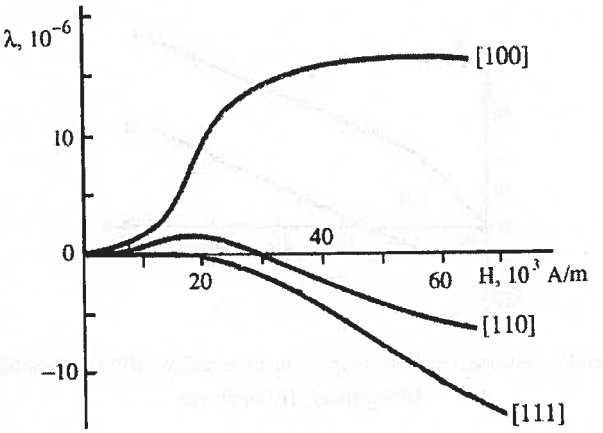

Fig. 1. Linear magnetostriction in monocrystalline sample of pure iron along different axis at room temperature

In most cases the magnetics have polycrystalline structure and the observed magnetostriction reveals some average value. Figure 2 shows the curves of magnetostriction for different polycrystalline materials. In pure Co and Ni magnetostriction is negative – it means that the samples shorten along the applied field. An iron sample shortens in low field and elongates in high field. Most alloys such as Fe-Ni, Fe-Co, Fe-Pt and some others, elongate in magnetic field.

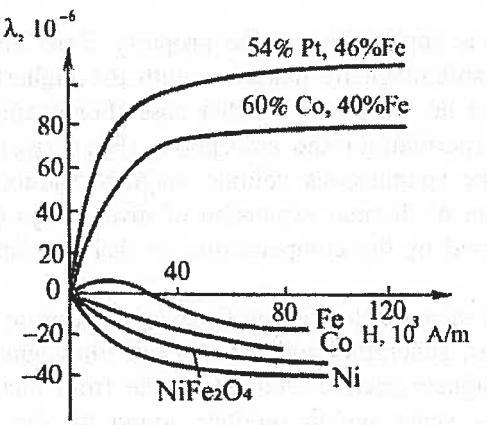

Fig. 2. Magnetostriction curves for polycrystalline samples of pure metals (Co, Ni, Fe), alloys (Fe-Ni, Fe-Co, Fe-Pt) and ferrite ($NiFe_2O_4$) measured at room temperature

Longitudinal and transverse magnetostrictions in invar alloy have opposite signs in low field (figure 3). In high magnetic field (the region of paraprocess), the magnetostriction is positive in both directions, so this is the case of volume magnetostriction.

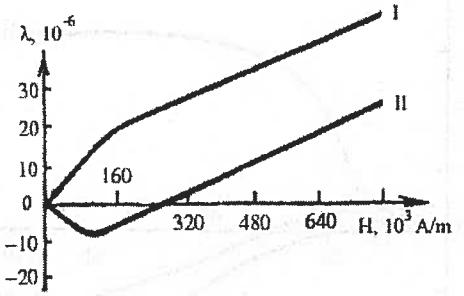

Fig. 3. Longitudal and transverse magnetostriction in invar alloy (36%Fe- 64%Ni), room temperature
I-longitudal, II-transverse

Magnetostriction in antiferromagnetic materials has some specific features [5]. Magnetostriction loops of Dy, measured at different temperatures show the change of the type of magnetic ordering in Dy (figure 4 a). At temperature lower than 85K, the loop has usual form. At the temperature higher than 85K, which is the temperature of magnetic transition from ferromagnetic to helical antiferromagnetic state, some critical field, responsible for destroying antiferromagnetic state appears on the loops. The increase of the temperature leads to decrease of magnetostriction value and some increase of critical field destroying antiferromagnetic state. It was found that grain size of crystallites effects on the magnetic state of Dy (figure 4b). The decrease of grain size to submicron scale caused some destruction of antiferromagnetic state. Critical field disappeared and the loops at high temperature had the same character as in ferromagnetic state.

Magnetostriction is application related property. Zero linear magnetostriction is useful for extremely soft magnetic materials with the highest possible permeability, because strains induce no anisotropy in that case. For example, this is achieved in crystalline $Fe_{0.2}Ni_{0.8}$ (permalloy) and amorphous $(Fe_{0.1}Co_{0.9})_{75}Si_{15}B_{20}$ alloys, where $\lambda_s \sim 0$. Regarding the spontaneous volume magnetostriction, the anomalous small value of the coefficient of thermal expansion of invar alloys (Fe-Ni, Fe-Pt and some other systems) is caused by the compensation of thermal expansion by spontaneous magnetostriction.

The phenomenon of magnetostriction finds application in magnetostriction transmitters and relay lines, generators and receivers of ultrasound, filters and stabilizers of frequency, etc. Magnetostrictive elements made from nickel alloys were used in SONAR devices sixty years ago to produce sound for the depth determining and to locate objects by echo sounding. The nickel- based alloys used in these devices have saturation value of magnetostriction only about $50*10^{-6}$ and later were gradually superseded by the piezoelectric ceramics.

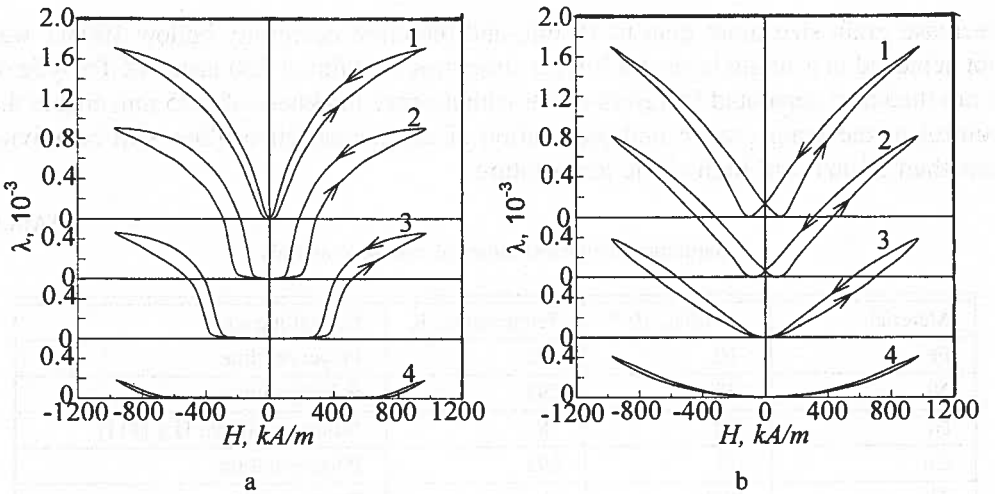

Fig. 4. Hysteresis loops of magnetostriction of Dy in different structural states at different temperatures: a – coarse grained polycrystalline sample, b – submicrocrystalline state. Measuring temperature: 1 – 78*K*; 2 – 100 *K*; 3 – 120 *K*; 4 – 140 *K*

Giant saturation magnetostriction of the range 10^{-3}, was found more than fifty years ago in pure rare earths [2]. This value is much higher than in pure 3d- metals Fe, Co, Ni (table 2). However, giant value of magnetostriction was revealed at temperature much lower than room temperature. Huge saturation magnetostriction at room temperature has been found forty years ago in some compounds based on rare earth-iron Laves phase RE-Fe_2 (RE = Tb, Sm, Dy, Ho, Er, Tm) [3]. However, as a result of a high value of magnetocrystalline anisotropy, impossibility to achieve giant magnetostrition in a weak magnetic field appeared to be the most serious problem. A combination of elements Tb and Dy made possible the development of the weak-field giant magnetostrictive material "Terfenol-D" ($Tb_{0.27}Dy_{0.73}Fe_2$) in which the magnetic anisotropy contributions of Tb and Dy are of opposite sign, resulting in the average zero value [3]. Fabrication of amorphous Terfenol films made possible further decrease of magnetocrystalline anisotropy (table 1) [6]. The drawback of amorphous alloys is the low value of Curie temperature, which is important for the stability of application related properties. Further improvement in amorphous films was concentrated on partial substitution of Fe by Co, leading to some increase of Curie point. Recent works of W i n z e k et al [7] show another way to combine high Curie temperature of crystalline films with high magnetostriction at low fields. According to the random anisotropy model the coercivity decreases with the grain size if the exchange length is larger than the grain size, so variation of the microstructure and preparation of ultra-fine grain structure should decrease coercivity of magnetostrictive films. Two methods were used to achieve nanocrystalline microstructure. The first one consists in the additions of Mo or Zr to alloys, preventing grain growth. The second one was to produce nanometer scaled multilayer structures. The additions, however, could not

decrease grain size more than to 10 nm, and therefore coercivity bellow 100mT was not achieved in a single layer. Multilayer structures containing 250 layers of TbDyFe of 5 nm thickness separated by layers of Nb with average thickness of 0.25 nm, enable the control of the grain growth and preparation of magnetostrictive films with coercivity less than 50 mT and high Curie temperature.

TABLE

Saturation magnetostriction of various materials

Material	$\lambda_s(\Delta l/l)_s$, 10^{-6}	Temperature, K	Crystalline state
Fe	-10	293	Polycrystalline
Ni	-37	293	Polycrystalline
Ni	-60	78	Monocrystalline, H ‖ [111]
Co	-71	293	Polycrystalline
Tb	1230	78	Polycrystalline
Dy	1400	78	Polycrystalline
Tb	5460	4.2	Monocrystalline, H ‖ a
Tb	22000	4.2	Monocrystalline, H ‖ c
$TbFe_2$	4700	300	Monocrystalline, H ‖ [111]
$TbFe_2$	1753	300	Polycrystalline, H=2*10^6 A/m
$SmFe_2$	-1560	300	Polycrystalline, H=2* A/m
$DyFe_2$	433	300	Polycrystalline, H=2*10^6 A/m
$HoFe_2$	85	300	Polycrystalline, H=2*10^6 A/m
$ErFe_2$	-229	300	Polycrystalline, H=2*10^6 A/m
$TmFe_2$	-123	300	Polycrystalline, H=2*10^6 A/m
$(Tb_{0.3}Dy_{0.7})$ Fe_2	1000	293	Polycrystalline, H=0.24*10^6 A/m
$(Tb_{0.3}Dy_{0.7})Fe_2$	600	293	Amorphous, H=0.08*10^6 A/m

Recent development of micro-electro-mechanical systems requires driving materials with a large output force. Sm-Fe and Tb-Fe or Terfenol amorphous films at room temperature possess excellent magnetostriction and fast response time, what makes them appropriate candidates for actuators in the microsystem technology. For example, linear ultrasonic motor was fabricated using a micromachined Si substrate and TbFe films [8]. It was also reported that combination of positively magnetostrictive Tb and negatively magnetostrictive Sm films allows the fabrication of magnetostrictive bimorphs which enhance the total effect, eliminate temperature coefficients due to bimetallic effect [8]. Another possible applications of magnetostrictive layers in micromechanics are cantilever-type, membrane-type actuators and driving mechanism for microvalves [9]. Partially crystallized amorphous films based on FeSiB alloy with Cu and Nb additions have the softest magnetostrictive characteristics in the combination with high permeabillity. It was reported, that these films may be used in magnetic devices for detecting parked vehicles, coding devices, current and voltage transformers, stress sensors [10].

For many potential applications response time at high frequencies ($f > 10^5$ Hz) is important and Terfenol suffers from the eddy currents, which is common to all metallic magnetic materials. Due to extreme brittleness Terfenol is difficult to laminate as is used to be done for example with transformer cores. The development of composite materials with a small particles of Terfenol, bonded with non-conducting polymer binder allowed to increase considerably the high-frequency response and to fabricate magnetostrictive elements with complicated shapes [11].

2. Summary

The improvement and completely new development of magnetostrictive materials occurred in last years. In the most cases the greatest progress was achieved on the smallest scale – in nanostructured multilayer materials. Giant magnetostriction in combination with soft magnetic properties may be promising in the micromechanical system application.

Acknowledgements

I wish to thank Prof. Kh. Ya. Mulyukov for fruitful discussion and some materials given to my disposal.

REFERENCES

[1] K.P. Belov, Magnetostiction effects and their application Moscow, Nauka publ., 1987.
[2] S.A. Nikitin, Magnetic properties of rare-earths and their alloys Moscow state University publ., 1989.
[3] A.E. Clark Magnetostrictive rare-earth – Fe_2 compounds in Ferromagnetic Materials, **1**, ed. E.P. Wohlfarth (Amsterdam: North-Holland) **7**, 531-589 (1980).
[4] A. del Moral et al J. Magn. Magn. Mater. **242-245**, 788-796 (2002).
[5] Kh. Ya. Mulyukov I.Z. Sharipov, S.A. Nikitin, Physics of Solid state **38** 5, 1629-1631 (1996).
[6] F. Schatz, M. Hirsher, G. Flik, H. Kronmuller, Phys. Stat. Sol. (a) **137**, 197-202 (1993).
[7] B Winzek, M. Hirsher, H. Kronmuller, JALCOM **283**, 78-82 (1999).
[8] E. Quandt JALCOM **258**, 126-132 (1997).
[9] E. Quandt Sensors and Actuators **A50**, 105-109 (1995).
[10] P. Marin, A. Hernando, J. Magn. Magn. Mater. **215-216**, 729-734 (2000).
[11] D. Kendall, A.R. Piercy Ferroelectrics **187**, 153-161 (1996).

Received: 3 November 2004.

A R C H I V E S O F M E T A L L U R G Y A N D M A T E R I A L S
Volume 49 2004 Issue 4

R. PORTIER*, P. VERMAUT*, M. HŸTCH**

FOURIER SPECTROSCOPY OF HREM IMAGES OF SHAPE MEMORY ALLOYS

SPEKTROSKOPIA FOURIERA WYSOKOROZDZIELCZYCH OBRAZÓW UZYSKANYCH DLA STOPÓW Z PAMIĘCIĄ KSZTAŁTU

The martensitic transformation which gives remarquable mechanical properties to the shape memory alloys is very sensitive to the chemistry of the alloys but also to its microstructure. Strains and chemical changes which take place at crystal defects and interfaces will greatly influence transformation temperatures and mechanical properties of the alloy. An analysis of the strain fields and of the structure of interfaces is very important to understand mechanical and thermal properties of these alloys. High resolution electron microscopy is a powerful technique to study the microstructure of the alloys. F o u r i e r analysis of high resolution electron microscope images is very usefull for the interpretation and determination of structure and microstructure in materials science. We discuss here the potential of the high resolution images analysis by the phase image technique.

Keywords: diffraction, F o u r i e r transform, local phase, Shape Memory Alloys, displacement field

Przemiana martenzytyczna, która stanowi podstawę własności stopów z pamięcią kształtu jest silnie zależna zarówno od składu chemicznego stopu jak i jego mikrostruktury. Naprężenia oraz zmiany składu chemicznego zachodzące w defektach kryształu i na granicach międzyfazowych wpływają silnie na temperatury przemiany i mechaniczne własności stopu. Analiza pól naprężeń oraz struktury granic międzyfazowych jest bardzo ważna dla zrozumienia mechanicznych i cieplnych własności tych stopów. Szczególnie skuteczną techniką do badania mikrostruktury tych stopów jest wysokorozdzielcza mikroskopia elektronowa. Zastosowanie analizy F o u r i e r a obrazów wysokorozdzielczych jest bardzo użyteczne w interpretacji i określaniu struktury w skali makro i mikro. W pracy dyskutowana jest możliwość interpretowania obrazów wysokorozdzielczych przy wykorzystaniu techniki obrazu fazowego.

* MÉTALLURGIE STRUCTURALE, ENSCP, 11 RUE P. ET M. CURIE, 75231 PARIS, FRANCE
** CECM-CNRS, 15 RUE G. URBAIN, 94407 VITRY-SUR-SEINE, FRANCE

1. Introduction

The topological and elemental exploration of matter at the atomic scale has been pursued by scientists since the first quarter of the 19th century. Experimental methods are based on the interaction between the specimen and an easily produced incident radiation, with the important requirements of a wavelength similar to, or smaller than, the pertinent dimensions in matter, the interatomic distance, and of an adequate signal-to-noise ratio. Three radiations are good candidates for these investigations: X-rays, neutrons and electrons. Due to the pertinent length scales in the object, distance between the diffracting units, the atoms, the practical diffraction conditions are the so-called Fraunhofer conditions which means that both the source and the point of observation are at infinity. The information is averaged over the irradiated volume of the specimen, and in the case of weak interactions (X-ray or neutrons), this has the major implication that the investigated volume is necessarily large. On the other hand, the strong interaction of electrons allows the transmission of local information in diffraction, though measurement accuracy is limited by technological parameters (divergence of the beam, probe size and aberrations of the microscope).

2. Formalism of the diffraction process

This formalism is based on the kinematical approximation: elastic diffraction of a small diffracted intensity with respect to the transmitted beam intensity and only single scattering events. For such cases, with an elementary slab of matter, first order perturbation theory can be applied. This interaction between radiation and matter being completely characterised by a transmission function $f(\boldsymbol{r})$, assuming an incident plane wave $|\boldsymbol{k}_0\rangle$, the complex diffracted amplitude in a selected diffracted direction $\boldsymbol{k}$, is given by the first order perturbation contribution:

$$\langle \boldsymbol{k}_0 | f(\boldsymbol{r}) | \boldsymbol{k} \rangle. \tag{1}$$

If the crystal is as large as for X-Ray or neutrons experiments, it can be assumed to be infinite. For a periodic crystal, $f(\boldsymbol{r})$ can be expanded as a Fourier series on the nodes of the reciprocal lattice and that means that a diffracted amplitude is associated only with $\boldsymbol{k}$ directions such that the diffraction vector $\boldsymbol{k} - \boldsymbol{k}_0$ is a reciprocal lattice vector (Bragg conditions). Considering the crystal built with these elementary slabs, the previous result is still valid and the diffracting intensity is the square modulus of expession (1) corrected by an absorption factor corresponding to the thickness of the specimen in the incident direction (Fig. 1). For electron diffraction with a strong interaction, we have to take into account two new aspects. Matter is transparent to electrons only if the thickness is very small. For such thin crystals, the integration can be performed at infinity only if we multiply the transmission function by a function $\chi(\boldsymbol{r})$, with the value 1 inside the investigated crystal and 0 outside:

$$\langle \boldsymbol{k}_0 | f(\boldsymbol{r})\chi(\boldsymbol{r}) | \boldsymbol{k} \rangle = \langle \boldsymbol{k}_0 | f(\boldsymbol{r}) | \boldsymbol{k} \rangle * \langle \boldsymbol{k}_0 | \chi(\boldsymbol{r}) | \boldsymbol{k} \rangle. \tag{2}$$

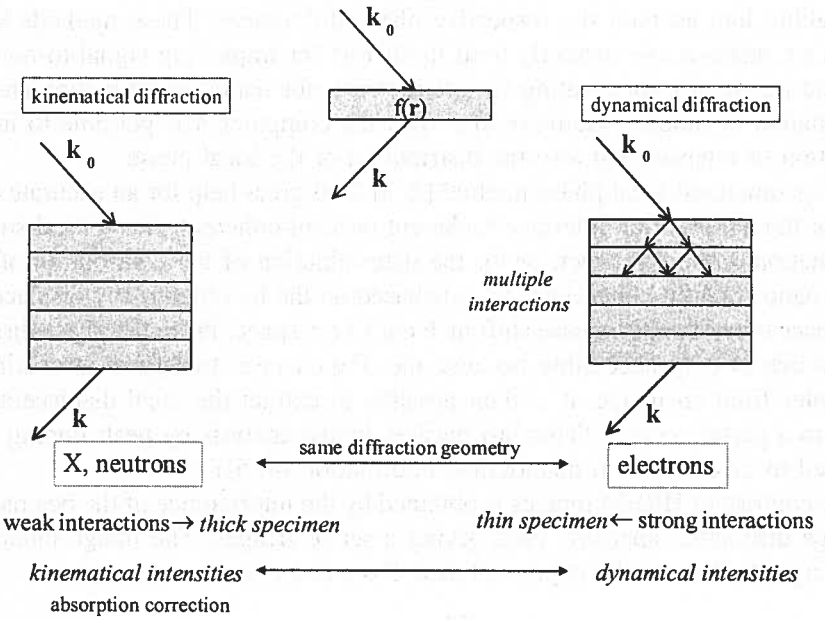

Fig. 1. Kinematical (X-Rays and neutrons) and dynamical diffraction (electrons) conditions

The previous contribution is then convoluted (represented by $*$) by the Fourier transform of the specimen shape and the consequence is a softening of the Bragg conditions. Moreover, if each individual diffraction event can be formalized as before, we are in the case of dynamical multiple diffraction with coupling between diffracted beams and the calculation of the diffracted intensities is performed by the resolution of the dynamical equation which are built with elements from the Fourier transform of the transmission function and with the deviation from exact Bragg conditions for the different diffracted directions.

In both cases, the Fourier transformation is the basic ingredient of the diffraction process for the geometrical location of the diffracted beams. Nevertheless, the experimental diffraction experiment is performed by measurement of intensities and for many years, scientists have tried to address the problem of the associated loss of phase information, and many complicated schemes have been derived for «phase retrieval».

3. Local phase image technique

In material science, high resolution electron microscopy is able to produce images correlated with atoms or atom group distributions in the direction of the incident beam. Starting from digitised images, it is easy to obtain from a simple Fourier transform algorithm the distribution of complex amplitudes and after that to manipulate

them, taking into account the respective phase differences. These methods based on Fourier analysis are currently used in HREM for improving signal-to-noise ratios (cosmetic treatment), for creating fringes patterns, for nanosize diffraction and for the determination of hidden symmetry [1]. With the computer it is possible to image the distribution of intensity but also the distribution of the local phase.

The geometrical local phase method [2, 3] is of great help for an accurate determination of the nature of an interface (coherent or semi-coherent), for a local strain field determination around a defect, or for the determination of the distribution of domain sizes in nanostructured materials [1]. It is based on the fact that to any displacement in direct space corresponds a phase shift in Fourier space. From the phase distribution image which is only accessible because the Fourier transform is obtained with a computer from an image, it is then possible to extract the local displacement with respect to a perfect crystal (This last decade, image analysis by peak finding has also been used to give access to quantitative information [4, 5]).

The contrast of HREM images is obtained by the interference of the beams selected in a large diffraction aperture, each giving a set of fringes. The image intensity of a perfect crystal, $I(\boldsymbol{r})$, can be expressed as a Fourier sum:

$$I(\boldsymbol{r}) = \sum_{g} I_g \exp\{2\pi i \boldsymbol{g} \cdot \boldsymbol{r}\}, \tag{3}$$

where $\boldsymbol{g}$ are the lattice fringe periodicities and I_g, the corresponding Fourier components. Local Fourier components have an amplitude and phase such that:

$$I_g = A_g \exp\{iP_g\}. \tag{4}$$

In the Fourier transform of such an image, all the information is concentrated in the Bragg spots. Crystal defects such as interfaces, displacement fields will give information around these spots. It has been shown that the effects of these defects can be described by allowing the Fourier components I_g to acquire a "local" value $I_g(r)$ depending on the position in the image [4]:

$$I(\boldsymbol{r}) = \sum_{g} I_g(\boldsymbol{r}) \exp\{2\pi i \boldsymbol{g} \cdot \boldsymbol{r}\}. \tag{5}$$

As for the Fourier components in a perfect crystal, the local Fourier components have an amplitude and phase such that:

$$I_g(\boldsymbol{r}) = A_g(\boldsymbol{r}) \exp\{iP_g(\boldsymbol{r})\}. \tag{6}$$

The amplitude $A_g(\boldsymbol{r})$ represents the local degree of contrast of a particular set of lattice fringes $\boldsymbol{g}$, and $P_g(\boldsymbol{r})$ determines their position with respect to the perfect lattice chosen as a reference. The local phase images, $P_g(\boldsymbol{r})$, have particularly interesting properties. Two cases can be distinguished. The displacement of the atomic positions can be treated as a local $\boldsymbol{g}$ value or as a displacement field.

Let us take the example of a g vector change across an interface, $g \rightarrow g + \Delta g(r)$ corresponding to a change of lattice parameters, orientation (grain boundary), or both. The intensity associated to a specific set of fringes can be expressed as follows:

$$I_g \exp\{2\pi i g \cdot r + P_g\} \rightarrow I_g \exp\{2\pi i g \cdot r + 2\pi i \Delta g(r) \cdot r + P_g\}, \tag{7}$$

By comparison with eq. (6), the phase function of the position, can be written:

$$P_g(r) = 2\pi \Delta g(r) \cdot r \qquad \text{then} \qquad \nabla P_g(r) = 2\pi \Delta g(r). \tag{8}$$

In the case of translation boundaries such as anti phase boundaries or for example defects in interfaces associated to a stress field, the displacement of the atomic columns in the image can be expressed by a displacement field. Then, as previously for the g vector change case, it can be shown, that a displacement field, associated with a particular set of lattice planes is directly related to the phase:

$$P_g(r) = -2\pi g \cdot u(r) \tag{9}$$

and by combining the information from two lattice planes, $g1$ and $g2$, the two dimensional displacement field can be obtained:

$$u(r) = -\frac{1}{2\pi}\left[P_{g1}(r)a_1 + P_{g2}(r)a_2\right], \tag{10}$$

where a_1 and a_2 represent the lattice in real-space corresponding to the reciprocal lattice vectors g_1 and g_2.

The phase image technique present several advantages. Its use is easy and does not require long time calculations. The images are processed using routines specially written within the software package Digital Micrograph [6]. It can be used to analyse HREM images with complex image patterns, and not only images with single gaussian profile dot pattern.

4. Shape memory alloys

Shape memory alloys have remarkable mechanical and thermal properties like shape memory effect and superelasticity. Such properties are due to a thermoelastic martensitic transformation where the interfaces play a key role. This transformation between a high temperature phase, austenite, and a low temperature phase, martensite, is displacive and governed by the shear of the austenite, keeping one plane invariant called the habit plane. Due to the shape change associated with the shear, the transformation parameters and the microstructure are controlled by the deformation energy. The martensite plates nucleate in austenite, and grow with the gliding of the austenite/martensite interfaces. At the reversion for a thermoelastic transformation, the interfaces move back and the initial austenite is restored exactly. Starting from a

cubic structure, there are 24 combinations of shear possibilities associated to invariant planes, leading to 24 crystallographically equivalent variants of martensite. Without any applied stress, all these variants have the same probability to nucleate and grow. As a consequence, when the temperature decrease, the transformation occur without any shape change of the sample. The martensite variants nucleate and grow forming self accommodated groups. The intrinsic deformation of each martensite variant is accommodated by all the surrounding variants, minimising the shape change. If an external stress is applied, the free Gibbs energy, associated to the martensite variants for which the intrinsic shear respond to the stress, will decrease. More stable, these variants will grow by gliding of the intervariants interfaces.

As an illustration of the importance of deformation energy in martensite, we will present an analysis of self-accommodated martensite plates in a CuZnAl Shape Memory Alloy and the effect of an internal displacement field due to a precipitate in NiTiCo SMA. We will also briefly discuss the analysis of an interface.

5. Strain fields and self-accommodation in CuZnAl SMA

Tensile specimens (gauge length = 10 mm and diameter 6 mm) from Zn 15.34 at. %, Al 16.33 at. % Cu-rest (e/a = 1.48) β phase single crystal with a $M_s = -10°C$ are heated to 850°C for 20 min. and air quenched, then left at room temperature for at least 4 days to anneal out excess vacancies and to allow the ordering of the alloy. Under tensile stress, the samples were pseudoelastically cycled 3000 times with a maximum strain that leads to a 100 % martensitic formation, in a closed loop at 0.8 Hz at 25.5 °C [7]. Several discs parallel to the family of planes $\{001\}_\beta$ were cut from the cycled specimens for Transmission Electron Microscopy analysis (TEM). Thin foils were obtained by double jet electro-polishing at room temperature (30 % orthophosphoric acid in distillated water, $V = 2$ V, $I = 30$ mA). HRTEM observations were carried out on a Topcon 002B electron microscope operating at 200 kV with a point to point resolution of 0.18 nm (Cs = 0.4 mm). Negatives were digitised with an Agfa Duoscan scanner and the resulting images have a resolution of 0.038 nm/pixel.

The specimen is still a single crystal of the ordered β_1 phase (L_{21}, a = 0.586 nm) with large dislocation bands introduced by the pseudoelastic tensile cycling and in addition to these bands, in thin parts of the specimen, small plates of martensite phase are observed (high resolution image in [100] orientation, Fig. 2). Their formation is eased by the M_s temperature closed to room temperature. When the electron is focused on such plates, they are observed to grow, with the austenite/martensite interface at the tip of the plates gliding to the inner parts of the specimen and this phenomena can be attributed to an accommodation of the local stress intruded by the bending of the thin foil under the electron beam. The exact nature of the martensitic phase has not been determined (with e/a = 1.48, a 18R martensite is expected to be formed) but no confusion can be made with surface martensite which does not form on (100) surfaces. In this paper, we focus our attention on the potential of the method to determine the

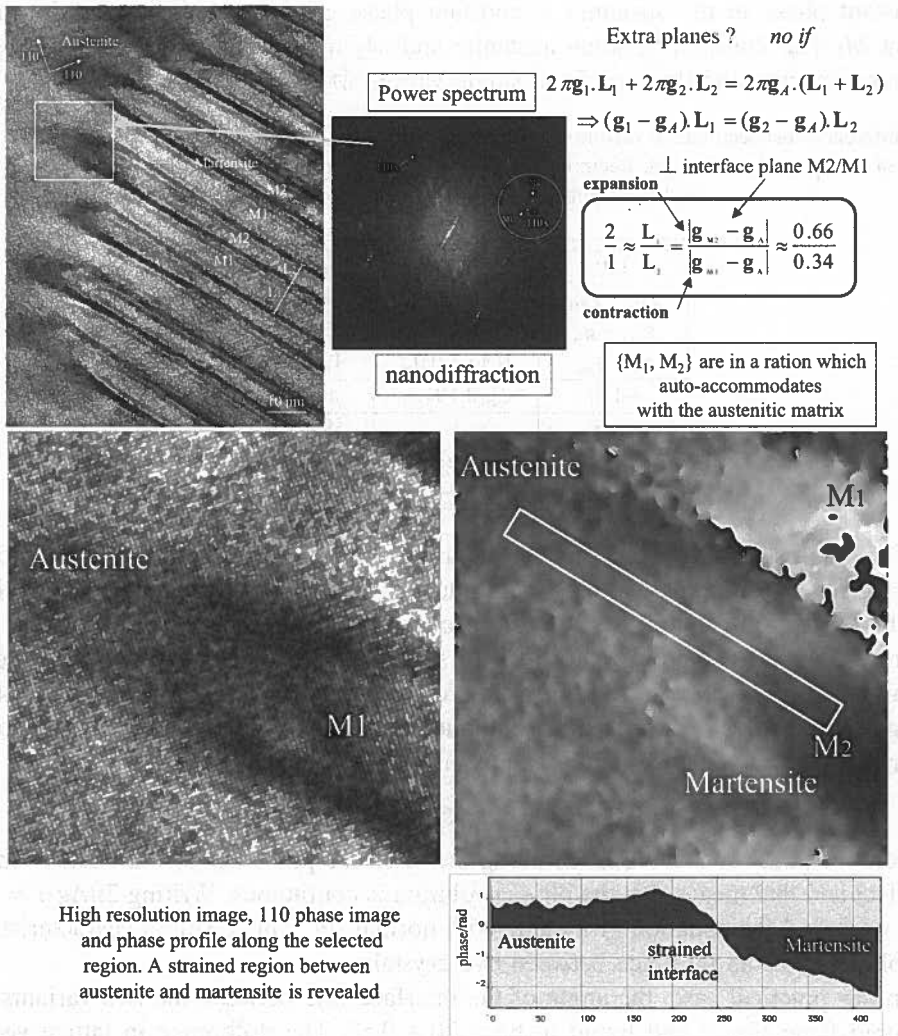

High resolution image, 110 phase image and phase profile along the selected region. A strained region between austenite and martensite is revealed

Fig. 2. Fourier analysis of auto-accommodated martensitic variants in CuZnAl SMA

local strain of the lattice. To calculate the local phase image, a Fourier transform (power spectrum) was taken of the region shown in Fig. 2. A mask was applied around the periodicity corresponding to the 110 planes in the austenite and the phase image calculated from the inverse Fourier transform. Where the phase image has a gradient of zero, the local lattice vector $\boldsymbol{g}$ corresponds exactly to that of the reference lattice (region in austenite). By measuring the gradient of the phase, the deviation from the austenite lattice, $\Delta\boldsymbol{g}$, can be determined. It was found from this analysis that the plates were of two different martensitic variants M_1 and M_2, as marked on Fig. 2.

The results are summarised in Table and the position of the periodicities in reciprocal space indicated on the power spectrum. The 110 phase image clearly shows

a constant phase in the austenite, a constant phase gradient in the martensite phase variant M_2 (Δg constant between austenite and M_2 martensite) and a strained region between austenite and the top of the single variant M_2.

TABLE 1

Differences between lattice vectors in the austenite and martensite measured from the gradient of the local phase images. Reciprocal lattice lengths, Δg, are expressed as a fraction of g_A, and the orientation with respect to the horizontal.

110	$\Delta g/0.134 g_A$	angle (°)
$g_{M_2} - g_{M_1}$	1	59.3 ± 0.2
$g_{M_2} - g_A$	0.65 ± 0.01	65.9 ± 0.3
$g_A - g_{M_1}$	0.36 ± 0.02	47.2 ± 0.5
−110	$\Delta g/0.104 g_A$	angle (°)
$g_{M_2} - g_{M_1}$	1	58.0 ± 0.3
$g_{M_2} - g_A$	0.66 ± 0.01	53.8 ± 0.4
$g_A - g_{M_1}$	0.34 ± 0.02	66.0 ± 0.7

The microstructure shows that the martensite is composed by the alternance of two variants of different widths. So the analysis of such a groups of two variants must be carried out. Before we have to introduce the case of a coherent interface with the crystallographic continuity between to sets of lattice planes in two crystal, $\boldsymbol{g}_1$ in crystal 1 and $\boldsymbol{g}_2$ in crystal 2 and a mask around the two spots, the phase in crystal 1 is $2\pi \boldsymbol{g}_1 \cdot \boldsymbol{r}$ and $2\pi \boldsymbol{g}_2 \cdot \boldsymbol{r}$ in crystal 2 (without a constant term). The local phase image with respect to crystal 1 is therefore zero in crystal 1 and:

$$P_g(\boldsymbol{r}) = 2\pi(\boldsymbol{g}_2 - \boldsymbol{g}_1) \cdot \boldsymbol{r} = 2\pi \Delta \boldsymbol{g} \cdot \boldsymbol{r}. \tag{11}$$

The relative phase is then constant along the interface plane because the lattice match is perfect and that means that the phase evolution is continuous. Writing $2\pi \Delta \boldsymbol{g} \cdot \boldsymbol{r}$ = constant, we found the equation of a plane with normal $\Delta \boldsymbol{g}$. This result is characteristic of the coherency of an interface between two crystals.

In our practical case, the angle of the interface line between the two variants was measured from Fig. 2 and found to be − 30 ± 0.5°. The difference in lattice vectors $\Delta \boldsymbol{g} = \boldsymbol{g}_{M_1} - \boldsymbol{g}_{M_2}$ for both the {110} lattice planes are almost perpendicular to this line at 59.3 ± 0.2°and 58.0 ± 0.3°(see Table 1). This means from eq. (11) that the {110} lattice planes in the two martensitic variants are almost perfectly coherent and form a near invariant line. Through the conditions for both lattice planes cannot be satisfied exactly, a deviation of 1°from the ideal coherent interface line would only mean a dislocation every 110 nm!

Now we have to consider the behaviour of these two variants with respect to the austenite matrix. In the direction of these two plates of martensite, it is interesting to calculate if any extra planes, and hence dislocations, are necessary for matching with the austenitic phase. For no extra planes, the phase difference across two martensitic plates must equal that for the austenite along the same $L_1 + L_2$ distance. Therefore:

$$2\pi \boldsymbol{g}_1 \cdot \boldsymbol{L}_1 + 2\pi \boldsymbol{g}_2 \cdot \boldsymbol{L}_2 = 2\pi \boldsymbol{g}A \cdot (\boldsymbol{L}_1 + \boldsymbol{L}_2) \Rightarrow (\boldsymbol{g}1 - \boldsymbol{g}_A)\boldsymbol{L}_1 = (\boldsymbol{g}2 - \boldsymbol{g}A)\boldsymbol{L}_2 \tag{12}$$

and since these difference vectors are almost parallel to the interface between anstenite and martensite variants, we can write:

$$\frac{L_1}{L_2} = \frac{g_{M_2} - g_A}{g_{M_1} - g_A}. \tag{13}$$

From Fig. 2, the ratio of the widths of the two plates, L_1 to L_2, was measured to be approximately 1 : 2. Comparing with the values given in Table 1, this means that the relative widths of the two martensitic variants were such that the plates were auto-accommodated with the austenic phase.

Using two independent g-vectors, we can obtain the two-dim. displacement filed (eq. 10) and from that data, it is possible to calculate the element of the two-dim. deformation tensor with:

$$\varepsilon_{ij} = \frac{1}{2}\left(\frac{\partial u_i}{\partial x_j}\frac{\partial u_j}{\partial x_i}\right)$$
$$\overline{\omega}_{ij} = \frac{1}{2}\left(\frac{\partial u_j}{\partial x_i}\frac{\partial u_i}{\partial x_j}\right). \tag{14}$$

The deformation ε_{xx}, with x along the martensite plates, shows that the transition region between anstenite and martensite extends over about 30 nm and the deformation appears to be inhomogeneous in the direction y-axis parallel to the anstenite/martensite interface (Fig. 3).

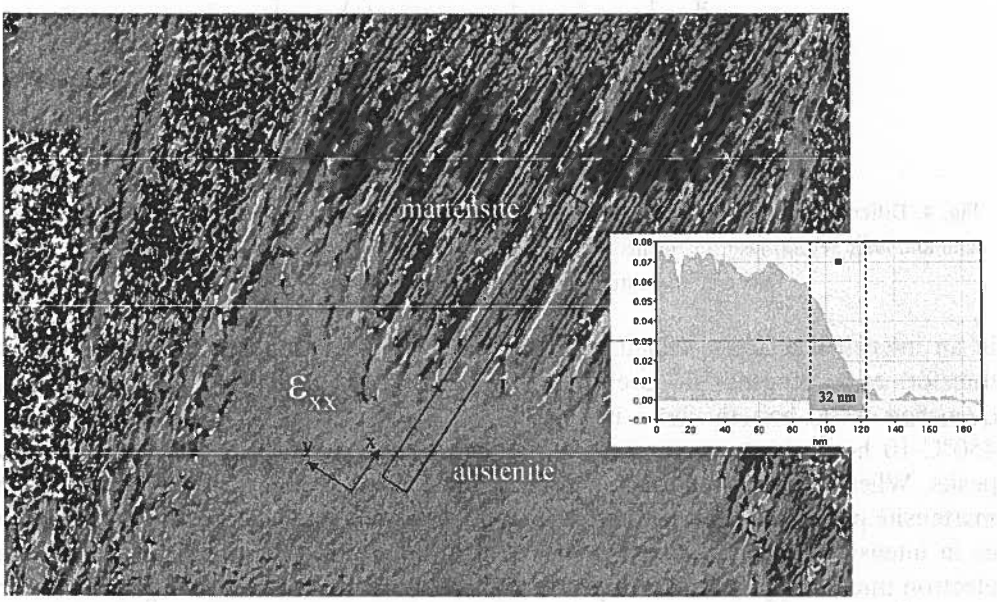

Fig. 3. Deformation component ε_{xx}

6. Displacement field associated to precipitates (Ni 47 at.% Ti 50% Co 3 at.%)

Multiple martensitic transformations can occur in Shape Memory Alloys for several reasons (two different kinds of martensite, dislocations walls, presence of coherent precipitation associated with a displacement field, bimodal grain size distribution after crystallization of a partly amorphous ribbons).

A $Ni_{47}Ti_{50}Co_3$ alloys have been cast using the planar flow technique giving directly 30-50 μm thick ribbons. The high cooling rates (10^5–10^6 $K{\cdot}s^{-1}$) of this technique can lead to fine-scale microstructures, and in some cases, to amorphous and other metastable phases. In the present case, thermal analysis of these ribbons shows that the martensitic transformation is shifted down to low temperatures and proceed in several steps as visible on the differential scanning calorimetry cooling curves shown Fig. 4. The first exothermal peak is associated to the transformation of the austenite

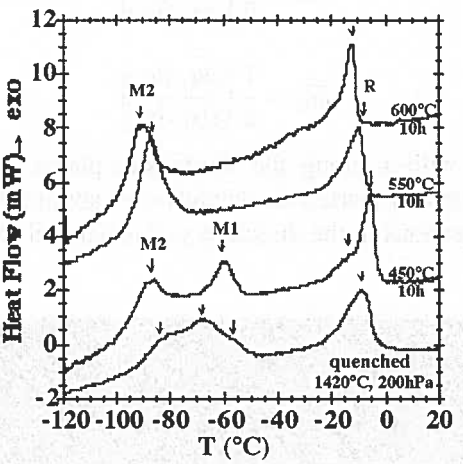

Fig. 4. Differential scanning calorimetry cooling curves of NiTiCo melt spun ribbons in as quenched state and after several heat treatments. The multiple martensitic transformation disappears after higher temperature treatments leaving a single transformation peak

in an intermediate phase called R-phase before to transform in martensite. This last transformation proceeds in several steps depending of the state of the sample. In as quenched state, bottom curve in Fig. 4, the martensite peak is broad, but after a 450°C-10 hours heat treatment under vacuum, this peak is well separated into two peaks. When the heat treatment is done at higher temperatures, the high temperature martensite peak disappears whereas the low temperature one is maintained and increases in intensity [9]. The analysis of the microstructure of the ribbons by transmission electron microscopy at room temperature showed that all the austenite grains contains fine plate-like precipitates (Fig. 5).

HREM image of a plate-like precipitate in an as quenched sample is presented in Fig. 6 with the power spectrum. The first phase image is obtained with $\boldsymbol{g}_1$ = 100 and

some phase profiles across and around the precipitate revealing the displacement field around the precipitate associated to the (100) lattice plans (reference is the austenite phase). On both sides of the precipitate, horizontal profiles c and d shows a quasi-linear phase change and the sign of this phase change clearly shows that the displacement of (100) planes are symmetrical with respect to the precipitates, in the [100] direction for the upper region and in the opposite direction for the lower region. Another quasi-linear phase change is observed along the vertical line b at the left of the precipitate but, across it, a step evolution of the phase indicates a rigid body displacement across the precipitate (2/6 of the interplanar distance on each side). For the phase image obtained with $g_2 = 010$, there is no phase change across the precipitate. For such a precipitate observed along a direction perpendicular to the plate, no phase change is observed. According to these results, a schematic representation of the strain field around the precipitate clearly shows that the maximum of deformations are located at the four corners of the precipitate.

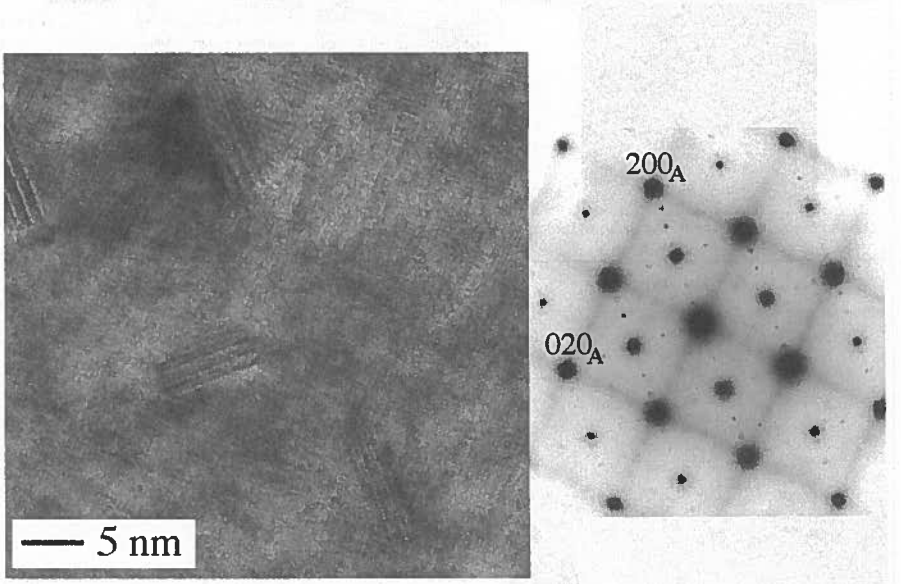

Fig. 5. Low magnification of a HREM image of an austenite grain in the as quenched sample showing fine plate-like precipitates and SADP of the same grain taken along the $[001]_{Austenite}$ direction. Extra spots due to the precipitates are clearly visible and give information on the orientation relationship with the matrix

As a consequence, the displacements of the (100) lattice planes clearly revealed, will promote the martensite transformation on the corner of the precipitate plates and thus they will explain the $M1$ peak on the DSC curves (Fig. 4). Far from the precipitates, in a nearly perfect austenite, the martensite will appear for a lower temperature giving the $M2$ peak. TEM observations on the heat treated samples at higher temperatures than 550°C have shown that these plates become incoherent rounded precipitates. The

displacement field associated to these precipitates is relaxed and thus the $M1$ peak on the DSC curves disappears. The $M2$ peak does not move but increase in intensity.

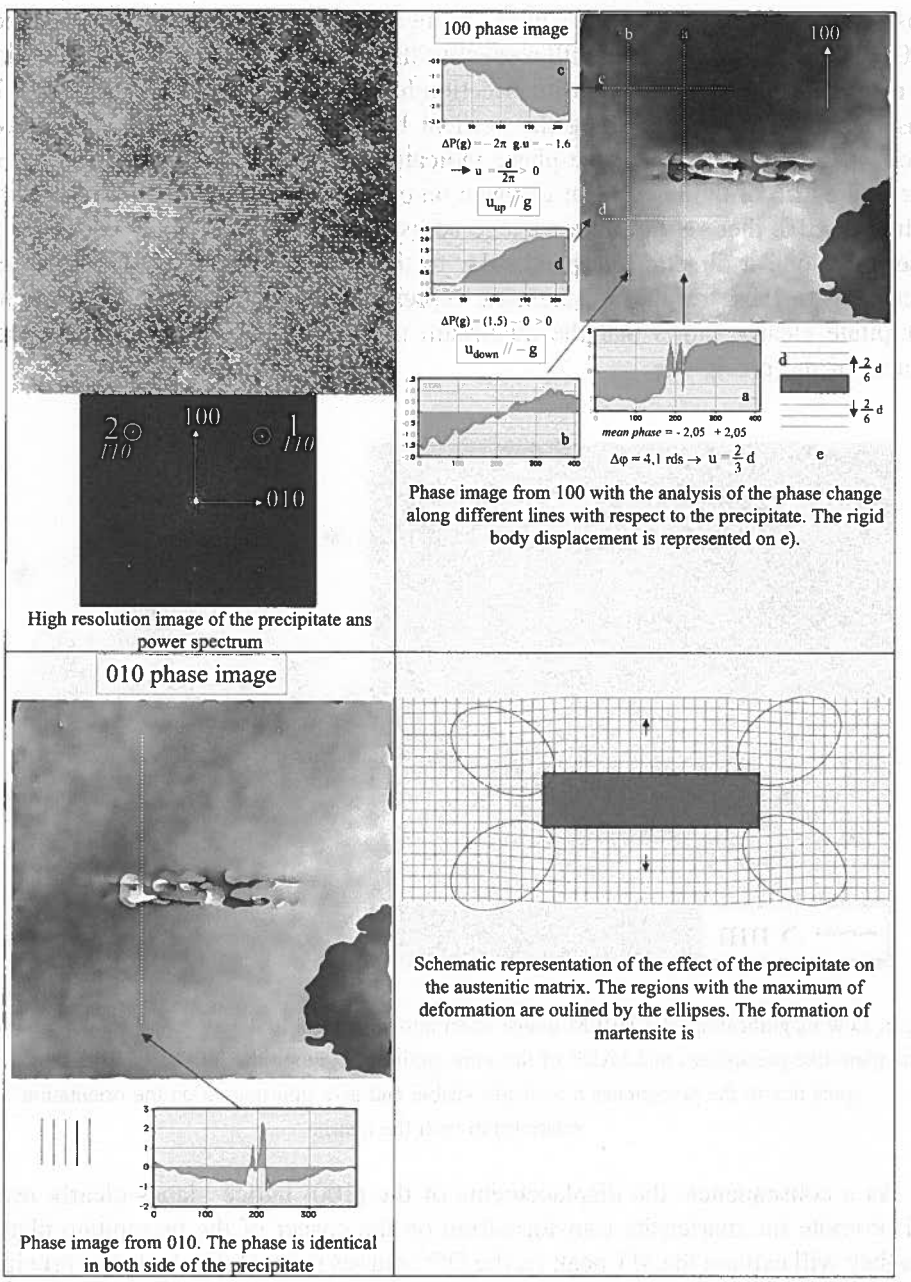

Fig. 6. Analysis by the technic of phase images of the displacement field in the austenite around a precipitate in Cu-Zn-Al

7. Interfaces in SMA

Interface properties controls the mechanical behaviour of SMA. For instance, martensitic intervariant interface mobility is responsible for the variant reorientation process when the specimen is deformed at low temperature in the martensitic state, property related to the shape memory effect. So, the study of interfaces with the phase image technique is very fruitfull [10]. Here, we shall only consider the case of a martensite intervariant interface in CuAlNi-type alloy (Fig. 7). The interface is definitely coherent, the phase image obtained with g1

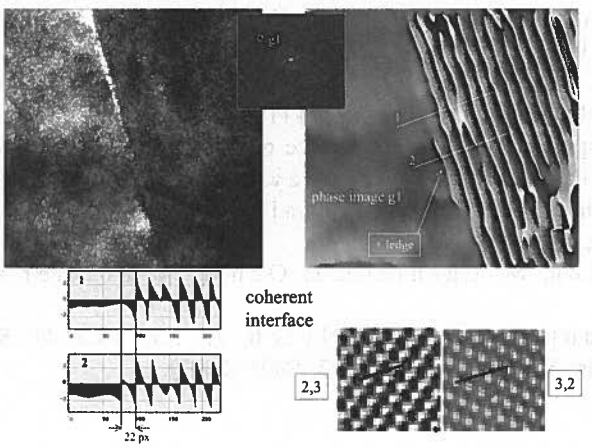

Fig. 7. Coherent interface between two martensitic variants in a CuAlNi-based alloys, with phase image and two phase profiles. The height of the ledge correspons to lattice vectors in the two variants

reflexion shows a progressive phase evolution at the level of the interface. Furthermore, a ledge is clearly visible, with an extra fringe parallel to the interface. The thickness of the ledge, evaluated from two profiles marked 1 and 2, approximately corresponds to lattice periodicities in the two variants, so no extra defect is associated with the ledge which must be involved in the reorientationnal process.

8. Concluding remarks

Fourier analysis and, specially, phase images are very efficient tools for extracting quantitative data from high resolution images or for the analysis of an interface with respect to coherency, semi-coherency or incoherency. The displacement field is also accessible from this method. Nevertheless, the interpretation of then results must be considered with care because we are working with 2-dim images from 3-dim specimen, we have very thin specimen and the effect of the free surfaces can be important for the

relaxation of strains. For better results, it is also important to correct the image from the projectors lens distortions (11).

REFERENCES

[1] R. Portier, P. Vermaut, M. J. Hÿtch, Applied Crystallography, ed. H. Morawiec and D. Stróż, World Scientific **86**, 2004-10-29.

[2] M. J. Hÿtch, Microsc. Microanal. Microstruct. **8**, 41-57 (1997).

[3] M. J. Hÿtch, E. Snoeck, R. Kilaas, Ultramicroscopy **74**, 131-146 (1998).

[4] R. Bierwolf, H. Hohenstein, F. Philipp, O. Brandt, G. E. Crook, K. Ploog, Ultramicroscopy **49**, 273 (1993).

[5] P. Bayle, T. Deutsch, B. Gilles, F. Lançon, A. Marty, J. Thibault, Ultramicroscopy **56**, 94 (1994).

[6] Digital Micrograph 2.5, Gatan Inc., phase routines available at http://ncem.lbl.gov.

[7] J. Malarria, M. Sade, F. Lovey, Z. Metallkd **87** 953 (1996).

[8] M.J. Hÿtch, P. Vermaut, J. Mallaria, R. Portier, Mat. Sc. & Eng A, **273-275**, 266, (1999).

[9] C. Elgoyhen, M. Larnicol, P. Ochin, R. Portier, J. Phys. IV, **7**, C5, 191 (1997).

[10] Ph. Vermaut, F. Dalle, M. Hÿtch, A. Kotska, D. Stroz, R. Portier, Ann. Chim. Sci. Mat, 27 suppl. **12**, S303 (2002).

Received: 3 November 2004.

A R C H I V E S O F M E T A L L U R G Y A N D M A T E R I A L S
Volume 49 2004 Issue 4

V. KOLOMYTSEV*, A. PASKO*, A. SEZONENKO*

SELECTION RULES FOR THE PRODUCTION OF BULK METALLIC GLASS PRECURSORS FOR SHAPE MEMORY MATERIALS

ZASADY WYBORU MASYWNYCH SZKIEŁ METALICZNYCH JAKO PREKURSORÓW DO PRODUKCJI MATERIAŁÓW Z PAMIĘCIĄ KSZTAŁTU

The paper is focused on the development of the following technological paths: (metallic melt) → (bulk metallic glass precursor of shape memory material) → (superplastic deformation on heating through the supercooled liquid region) → (crystallization and final microcrystalline material with martensitic transformation in a predetermined temperature range). Main attention is paid to design of multicomponent $(Ti,Zr,Hf)_A(Co,Ni,Cu,Pd)_B$ alloys with compositions varied around an effective intermetallic compound AB (A:B = 45:55; 50:50; 55:45). One of the challenging problems here is to find a chemical composition window of our multicomponent systems fitting the known empirical rules for a high amorphization ability and keeping the martensitic transformation and good shape memory properties after crystallization.

Keywords: bulk metallic glasses, rapid solidification, shape memory alloys, martensitic transformation.

Artykuł przedstawia rozwój następującej ścieżki technologicznej: (ciecz metaliczna) → (masywne szkło metaliczne jako prekursor materiału z pamięcią kształtu) → (nadplastyczne odkształcenie w zakresie cieczy przechłodzonej) → (krystalizacja w określonym zakresie temperatur i uzykanie końcowego mikrokrystalicznego materiału z przemianą martenzytyczną). Główną uwagę zwrócono na zaplanowanie wieloskładnikowych stopów $(Ti, Zr, Hf)_A(Co, Ni, Cu, Pd)_B$ o składzie zmieniającym się w pobliżu składu związku międzymetalicznego AB (A:B = 45:55, 50:50, 55:45). Jednym z podstawowych problemów jest znalezienie zakresu składów chemicznych dla układów wieloskładnikowych, pasujących do znanych regół empirycznych tworzenia stopów o dużej zdolności do amorfizacji, i równocześnie zachowania przemiany martenzytycznej oraz dobrego efektu pamięci kształtu po krystalizacji.
Słowa kluczowe: masywne szkła metaliczne, szybkie krzepnięcie, stopy z pamięcią kształtu, przemiana martenzytyczna.

* INSTITUTE OF METAL PHYSISC NATIONAL ACADEMY OF SCIENCES OF THE UKRAINE, 36 VERNADSKOGO BLVD., 03680 KYIV, UKRAINE

1. Introduction

The bulk amorphous alloys (bulk metallic glasses, BMG), a novel strategically important class of materials attracted attention as precursors to produce (by crystallization) the nanostructured materials. The development of amorphous and nanocrystalline alloys has increased interest for the past several years due to their specific mechanical properties: at room temperature some materials have the tensile fracture strength of 2000 MPa with 2% elastic strain prior to fracture [1–3]. The amorphous alloys were found to have features of new alloy compositions and new atomic configurations which are different from those for the crystalline alloys. These features lead to various specific characteristics such as good mechanical properties, useful physical properties and unique chemical properties [1]. The nanostructured materials produced from BMG precursors show good mechanical properties, soft and hard magnetism, high magnetostriction in low applied field, high catalytic properties. Moreover, some BMG show an extremely large elongation (several hundreds, even thousands percent) obtained by tensile deformation in the supercooled liquid region. Recently, Zr- and Ti-based bulk amorphous alloys were produced by arc-melting with drop casting and induction melting with injection casting [1, 3, 16].

Shape memory alloys (SMA) have been of increasing interest both from the academic and industrial communities due to their unique functional properties: the one- and two-way shape memory (up to several percent of recoverable deformation) and superelasticity effects caused by reversible martensitic transformation. The shape memory effect consists in the following: a specimen deformed (by tension, compression, bending, etc.) in the martensite (low-temperature phase) state recovers its original shape upon heating due to the reverse martensitic transformation. Among others, a very important condition of obtaining the shape memory effect is a thermoelastic equilibrium between the coexisting parent and martensite phases (so-called K u r d y u m o v's effect) and formation of self-accommodated groups of martensite crystals (having the same crystal structure but different orientations) with highly mobile interfaces.

Despite a long-term history of the shape memory materials, the NiTi- and CuAl-based alloys remain two major groups of commercially used materials for which industrial, in particular, medical applications have been developed [4]. The shape recovery and service temperatures in such applications are below ~100°C, and requirements of thermoelastic martensitic transformation and fine martensite morphology are easily fulfilled. About 15 years ago, C . M . W a y m a n and T . W . D u e r i g reported more than 15 different SMA systems [4]. Recently, a number of other alloys and ceramics have been developed, in particular, for enhanced temperature applications. The sensor and actuator applications in the automotive, electrical and power industries require higher service and shape recovery temperatures up to 200°C and above [5].

Strictly speaking, a design of chemical compositions themselves exhibiting martensitic transformation is not a difficult problem. Up to now, researchers have proposed a large group of conventional paramagnetic SMA for high-temperature applications (the shape recovery temperature A_F up to 1000°C) starting with binary TiPd [6, 7],

TiPt [8], NiAl [9], etc. In many cases, however, the shape memory applications are limited by poor ductility of currently available SMA that leads to difficulties in their processing and providing stability of the microstructure and shape memory effect. To overcome the brittleness of binary SMA, two approaches can be effective:

1. Modification of the alloy chemical composition with the third and forth elements in order to improve mechanical properties and make the alloy ductile, adjusting simultaneously the martensitic transformation temperatures to fit the required temperature interval.

2. Development of alternative production technologies which enable to obtain materials in forms close to requirements of end-users, such as the physical vapour deposition, magnetron sputtering, laser oblation, powder metallurgy, rapid solidification techniques. It should be admitted that very often in these methods the materials are received in amorphous state.

Here, we are going to present some considerations regarding the SMA selection for rapid solidification techniques keeping in mind the main idea to develop the following innovative technological paths: [metallic melt] → [bulk metallic glass precursor of shape memory material (BMG/SMA-precursor)] → [superplastic deformation on heating from the glassy state through the supercooled liquid region] → [crystallization and final microcrystalline material with martensitic transformation in a predetermined temperature range].

The development of amorphous precursors for shape memory alloys has long-term history, nevertheless, the nature of amorphous microstructure was not fully understood until a principally new approach – bulk metallic glass precursors for shape memory alloys – appeared several years ago [10]. Such "glassy" approach to amorphous phase has been successfully applied to further development of the muticomponent SMA systems [36–40]. Importance of BMG/SMA-precursors for practical applications is evident since the formability during the glassy-to-crystalline transition enables to obtain SMA semi-products in forms close to the end-user requirements. It has been found that, for obtaining alloys with high functional properties, it is not sufficient to optimise only the technological parameters of their production by "non-traditional" (for SMA) technologies. The reverse task is becoming an important factor, namely, the search and development of shape memory alloys with certain chemical compositions fulfilling maximally the requirements of a specific technology. One of the challenging problems here is to find a chemical composition window of our multicomponent systems fitting the known empirical rules for a high amorphization ability and keeping the martensitic transformation and good shape memory properties after crystallization. It is important to admit that the main alloy constituent elements are often the same for good BMG formers and good SMA.

In this paper our attention is concentrated on development of the multicomponent pseudobinary AB-type intermetallic compound with effective Ti + Zr + Hf mixture as an element A and effective Co + Ni + Cu + Pd mixture as an element B.

2. General view on bulk metallic glasses

It is widely stated that most of the metallic melts can keep the amorphous structure of liquid during rapid solidification with sufficiently high cooling rate. In the temperature regime of the glass formation, on cooling from the metallic melt state, any physical property (enthalpy, density, viscosity) changes gradually with temperature in the supercooled liquid area so that there is no abrupt variation or drop and only change in slope is detected (see Fig. 1 for a thermodynamic potential variation [11]). The onset temperature T_G, called the glass transition temperature, separates two qualitatively different material states: a supercooled liquid state at higher temperatures and a glassy (solid) state at lower temperatures which is energetically highly excited (metastable). The exact position of T_G is strongly dependent on the metallic melt cooling rate: the slower is the metallic melt temperature variation on cooling (but enough to avoid crystallization) the lower is the position of glass transition temperature and more stable glassy state is reached (see relative position of T_G in Figure 1 : $T_G^a > T_G^b$ for cooling rate "a" > cooling rate "b"). On heating (curve "c" in Figure 1), the reverse sequence of phase transitions takes place from metallic glass state to supercooled liquid one (small temperature hysteresis is possible) and position of glass transition temperature T_G^c depends on heating rate "c" (usually it coincides with T_G position for equal cooling rate, i.e. $T_G^b = T_G^c$ for cooling rate "b"=heating rate "c").

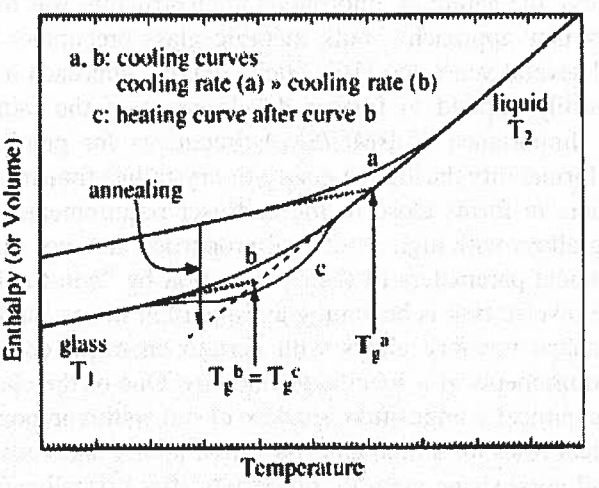

Fig. 1. A thermodynamic potential in the temperature regime of the glass transition: (a) and (b) – different cooling rates, (c) – the temperature dependence during heating [11]

To differentiate different alloy systems with respect to stability of their supercooled liquid against nucleation and growth of crystalline phases and thus different tendency to the glass formation, several parameters have been used for characterisation of the glass forming ability. Glass forming ability (GFA), as related to the ease of devitrification,

is very crucial for understanding the origins of glass formation and simultaneously very difficult for interpretation. Many different criteria have been proposed based on the characteristic temperatures measurements by differential scanning calorimetry or differential thermal analysis [1, 3, 12, 13, 34]. In such experiments, mostly only heating stage from glassy state through supercooled up to stable metallic melt state is detected with the crystallisation and melting events (i.e., see DSC curves in Figure 2a showing glass transition temperature T_G and crystallisation temperatures T_{Xi}, and DTA curves (Figure 2b) showing melting temperature T_M and liquidus temperature T_L).

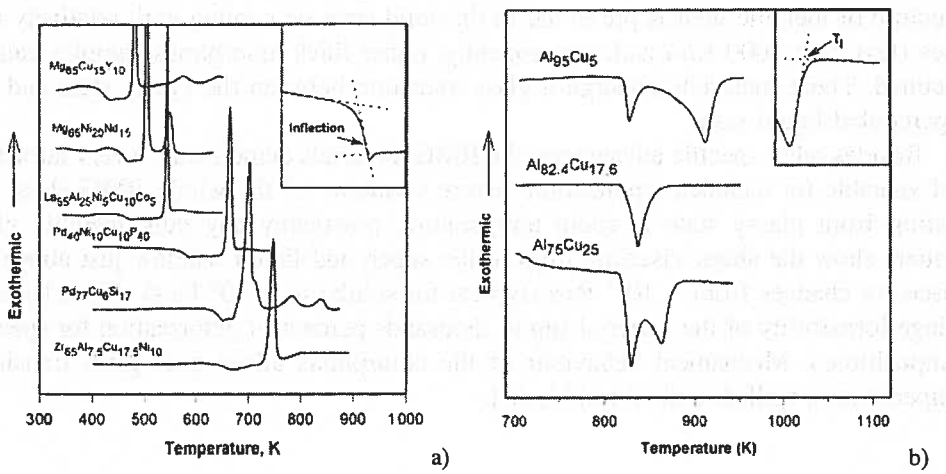

Fig. 2. a. Typical DSC curves for some bulk metallic glasses, the insert shows the determination of glass transition [34] b. Typical DTA melting curves, the insert indicates the definition of T_l melting point [34]

Some researchers used for long time the definition of the GFA by means of the reduced glass transition temperature $T_{RG} = T_G/T_M$ (glass transition temperature over the melting point) and value of the supercooled liquid window $\Delta T = (T_X - T_G)$ [1, 12]. Intuitively, the higher T_{RG} the narrower is the temperature interval between the metallic melt and metallic glass states. Consequently, it is easier to prevent crystallisation and to keep amorphous state to lower temperatures. The best bulk metallic glass formers have the reduced glass transition temperature value $T_{RG} > 0.6$ and $\Delta T > 60$K.

In addition to supercooled liquid range $\Delta T = (T_X - T_G)$, the most extensively used now is a new indicator of the GFA defined as $\gamma = T_X/(T_G + T_L)$, where T_X is the onset crystallization temperature, T_G and T_L are the glass transition temperature and liquidus temperature, respectively [13]. For the best metallic glass formers its value has found to be $\gamma \geqslant 0.35$. The relationship between parameter γ and other traditional parameters such as the critical cooling rate R_C and critical section thickness Z_C is formulated and discussed by L u and L i u [13].

The GFA of a metallic melt is evaluated in terms of a critical cooling rates (R_C) for glass transition, which is a minimum cooling rate necessary to keep the melt amorphous

without precipitation of any crystals during solidification. The smaller critical cooling rate the higher GFA should be and consequently larger the maximum sample thickness for glass formation (t_{max}) or critical amorphous section thickness (Z_C). However, critical cooling rate is a parameter that is difficult to measure precisely. Nevertheless, general tendency "the smaller cooling rate → the higher GFA → the thicker amorphous layer" is still valid for a large group of metallic alloy systems according to a relationship between the critical cooling rate (R_C) for glass transition, maximum sample thickness (t_{max} or Z_C) and reduced glass transition temperature (T_G/T_M) [1, 12].

Thus, the bulk metallic glasses are metallic alloy systems in which the amorphous structure of metallic melt is preserved in the solid state on cooling with relatively low rates (less than 1000 K/s) and, consequently, rather thick amorphous samples can be obtained. These materials undergo a glass transition between the glassy state and the supercooled liquid state.

Besides other specific advantages, the BMG materials demonstrate a very attractive and valuable for technical application feature common for the whole BMG class. On heating from glassy state at room temperature, practically any bulk metallic glass formers show the sharp viscosity drop in the supercood liquid window just above T_G (viscosity changes from ~ 10^{12} Pa·s (typical for solids) to ~ 10^6 Pa·s) which leads to a huge formability of the material (up to thousands percent of deformation for specific compositions). Mechanical behaviour of the amorphous alloys near glass transition temperature is well described in [14, 15].

3. Selection of the bulk metallic glass compositions

As already mentioned, most of the metallic melts may kept the liquid amorphous structure during rapid solidification with sufficiently high cooling rates, i.e. critical cooling rate for monoatomic melts is well above 10^8K/s, while for binary metallic melts it may be much lower, up to 10^6K/s. Recently developed bulk metallic glasses have relatively low critical cooling rates (below 10^3 K/s, even several degree per second), so, appropriate for variety of conventional solidification/casting techniques. Selection of chemical compositions for such bulk metallic glasses is based on empirical rules summarised in [1, 12] in following manner: 1. multicomponent systems consisting of more than three elements; 2. significant difference in atomic size rations above about 12% among three main constituent elements; 3. negative heats of mixing among the three main constituent elements. Those rules suit well also for formation of the Laves λ-phases (A2B-type), Hume-Rothery electronic driven phases, Frank-Kasper phases, however, Inoue [1, 12] was the first who formulated them in such way for BMG and proposed schema "how do they work". Based on these principles, a large group of bulk metallic glasses has been developed such as: "rear-earth metal - late transition metal - simple metals", "early transition metal - late transition metal - simple metal" [12, 16-19].

Despite multicomponent criteria for BMG, in actual cases very often a model binary A-B (Lennard-Jones type) alloy systems are considered. It seems worth to emphasise several consequences from empirical rules mentioned above:

1. requirement of different atomic radii R_A and R_B defines the concentration range of easy amorphization through the minimum critical concentration according to [20, 21]: $C_{min} = 0.1/|(R_B/R_A)^3 - 1|$;

2. the vast majority of metallic glasses produced to date in easy glass-forming systems with negative heat of mixing: negative heats of mixing and asymmetry in the enthalpy versus composition variation in real metallic systems define position of "deep eutectic" for a given alloy system [22-25];

3. analysis of available literature data showed that for given alloy system, the largest critical section thickness and lowest critical cooling rates occur for chemical compositions at or near their eutectic points [13]. In model binary alloys "deep" eutectic is located mostly around A65B35 or A35B65; in model ternary alloys "deep" eutectic is located around A65B25C10 composition and/or vice versa [25].

4. density variation on melting for BMG alloys is much lower (~ 0.5%) than for ordinary amorphous alloys (up to 5-6%), so the bulk metallic glasses have more dense metallic melt structure [26, 27]. From topological point of view, the increase in the degree of the dense random packed structure for BMG is reflected in the difference of the atomic size distribution plots (ASDP) for ordinary amorphous alloys and bulk metallic glasses [26, 27].

Thus, for multicomponent pseudobinary AB alloys with appropriate ASDP, the highest GFA range may be fitted to the requirements for shape memory alloys, namely, "deep" eutectic near $A_{50}B_{50}$ for TiNi-based alloys or "deep" eutectic near $A_{75}B_{25}$ for CuAl- and NiAl-based alloys.

4. Phase Selection for shape memory alloys and specific features of pseudobinary phase diagrams

The martensitic transformation is a structural phase transition occurring by coordinated movement of atoms that does not need diffusion (diffusionless transformation) and accompanying with a macroscopic shape change of the transformed region. In paramagnetic SMA, the martensitic transformation underlying the shape memory effect is induced by change in either temperature or mechanical stress. In ferromagnetic SMA, the magnetic field plays a role of additional driving force. As already mentioned, the shape memory effect consists in the following: a specimen deformed (by tension, compression, bending, etc.) in the martensite (low-temperature phase) state recovers its original shape upon heating due to the reverse martensitic transformation.

General requirements for SMA composition and microstructure to demonstrate high functional property may be summarised as follows for model (Ti,Zr,Hf)A(Co,Ni, Cu,Pd)B alloys:

1. Precise alloy composition both for intermetallic compound line and inside B2 homogeneity range (maximum deviation < (0.5 – 1.0) at. % will be invited).

2. Ordered parent phase (B2, D03 or $L2_1$), optimal mean grain size and >90% volume fraction of parent phase.

3. Reversible and thermoelastic martensitic transformation: coherent and mobile parent phase – martensite phase boundaries; the orientation relationship between the parent and martensite crystal lattices facilitates formation of an appropriate habit plane and, consequently, self-accommodation groups of martensite crystals (having the same crystal structure but different orientations) with highly mobile interfaces.

4. Relatively narrow martensitic transformation hysteresis.

Keeping in mind development of SMA through devitrification, the BMG SMA precursor should satisfy also general requirements to BMG:

1. Precision composition around «deep» eutectic ± (0.5 – 1.0) at.%.

2. Empirical rules mentioned above [1, 12]: 1) $N > 3$; 2) $\Delta R > 12\%$; 3) $\Delta H < 0$.

3. Minimum critical solute concentration [20, 21]: $C_{min} = 0.1/|(R_B/R_A)^3 - 1|$;

4. Atomic size distribution plot (ASDP) [26, 27] – difference for ordinary amorphous and bulk metallic glasses.

5. Crystallization path: Better polymorphous crystallization Am $\rightarrow \beta^* \rightarrow \alpha + \beta$(or $\beta+\gamma$), nevertheless, primary crystallization is also appropriate Am $\rightarrow$ Am*+$\alpha^{**} \rightarrow \alpha + \beta$ [28].

6. Glass forming ability indicators (GFA):

$$T_{RG} = \frac{T_G}{T_L} \geqslant \frac{2}{3} \qquad [35]$$

$$\gamma = \frac{T_X}{T_G} + T_L \geqslant 0.4 \qquad [13, 34]$$

$$\Delta T = T_X - T_G > 60\ K \qquad [1, 3, 12, 13, 16, 34].$$

Conventional strategy for multicomponent pseudobinary BMG_ SMA development starts with binary through ternary, quaternary, quinary till higher-order model $(Ti,Zr,Hf)_A(Co,Ni,Cu,Pd)_B$ alloy systems. Nevertheless, when selecting chemical composition, some restriction can arise due to specific features of a binary alloy diagrams, see summary in Table 1. Indeed, B2 phase is not available for binary TiCu (B11), ZrNi (CrB) and HfNi (CrB), moreover, Hf did not form AB-type intermetallic compound with Cu, situation with HfPd is not clear due to lack of data. The situation with limited number of B2-type intermetallic compounds is well-known phenomena for ternary Ti-Zr-Ni, Ti-Hf-Ni and Ti-Ni-Cu alloys. So, based on experimental data, the pseudobinary TiNi-ZrNi and TiNi-HfNi cross-sections were reviewed, and the limitation in B2-phase composition range up to 25 at.% of Zr and Hf, respectively, were found [29-31] (both ZrNi and HfNi have CrB-type orthorhombic structure). For TiNi-TiCu quasibinary cross-section, the B2-phase homogeneity range reaches up to 32 at.%Cu, TiCu has B11 tetragonal structure [32].

TABLE 1

Specific features of the binary AB microstructure in (Ti,Zr,Hf)(Co,Ni,Cu,Pd) systems

	Co	Ni	Cu	Pd
Ti	B2(CsCl) ↔ B19'	B2(CsCl) ↔ B19'	B11	B2(CsCl) ↔ B19'
Zr	B2(CsCl) ↔ B19'	CrB	B2(CsCl) ↔ B19'	B2(CsCl) ↔ B19'
Hf	B2(CsCl)	CrB	No AB_ IMC	B2(CsCl) ↔ B19'

Effective elemental combinations in quasibinary AB_1-AB_2 and A_1B-A_2B cross--sections are summarised in Table 2 for $(Ti+Zr=Hf)_A(Co+Ni+Cu+Pd)_B$ system. Thirteen appropriate ternary elemental combinations in pseudobinary system reduce to three quaternary and one quinary alloy combinations.

TABLE 2A

Effective elemental combinations in quasibinary AB_1-AB_2 cross-sections

	System	Counterparts AB1 AB2	B2-range	Max width of AB— homog. range, at.%	Remarks	A_F, K
A1	TiCo – TiNi	B2 B2	0.....50	~ 7 ↔~ 7		37 → 400
R1	TiCo – TiCu	B2 B11	0...~ 30	~ 7 ↔~ 7		
A2	TiCo – TiPd	B2 B2	0.....50	~ 7 ↔~ 6		37 → 820
R2	TiNi – TiCu	B2 B11	0...~ 30	~ 7 ↔~ 7		
A3	TiNi – TiPd	B2 B2	0.....50	~ 7 ↔~ 6		400 → 820
R3	TiCu – TiPd	B11 B2	~ 25...50	~ 7 ↔~ 6		
R4	ZrCo – ZrNi	B2 CrB	0...~ 25	~ 1 ↔~ 1	Line	
A4	ZrCo – ZrCu	B2 B2	0.....50	~ 1 ↔~ 1	Line	300 → 600
A5	ZrCo – ZrPd	B2 B2	0.....50	~ 1 ↔~ 1	Line	300 → 400
R5	ZrNi – ZrCu	CrB B2	~ 25...50	~ 1 ↔~ 1	Line	
R6	ZrNi – ZrPd	CrB B2	~ 25...50	~ 1 ↔~ 1	Line	
A6	ZrCu – ZrPd	B2 B2	0.....50	~ 1 ↔~ 1	Line	600 → 820
R7	HfCo – HfNi	B2 CrB	0...~ 25	~ 2 ↔~ 1		
R8	HfCo – HfCu	B2 no IMC	0...~ 25?	~ 2 ↔ No	?	
A7	HfCo – HfPd	B2 B2	?0.....50	~ 2 ↔~ 1	?	?
F1	HfNi – HfCu	CrB no IMC	No	~ 1 ↔ No	?	
R9	HfNi – HfPd	CrB B2?	? ~ 25...50	~ 1 ↔~ 1	Line	
R10	HfCu – HfPd	No IMC B2?	? ~ 25...50	No ↔ ~ 1	?	

To "precise composition for SMA": The homogeneity range of B2-type structure in Ti-based alloys is relatively large (up to 6_ 7 at.% around AB-composition). In Zr- and Hf- based alloys, the stronger interatomic interaction results in narrowing of the AB-type compound composition window (homogeneity range becomes narrower

TABLE 2B

Effective elemental combinations in quasibinary A_1B-A_2B cross-sections

	System	Counterparts A1B A2B	B2-range	Max width of AB— homog. range, at.%	Remarks	A_F, K
A8	TiCo – ZrCo	B2 B2	0.....50	~ 7 ↔~ 1		37 → 400
R11	TiNi – ZrNi	B2 CrB	0...~ 25	~ 7 ↔~ 1		
R12	TiCu – ZrCu	B11 B2	~ 25...50	~ 7 ↔~ 1		
A9	TiPd – ZrPd	B2 B2	0.....50	~ 6 ↔~ 1		37 → 400
A10	TiCo – HfCo	B2 B2	0.....50	~ 7 ↔~ 2		37 → ??
R13	TiNi – HfNi	B2 CrB	0...~ 25	~ 7 ↔~ 1		
F2	TiCu – HfCu	B11 No IMC	No	~ 7 ↔ No		
A11	TiPd – HfPd	B2 B2?	0.....50	~ 6 ↔~ 1		820 → ??
A12	ZrCo – HfCo	B2 B2	0.....50	~ 1 ↔~ 2	Near Line	300 → ??
F3	ZrNi – HfNi	CrB CrB	No	~ 1 ↔ No	Line	
R14	ZrCu – HfCu	B2 No IMC	0... ~ 50	~ 1 ↔ No	Line	
A13	ZrPd – HfPd	B2 B2?	0.....50	~ 1 ↔~ 1	Line	820 → ??

and closer to lines approximately 1 at.% width near AB- composition). Deviation in chemical composition from ratio A:B=50:50 up to ~1 at.% in binary Ti-Ni and ternary Ti-Ni-Hf alloys (up to 6 vol.% of A2B-type precipitate) [33] even up to 3 at.% in ternary Ti-Ni- Zr and Ti-Hf-Ni alloys [5] did not change considerably the martensite transformation temperatures, while suppress strongly the shape memory property.

So, taking into account the features mentioned above many multicomponent SMA have been developed [36-42]. The reference binary Ti-Ni SMAs are typical representatives of the transition metal AB-type compounds. In bulk material condition, they undergo the B2-B19' or B2-R-B19' martensite transformations. The main factors influencing the characteristics of the martensite tranformation temperatures and functional properties are the chemical composition and microstructure, i.e. grain sizes, presence and distribution of precipitates, etc.

The introduction of a small quantity of the third and fourth transition metal elements acts additionally on the martensite transformation temperatures, usually shifting them to the lower temperature interval with the rate depending on the type/nature of an individual element. Introduction of a bigger quantity (mostly, above 2-5 at.%) of alloying elements generally results in formation of "a new matter" corresponding to the multicomponent solid solution. In this case, introduction of the beta-phase stabilizers (like Cr, Mn, Fe, Co, Mo, Tc, Ru, Rh, W, Re, Os, Ir) usually results in further decrease of the martensite transformation temperatures or even to full suppression of the martensite transformation. On the contrary, introduction of the elements from the very beginning (V, Zr, Y, Nb, Hf, Ta) or from the end (Cu, Pd, Pt, Au) of each transition metal series often results in the increase of the martensite transformation

temperatures. The degree of the increase to be more higher for elements from the end of each transition metal series than from the beginning.

The reference multicomponent alloys of the A:B type (Ti50Ni50) are formed with "A"=(Ti, Zr, Hf) and "B"=(Co, Ni, Cu, Pd). Substitution of Zr and Hf instead of Ti increases the martensite transformation temperatures. Introduction of Co, Cu and Pd instead of Ni has been chosen according to the golden rules. Some representative compositions with the ratio "A/B" = 45:55, 50:50 and 55:45 are presented in Table 3. Experimental results on XRD, DSC and mechanical testing for representative melt-spun ribbons are shown in Figures 3 and 4. Most rapidly solidified ribbons are fully amorphous (Figure 3 a). For all ribbons a classical behaviour characteristic of amorphous material is observed: a broad region of exothermic relaxation, an endother-

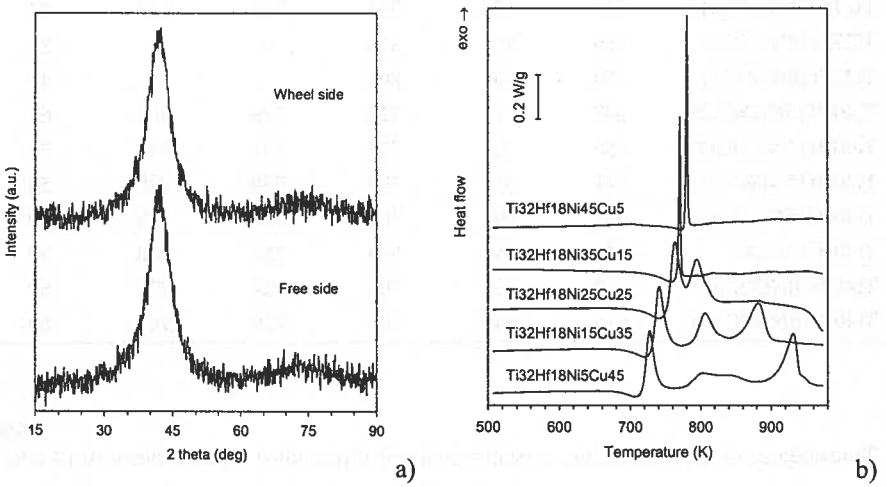

Fig. 3. a. Typical X-ray diffraction spectra of rapidly solidified ribbons (amorphous) b. Typical calorimetry of rapidly solidified ribbons: crystallization of amorphous phase (heating rate 0.17 K/s)

mic glass transition (T_g) and one or several exothermic peaks (T_{x1}, T_{x2}) corresponding to successive transformations from a metastable supercooled liquid state to the equilibrium crystalline intermetallic phases at different temperatures (Figure 3 b). Those temperatures are given in Table 3 together with the supercooled liquid window ΔT. The superplasticity effect near the glass transition temperature is well known phenomena for bulk amorphous alloys [14]. To study the superplasticity effect in TiNi-based ribbons, the"dynamic constant load experiment" was used, namely, deformation behaviour under constant load on heating from room temperature up to crystallisation temperature T_x and above was studied. In Figure 4, typical representatives of the stress-strain (a) and strain-temperature (b) curves obtained in the dynamic constant load experiment are presented. After crystallisation at appropriate temperatures, the superelastic deformation property (Figure 4 c) caused by martensitic transformation is detected up to 2–3% of recoverable deformation.

TABLE 3A

Temperatures of glass transition, crystallization and supercooled liquid window (0.17 K/s)

Alloy	T_g (K)	T_{x1} (K)	T_{p1} (K)	T_{x2} (K)	T_{p2} (K)	ΔT (K)
Ti32Hf18Ni45Cu5	738	778	780	–	–	40
Ti32Hf18Ni35Cu15	722	766	769	–	–	45
Ti32Hf18Ni25Cu25	705	752	763	782	795	47
Ti32Hf18Ni15Cu35	684	73	74	790	806	47
Ti32Hf18Ni5Cu45	673	718	727	780	803	44
Ti25Zr25Ni25Hf25	669	718	730	767	788	50
Ti27Hf18Ni50Cu5		791	795	–	–	
Ti27Hf18Ni40Cu15	747	779	782	815	827	33
Ti27Zr18Ni50Cu5	789	816	820	–	–	27
Ti27Zr18Ni40Cu1	759	799	802	–	–	40
Ti40Hf15Ni18Cu27	648	712	728	779	801	64
Ti40Hf15Ni13Cu32	656	70	721	771	793	53
Ti40Hf15Ni8Cu37	641	695	707	759	780	55
Ti40Hf15Ni3Cu42	642	691	702	756	773	49
Ti40Hf15Cu45	640	687	699	753	768	47
Ti45Zr10Ni20Cu25	629	690	706	754	777	62
Ti40Zr15Ni20Cu25	615	685	705	759	781	69

TABLE 3B

Temperatures of glass transition, crystallization and supercooled liquid window (0.17 K/s)

Alloy	$A:B$	T_g (K)	T_x (K)	T_p (K)	ΔT (K)
Ti48Zr2Ni23Cu23Pd2Al2	50:50	702	726	736	24
Ti47Zr3Ni23Cu20Pd2Al5	50:50	710	756	763	46
Ti45Zr5Ni23Cu20Pd2Ag1Al4	50:50	708	753	760	45
Ti47Hf3Ni23Cu24.5Pd2Ag0.5	50:50	706	747	752	41
Ti47Nb3Ni23Cu22Pd2Al3	50:50	704	742	751	38
Ti48Zr2Ni20Cu25Co5	50:50	697	730	735	33
Ti40Zr10Ni20Cu25Co5	50:50	709	748	753	39
Ti47Hf8Ni18Cu24.5Pd2Ag0.5	55:45	661	707	720	46
Ti48Zr7Ni18Cu23Pd2Ag2	55:45	660	706	718	46
Ti48Zr7Ni18Cu25Co2	55:45	690	723	731	33
Ti48Zr7Ni18Cu22Co5	55:45	684	719	730	35
Ti40Zr15Ni18Cu25.7Pd1Ag0.3	55:45	684	723	733	39
Ti40Hf15Ni18Cu25.7Pd1Ag0.3	55:45	671	714	730	43
Ti40Hf15Ni11Cu32Co2	55:45	658	701	715	43

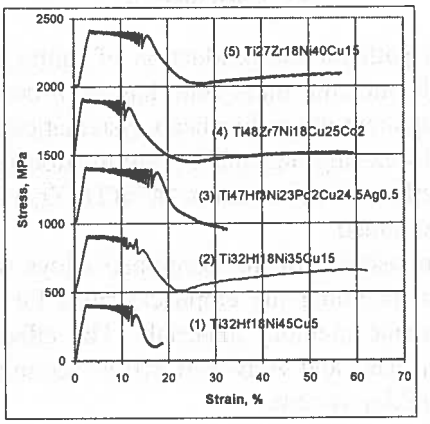

a)

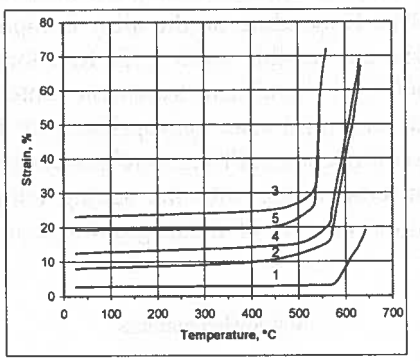

b)

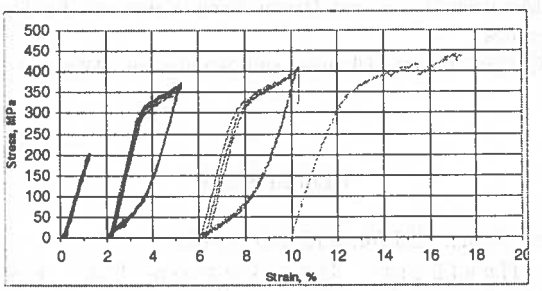

c)

Fig. 4. Typical stress-strain (a) and strain-temperature (b) curves in the dynamic constantmload experiment; (c) superelastic deformation property caused by martensitic transformation in Ti32Hf18Ni35Cu15 ribbon after crystallisation

5. Conclusions

1. The technological path for the production of multicomponent shape memory alloys initially in the bulk metallic glass state has been developed. A general series of the AB-type multicomponent alloys has been systematically produced by means of induction melting prior to casting and rapid solidification (planar flow casting technique). The alloys with effective constituents "A"=(Ti, Zr, Hf) and "B"=(Ni, Cu, Co, Pd, Ag, Al) have been examined.

2. The chemical compositions of the developed alloys were optimised according to sets of selection rules including the empirical rules for bulk amorphous material and requirements to shape memory materials. The effective elemental combinations in quasibinary AB_1-AB_2 and A_1B-A_2B cross- sections have been defined for $(Ti+Zr+Hf)_A(Co+Ni+Cu+Pd)_B$ system.

3. Most of developed amorphous alloys can be easily crystallised into b.c.c. phase in a simple crystallisation step or during subsequent heat treatments at temperatures varied from 400°C to 900°C. Depending on the alloy composition and microstructure condition, they may undergo a reversible martensitic transformation in the temperature range from –150°C to +300°C. Several heat treatment routes have been performed in order to find the optimised structural state appropriate both for the reversible martensitic transformation and good mechanical/functional properties. Smooth increase of the martensitic transformation temperature with the ageing temperature has been found, which demonstrate the important role of mean grain size in the martensitic transformation onset position.

Acknowledgements

The authors are grateful to all the friends and colleagues for collaboration in BMG/SMA research: Richard Portier (Paris), Patrick Ochin (Paris, Vitry), Eduard Cesari (Palma de Mallorca), Jan Van Humbeeck (Leuven), Henryk Morawiec (Katowice), Danuta Stróż (Katowice), Jan Dutkiewicz (Krakow), Yury Koval (Kiev), and their groups.
Sponsorship of PICS, ECONET (France-Ukraine) and Nanosystem (Ukraine) projects is gratefully acknowledged.

REFERENCES

[1] A. Inoue, Mater. Trans. JIM **36**, 866-875 (1995).
[2] C.T. Liu, L. Heatherly, D.S. Easton, C.A. Carmmichael, J.H. Schneibel, C.Y. Chen, J.L. Wright, M.H. Yoo, J.A. Horton, A. Inoue, Metall. Mater. Trans. **29 A**, 1811-1820 (1998).
[3] H.A. Bruck, T. Christman, A.J. Rosakis, W.L. Johnson, Scripta Metall. Mater. **30**, 429-434 (1994).
[4] T.W. Duerig, K.N. Melton, D. Stoekel, C.M. Wayman, "Engineering Aspects of Shape Memory Alloys", Butterworth and Heinemann, 1990.
[5] G.S. Firstov, J. Van Humbeeck, Y.N. Koval, Mater. Sci. Eng. **A378**, 2-10 (2004).

[6] N.M. Matveeva, V.N. Khachin, V.P. Sivokha, "Stabil'nye i Metastabil'nye Fazovye Ravnovesiya v Metallicheskikh Sistemakh", Moskva, Nauka Publ., 1985, p. 25 (in Russian).
[7] K. Enami, Y. Nakagawa, Proc. Int. Conf. ICOMAT-92 (20-24 July 1992, Monterey, USA), Eds. C.M. Wayman, J. Perkins, pp. 521-526. Appl. Phys. Lett
[8] T. Biggs, M.J. Witcomb, L.A. Cornish, Mater. Sci. Eng. **A273-275**, 204-207 (1999).
[9] T.R. Finlayson, G.L. Kelly, T.F. Smith, Mater. Sci. Eng. **A273-275** (1999) 366-369.
[10] T. Zhang, A. Inoue, T. Masumoto, Mater. Sci. Eng. **A181-182**, 1423-1426 (1994).
[11] G. Wilde, G.P. Görler, R. Willnecker, H.J. Fecht, J. Appl. Phys. **87**, 1141-1152 (2000).
[12] A. Inoue, Acta Mater. **48**, 279-306 (2000).
[13] Z.P. Lu, C.T. Liu, Acta Mater. **50**, 3501-3512 (2002).
[14] Y. Kawamura, T. Shibata, A. Inoue, T. Masumoto, Appl. Phys. Lett. **69**, 1208- 1210 (1996).
[15] H. Kato, Y. Kawamura, A. Inoue, H.S. Chen, **73**, 3665-3667 (1998).
[16] T.A. Waniuk, J. Schroers, W.L. Johnson, Appl. Phys. Lett. **78**, 1213-1215 (2001).
[17] L.Q. Xing, P. Ochin, M. Harmelin, F. Faudot, J. Bigot, J.P. Chevalier, Mater. Sci. Eng. **A 220**, 155-161 (1996).
[18] L.Q. Xing, P. Ochin, J. Mater. Sci. Lett. **16**, 1277-1280 (1997).
[19] K.B. Kim, P.J. Warren, B. Cantor, Mater. Sci. Eng. **A375–377**, 317-321 (2004).
[20] T. Egami, Y. Waseda, J. Non-Cryst. Solids **64**, 113-134 (1984).
[21] T. Egami, Mater. Sci. Eng. **A 226-228**, 261-267 (1997).
[22] J.H. He, E. Ma, Phys. Rev. **B64**, 144206 (2001).
[23] A.A. Turchanin, I.A. Tomilin, M.A. Turchanin, I.V. Belokonenko, P.G. Agraval, J. Non-Cryst. Solids **250-252**, 582-585 (1999).
[24] P.G. Agraval, "Temperature-Concentration Dependence of Thermodynamic Properties of Liquid Alloys of Cobalt, Nickel and Copper with Tutanium, Zirconium and Hafnium", Thesis for a candidate's degree in chemistry, I.N. Frantsevich Institute for Problems of Materials Science, NAS Ukraine, Kiev, 2004 (in Ukrainian).
[25] J.C. Foley, D.R. Allen, J.H. Perepezko, Mater. Sci. Eng. **A226-228**, 569-573 (1997).
[26] D.B. Miracle, O.N. Senkov, Mater. Sci. Eng. **A347**, 50-58 (2003).
[27] D.B. Miracle, O.N. Senkov, W.S. Sanders, K.L. Kendig, Mater. Sci. Eng. **A375–377**, 150–156 (2004).
[28] K. Hono, D. H. Ping, Materials Characterization **44**, 203-217 (2000).
[29] V.N. Eremenko, E.L. Semenova, L.A. Tretyachenko, Z.G. Domatyrko, Izv. Vuzov Tsvetn. Metall., No. 6, 85-88 (1990) (in Russian).
[30] J.H. Mulder, Ph.D. Thesis, University of Twente, Enschede, Netherlands, 1995.
[31] K.P. Gupta, J. Phase Equilibria **20**, 441-448 (1999).
[32] F.J.J. Van Loo, G.F. Bastin, A.J.H. Leenen, J. Less Common Metals **57**, 111-121 (1978).
[33] P.E. Thoma, J.J. Boehm, Mater. Sci. Eng. **A273–275**, 385-389 (1999).

[34] Z.P. Lu, Y. Li, S.C. Ng, J. Non-Cryst. Solids **270**, 103-114 (2000).
[35] D. Turnbull, Contemp. Phys. **10**, 473 (1969).
[36] V. Kolomytsev, M. Babanly, R. Musienko, A. Sezonenko, P. Ochin, A. Dezellus, P. Plaindoux, R. Portier, P. Vermaut, Metallofiz. Noveishie Tekhnol. (special issue) **23**, 111-123 (2001).
[37] V. Kolomytsev, M. Babanly, R. Musienko, A. Sezonenko, P. Ochin, A. Dezellus, P. Plaindoux, R. Portier, P. Vermaut, Metallofiz. Noveishie Tekhnol. (special issue) bf23, 124-136 (2001).
[38] P. Ochin, A. Dezellus, P. Plaindoux, F. Dalle, M. Larnicol, P. Vermaut, R. Portier, A. Pasko, V. Kolomytsev, J. Pons, E. Cesari, L. Lityńska, J. Morgiel, J. Dutkiewics, T. Goryczka, D. Stróż, H. Morawiec, Metallofiz. Noveishie Tekhnol. (special issue) **23** (2001) 83-92.
[39] V. Kolomytsev, M. Babanly, R. Musienko, A. Sezonenko, P. Ochin, A. Dezellus, P. Plaindoux, R. Portier, P. Vermaut, J. Phys. IV France **11**, Pr8 457-462 (2001).
[40] V. Kolomytsev, M. Babanly, R. Musienko, A. Sezonenko, P. Ochin, A. Dezellus, P. Plaindoux, F. Dalle, P. Vermaut, R. Portier, J. Phys. IV France **11**, Pr8 475-480 (2001).
[41] A. Pasko, V. Kolomytsev, M. Babanly, A. Sezonenko, P. Ochin, R. Portier, P. Vermaut, J. Phys. IV France **112**, 1055-1058 (2003).
[42] A. Sezonenko, V. Kolomytsev, M. Babanly, A. Pasko, P. Ochin, R. Portier, P. Vermaut, J. Phys. IV France **112**, 889-892 (2003).

Received: 3 November 2004.

A R C H I V E S O F M E T A L L U R G Y A N D M A T E R I A L S
Volume 49 2004 Issue 4

J. MORGIEL*, J. DUTKIEWICZ*

IN-SITU OBSERVATIONS OF REVERSIBLE MARTENSITIC TRANSFORMATIONS IN SHAPE MEMORY ALLOYS

OBSERWACJE IN-SITU ODWRACALNYCH PRZEMIAN MARTENZYTYCZNYCH W STOPACH WYKAZUJĄCYCH EFEKT PAMIĘCI KSZTAŁTU

The conditions of performing *in-situ* TEM and OM straining and *in-situ* TEM heating experiments with CuAlMn and TiNiCu shape memory alloys were discussed. It was shown that correlating the bulk straining tests with in-situ straining experiments allow to determine the strain temperature phase diagrams for CuAlMn martensitic phases. The *in-situ* heating experiments helped to explain the influence of different elements of microstructure, like grain size, precipitates or dislocations in TiNiCu alloy on nucleation and grow of martensite.
Keywords: *in-situ* TEM, *in-situ* optical microscopy, pseudo-elasticity, shape memory

W pracy przedyskutowano warunki prowadzenia eksperymentów *in-situ* odkształcania oraz *in-situ* grzania stopów wykazujących efekt pamięci kształtu z wykorzystaniem transmisyjnego mikroskopu elektronowego oraz mikroskopu optycznego. Wykazano, że porównanie serii pomiarów odkształcenia próbek masywnych z obserwacjami zmian mikrostruktury w czasie odkształcenia cienkich folii z wykorzystaniem mikroskopu transmisyjnego umożliwia tworzenie diagramów stabilności faz pseudo-sprężystego stopu CuAlMn w funkcji temperatura – naprężenie. Eksperymenty *in-situ* grzania cienkich folii z taśm TiCuNi pozwoliły nakreślenie wpływu poszczególnych elementów mikrostruktury jak wielkości ziarna, gęstości wydzieleń, czy dyslokacji na zarodkowanie i wzrost przemiany martenzytycznej.

1. Introduction

The shape memory (SM) effect observed in some alloys results from the possibility of reverting of the coordinated movement of atoms undergoing martensitic transformation called in the past also "military transformation" [1, 2]. Therefore, the changes of shape are totally dependent on martensitic transformation temperature range being sensitive to stress level, alloy composition and microstructure [3]. Additionally, in some

* INSTITUTE OF METALLURGY AND MATERIALS SCIENCES, POLISH ACADEMY OF SCIENCES, 25 REYMONTA ST., 30-059 KRAKÓW, POLAND

alloys not only the cooling of parent phase might results in formation of a sequence of martensite phases [4], but sometime martensite to martensite either on cooling [5, 6] or straining [7] are also possible modifying the final shape memory of the investigated material.

As most applications of SME require good knowledge of the start, finish and extent of reproducible shape change, therefore understanding of the influence of different microstructure features on martensitic transformation is of primary importance. The heating, cooling or straining experiments performed in the optical microscope (OM) or even more in transmission electron microscope (TEM) i.e. *in-situ* OM or TEM [8] seem to be an obvious choice for tasks like that. However, the events taking place in microstructure during *in-situ* TEM experiments may differ from that taking place in bulk material due to the so called thin foil effects [9] including either stress relaxation or accumulation caused by extreme thinness of the thin foil. Therefore, they routinely should be checked with the ex-situ experiments like with the furnace treated bulk samples. Because, in case of reversible martensitic transformation no such ex-situ proof is possible, so support from other experiments basing on detail either "macro" straining or differential scanning callorymetry (DSC) has to be produced. Coupling of the *in-situ* TEM with *in-situ* OM might also help better explain analyzed relations. Another problem during *in-situ* TEM experiments is a lack of precision of temperature or strain level determination. Special calibration procedures using samples with well know transformation temperature help only to some extent, as every thin foil is slightly different and even on the same thin foil different places of interest are located closer or farther from holder furnace and in effect will remain at different temperature. The calibration of strain holder is even more problematic and usually only the elongation is used. However, the uncertainties of exact temperature or strain can be accepted as long as one rely rather on the sequence of events than on their correlation with exact temperature or strain level.

Taking into account the mentioned above limitations the present paper reviews the possibilities of application of *in-situ* straining and heating OM, SEM and TEM experiments for analysis of reversible martensitic transformation in CuAlMn and TiNiCu shape memory materials.

2. *In-situ* straining experiments with CuMnAl SM alloys

The Cu-23 at% Al-7 at% Mn and Cu-20 at% Al-10 at% Mn alloys undergo martensitic transformation on cooling from β_1 parent to γ_1' (2H type) phases. This phase transformation results in change of electrical resistance (Fig. 1), which helped to determined martensitic transformation characteristic temperatures (Table). The defining characteristic temperatures through tangent lines, allows to use them as characteristic temperatures for shape memory effect, but "cutting of" the tails of sigmoid curves left place for small amount of martensite even above of the M_f temperature, what might show later in *in-situ* experiments.

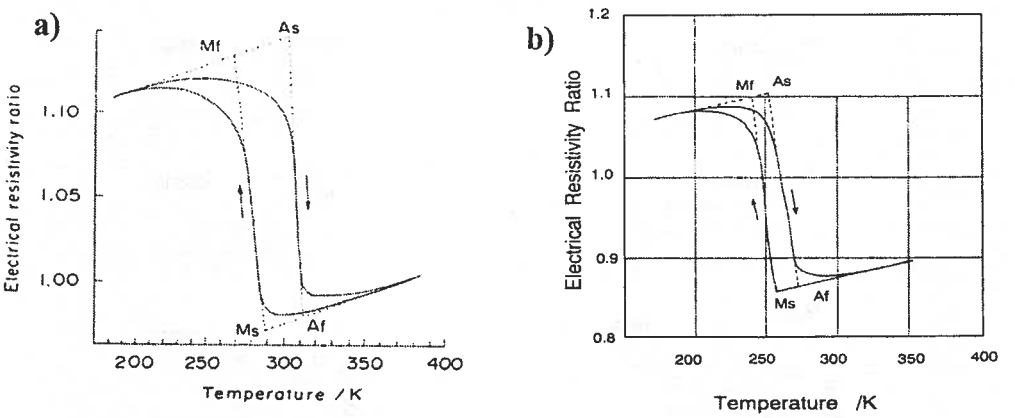

Fig. 1. Change of electrical resistivity vs. temperature of Cu-23Al-7Mn (a) and Cu-20Al- 10Mn (b) alloys allowing to determine the characteristic martensitic temperatures [10, 11]

TABLE

Martensitic transformation characteristic temperatures of CuAlMn alloys

Alloy	M_s[°C]	M_f[°C]	A_s[°C]	A_f[°C]
Cu-23Al-7Mn	287	268	305	313
Cu-20Al-10Mn	256	241	254	268

The stress-strain curves for CuMnAl alloys obtained below M_f temperature show characteristic for SM alloys deformation on unloading, recovered after heating above A_f temperature (Fig. 2a, 3a). However, above A_f the stress-strain curves for these alloys show strong stress relief jumps (Fig. 2b,c, 3b,c), while similar curves for most widely investigated CuAlNi alloys show relatively smooth response to stress in that range [10]. Relying on R.T. X-ray diffractometry one may assume formation of different martensite phases at different strain levels in a way marked for curves in Fig. 2. However, assigning one part of curve to $\beta_1 \rightarrow \beta_1'$ and another to $\beta_1 \rightarrow \gamma_1'$ transformations remain at that stage only a hypothesis.

The *in-situ* OM straining experiments add some support to above consideration, i.e. possibilities of formation of two different martensite phases in lower temperatures (just below A_f temperature) and only one at higher temperatures (above A_f) as in former case different variants form, while in the latter only one set of plates develop (Fig. 4). Additionally, in case of straining at lower temperature a presence of large plates were noted, while during the other experiment the transformation progressed only by formation of fine parallel plates. The dark arrow present on micrographs is aimed at reference point chosen for each experiment to help to locate of movement of glissile boundaries of martensite plates. The strain-stress characteristics showed slightly stronger serration in "plateau" area, than the one taken for bulk samples (Fig. 2, 3). The nucleation of larger plate (Fig. 4-1) or simultaneous nucleation of bunch of thinner

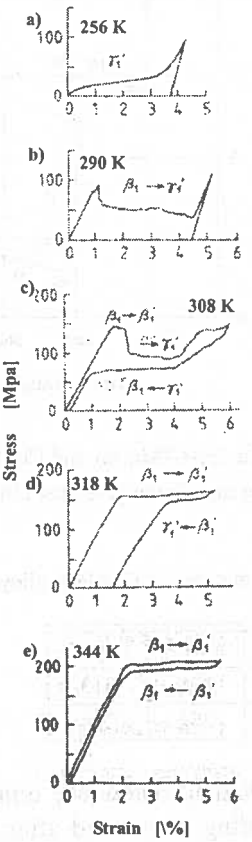

Fig. 2. Stress-strain curves of Cu-23Al-7Mn single crystal at [100]β orientation at various temperatures [10]

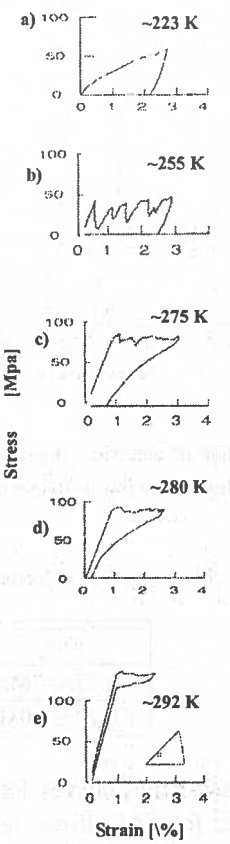

Fig. 3. Stress-strain curves of Cu-20Al-10Mn single crystal (orientation marked in triangle) at various temperatures [12]

parallel plates (Fig. 4-A) resulted in characteristic stress relief notch on strain-stress curves. The thin foils stressed at the lower temperature just behind the yield strain show, however much stronger stress jump marked by σ_U (upper) and σ_L(lower), than in other cases. It was again assumed that this situation might be due to the fact that significantly lower stress is required to form 2H martensite, than 18R, as observed in cases of other SM alloys like CuAlNi or CuAlFe [11, 12]. Continuing these experiments at different temperatures allowed to plot boundaries of stability of different martensitic phases in stress-temperature field (Fig. 5) for monocrystal stressed along the direction as marked in the same figure.

The *in-situ* straining in TEM might reproduce the standard stress-strain test only to some extent as the observations must be performed using thin foil, which are not only extremely thin but usually contain multiple cracks acting as notches on bulk samples.

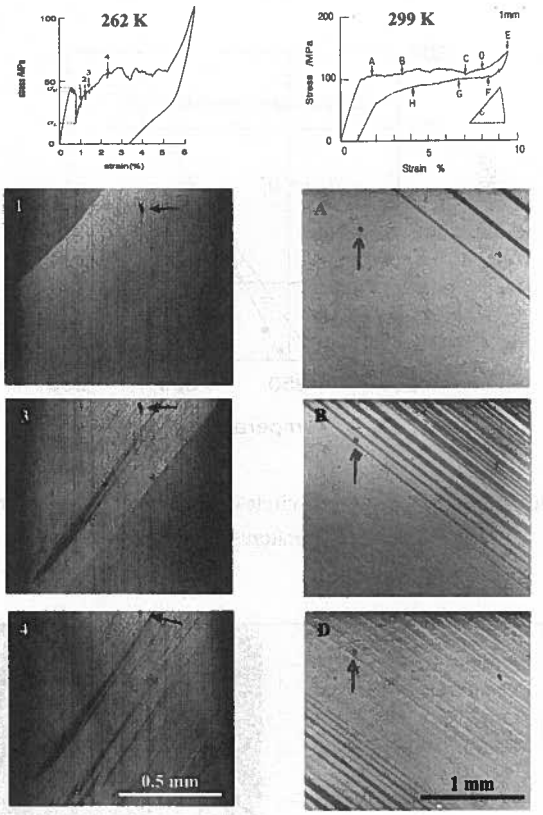

Fig. 4. *In-situ* OM stress-strain curves of Cu-20Al-10Mn single crystal with series of corresponding micrographs taken at increasing strain for experiments performed at 262 K and 299 K marked by numbers and letters respectively [11]

The application of High Voltage TEM like JEOL 1MV instrument giving access to slightly thicker areas is improving this situation only slightly. Even in such adverse situation, the straining of thin foil cut from Cu-20Al-10Mn monocrystal in [001]β_1 orientation allowed follow event from strain induced martensite transformation (Fig. 6).

The first micrograph reproduced from video recording taken just before the yield stress show already both presence of parent phase (lighter contrast area with curved extinction contours) as well as presence of large martensite plate (dark with characteristic parallel stacking faults). Presence of martensite in this alloy at that temperature might be only explain by local stress accumulation in thin foil. However, continuation of straining of this thin foil showed nucleation of a series of fine parallel needles arrange parallel to tensile axis. The presence of permanent deformation after stress relief in

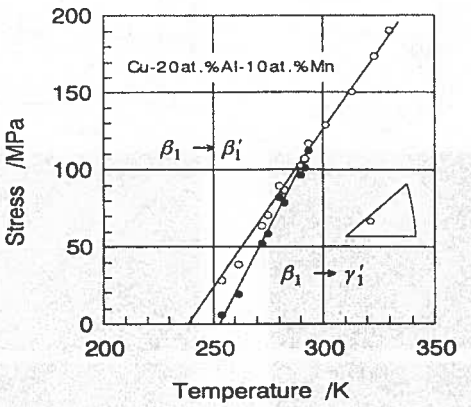

Fig. 5. Stresses required to induce $\beta 1'$ (open circles – σU) and $\gamma 1'$ (full circles – σL) at different temperatures [11]

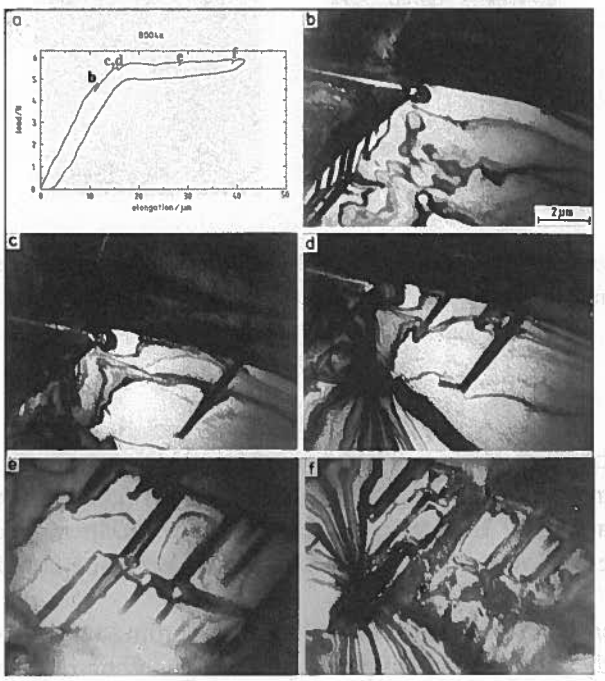

Fig. 6. Load-elongation curve from *in-situ* HVEM deformation in $\langle 100 \rangle \beta_1$ direction with corresponding electron micrographs taken at points marked by letters [11]

this pseudo-elastic at R.T. alloy is most probably due to inhomogeneous deformation in thin areas where plastic deformation of martensite might occur.

The electron diffractions, helped to prove that in the investigated alloy at first the parent β_1 transforms nearly exclusively into of γ_1' (2H) martensite forming both thick and fine plates (Fig. 7). At larger strains the transformation of parent β_1 to β_1' (18R) martensite proceeds most often through formation of parallel plates (Fig. 8).

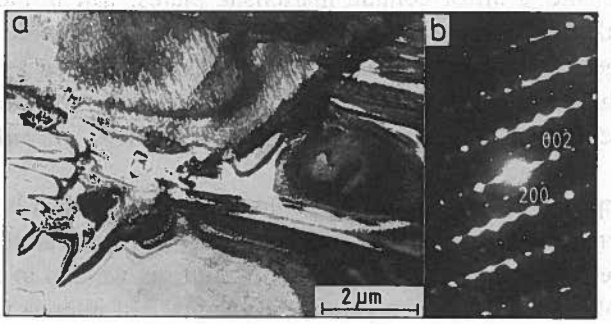

Fig. 7. Transmission electron micrographs presenting formation of martensite plates in Cu- 20Al-10Mn alloy at R.T. at initial stage of loading (a) and corresponding diffraction pattern (b) [12]

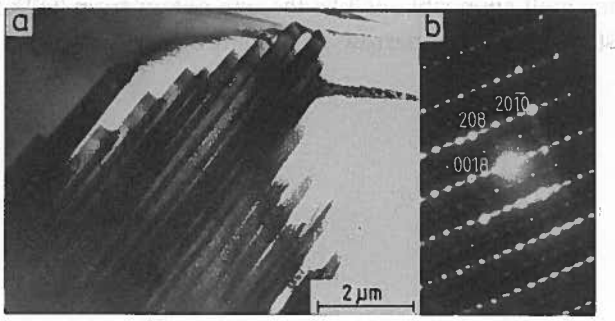

Fig. 8. Transmission electron micrographs presenting formation of martensite plates in Cu- 20Al-10Mn alloy at R.T. at final stage of loading (a) and corresponding diffraction pattern (b) [12]

The following crystallographic relationship between the parent and martensitic phases were observed $[001]\beta_1 \parallel [010]\gamma_1'$, β_1' and $[110]\beta_1 \parallel [001]\gamma_1'$, β_1'. At places of high stress concentration like those near cracks, a very high random stacking fault density was observed making identification of stacking structure of martensite impossible.

3. *In-situ* heating experiments with TiNiCu SM alloy

The simplest *in-situ* temperature controlled martensite transformation observations using transmission electron microscopy can be performed relying just on the small heating effect of the electron beam necessary to retransform martensitic plates to "austenitic" phase. Such experiments require an alloy for which the end of martenite transformation M_f is at or very close to R.T. Even than, some thin foils might either lack martensite at all or contain martensite plates, which due to specific stress concentration will not revert to parent phase within the accessible with this method temperature range. However, observations like the one published by Saburi and Neno [8], who using this technique were able to pinpoint martensite nucleation sites as well as crossing of the martensite plates through grain boundaries, proved it a quite capable technique.

The other approach relies on heating of thin foil using special holders having built in resistance "furnace", which allows to observe phase transformation up to 1000°C. As the thermocouple registering the nominal temperature is welded to the top of the furnace at the side of the holder the temperature at the place of interest will differ the more the higher the sample will be heated. The developed gradient of temperature depend not only on distance between thermocouple and place of interest (usually ~1,5 mm), but also on heat conductivity of investigated alloy, thin foil "geometry" and thin foil contact area with furnace sides. It is impossible to estimate effect of all mentioned above parameters, but rough calibration of "real" temperature with material of well now structure changes at sharply define temperature is still useful. One possibility present amorphous melt spun ribbons like the one obtain from Ti25Zr20Ni27.5Cu27.5 alloy, which crystallizes at very narrow temperature range (Fig. 9).

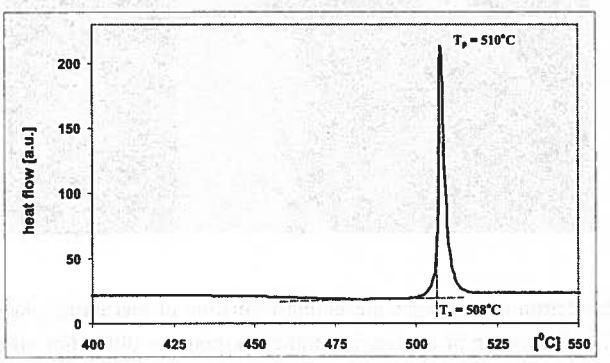

Fig. 9. Thermal effects registered during heating in DSC at 20°C/min of an amorphous ribbon obtained from Ti25Zr20Ni27.5Cu27.5 alloy [13]

Similar, i.e. at approximately the same heating rate treatment of the thin foil prepared from the amorphous ribbon also started to show changes in microstructure at above 500°C. However, fine homogenously nucleated crystallites – which formed as

first – turned out to be connected with some surface effect, like formation of surface oxides, as their density was similar in thinner and thicker areas (Fig. 10a). Next, at

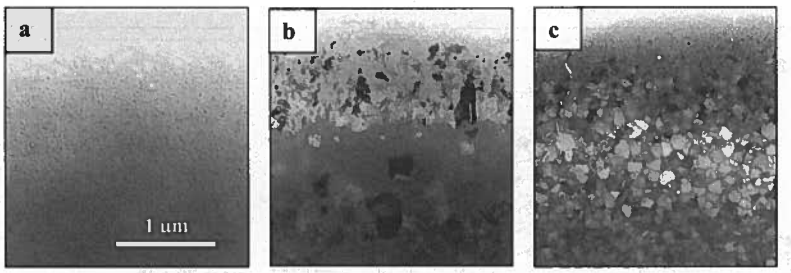

Fig. 10. Transmission micrographs of thin foils obtained from different thin foils from Ti25Zr20Ni27.5Cu27.5 alloy heated *in-situ* up to: a) 500°C, b) 550°C and c) 570°C (the last thin foil was significantly thicker than the two other foils)

around 550°C, coarser crystallites started to grow but only at the thin foil edges, which helped to classify them as artifacts as well (Fig. 10b). Only at around 600°C, the homogenous nucleation of fine crystallites started in the thicker parts of the same foil. One may also notice that in the amorphous zone between two crystalline areas the small surface crystallites like the ones in Fig. 10a are also present. The repeating above experiments with much thicker thin foil and heating it five time faster resulted in crystallization at even slightly higher temperature of 650°C of the whole foil except the edge. The longer times necessary to start crystallization of the edge indicates that it might be controlled by oxide from the microscope chamber.

The above experiments indicate that performing experiments at around 500°C one may expect an ~ 100°C lower temperature of the place of interest at thin foil in respect to nominal temperature. Additionally, to avoid surface effects connected with either stress accumulation or surface oxidation one should choose foils as thick as possible, i.e. at the transparency limit. In that case the diffraction contrast will be sacrificed to large extent but the observed events have a good chance to be close to those having place in bulk material.

Alloying of NiTi with copper allows obtaining material with larger shape memory recoverable strains in narrower temperature range at a penalty of increasing brittleness. This situation in natural way stimulated interest in non-conventional alloy preparation techniques like mechanical synthesis or melt spinning. The strong decrease of melting temperature with copper addition favored melt spinning, but easily obtained ribbons turned out amorphous. The proper heat treatment helped to transformed them into β phase but subsequent thermal cycling within the martensitic transformation temperature range showed wider than expected two stage transformation. The question was weather this negative effect resulted from martensite to martensitic transformation or other factors. The heat treatment in DSC showed that the final splitting of transformation peaks starts at the early stages of crystallization (Fig. 11). However, the

question remains weather in some places the martensitic transformation is retarded or just occupied by other martensitic phase which grow at lower temperature.

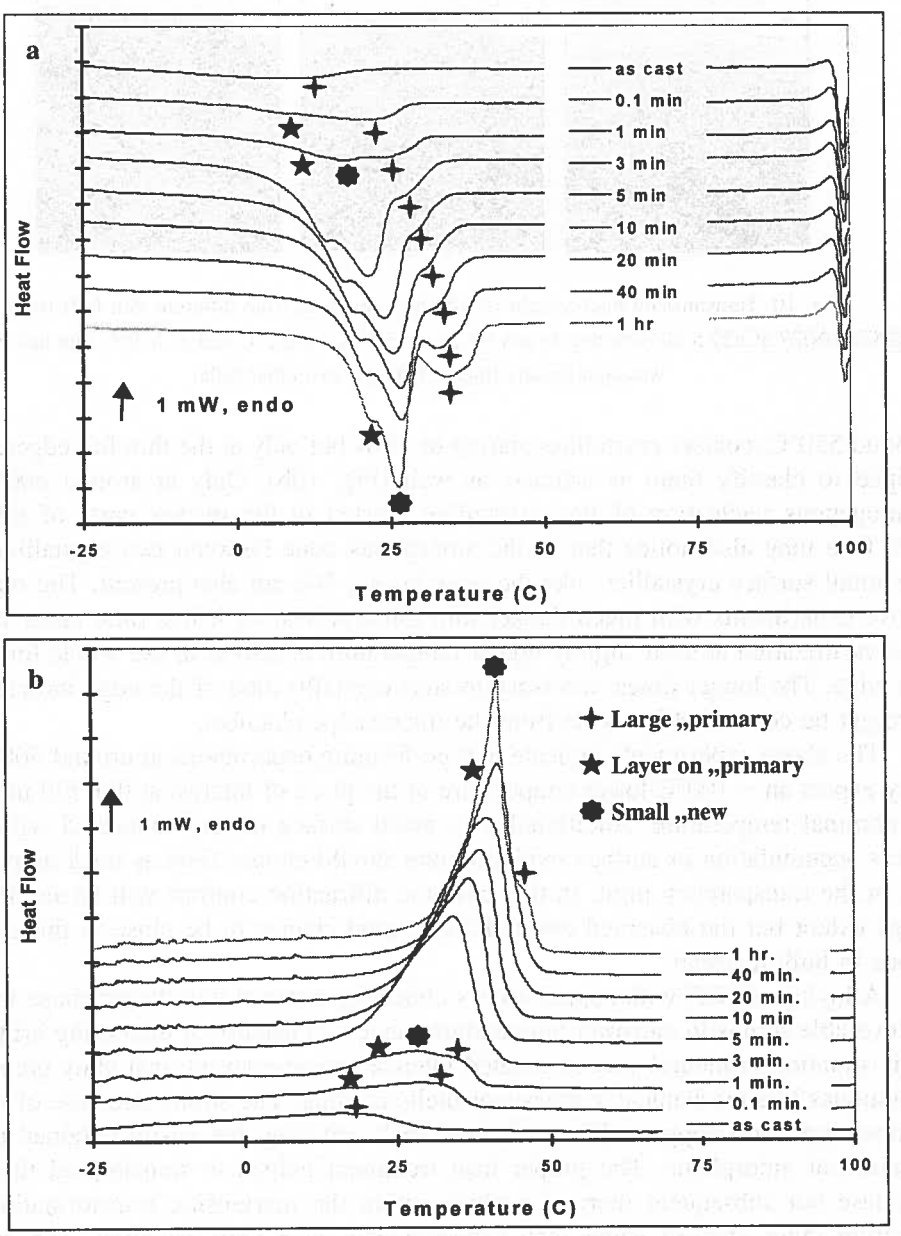

Fig. 11. DSC curves of martensitic (a) and reverse (b) transformation in Ti25Ni25Cu ribbon aged at 450°C for times up to 1 hour [14]

The TEM observations showed that the microstructure of the as cast ribbon is mostly amorphous with large – spherical in plan view – crystallites of B2 phase (Fig. 12a). These crystallites are either single or grouped in small colonies (Fig. 12b). The external boundaries of such colonies are smooth and always bowing out.

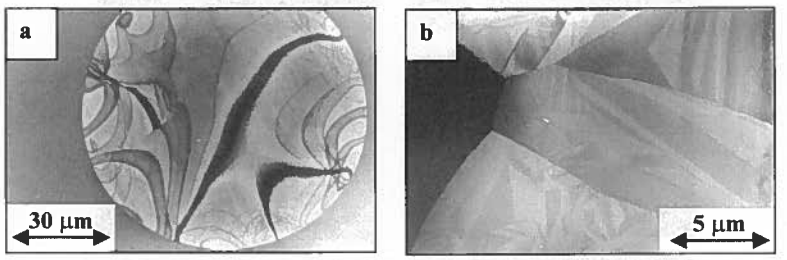

Fig. 12. Microstructure of as spun Ti25Ni25Cu ribbon: a) large single grains surrounded by amorphous matrix, b) group of grains surrounding pocket of amorphous material (weak plate like contrast is an imprint on surface oxide of martensite plates formed during electropolishing at low temperatures)

Heat treatment of ribbon either *ex-situ* in furnace or *in-situ* in TEM at 400°C first restart slow growth of big grains and simultaneous nucleation of plate like precipitates inside them (Fig. 13a). Both grain centers and especially narrow strips adjacent to

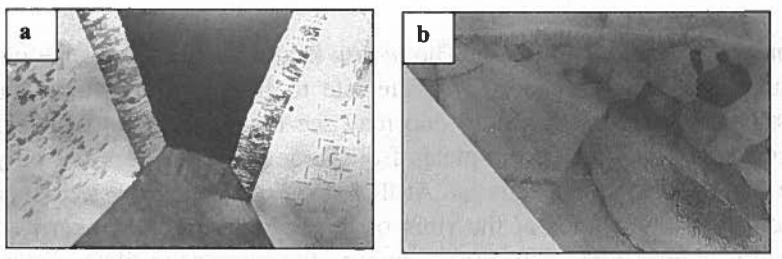

Fig. 13. Microstructure of Ti25Ni25Cu ribbon *in-situ* TEM heat treated at: a) 400°C/20 min, b) 450°C/3 min

original big grain boundaries remain free of these plates forming classical precipitate free zone. The strip of newly added crystalline material has the same orientation but is much more faulted than big grains. The defects are mostly dislocations running parallel to growth direction. Heat treatment at still higher temperature results in fast homogenous crystallization of the remaining amorphous matrix producing large areas filled with fine equiaxed β phase grains (13b).

Cooling of fully crystallized thin foils to room temperature (R.T.) usually resulted in their full transformation to martensite (Fig. 14 – R.T.), in the following sequence: first martensite plates form in the centers of large grains, next in newly formed small equiaxed grains and finally transforms the most heavily faulted strip re-grown at the surface of primary circular grains. The analysis of the diffraction patterns proved that in

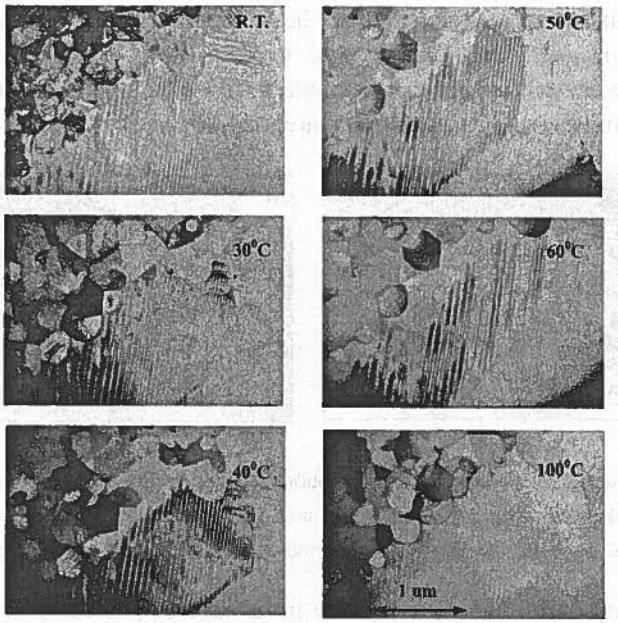

Fig. 14. *In-situ* heating of the ribbon from the alloy NiTi25Cu. After melt spinning the ribbon was heat treated at 450°C/20 min to crystallize the amorphous part [14]

all areas only B19 martensite forms. The *in-situ* heating causes a reverse of described above sequence of transformation of martensite to B2 phase as shown in series of images presented in Fig. 5. In detail one may see that heating up from R.T. first to 30°C causes "shrinking" of all the plates from large grains centers but only a few of martensite platelets from small grains. At that stage of heating the martensite formed in most heavily faulted strips at the rims of large grains remains nearly unchanged. Rising the foil temperature up to 40°C removes the martensite plates from the small grains but still leaving the bordering strip untouched, i.e. filled with martensite plates. Only further *in-situ* heating caused gradual removal of martensite plates from that strip changing it again to the β phase.

The performed *in situ* TEM experiments showed that only one type of martensite forms in the ribbons obtained from Ti25Ni25Cu as amorphous and crystallized afterwards. The delayed nucleation and growth of the same martensitic phase in different parts of the same thin foil was explained by differences in grain size as well as dislocation and precipitations density. The DSC measurements indicated that the reversible martensitic transformation for the thin foil having been kept at 450°C for 20 min. should have been finished at 40°C and indeed at that temperature martensite is gone from both large and small grains. The formation and disappearance of martensitic plates in the heavily dislocated rim around big grains was probably below sensitivity of this DSC, as the signal from the so named big grains itself was, judging from their transformation energy in respect to the transformation energy of the fully crystalline

ribbon, at the level of 10%. The rim might make up to 0,5%, but presence of grain colonies will push this estimation toward even lower values. At so low temperatures, i.e. below 100°C accordingly to the calibration performed at the opening to this paragraph, one may expect only few degrees difference between nominal and real temperature at the place of interest. Accordingly it cannot be accounted for the prolonged presence of martensite in the rim around big grains.

4. Summary

The *in-situ* straining and *in-situ* heating experiments require detailed support from other experiments like straining of bulk samples or DSC respectively, but are able to give us unique possibility to follow phase changes like reversible martensitic transformation. The side effects caused by extremely small thickness of thin foils should always be anticipated, but support from other experiments and proper calibration whenever possible should help to filter artifacts from events taking place in bulk materials. As during *in-situ* TEM experiments one has no possibility to measure neither real strain nor temperature at the place of interest, though the sequence of events is still very valuable information.

Properly executed *in-situ* straining experiments with shape memory alloys help to determine the sequence of phase transformation in pseudoelastic range and in consequence develop strain-temperature phase diagrams for them. The *in-situ* heating experiments may explain the influence of different elements of microstructure, like grain size, precipitates or dislocations on nucleation and grow of plates of martensite.

REFERENCES

[1] L.D. Shetky, Scientific American 241, 74 (1979).
[2] Martensitic transformations, ed. Z. Nishijama, Academic Press, N.Y. 1978.
[3] H. Warlimont, L. Delaey, Progress in Materials Science, **18**, Oxford 1974.
[4] C.M. Wayman, Metals Forum 4, 135 (1981).
[5] J. Perkins, Metals Forum 4, 153 (1981).
[6] K. Shimizu, C.M. Wayman, J. Materials Science,
[7] K. Otsuka, C.M. Wayman, K. Nakai, H. Sakamoto, K. Shimizu, Acta. Metall. 24, 207 (1976).
[8] T. Saburi, S. Nenno, Proc. ICOMAT p. 671, 1986.
[9] R. Sinclair, K.H. Min, Proc. ICEM XV, 931-932 (2002).
[10] H. Kato, J. Dutkiewicz, S. Miura, Acta metall. mater. **42**, 1359 (1994).
[11] J. Dutkiewicz, H. Kato, S. Miura, U. Messerschmidt, M. Bartsch, Acta. mater. **44**, 4597 (1996).
[12] J. Dutkiewicz, M. Bartsch, S. Miura, U. Messerschmidt, H. Kato, ICOMAT 95, suppl. Joural de Physique III 5, C2-275 (1995).

[13] J. Morgiel, M. Faryna, W. Maziarz, T. Czeppe, P. Ochin, J. Dutkiewicz, Proc. Advanced Materiale and Technologies, AMT 2004, *published in* Inżynieria Materiałowa 140, 224 (2004) (*in English*).
[14] J. Morgiel, E. Cesari, J. Pons, A. Pasko, J. Dutkiewicz, J. Mat. Sci. **37**, 5319 (2002).

Received: 3 November 2004.

A R C H I V E S O F M E T A L L U R G Y A N D M A T E R I A L S
Volume 49 2004 Issue 4

R. SZEWCZYK*, A. KOLANO-BURIAN**, ***, A. BIEŃKOWSKI****, J. SALACH****, T. KULIK***

THE POSSIBILITY OF APPLICATION OF NEWLY DEVELOPED ALLOYS AS STRESS AND FORCE SENSOR WITH EXTENDED OPERATION TEMPERATURE RANGE

NOWE MOŻLIWOŚCI ZASTOSOWANIA STOPÓW $Fe_{73,5-x}Co_xNb_3Cu_1Si_{13,5}B_9$ JAKO SENSORÓW NAPRĘŻENIA I SIŁY DZIAŁAJĄCYCH W SZEROKIM ZAKRESIE TEMPERATUR

The paper presents a new possibility for the utilizing of Fe-Co-Si-Cu-Nb-B alloys as the cores of stress and force sensors. Increasing of cobalt content in the $Fe_{73.5-x}Co_xNb_3Cu_1Si_{13.5}B_9$ alloys cause increase their Curie temperature. As a result sensors with cores made of such material can operate in higher temperature range than sensors based on the well known amorphous alloys or FINEMET-type ($Fe_{73.5}Nb_3Cu_1Si_{13.5}B_9$) alloys. In the paper both novel construction method of magnetoelastic sensors as well as magnetoelastic characteristics of $Fe_{73.5-x}Co_xNb_3Cu_1Si_{13.5}B_9$ alloys in the as-quenched and nanocrystalline states are presented. Some guidelines for magnetoelastic sensors constructors are indicated.

Keywords: magnetoelastic properties, nanocrystalline alloys, force sensors

W referacie przedstawiono nowe możliwości wykorzystania nanokrystalicznyh stopów Fe-Co- Si-Cu-Nb-B jako rdzeni magnetosprężystych sensorów naprężeń i sił. Stwierdzono, że wzrost zawartości kobaltu w tych stopach powoduje wzrost ich temperatury Curie. W rezultacie sensory wykonane z tych materiałów mogą pracować w szerszym zakresie temperatur niż sensory z rdzeniami z innych stopów nanokrystalicznych (np. z FINEMETu o składzie $Fe_{73,5}Nb_3Cu_1Si_{13,5}B_9$). W referacie przedstawiono zarówno nowe rozwiązania w zakresie konstrukcji sensorów magnetosprężystych jak i charakterystyki magnetosprężyste stopów o składzie $Fe_{73,5-x}Co_xNb_3Cu_1Si_{13,5}B_9$ zarówno w stanie wyjściowym jak i po relaksacji strukturalnej. W rezultacie sformułowano wytyczne dla konstruktorów sensorów magnetosprężystych na bazie stopów Fe-Co-Si-Cu-Nb- B.

* INDUSTRIAL RESEARCH INSTITUTE FOR AUTOMATION AND MEASUREMENTS "PIAP", AL. JEROZOLIMSKIE 202, 02-486 WARSAW, POLAND
** INSTITUTE OF NON-FERROUS METALS, SOWINSKIEGO 5, 44-100 GLIWICE
*** FACULTY OF MATERIAL SCIENCE AND ENGINEERING, WARSAW UNIVERSITY OF TECHNOLOGY, WOLOSKA 141, 02-507 WARSAW, POLAND
**** INSTITUTE OF METROLOGY AND MEASURING SYSTEMS, WARSAW UNIVERSITY OF TECHNOLOGY, SW. A. BOBOLI 8, 02-525 WARSAW, POLAND

1. Introduction

The mechanical stress changes the magnetization process of the soft magnetic material. This effect, known as magnetoelastic Villari effect, is especially important in the case of alloys, where the magnetocrystalline anisotropy is low and the proportion of magnetoelastic energy in the total free energy is especially significant. As a result such materials are highly stress-sensitive [1]. This high stress sensitivity creates possibility of construction of stress and force sensors with significant advantages. In a case of such sensors ferromagnetic material can be both sensing and construction element. Contrary to strain gauge sensors, in magnetolastic sensors, sensing element should not be mounted at elastic bar with adhesive layer. Moreover, due to significant changes of magnetic parameters of the material (e.g. magnetic permeability ? can change up to 70%) measuring signal form magnetoelastic stress and force sensors is convenient for both analog and digital processing.

Magnetoelastic sensors based on the classical crystalline materials (such as Fe-Ni--Co alloys) were successfully used in heavy industrial applications [2], but the possibilities of a new applications of these, classical materials were significantly depleted. The main barrier of application of such sensors in heavy industry is limited operation temperature range of sensors. On the other hand process of development of new magnetic materials for cores of inductive components operating at higher temperatures, such as FINEMET-type alloys with cobalt addition, can give fresh impetus for the construction of magnetoelastic sensors.

Finemet-type nanocrystalline alloys with cobalt addition create new possibilities of obtaining soft magnetic materials working at high temperatures and high frequency. The Fe-Co-Cu-Nb-Si- B nanocrystalline alloys, consisting of nanosized crystals surrounded by residual ferromagnetic amorphous matrix, have slightly worse magnetic properties at room temperature than the FeCuNbSiB alloys, but are more stable at elevated temperatures [3]. As a result these group of materials creates very interesting possibilities of industrial application in the area of stress and force sensors operating at higher temperatures.

2. Investigated material

In spite of the fact that the $Fe_{73.5-x}Co_xNb_3Cu_1Si_{13.5}B_9$ have slightly worse magnetic properties at room temperature than the $Fe_{73.5}Nb_3Cu_1Si_{13.5}B_9$ alloys, their properties are more stable at elevated temperatures. For this reason such material seems to be much more suitable for industrial applications. Increase of Co content in the alloy results in the increase of T_c, which is the highest for the alloy containing 40 at. %, and is then by 80°C higher than in the case of the alloy without Co. From the estimation of the Curie temperature T_c, the thermomagnetic analysis was performed using a Faraday magnetic balance. The measurements of saturation magnetization for alloys in the as-quenched state and after annealing in optimal temperatures were performed

starting from room temperature up to 800°C, at the heating rate of 3°C/min in the magnetic field of 0.5 T. The optimal annealing temperature was the temperature for which the best magnetic properties are obtained in case of the specific Co content [4]. Figure 1 shows evolution of the Curie temperature T_c for the amorphous matrix of the $Fe_{73.5-x}Co_xCu_1Nb_3Si_{13.5}B_9$ (x = 0 – 50) alloys after annealing at optimal temperatures and comparison with T_c value in the precursor amorphous phase.

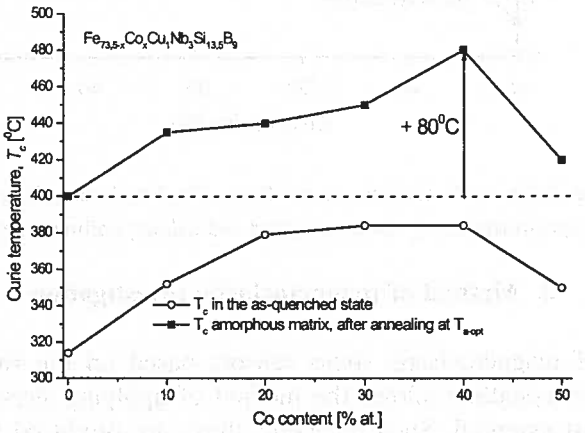

Fig. 1. The influence of the Co content, in the as-queched alloys and after nanocrystalization at the optimal temperatures, on its Curie temperatures

The influence of cobalt addition on the saturation magnetostriction of $Fe_{73.5-x}Co_x$ $Nb_3Cu_1Si_{13.5}B_9$ alloy, in both as-quenched and nanocrystalline state, is presented in Figure 2. All the investigated alloys are surprisingly soft despite of the relatively large value of λ_s. In the case of as-quenched alloys increasing of cobalt content results in a decrease of saturation magnetostriction λ_s of the alloy. This effect can be explained by the fact that magnetostriction of iron is positive and magnetostriction of cobalt – negative. It should be indicated, that in the case of nanocrystalline samples the value of saturation magnetostriction of the $Fe_{73.5-x}Co_xNb_3Cu_1Si_{13.5}B_9$ alloy first increase and than decrease with increasing cobalt content in the sample. This effect is connected with the fact, that addition of cobalt has significant influence on the process of nanocrystallization of $Fe_{73.5-x}Co_xNb_3Cu_1Si_{13.5}B_9$ alloy. The Co content dependence of λ_s for the nanocrystalline samples resembles the Co content dependence of λ_s for the Fe-Co binary alloy, where we have a minimum for K (magnetic anisotropy constant) and maximum for λ_s at Fe 50 : Co 50. Cobalt is distributed both in the crystalline grains and residual amorphous matrix, so the overall concentration of Co is not necessarily equal to the concentration in Fe-Co crystallites [5]. Investigation was carried out on six ring-shaped cores made of $Fe_{73.5-x}Co_xNb_3Cu_1Si_{13.5}B_9$ (and after nanocrystallization due to the heat treatment. The heat treatment was carried out at 550°C (x = 0), 500°C (x = 20) and 490°C (x = 40). The outer diameter of the samples was 32 mm, the inner diameter was 25 mm and the height was 10 mm.

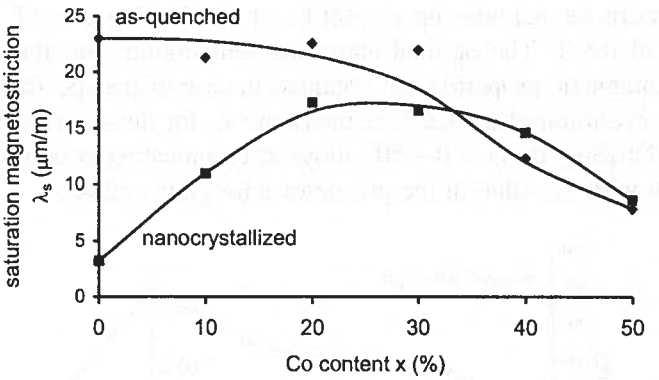

Fig. 2. The influence of the on Co-content x in the $Fe_{73.5-x}Co_xNb_3Cu_1Si_{13.5}B_9$ alloy on its saturation magnetostriction λ_s (in as-quenched and nanocrystalline state)

3. Method of magnetoelastic investigation

In the case of magnetoelastic stress sensors based on the ring cores made of amorphous or nanocrystalline alloys, the method of applying stresses to the sensing element is the most essential. Such magnetic alloys are produced as the ribbon ring cores. For this reason the frame- shape core [6], which is effective for bulk magnetic materials (i.e. ferrites), can not be applied. In previous applications compressive force was applied to the ring-shaped sensing element in direction of the diameter of the core [7]. In such a case distribution of stresses in the core was non-uniform. Moreover both compressive and tensile stresses were present in the sample. As a result both sensitivity and measuring range of such sensor was limited.

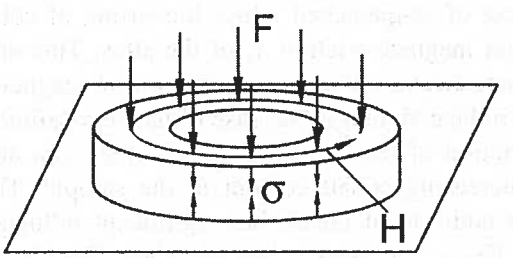

Fig. 3. The idea of the novel method of applying the uniform compressive stress to the ring-shaped sensing element

To overcome these problems the idea of novel method of the applying the compressive stress to the ring-shaped sensing element was developed. The idea of developed method is presented in Figure 3. In this method the compressive force F is applied to the ring-shaped cores perpendicularly to the magnetizing field H [8]. In such case uniform, compressive stress σ can be reached within the whole length of the magnetic

circuit of the sensing element. Moreover commercially available, ring shaped cores can be used as the magnetoelastic stress and force sensors [9].

For practical realization of this idea of application of compressive stress to the ring-shaped sensing element the special device was developed. Due to the special, nonmagnetic cylindrical backings the magnetic core can be subjected of the compressive force F. Measuring and magnetizing windings can be placed in radial grooves at the cylindrical backings. Additional, base backings allow a ring core to be subjected of the compressive force F.

Presented methodology crates possibility of obtaining of the uniform distribution of compressive stress at the all length of closed magnetic circuit of sensing core. As a result measuring range and sensitivity of magnetoelastic sensors utilizing this method may be significantly extended. Moreover new kind of basic research on the process of magnetization of amorphous magnetic materials subjected to stresses may be carried-out.

4. Results of magnetoelastic tests

The influence of the external compressive stresses on the shape of hysteresis loop of $Fe_{53.5}Co_{20}Nb_3Cu_1Si_{13.5}B_9$ alloy in as-quenched state and after nanocrystallization is presented in Figure 4. In the case of as-quenched sample (Fig. 4a) under the influence of stresses up to 10 MPa the value of flux density B increases monotonously. In the case of the sample in nanocrystalline state (Fig. 4b) the value of flux density B initially increase and than decreases.

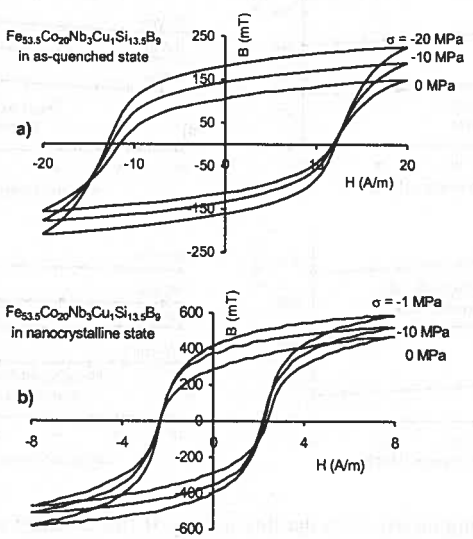

Fig. 4. The influence of compressive stresses σ on the magnetic hysteresis loop $B(H)_\sigma$ of $Fe_{53.5}Co_{20}Nb_3Cu_1Si_{13.5}B_9$ alloy in a) as-quenched state, b) nanocrystalline state

The influence of compressive stress σ on the flux density B in $Fe_{73.5-x}Co_xNb_3Cu_1Si_{13.5}B_9$ (x = 0, 20, 40) cores in the as-quenched and nanocrystalline state is presented in Figure 5. In the case of samples in as-quenched state (Fig 5a, c, e) under the compressive stresses up to 10 MPa, the linear increasing value of flux density B was observed. On the other hand, in the case of nanocrystalline sample the course of $B(\sigma)_H$ characteristics depends on the alloy composition. The highest stress sensitivity was observed in the case of $Fe_{73.5}Nb_3Cu_1Si_{13.5}B_9$ type alloys. In this case flux density B increases even by 300% for stresses up to 2 MPa. But for the highest cobalt addition (x = 40) stress sensitivity of $Fe_{73.5-x}Co_xNb_3Cu_1Si_{13.5}B_9$ alloy decreases significantly. For stresses up to 10 MPa flux density B changes only about 10%. It should be indicated, that also such changes of flux density can be utilized in construction of magnetoelastic sensors. Such sensors can be also more sensitive than known, the most sensitive semiconductor strain-gauge sensors, where resistance changes up to 0.5%.

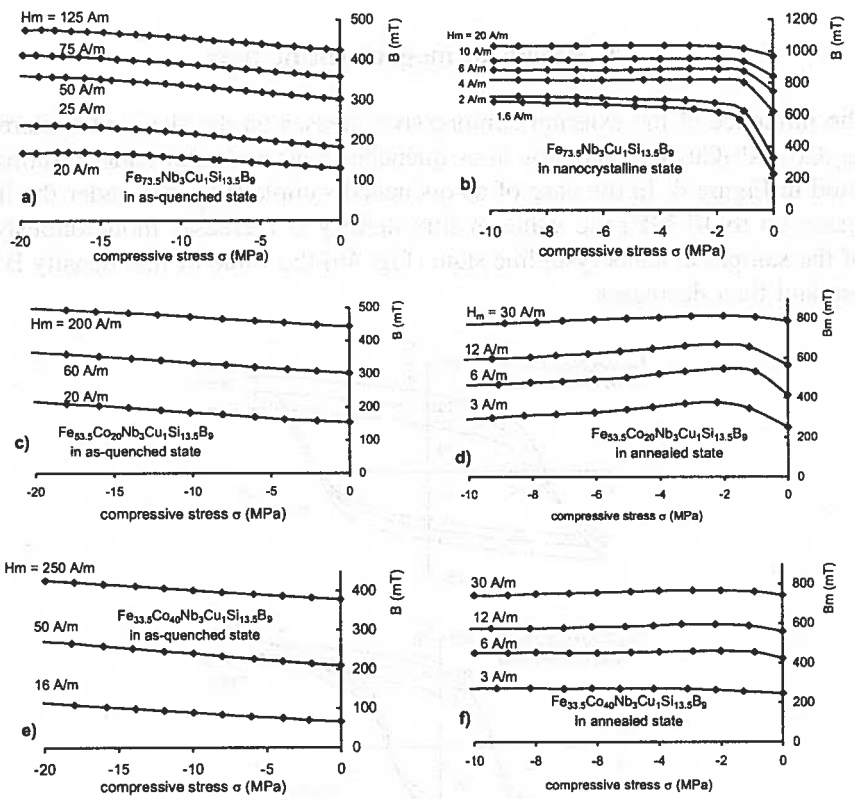

Fig. 5. The influence of compressive ? on the flux density B (for constant magnetizing field Hm) in the $Fe_{73.5-x}Co_xNb_3Cu_1Si_{13.5}B_9$ alloys: a) x = 0, as- quenched state, b) x = 0 nanocrystalline state, c) x = 20, as-quenched state, d) x = 20 nanocrystalline state, e) x = 40, as-quenched state, f) x = 40, nanocrystalline state

In the case of magnetoelastic $B(\sigma)_H$ characteristics of all nanocrystalline samples it was found that the relative increase of flux density B under stresses was higher for smaller values of magnetizing field H_m. This phenomenon is connected with the fact, that for smaller values of magnetizing field H_m participation of the magnetic energy in a total free energy of the core is lower [10]. As a result participation of the magnetoelastic anisotropy energy in total free energy of the sample is significantly higher for lower values of magnetizing field H_m. For this reason the stress sensitivity is higher for lower values of magnetizing field H_m.

5. Conclusions

In the paper the new possibility of application of $Fe_{73.5-x}Co_xNb_3Cu_1Si_{13.5}B_9$ alloys in construction of high-temperature stress and force sensors was indicated. Moreover the novel methodology of applying the uniform compressive stress to the ring-shaped sensing element is presented. Sensors utilizing this methodology have a wider measuring range and a higher sensitivity than sensors with ring- shaped sensing elements presented previously.

The presented experimental results confirmed that both alloy composition as well as nanocrystalline or as-quenched state of the cores have significant influence on the shape of $B(\sigma)_H$ characteristics. The highest stress sensitivity was observed in the case of $Fe_{73.5}Nb_3Cu_1Si_{13.5}B_9$ type alloys. But for the temperature-resistant alloy compositions (with higher cobalt addition, x=40), under the influence of stresses up to 10 MPa, the value of flux density B in the core decreases about 10% (Fig. 5). This information should be taken into consideration by constructors of the high-temperature magnetoelastic sensors..

Acknowledgements

Roman Szewczyk is the holder of the scholarship of Foundation for Polish Science. We would like to express our thanks to Dr Gabriel Vlasak for measurements of saturation magnetostriction.

REFERENCES

[1] R. O'Handley, Moderm magnetic materials – principles and applications, John Wiley & sons, New York, 2000.

[2] D. Jiles, Introduction to Magnetism and Magnetic Maerials, Chapman&Hall, London 1998.

[3] J. Zbroszczyk, J. Olszewski, W. Ciurzynska, B. Wyslocki, R. Kolano, A. Mlynczyk, M. Łukiewski, A. Kolano, J. Lelatko, Microstructure and some magnetic characteristics of amorphous and nanocrystalline $Fe_{83-x}Co_xNb_3B_{13}Cu_1$ (x = 0 or 41.5) alloys, Journal of Magnetism and Magnetic Materials **254-255**, 513-15 (2003).

[4] A. Bieńkowski, Magnetoelastic Villari effect in Mn-Zn ferrites, Journal of Magnetism and Magnetic Materials **215-216**, 231-3 (2000).

[5] K. Mohri, E. Sudoh, New extensometer using amorphous magnetostrictive ribbon wound cores, IEEE Trans. Magn. **17**, 1317-19 (1981).
[6] A. Bieńkowski, R. Szewczyk, Patent Pending, P-345758, 2001.
[7] R. Szewczyk, A. Bieńkowski, A. Kolano-Burian, Magnetosprężyste zjawisko Villariego w magnetykach amorficznych i nanokrystalicznych, Rudy i Metale Nieżelazne R-**47**, 445-448 (2002).
[8] A. Kolano-Burian, J. Ferenc, T. Kulik, Structure and magnetic properties of high temperature nanocrystalline Fe-Co-Cu-Nb-Si-B alloys, Materials Science and Engineering A 375-377, 1078-1082 (2004).
[9] A. Kolano-Burian, T. Kulik, G. Vlasak, J. Ferenc, L.K. Varga, Effect of Co addition on nanocrystallization and soft magnetic properties of $(Fe_{1-x}Co_x)_{73.5}Cu_1Nb_3Si_{13.5}B_9$ alloys, Journal of Magnetism and Magnetic Materials **272–276**, 1447-1448 (2004).
[10] R.M. Bozorth, Ferromagnetism, D. van Nostrood, New York 1956.

Received: 3 November 2004

A R C H I V E S O F M E T A L L U R G Y A N D M A T E R I A L S
Volume 49 2004 Issue 4

A.S. SOLOGUBENKO*, P. MÜLLNER*, H. HEINRICH*, G. KOSTORZ*

FORMATION OF TWINNED TETRAGONAL FERROMAGNETIC $L1_0$ – MnAl-C

POWSTAWANIE ZBLIŹNIAKOWANEGO TETRAGONALNEGO FERROMAGNETYKU $L1_0$-MnAl-C

The plate-like modification of the τ-MnAl-C ($L1_0$-structure) is a promising material for magnetoplastic applications. The formation of the metastable plate-like τ from the supercooled high- temperature ε-phase (A3-structure) is a discontinuous displacive process. It thus becomes possible to control the appearance of particular variants of the twin-related structural domains of τ at the intermediate stages of the $\varepsilon \rightarrow \tau$ transformation. The displacive mechanism of the plate- like τ-formation was studied by transmission electron microscopy. The intermediate ε'-phase (B19-structure) forms from the ε-phase and transmits the crystallographic correspondence from the matrix ε to the plate-like τ. The structural domain boundaries of the intermediate ε'-phase are the nucleation sites of the plate-like τ. The crucial role of these structural domain boundaries for the formation of the plate-like τ-phase is demonstrated.

Keywords: displacive transformation, MnAl-C alloys, structural domains, nucleation sites.

Płytkowa modyfikacja τ-MnAl-C (o strukturze $L1_0$) jest obiecującym materiałem do zastosowań magnotoplastycznych. Tworzenie się metastabilnych płytek τ z przechłodzonej wysokotemperaturowej fazy ε (o strukturze A3) wynika z nieciągłego procesu przemiany bezdyfuzyjnej. Istnieje możliwość kontroli pojawiania się określonych wariantów domen strukturalnych mających relacje bliźniacze fazy τ w stanach przejściowych przemiany $\varepsilon \rightarrow \tau$. Mechanizm przemieszczeń podczas tworzenia się płytek τ był badany przy użyciu transmisyjnej mikroskopii elektronowej. Przejściowa faza ε' (o strukturze B19) tworzy się z fazy ε i przenosi zależność krystalograficzną z matrycy ε do płytek τ. Granice strukturalnych domen przejściowej fazy ε' są miejscami zarodkowania płytek τ. W pracy przedstawiono decydującą rolę granic domen strukturalnych w tworzeniu się płytek fazy τ.

1. Introduction

Large magnetocrystalline anisotropy and mobile twin boundaries are required for a magnetoplastic response of a material. A few binary and quasi-binary alloys with $L1_0$

* INSTITUTE OF APPLIED PHYSICS IAP, ETH HÖNGGERBERG, CH-8093 ZÜRICH, SWITZERLAND

structure exhibit high uniaxial magnetic anisotropy and form twins upon loading. The low cost of raw materials of the τ-MnAl and τ-MnAl-C alloys favors them among other twinned $L1_0$-type ferromagnets. The metastable ferromagnetic τ-phase ($L1_0$ structure) of MnAl forms from the high-temperature supercooled ε-phase (A3 structure) obtained after quenching to room temperature, upon annealing at temperatures between 350–750°C. It appears in the concentration range of 52–60 at.% Mn. Addition of carbon (within the solubility limit) delays the decomposition of both ε and τ to the equilibrium phases β and γ [1].

Two different modes of the $\varepsilon \rightarrow \tau$ transformation result in two different modifications of τ [2, 3], distinguished by their different microstructures (see Fig. 1). The "flower-like" modification is highly segmented and contains many defects. This phase is formed by a thermally activated, compositionally invariant process akin to a

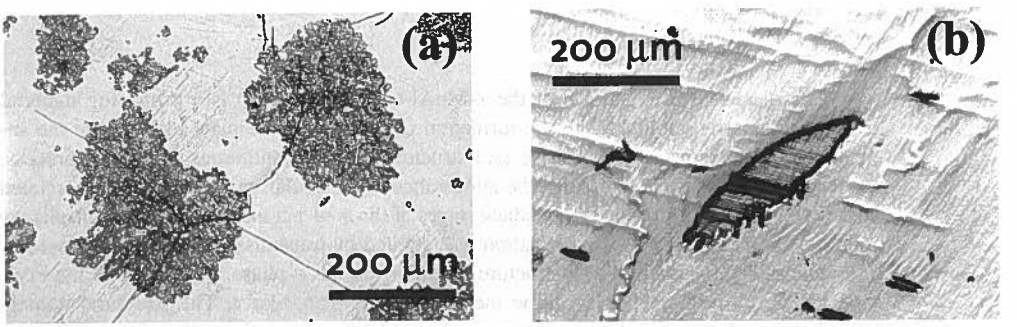

Fig. 1. (a) Metallographic image of a Mn-41.57 at.% Al-3.61 at.% C crystal, annealed at 500°C for 2.5 h. The darker, highly segmented areas in the image correspond to the "flower-like" τ regions; (b) Metallographic image of a Mn-39.2 at.% Al-0.8 at.%C crystal, annealed at 400°C for 5 h. The dark striated region in the middle of the image corresponds to the "plate-like" τ. The lighter background in both images corresponds to the ε-phase.

massive transformation [3]. The "flower-like" τ-phase nucleates mainly at impurities and grain boundaries and grows without any specific crystallographic relationship to the matrix ε-phase (see Fig. 1a). The "plate-like" τ nucleates within ε-grains and has a specific crystallographic correspondence to the matrix. It is formed by a discontinuous displacive process.

The shear process of "plate-like" τ-formation involves participation of the intermediate metastable ε'-phase (B19 structure) [4, 5] that appears at temperatures below about 600°C [6]. The intermediate ε'-phase transmits the crystallographic correspondence from the matrix-phase ε to the product-phase τ [4, 5]. In the present work, a detailed description is given of the displacive transformation mode of the formation of the twinned τ-phase in a Mn-39.2 at.% Al-0.8 at.%C single crystal.

2. Results and disscusion

The transformation was studied by transmission electron microscopy (TEM) with the goal to describe details of the microscopic mechanisms of nucleation and growth of the τ-phase. The transformation starts with an ordering process. The hexagonal ε-phase (A3) transforms to the orthorhombic ε'-phase (B19). Mn and Al atoms form chains along close-packed directions on close-packed planes. Symmetry reduction results in three crystallographically equivalent orientation variants of ε'. These orientation variants nucleate and grow simultaneously within the matrix ε. They are fully coherent and space-filling (see Fig. 2a). Electron diffraction reveals that ε'-domains are already

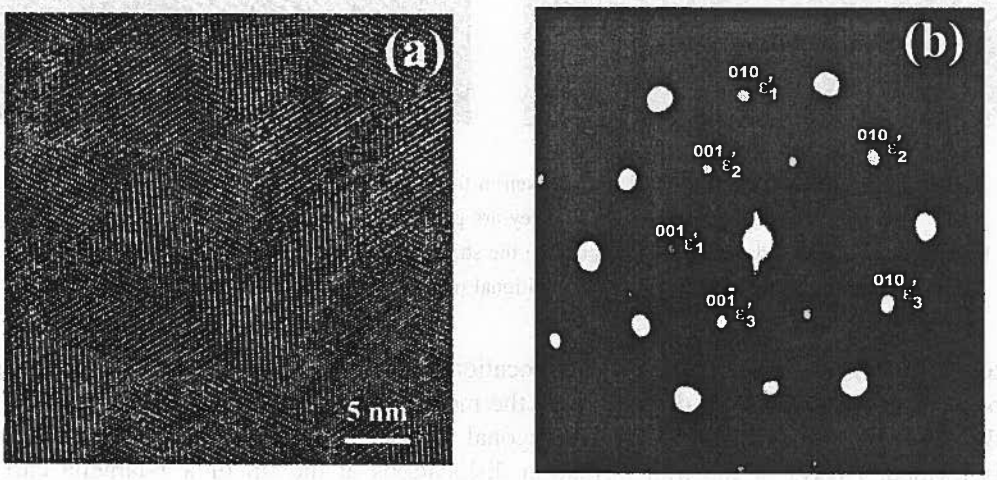

Fig. 2. (a) High-resolution TEM image of a Mn-39.2 at.% Al-0.8 at.% C single crystal, annealed at 300°C for 21 h, taken along the $100\varepsilon'$ zone axis. Structural domains of ε'_i orientation variants are seen as differently hatched regions; (b) Electron diffraction pattern of the $100\varepsilon'_i$ zone axis taken from the much larger area. Reflections of all three ε'_i variants are present

long-range ordered at the early stages of the transformation (see Fig. 2b). The coherent growth of ε'-domains within the matrix ε causes misfit strains at domain interfaces. When a critical domain size is reached, stacking faults (SFs) on the basal planes of the ε-phase are formed to reduce these stresses. SFs appear within single ε'-domains, locally altering the AB stacking sequence of the ε'-phase. Upon progressing transformation, the SFs become more numerous and accumulate between domain boundaries (see Fig. 3a), causing streaks in electron diffraction patterns parallel to the c^*-axis of the ε-phase (see Fig. 3a, inset). Partial dislocations limiting the SFs, carry the transformation stresses that build up at the domain interfaces. The stresses are reduced when partial dislocations of opposite signs form ordered arrays (polytypes). Periodic arrangements of SFs cause additional reflections in electron diffraction patterns. Polytypes of large periodicity are formed along $[100]\varepsilon'$ (see Fig. 3b, inset). The polytype plates are confined to single ε'-domains. The domain boundaries are obstacles to the propagation

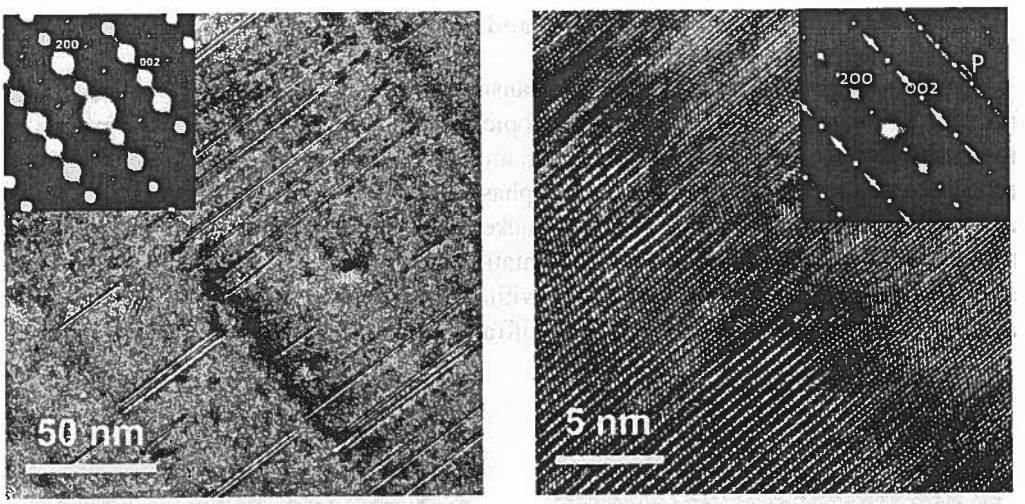

Fig. 3. (a) Near high-resolution TEM image taken in the $[11\bar{2}0]\varepsilon$ zone axis orientation. The striations are traces of stacking faults seen edge-on. They are parallel to $(0001)\varepsilon$ and terminate at a domain boundary (contrast bands lying perpendicular to the striations). (b) High-resolution TEM. Periodically arranged stacking faults (polytypes) cause additional reflections (P) in the diffraction pattern (inset)

of transformation dislocations. The dislocations overcome the boundaries by forming ordered arrays over larger distances. By the motion of an array of partial dislocations, the ABC stacking sequence of the tetragonal τ-phase ($L1_0$), a short-period polytype, is formed. Arrays of the transformation dislocations at the tip of a τ-lamella carry stresses that are reduced by twinning. Thereby, the long-range stresses of dislocations of opposite signs are mutually cancelled [5]. Thick twinned τ-lamellae appear and grow.

Cooperative motion of partial dislocations on basal planes of the ε-phase transmits the coherency from $\varepsilon \rightarrow \tau$, via intermediate steps: $\varepsilon \rightarrow \varepsilon'$, $\varepsilon' \rightarrow$ SF, and SF $\rightarrow$ polytypes. Thus, the transformation is a discontinuous sequence of clearly distinguishable transformation steps, namely, $\varepsilon \rightarrow \varepsilon' \rightarrow$ SF $\rightarrow$ polytypes $\rightarrow$ twinned τ. The stepwise nature of the process is caused by the occurrence of structural domains of the intermediate phase, their mutually coherent growth, accompanied by stress accumulation at the interfaces. The ε'-domain boundaries are sites of nucleation for each successive step, and they also limit the spatial extension of the transformation until the very last step, which is the formation of the twinned τ-phase.

Acknowledgments

The authors are grateful to the Swiss National Science Foundation for partial support of this work (project no. 200020-101468/1).

REFERENCES

[1] J. H. Huang, P. C. Kuo, Mater. Sci. Eng. **B22**, 156 (1994).
[2] A. S. Sologubenko, P. Müllner, H. Heinrich, M. Wollgarten, G. Kostorz, J. Phys. IV France 112, 1071 (2003).
[3] C. Yanar, J. M. K. Wiezorek, V. Radmilovic, W. A. Soffa, Mettal. Mat. Trans. A **33**, 1 (2002).
[4] S. Kojima, T. Ohtani, N. Kato, K. Kojima, Y. Sakamoto, I. Konno, M. Tsukahara, T. Kubo, AIP Conf. Proc. **24**, 768 (1975).
[5] P. Müllner, B.E. Bürgler, H. Heinrich, A.S. Sologubenko, G. Kostorz, Phil. Mag. Lett. **82**, 71 (2002).
[6] V. M. Gundyrev, M. A. Uimin, A. E. Ermakov, O. B. Andreeva, Phys. Stat. Sol. (a) **91**, K55 (1985).

Received: 3 November 2004.

A R C H I V E S O F M E T A L L U R G Y A N D M A T E R I A L S
Volume 49 2004 Issue 4

P. VERMAUT* , K. CHASTIAING*, P. OCHIN**, C. SEGUI***, J.Y. LAVALL****, R. PORTIER*

EFECT OF Cu ADDITIONS IN $Ni_{49.8}Ti_{40.2}Hf_{10}$ SHAPE MEMORY ALLOYS

EFEKT DODATKU Cu W STOPIE $Ni_{49.8}Ti_{40.2}Hf_{10}$ WYKAZUJĄCYM PAMIĘĆ KSZTAŁTU

The effect of the combination of two different additions on NiTi shape memory alloy is not straight forward. In order to investigate the effect of Hf and Cu additions on the martensitic transformation, a set of 5 alloys has been prepared with the following compositions: $Ni_{49.8-x}Cu_xTi_{40.2}Hf_{10}$ with x = 0, 6, 10, 15, 20. The transformation temperatures and the microstructures obtained have been analysed by differential scanning calorimetry and transmission electron microscopy.

Whereas the hysterese are smaller with the addition of Cu like in the ternary $Ti_{50}Ni_{50-x}Cu_x$ alloys, the Ms martensitic transformation temperatures decrease rapidly. The structure of the B19′ martensite has been also modified with a decrease of the unit cell monoclinicity. The twining modes are not modified but the martensite plates are longer and contain fewer defects with comparison to the ternary NiTiHf alloy.

Internal friction analysis has been carried out in order to compare the damping properties of the NiTiHf10, Cu10 and Cu15 alloys. It appears that the Hf addition decreases the damping properties in comparison to the $Ni_{50}Ti_{50}$, while the addition of Cu to NiTiHf10 improves these properties. The evolution of the shear modulus with temperature in the Hf containing alloys is different from that of NiTi ones, with a shear modulus higher in martensite than in austenite.

Keywords: shape memory alloy; NiCuTiHf; martensitic transformation; TEM; DSC; internal friction.

Efekt wprowadzenia dwóch różnych dodatków do stopu NiTi wykazującego pamięć kształtu nie jest dotychczas dokładnie poznany. W celu zbadania wpływu dodatków Hf oraz Cu na przemianę martenzytyczną przygotowano zestaw 5 stopów o następujących składach: $Ni_{49.8-x}$ Cu_x $Ti_{40.2}Hf_{10}$, gdzie x = 0, 6, 10, 15, 20. Temperatury przemiany i mikrostruktura stopów były analizowane przy użyciu różnicowej kalorymetrii skaningowej oraz transmisyj-

* LABORATOIRE DE MÉTALLURGIE STRUCTURALE – ECOLE NATIONALE SUPÉRIEURE DE CHIMIE DE PARIS, 11 RUE P. ET M. CURIE 75231 PARIS CEDEX 05, FRANCE

** CENTRE D'ETUDES DE CHINIE MÉTALLURGIQUE UPR CNRS 2801, 15 RUE G. URBAIN 94400 VITRY/SEINE, FRANCE

*** DEPARTAMENT DE FISICA, UNIVERSITAT DE LES ILLES BALEARS, CRA DE VALLDEMOSSA, KM 7.5, E-07122, PALMA DE MALLORCA, SPAIN

**** LABORATOIRE DE PHYSIQUE DU SOLIDE CNRS-ESPCI, 10 RUE VAUQUELIN 75231 PARIS CEDEX 05, FRANCE

nej mikroskopii elektronowej. Podczas gdy histerezy zmniejszają się wraz z dodatkiem Cu podobnie jak w potrójnych stopach $Ti_{50}Ni_{50-x}$ Cu_x, temperatury Ms przemiany martenzytycznej gwałtownie spadają. Struktura matrenzytu B19′ również ulega modyfikacji poprzez zmniejszenie się jednoskośności komórki elementarnej. Sposób bliźniakowania nie ulega modyfikacji, lecz płytki martenzytu są dłuższe i zawierają mniej defektów w porównaniu do potrójnego stopu NiTiHf. Analizę tarcia wewnętrznego prowadzono w celu porównania własności tłumiących stopów NiTiHf10 oraz zawierających 10 i 15% Cu. Okazuje się, że dodatek Hf obniża własności tłumiące w porównaniu do stopu $Ni_{50}Ti_{50}$, podczas gdy dodatek Cu do stopu NiTiHf10 poprawia te własności. Zmiany modułu sprężystości poprzecznej z temperaturą w stopach zawierających Hf różnią się od stopu NiTi i moduł ten jest wyższy w martenzycie niż w austenicie

1. Introduction

NiTi alloys are the most popular shape memory alloys due to their excellent properties, good corrosion resistance, biocompatibility, good workability and good shape memory and pseudoelasticity [1, 2]. These alloys enter in many applications in the medical domain through the fabrication of medical tools and prostheses [3]. Many ternary NiTiX alloys have been studied with X = Cu, Co, Fe, Pd, Hf, Zr, Nb. So far, the area of applications of NiTi based alloys is restricted to specific fields, which require martensitic transformation temperatures around or below the room temperature. An increase of the transformation temperatures could bring challenging opportunities in automotive and electro-technique industries [4]. High temperature shape memory properties have been obtained by addition of precious metals. Unfortunately, the use of such elements greatly increases the cost of the alloy, which becomes too high for any industrial application. A good candidate is Hf in substitution of Ti, combining high temperature shape memory properties with a reasonable price. However, the poor ductility of such alloy makes the production of wires and strips still difficult.

An other addition commonly used and widely studied is Cu. Added in substitution of Ni, it does not affect too much the martensitic transformation temperatures which although remain above the room temperature. Moreover, it improves several properties such as good thermal stability, lower hysteresis, lower sensitivity to the stoichiometry and good damping properties [5]. When the Cu content is lower than 8 at.%, it also improves the workability of the alloy. Above this limit, the ductility decreases considerably. The martensitic transformation is also modified. The austenite transforms at first in an intermediate orthorhombic B19 martensite followed by the monoclinic B19′ one [6, 7].

Independently of the shape memory properties, it has been recently shown in several studies that the addition of such elements improves the glass forming ability of the alloy [8]. Rapid solidification by planar flow casting lead to fully or partially amorphous ribbons. The present study is carried out in the frame of a project on production of bulk amorphous alloys, which undergo, after crystallisation, a martensitic transformation and displaying high temperature shape memory properties. The

amorphous state is then used as an intermediate state which helps to overcome the poor ductility of the alloy. In the temperature range between the glass transition and crystallisation, the amorphous alloy present superplasticity properties which allow the production of very small and complex shape pieces. The composition of such amorphous precursors of shape memory alloys involves 5–9 elements in substitution of Ni and Ti in the NiTi compound. Many compositions are based on combined substitutions with Cu and Hf. While the ternary alloys have been widely studied, only few studies focus on the quaternary alloys [9–11]. The aim of this work is to compare the properties of the quaternary alloys with 10 at.% Hf and a Cu content up to 20 at.%, to those of the ternary NiTiHf10 alloy, in terms of ductility, transformation temperatures, microstructure of the martensite, and damping properties.

2. Experimental details

A set of 4 alloys has been elaborated from elements of commercial purity. The compositions are $Ni_{49.8-x}Cu_xTi_{40.2}Hf_{10}$ with x = 6, 10, 15, 20. In the following, the alloys will be referred as NiTiHf10, Cu6, Cu10, Cu15, Cu20 respectively. The ternary alloy NiTiHf10 used as a reference for the comparison was provided by @MT company. The alloys were melted several times by HF furnace in a copper cooled crucible to improve the homogeneity. The produced ingots were 50 mm long with a 10 mm diameter. An attempt to hot roll the quaternary alloys showed that the ductility of the NiTiHf alloy is altered by addition of Cu even for a content as low as 6 at.%. The production of 0.5 mm thick hot rolled strips was possible only for the ternary NiTiHf10 alloy. For the NiCuTiHf alloys, after homogenisation heat treatment for 5 h at 850°C, 1 mm thick slices have been cut and hot rolled (thickness reduced by ~ 30%). The samples were then recrystallised 1h at 800°C and water quenched. In parallel, the rest of the ingot is used to produce 0.4 mm thick strips by the twin roll casting (TRC) technique [12].

Martensitic transformation temperatures have been analysed by differential scanning calorimetry (DSC) on a Mettler Toledo DSC 822^e apparatus in the range of [-100°C ; 300°C]. Thin foils for transmission electron microscopy (TEM) have been produced by the twin jet technique on a Struers Tenupol 4 using a 20% nitric acid in methanol solution at –20°C. TEM observations were carried out on a Jeol electron microscopes 120 CX II and 2010 F.

Internal friction experiments have been carried out on a homemade inverted torsion pendulum working at a frequency of 1Hz. Samples dimensions were $8 \times 50 \times 0.5$ or 0.4 mm. The cooling and heating rate for all experiments is 60°C/hour and deformation amplitude was $\gamma = 2.10^{-6}$. Q^{-1} was deduced from the decay of free oscillation amplitudes and the shear modulus from the square value of free oscillation frequency.

3. Results and discussion

1) Thermal analysis

Two set of experiments have been carried out in order to compare the martensitic transformation in the bulk samples after hot rolling and 800°C-1h annealing and twin roll casting (TRC) samples after the same thermal treatment. The curves are presented in figure 1a and b. The results are similar for samples obtained in both elaboration technique. TRC is a rapid solidification technique but the cooling rate is not as high as in the planar flow technique and does not lead to very small grain material. Then, the martensitic transformation temperatures are not affected. This result is consistent with those reported on Cu-based shape memory alloys obtained by conventional, twin roll and planar flow casting techniques [12]. The curves in figure 1 show clearly that the Cu additions to NiTiHf10 alloy lead to a rapid decrease of the transformation temperatures. A plot of these temperatures as a function of the Cu content (figure 2a)

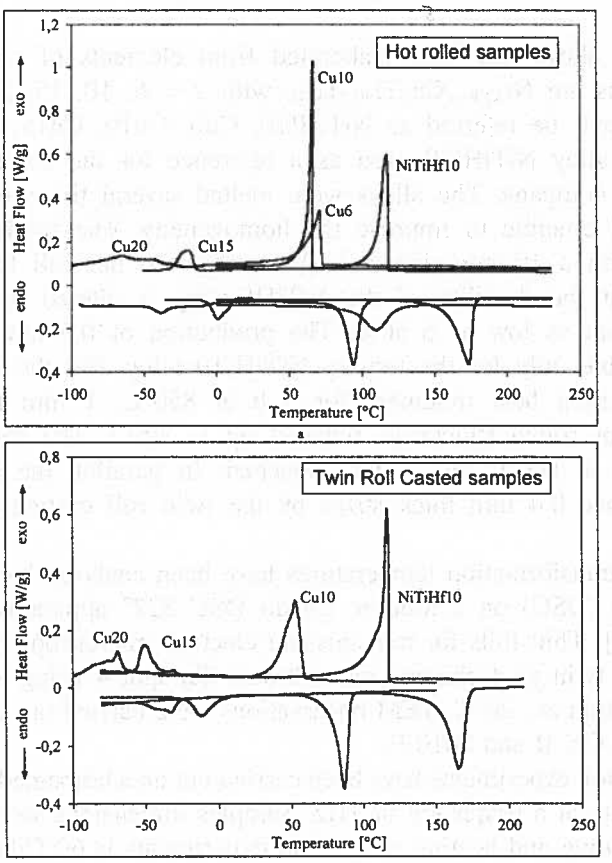

Fig. 1. DSC curves obtained for a) hot rolled samples b) samples obtained by the Twin Roll Casting technique. The results are similar independently of the production method

shows that the transformation temperatures decrease in average by 10°C per 1 at.% Cu.

The similar plot of the hysteresis (Ap-Mp) (figure 2b) shows that it decreases for the small amounts of Cu and it stabilises around 30°C at higher Cu contents. These results are mostly consistent with those reported in the literature but refer to lower Cu content [11] or 15 at.% Hf alloys [10] or those obtained by planar flow casting [9]. In the case of the Cu15 and Cu20 alloys, the DSC peaks are small and broad. This can be attributed to the presence of obstacles, which prevent the transformation at a large volume fraction of the parent phase.

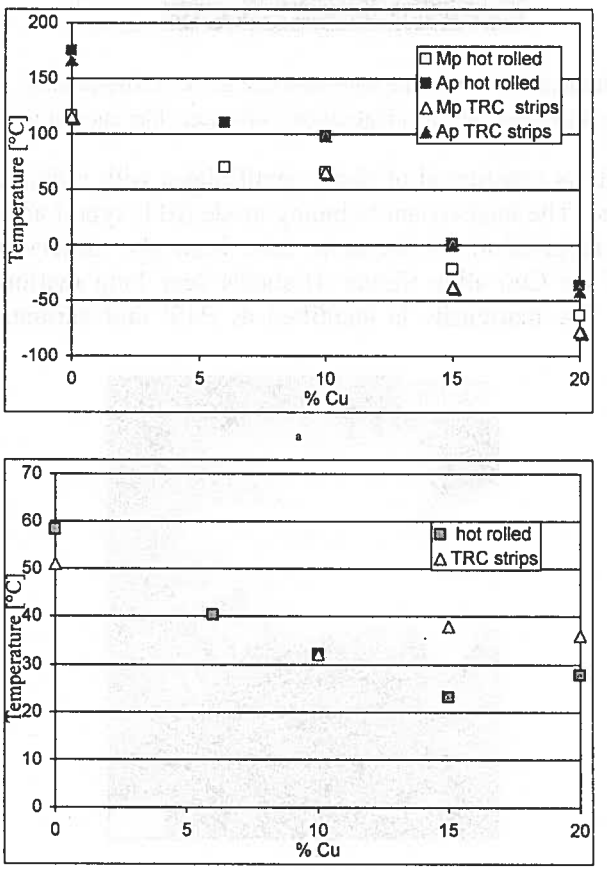

Fig. 2. Comparison of a) the transformation temperatures and b) hysterese (Ap-Mp) evolution with the Cu content for samples obtained by hot rolling and the twin roll casting technique

2) Microstructure

The TEM observations carried out on the NiTiHf10 alloy (figure 3) confirm the results reported in many studies on the microstructure of the martensite of these ternary alloys [13, 14].

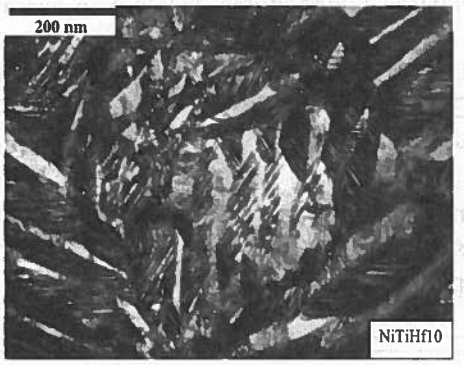

Fig. 3. Bright field image of the martensite microstructure in the NiTiHf10 alloy. The martensite plates are small and contain a high density of defects like internal twins

The martensite is constituted of many small plates with a high density of defects and highly twinned. The intervariant twinning mode (011) type I and internal twinning (001) compound reported in the literature have been also observed. In contrast, the microstructure of the Cu6 alloy (figure 4) shows very long martensite plates across the whole grain. The martensite is identified as B19' and variants are twin related

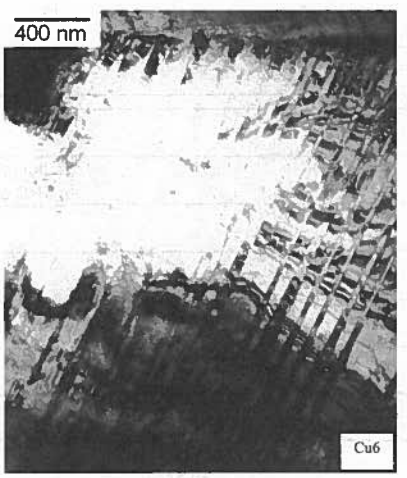

Fig. 4. Bright field image of the martensite microstructure in the Cu6 alloy. The martensite plates are thin and long, crossing the whole grain. Intervariant twining is identified as (011) type I mode

with a (011) type I mode. Only few internal twins are observed. A selected area diffraction pattern (SADP) has been recorded along the $[010]_B19'$ direction which allows to measure the β angle of the monoclinic unit cell (figure 5a) The result is 99°, which is smaller than the value reported by Gao et al [15] for a NiTiHf10 alloy. These results are confirmed by the observations made in the Cu10 alloy. The martensite is

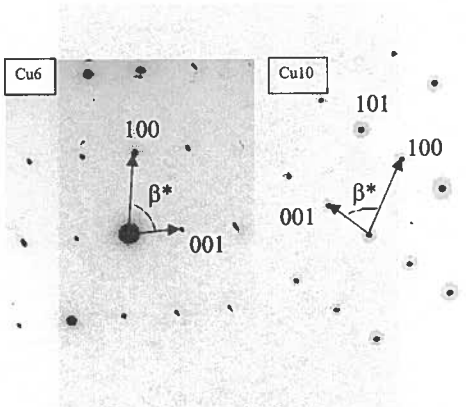

Fig. 5. Selected Area Diffraction Patterns recorded along the $[010]_{B19'}$ direction allowing the measurement of the β angle ($180° - \beta^*$) of the monoclinic unit cell a) $\beta = 99°$ in Cu6, b) $\beta = 97°$ in Cu10

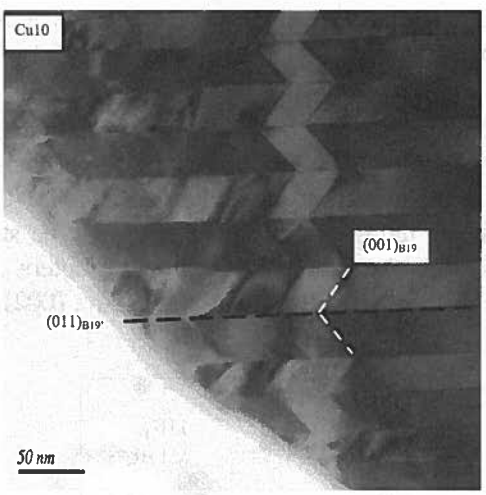

Fig. 6. Bright field image of the martensite microstructure in the Cu10 alloy, similar the that of Cu6. Intervariant twining is identified as (011) type I mode and some internal (001) compound twins are also observed. Traces of the $(011)_{B19'}$ and $(001)_{B19'}$ planes for both variants are indicated in the figure

very similar to that of the Cu6 with the same twining modes (figure 6) The SADP recorded along the [010] direction (figure 5b) gives $\beta = 97°$. One can conclude that the monoclinicity of the B19′ martensite unit cell decreases with the addition of Cu.

In the case of the Cu15 and Cu20 alloys, since the TEM observations are carried out at room temperature, the samples are in the austenitic state. When observed along the $[001]_{B2}$ direction, the austenite in the Cu15 alloy present (figure 7) a high density of a few nanometer thick plate-like precipitates lying in the $\{001\}_{B2}$ type planes. A

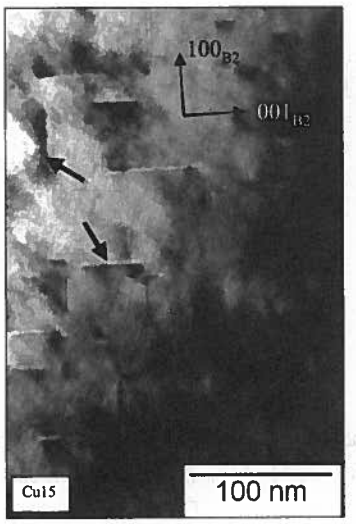

Fig. 7. Bright field image of the austenite microstructure in the Cu15 alloy. Arrows indicate position of thin plate-like precipitation lying in the $\{001\}_{B2}$ planes

nanobeam electron diffraction pattern of a single precipitate recorded along the $[011]_{B2}$ direction is presented in figure 8. In addition to the larger spots due to the austenite phase, extra spots due to this coherent precipitate are visible. The indexation of these spots is consistent with the tetragonal structure ($MoSi_2$-type structure) of the Hf_2Cu and Ti_2Cu compounds with the following lattice parameters : a_p = 0.298 nm and c_p = 10.78 nm, and the following orientation relationship : $(002)_p$ // $\{001\}_{B2}$ and $(110)_p$

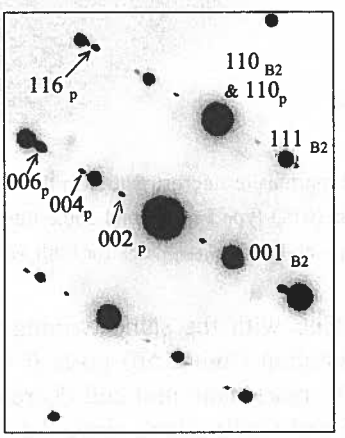

Fig. 8. NanoBeam Diffraction Pattern recorded along the $[011]_{B2}$ direction of a thin precipitate in the Cu15 alloy. Extra spots are indexed and identify the precipitates as $(Ti,Hf)_2Cu$ phase

// $\{110\}_{B2}$. Since Ti and Hf can substitute one another in such a crystal structure, these precipitates are supposed to be $(Ti,Hf))_2Cu$. Their presence can explain the weakness of the peak on the DSC curve, such precipitation forming obstacles for the growth of the martensite plates.

3) Internal friction

Internal friction experiments have been carried out on alloys for which it was possible to prepare a sample with suitable dimensions: hot rolled NiTiHf10, TRC Cu10 and TRC Cu15. The Q^{-1} versus temperature curves are shown in figure 9. Such curves in the case of shape memory alloys present a low internal friction level at high temperature, when the alloy is in austenite state. At low temperature, the internal friction is higher due to the high density of interfaces and defects in the martensite. At the transformation temperatures, the curves present a transitory peak connected to the transformation kinetic ie the transformed volume fraction per time unit [16]. Thus, it is strongly dependent on the cooling or heating rate. When one compare the curves of two samples with the same rates, the amplitude of the peak depends on the mobility of the austenite/martensite transformation. In a previous work, it has been shown that the interface mobility of the B2->B19′ transformation in the NiTiHf alloy is lower than in the Ni-Ti ones [17], because of a distortion of the habit plane due to the lattice invariant shear (001) compound twining mode. A comparison of the curves recorded in the present study for NiTiHf10 and Cu10 shows that addition of Cu to NiTi-Hf improves the mobility of austenite/ martensite interfaces. This could be connected to the decrease of the monoclinicity of the B19′ martensite unit cell with the Cu addition, and then a decrease of the twins shear amplitude. The damping coefficient Q^{-1} of the Cu15 alloy is much lower than in the other alloys, but in this case it can be attributed to the small volume fraction which transforms.

The evolution of the apparent shear modulus with temperature calculated from the square frequency of the free oscillations of the sample during the internal friction experiments is shown in figure 10. A curve recorded for a binary equiatomic and annealed NiTi alloy is included in the figure as a reference for the general behaviour of shape memory alloys. One can observe that the shear modulus of the NiTi alloy in the austenitic state decreases slowly during cooling, and rapidly when the martensitic transformation starts. At the end of the transformation, the slope of the curve changes. The shear modulus of the martensite increases but remains lower than in austenite in a large range of temperature. On heating, the curve of shear modulus is similar but shifted towards higher temperatures because of the martensitic transformation hysteresis. In the case of the ternary NiTiHf10, the shear modulus behaves similarly to NiTi, when it is fully austenitic or martensitic, but differently during the transformation. On cooling, as soon as the transformation starts, the shear modulus increases rapidly. The slope becomes less steep at the end of the transformation. The curve for the Cu10 alloy shows that this surprising evolution of the modulus is ever more pronounced. The results recorded for the Cu15 alloy confirmed that result. Even if, from DSC curves,

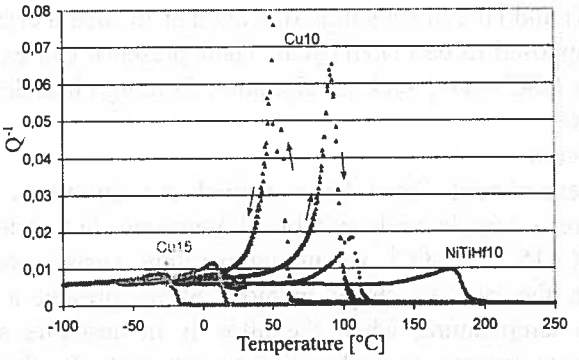

Fig. 9. Comparison of the evolution of the damping coefficient Q^{-1} recorded for the NiTiHf10, Cu10 and Cu15 alloys under cooling and heating. Arrows allow to follow the curve on cooling and heating. The Cu10 alloy shows very good damping properties in comparison to NiTiHf10. The small peak of the Cu15 alloy is attributed to the small volume fraction that transforms. Temperature rate is 60°C/hrs

it was noticed that the martensitic transformation involves a small volume fraction of austenite in this alloy, an abrupt jump of the shear modulus is observed on cooling during the transformation. In contrast, the transition peak of the Q^{-1} curve is very small.

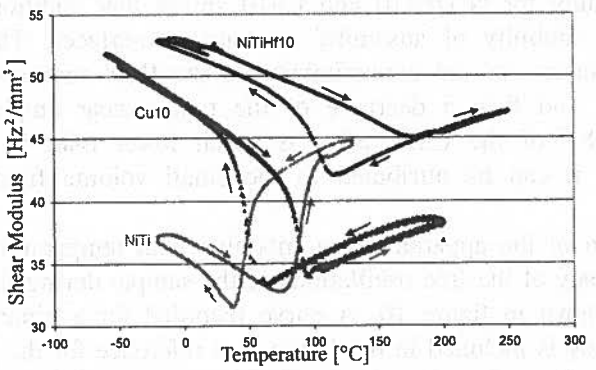

Fig. 10. Evolution of the shear modulus obtained from the square value of the free oscillations frequency, for the NiTiHf10 and Cu10 alloys. The curve for a $Ni_{50}Ti_{50}$ alloy is included as a reference, to show the usual evolution of the modulus during martensitic transformation in shape memory alloys. Addition of Cu in NiTiHf alloys emphasises this unusual behaviour

4. Conclusion

The addition of Cu to the NiTiHf10 alloy does not improve the ductility. The Cu modifies the martensitic transformation by a rapid decrease of the transformation temperatures, a small reduction of the hysteresis. No evidence of a two step transformation

B2->B19->B19′ have been found. The martensites observed at room temperature in the NiTiHf10Cu6 and NiTiHf10Cu10 alloys have the monoclinic B19′ structure. The β angle of the unit cell decreases when Cu is added. A plate-like precipitation of $(Ti,Hf)_2Cu$ has been identified in the NiTiHf10Cu15 alloy which act as obstacles for the martensite growth.

Internal friction experiments have pointed out good damping properties of the Cu10 alloy. The Cu additions proved the non conventional behaviour of the shear modulus of the NiTiHf alloys.

REFERENCES

[1] K. Otsuka, X. Ren, Intermetallics **7**, 511-528 (1999).

[2] J. Van Humbeeck, Advanced Engineering Materials **3**, 837-850 (2001).

[3] T. Duerig, A. Pelton, D. Stöckel, Mat. Sci. Eng. **A273**, 149-160 (1999).

[4] K. Wu, J.L. Ma, Proceedings of the international conference on shape memory and superelastic technologies, SMST-2000, Asilomar conference center, 153- 161 (2000).

[5] W.J. Moberly, K.N. Melton, Engineering aspects of shape memory alloys, Ed. T. W. Duerig, K. N., Melton, D. Stöckel, and C. M. Wayman, Butterworth- Heinemann (London), 46-53 (1990).

[6] Y.C. Lo, S.K., Wu, H.E. Horng, Acta Metall. & Mater. **41**, 747-759 (1993).

[7] V.G. Pushin, S.B. Volkova, N.M. Matveeva, L.I. Yurchenko, A.S. Chistyakov, The Physics of Metals and Metallography **84**, 441-448 (1997).

[8] V. Kolomytsev, M. Babanly, R. Musienko, A. Sezonenko, P. Ochin, A. Dezellus, P. Plaindoux, R. Portier, F. Dalle, P. Vermaut, J. Physique IV **11**, Pr8-457-462 (2001).

[9] P. Schlossmacher, H. Rösner, A.V. Shelyakov, Proceedings of the international conference on shape memory and superelastic technologies, SMST- 2000, Asilomar conference center, 123-130 (2000).

[10] X.L. Meng, Y.X. Tong, K.T. Lau, W. Cai, L.M. Zhou, L.C. Zhao, Materials Letters **57**, 452-456 (2002).

[11] X.L. Liang, Y. Chen, H.M. Shen, Z.F. Zhang, W. Li, Y.N. Wang, Solid State Communications **119**, 381-385 (2001).

[12] F. Dalle, C. Elgoyhen, G. Despert, J. Malarria, R. Portier, A. Dezellus, P. Plaindoux, P. Ochin, J. Physique IV **11**, Pr8-463-468 (2001).

[13] Y.F. Zheng, L.C. Zhao, H.Q. Ye, Scripta Mater. **38**, 1249- 1253 (1998).

[14] X.D. Han, W.H. Zou, R. Wang, Z. Zhang, D.Z. Yang, Acta Mater. **44**, 3711-3721 (1996).

[15] Y. Gao, Z.J. Pu, K.H. Wu, Proceedings of the international conference on shape memory and superelastic technologies, SMST-1997, Asilomar conference center, 83-88 (1997).

[16] J. San Juan, M.L. Nó, J. of Alloys and Compounds **355**, 65-7 (2003).

[17] F. Dalle, E. Perrin, P. Vermaut, M. Masse, R. Portier, Acta Mater. **50**, 3557-3565 (2002).

Received: 3 November 2004

A R C H I V E S O F M E T A L L U R G Y A N D M A T E R I A L S
Volume 49 2004 Issue 4

R. SANTAMARTA* , A. PASKO** , J. PONS*, E. CESARI*, P. OCHIN***

THERMAL AND MICROSTRUCTURAL EVOLUTION DURING THE CRYSTALLIZATION OF A $Ni_{50}Ti_{32}Hf_{18}$ MELT SPUN RIBBON

EWOLUCJA STRUKTURY I EFEKTY CIEPLNE PODCZAS KRYSTALIZACJI SZYBKO CHŁODZONYCH TAŚM STOPU $Ni_{50}Ti_{32}Hf_{18}$

A partially amorphous $Ni_{50}Ti_{32}Hf_{18}$ melt spun ribbon has been characterized by means of calorimetry (DSC) and transmission electron microscopy (TEM). Special emphasis has been given to the crystallization process of the amorphous regions, studying the evolution of the microstructure and the martensitic transformation. Although several crystallization procedures have been carried out by thermal treatments, either slightly under or over the crystallization temperature, T_C, measured by DSC, the final microstructure and calorimetric behavior of the fully crystalline samples does not depend on the applied temperature. The fully crystalline samples contain regions with small crystallites produced during the thermal treatment together with the large crystals originated during the melt-spinning. At room temperature (RT), both types of crystals are in martensitic state. However, the new crystallized regions with small grain size show notably lower transformation temperatures and wider hysteresis as compared to the big crystals already existing before the crystallization treatments. In addition to that, a supplementary mechanism, apart from the crystal size, affects the transformation temperatures, likely related to the higher energy surface of the crystalline-amorphous interfaces.

Keywords: crystallization, melt-spinning, nickel titanium based alloys, martensitic transformation.

Częściowo amorficzne taśmy stopu $Ni_{50}Ti_{32}Hf_{18}$ odlewane na walcu miedzianym badano metodami mikrokalorymetryczną (DSC) i transmisyjnej mikroskopii elektronowej (TEM). Szczególną uwagę zwrócono na proces krystalizacji regionów amorficznych pod kątem przemiany martenzytycznej. Jakkolwiek procesy krystalizacji prowadzono wielokrotnie poniżej lub powyżej temperatury krystalizacji T_c (zmierzoną przy pomocy DSC), to stwierdzono, że finalne mikrostruktury krystaliczne nie zależą od temperatury krystalizacji. Całkowicie skrystalizowane próbki posiadają mikrostrukturę składającą się z dużych krysz-

* DEPARTAMENT DE FÍSICA, UNIVERSITAT DE LES ILLES BALEARS, CRA. DE VALLDEMOSSA KM 7.5, E-07122 PALMA DE MALLORCA, SPAIN

** INSTITUTE OF METAL PHYSICS, NATIONAL ACADEMY OF SCIENCES OF UKRAINE, VERNADSKY BLVD. 36, 03142 KIEV, UKRAINE

*** CENTRE D'ETUDES DE CHIMIE MÉTALLURGIQUE, 15, RUE GEORGES URBAIN, F-94407 VITRY- SUR-SEINE, FRANCE

tałów powstałych przy odlewaniu i małych utworzonych podczas krystalizacji. W temperaturze pokojowej obydwa rodzaje krystalitów posiadają strukturę martenzytyczną, jakkolwiek drobne krystality wykazują niższą temperaturę transformacji i szerszą histerezę w porównaniu do dużych kryształów. Dodatkowy wpływ na mechanizm przemiany posiadają czynniki związane z energią granic jak granic faz amorficznych i krystalicznych.

1. Introduction

Almost-ready-to-use metallic ribbons may be produced by melt spinning, avoiding complex thermomechanical treatments needed after conventional casting, and thus leading to cheaper shape memory alloys (SMA) for certain applications. However, this rapid solidification technique also introduces particular microstructures, e.g. a reduction of the grain size when increasing the wheel velocity (i.e. cooling rate) [1, 2], and a decrease in the transformation temperatures [1, 3]. In certain alloys, a high cooling rate can even produce amorphous as cast melt-spun ribbons, which has been used in other fields for casting amorphous metals [4, 5]. Among Ni-Ti based SMA, $Ti_{50}Ni_{50-x}Cu_x$ and $Ni_{50}Ti_{50-x}Me_x$ alloys (with Me = Hf, Zr, Nb) have been reported to be partially or completely amorphous after melt-spinning when using a significant amount of the third element as well as a high cooling rate [6, 7].

Although production of amorphous material may seem useless in the field of SMA, the exceptional ductility of metallic amorphous alloys can be used for shaping the materials, which will exhibit shape memory properties after crystallization. Then, by modifying the crystallization parameters during the subsequent crystallization process, it might be possible to control the final crystalline structure and, therefore, some characteristics of the martensitic transformation. Several works on this new attractive idea have been carried out in $Ti_{50}Ni_{25}Cu_{25}$ [8, 9] together with further investigations on initially (partially) amorphous [10-13] or crystallized [14] $Ti_{50}Ni_{25}Cu_{25}$ ribbons. On the other hand, most investigations on the crystallization of Zr-Ti-Ni based alloys have been performed away from compositions giving martensitic transformation. Amorphous Ni-Ti-Hf-(Re) alloys can also be obtained by melt-spinning and some first characterizations have already been reported [15, 16].

Conventionally cast Ni-Ti-Hf alloys are well known for their high martensitic transformation temperatures when Hf exceeds 10 at.% [17, 18]. Despite the reduction of the transformation temperatures with respect to the bulk alloy, melt spun Ni-Ti-Hf ribbons still may show high transformation temperatures [19, 20].

In the present contribution, an extensive characterization of a partially amorphous $Ni_{50}Ti_{32}Hf_{18}$ melt spun ribbon has been performed by means of differential scanning calorimetry (DSC) and transmission electron microscopy (TEM). Special emphasis has been given to study the crystallization process of the amorphous regions by different thermal treatments above and below the crystallization temperature, T_C, measured by DSC, as well as the evolution of its microstructure during these processes. In addition, some comparisons with previous results on $Ti_{50}Ni_{25}Cu_{25}$, which is the most studied

SMA among the ones capable to be cast in amorphous state by melt- spinning, are presented.

2. Experimental procedure

A $Ni_{50}Ti_{32}Hf_{18}$ ribbon was prepared under helium atmosphere by planar flow casting from conventionally produced ingots of the same composition. The ingots were molten under He atmosphere and ejected at 200 hPa onto a rotating wheel with a surface speed of 19 m/s, producing a metallic ribbon 30 μm thick and 9.5 mm wide.

Calorimetric measurements were performed in a Perkin Elmer DSC-7 working between 235 and 875 K. A rate of 0.33 K/s was used in most of the runs. Faster runs at ~ 3.3 K/s up to 755 or 775 K with subsequent plateaus at those temperatures were also used for the crystallization experiments below the crystallization temperature, T_C, measured by DSC, which is 793 K for this alloy. Other samples were completely crystallized over T_C, either by fast runs in the DSC up to 875 K followed by rapid cooling to room temperature (RT) or by upquenching in a salt bath at 835 K during 1 minute.

Observations by transmission electron microscopy (TEM) were carried out in a Hitachi H-600 operating at 100 kV equipped with double-tilt holder and energy dispersive X-ray (EDX) spectrometer; heating and cooling single tilt holders were also used for *in-situ* experiments. Samples for TEM were obtained from 3 mm discs by double-jet electropolishing at ~ 15 V and 240 K using a solution of 30% nitric acid in methanol.

3. Results

3.1. Differential Scanning Calorimetry

DSC measurements performed to as cast samples in order to check the presence of martensitic transformation exhibit one single peak during cooling and heating around 440 and 500 K, for the forward and reverse transformation respectively, with an enthalpy change of 7 J/g (Fig. 1). The latter value is rather low in comparison to a completely crystalline melt-spun ribbon with the same nominal composition, which showed an enthalpy change slightly higher than 20 J/g [20]. The presence of amorphous regions in the ribbon, as it can be confirmed by means of direct methods like XRD [16] and TEM (next section), leads to this low enthalpy change.

In order to characterize the evolution of the transformation after a gradual crystallization at temperatures slightly under T_C, thermal treatments at 755 and 775 K in series of increasing times have been carried out. After each step of the progressive crystallization, the martensitic transformation has been controlled by DSC runs between 235 and 575 K (temperatures far below from T_C). The evolution of the martensitic transformation is quite similar for both temperatures of thermal treatment, apart from an

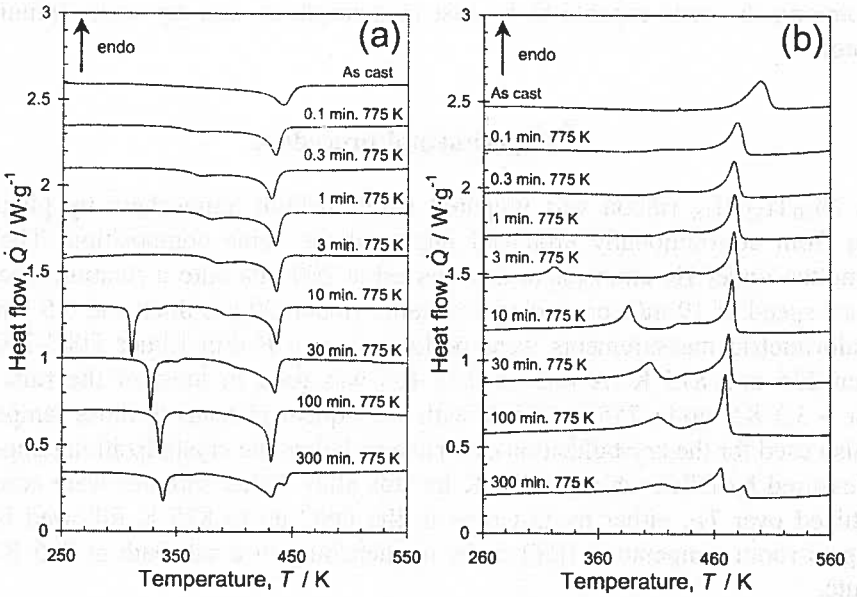

Fig. 1. Evolution of the direct (a) and reverse (b) transformation of the $Ni_{50}Ti_{32}Hf_{18}$ after heat treatments at 775 K for different times

evident shift to lower times for the 775 K series with respect to the 755 K one. Fig. 1 shows that the thermograms from the direct and reverse transformations performed after the shortest times of the series at 775 K produce a second and broad calorimetric peak at lower temperatures. An additional peak arises at lower temperatures when increasing the holding time at 775 K, approaching to the peaks at higher temperatures at the end of the crystallization series. This third peak exhibits a high value of the enthalpy change, which increases the total energy of the transformation close to the values reported on a fully crystalline sample with the same composition [20]. The qualitative and quantitative calorimetric results obtained at the last step are similar to the ones obtained after any of the crystallization treatments that have been described in the previous section, i.e. the martensitic transformation is split in two important calorimetric peaks (Fig. 1).

3.2. Transmission Electron Microscopy

The observations carried out by TEM on as cast specimens reveal the presence of large completely amorphous areas. In addition to these amorphous regions, large crystalline zones with big grains (several μm in size) are also present. Although the observation of one or the other of these microstructures depends mainly on the sample that is observed in the microscope, both have been frequently found to coexist together in adjacent zones of the same region as well, revealing a spherical shape of the big crystalline regions, which form smooth interfaces with the surrounding amorphous

material (Fig. 2a). All selected-area electron diffraction patterns (SAEDP) from these big platelets have been successfully indexed as monoclinic martensite (B19′).

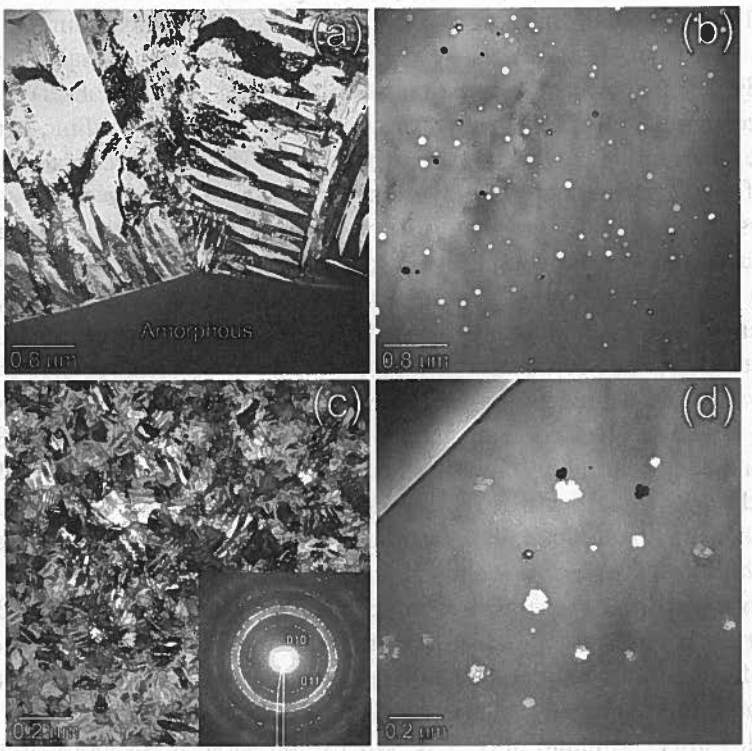

Fig. 2. TEM micrographs of the $Ni_{50}Ti_{32}Hf_{18}$ ribbon in the as cast state showing (a) the interface between an amorphous zone and a crystalline region consisting of two big crystals and (b) a region with smaller spherical crystals of austenite. (c) Area of fine grain filled with martensite plates and the corresponding SADP in a $Ni_{50}Ti_{32}Hf_{18}$ melt spun ribbon crystallized in the DSC with a fast run up to 875 K. (d) Bright field micrograph of the $Ni_{50}Ti_{32}Hf_{18}$ ribbon annealed at 775 K for 1 minute

Occasionally, small crystals embedded in the amorphous matrix have also been observed in as cast samples. The regions with small crystals exhibit different distributions, ranging from densely concentrated with relative larger sizes to areas with lower concentration and size. The shape of the small crystals is spherical in regions with lower density and size (Fig. 2b), whereas this sphericity is lost in zones with almost no amorphous phase and crystals contacting each other. The diameters of the small crystals are normally below 0.4 μm (or even 0.1 μm in some regions) and their SAEDP show that they are mainly austenitic. However, some of these regions with crystal sizes slightly larger than 0.4 μm exhibit martensitic structures in SAEDP as well as the typical contrast of self-accommodated plates within the small crystals in bright field images.

TEM observations performed after any of the crystallization treatments over T_C described in the previous section, or in samples after 10 min at 775 K, confirm the complete crystallization of the previously existing amorphous areas. The microstructure of the fully crystallized specimens shows big crystalline areas similar to the ones in the as cast state. In addition, new crystallites with sizes usually below 0.2 μm and mainly filled by even tinier martensite plates (Fig. 2c) are observed in the fully crystallized samples; SAEDP from such areas confirm the monoclinic structure of the martensite (inset in Fig. 2c). These dense polycrystalline regions containing such a high amount of small grains may be only obtained if a high density of crystal nucleation points exists, with almost no place for growing. This means that the energetic cost for the nucleation of new crystals from the amorphous phase in this alloy is rather similar to the growth energy, which promotes a massive crystal nucleation almost independently of the temperature of the thermal treatment, contrary to the case of $Ti_{50}Ni_{25}Cu_{25}$ [12]. The microstructure of the fully crystallized samples is irrespective of the crystallization process, as the absence of important differences between their DSC runs already suggested. Thus, attending to the present TEM and DSC results, it can be concluded that aging slightly under T_C during enough time produces similar results to the crystallization over T_C. The lack of correlation between the microstructure and the annealing temperature, under isothermal treatments above T_C, was also reported by Shi *et al.* for a $Ti_{50}Ni_{25}Cu_{25}$ alloy [8].

No changes on the chemical composition between regions with different microstructures have been observed by EDX measurements, neither in the as cast samples nor in the fully crystallized ones. Therefore, the crystallization into various microstructures is not promoted by any composition partitioning.

Samples after 1 minute at 775 K still exhibit large amorphous areas, since the ribbon has not been completely crystallized. After this short treatment, the small crystallites embedded in the amorphous regions do not show sharp and perfect spherical shapes any more (Fig. 2d), as in the as cast samples, which is an indication of a not completely isotropic growth like the one in $Ti_{50}Ni_{25}Cu_{25}$ [12].

Increasing the aging time at 775 K up to 100 minutes causes the growth of precipitates in the big crystals (and possibly in the small ones as well), which was not detected in previous stages. Therefore, the calorimetric changes observed here in the last stage of the treatment at 775 K are likely dominated by the rapid nucleation and growth of precipitates, as it has been already reported in the case of as cast fully crystalline $Ni_{50}Ti_{32}Hf_{18}$ ribbons annealed at 775 K [20].

Finally, *in-situ* heating experiments in the microscope produce the fully reverse martensitic transformation in the sample. However, the small crystallites undergo the reverse transformation relatively close to RT, whereas the large crystals require considerably higher temperatures. In a similar way, small crystals transform under cooling at much lower temperatures than the larger crystals. These experiments verify the previous thermal results from the fully crystallized ribbons and illustrate that the calorimetric peak at lower temperatures corresponds to the martensitic transformation of the small

crystals, whereas the peak at higher temperatures is associated with the transformation of the as cast larger crystals.

4. Discussion

In the present contribution it has been shown that the crystallization experiments promote the splitting of the martensitic transformation in two important separated stages, independently of using crystallization temperatures either above or below T_C. The additional calorimetric peak at lower temperatures in respect to the as cast state is related to the transformation of the new crystalline regions formed during the crystallization. The much lower grain size of these regions as compared to the crystals that already existed in the as cast alloy promotes a significant decrease in the transformation temperatures. In addition to this difference, the small crystals in this alloy also show a wider hysteresis than the big crystalline regions. Thermodynamically speaking, the decrease of the transformation temperatures for the new small crystals implies some rising of the elastic term (*e.g.* due to increased difficulties in the accommodation of the martensitic variants), whereas a larger hysteresis is related to higher frictional terms, indicating that the same martensite exhibits more difficulties to retransform.

In as cast $Ni_{50}Ti_{32}Hf_{18}$ samples, the big crystalline regions surrounded by amorphous areas forming smooth interfaces are similar to the ones reported in $Ti_{50}Ni_{25}Cu_{25}$, where some controversy has been generated around this topic. In [12, 20] the spherical shape and smooth interfaces of the crystals have been related to an isotropic nucleation/growth of the crystals by thermal treatments performed after casting the ribbon. However, spherical crystals with diameters up to 10 μm [11] or 22 μm [10] are also observed in the initial state in the $Ti_{50}Ni_{25}Cu_{25}$ alloy. The spherical shape and the smoothness of the interfaces in these works were attributed to the fact that the spherical grains were produced somehow during the fast solidification [10]. Also, in the present work, spherical crystals with smooth interfaces have been already observed in as cast state, thus being evident that they were produced during the fast solidification. Furthermore, the formation of new grains by thermal treatments (or the growth of the existing ones) in $Ni_{50}Ti_{32}Hf_{18}$ samples do not lead to crystals with so perfect spherical shape and sharp interfaces with the amorphous regions but with local wavy interfaces (Fig. 2d), contrary to what was observed in $Ti_{50}Ni_{25}Cu_{25}$ ribbons [12].

Concerning the presence of crystals either in the martensitic or austenitic phase at RT in the as-spun state, the variation in the structure is mainly a consequence of the difference in the grain size (*i.e.* difference in the transformation temperatures). Thus, crystals with grain diameters higher than about 0.4 μm are observed at RT in martensite, whereas the smaller ones are in austenite. On the other hand, the presence at RT of martensitic crystals with diameters below 0.2 μm in fully crystallized samples shows that another factor should play an important role in the transformation temperatures of the small crystals. This additional factor could be, most probably, the higher surface

energy of the crystalline-amorphous interfaces, which has been proved to decrease the transformation temperatures in a $Ti_{50}Ni_{25}Cu_{25}$ ribbon [22].

5. Conclusions

In the present contribution it has been shown that the as-cast $Ni_{50}Ti_{32}Hf_{18}$ exhibits a mixture of amorphous and crystalline phases with a rich variety of microstructures. The first steps during the growth of crystals from the amorphous areas by subsequent crystallization treatments below T_C lead to crystals with wavy crystalline-amorphous interfaces and, therefore, with non-perfect spherical shapes.

However, the microstructure and the calorimetric behavior of the fully crystalline sample is independent of the thermal treatment and whether the latter is performed over or below T_C. The microstructure at RT of the fully crystallized samples consists of regions with small crystallites (~ 0.2 μm), mainly in martensite, produced during the thermal treatment, together with the large crystals originated during casting. The new crystallized regions with small grain size show lower transformation temperatures and higher hysteresis in comparison to the big crystalline zones already existing before crystallization, leading to a two-step transformation in DSC runs. This shows a clear example of the dependence of the transformation temperatures on the grain size, although additional mechanisms have to be considered when dealing with small grains, as the presence of crystalline-amorphous interfaces that could further lower the transformation temperatures.

Acknowledgements

Partial financial support from DGI (HF1999-0056, MAT2000-0862-C03-02 and MAT2002-00319 projects) are acknowledged.

REFERENCES

[1] J. Dutkiewicz, T. Czeppe, J. Morgiel, Mat Sci Eng A **273-275**, 703-707 (1999).
[2] C. T. Hu, T. Goryczka, D. Vokoun, Scripta Mater **50**, 539-542 (2004).
[3] J. H. Zhu, D. P. Dunne, G. W. Delamore, N. F. Kennon, Proc. of the ICOMAT-92, ed. by C.M. Wayman, J. Perkins (Monterey Institute of Advanced Studies, Carmel), 1083-1088 (1993).
[4] N. DeCristofaro, Mater Res Bull **23**, 50-56 (1998).
[5] Z. Stoklosa, J. Rasek, P. Kwapulinski, G. Haneczok, G. Badura, J. Lelatko, Mat Sci Eng C **23**, 49-53 (2003).
[6] V. Kolomytsev, M. Babanly, R. Musienko, A. Sezonenko, P. Ochin, A. Dezellus, P. Plaindoux, R. Portier, Ph. Vermaut, J Phys IV **11**, 457-462 (2001).

[7] F. Dalle, A. Dezellus, C. Elgoyhen, M. Larnicol, M. Masse, P. Ochin, P. Plaindoux, R. Portier, Ph. Vermaut. Final report of the E.U. INCO-Copernicus project IC15-CT96-0704 (1999).
[8] J.D. Shi, J.L. Ma, T. Gao, Z.J. Pu, K.H. Wu, Materials Research Society Symposium Proceedings Vol 400, ed. by R. Bormann, G. Mazzone, R.D. Shull, R.S. Averback, R.F. Ziolo (Warrendale: The Materials Research Society), 221-226 (1996).
[9] P. Schloßmacher, N. Boucharat, H. Rösner, G. Wilde, A.V. Shelyakov, J Phys IV **112**, 731-734 (2003).
[10] Z.L. Xie, J. Van Humbeeck, Y. Liu, L. Delaey, Scripta Mater **37**, 363-371 (1997).
[11] J. Morgiel, E. Cesari, J. Pons, A. Pasko, J. Dutkiewicz, J Mater Sci **37**, 5319-5325 (2002).
[12] R. Santamarta, D. Schryvers, Mater Trans **44**, 1760-1767 (2003).
[13] R. Santamarta, D. Schryvers, Intermetallics **12**, 341-348 (2004).
[14] H. Rösner, A.V. Shelyakov, A.M. Glezer, P. Schloßmacher, Mat Sci Eng A **307**, 188-189 (2001).
[15] F. Dalle, V. Kolomytsev, P. Ochin, R. Portier, Scripta Mater **44**, 929-934 (2001).
[16] R. Santamarta, A. Pasko, J. Pons, E. Cesari, P. Ochin, Mater Trans **45**, 1811-1818 (2004).
[17] D.R. Angst, P.E. Thoma, M.Y. Kao, J. Phys. IV **5**, 747-752 (1995).
[18] J. Beyer, J.H. Mulder, Materials Research Society Symposium Proceedings 360, ed. by S. Trolier-McKinstry, K. Uchino, M. Wun-Fogle, E.P. George, S. Takahashi (Materials Research Society), 443-454 (1995).
[19] R. Santamarta, C. Seguí, J. Pons, E. Cesari, Scripta Mater **41**, 867-872 (1999).
[20] E. Cesari, J. Pons, R. Santamarta, C. Seguí, D. Stróz, H. Morawiec, Proc. of XVIII Conf. on Applied Crystallography, ed. by H. Morawiec and D. Stróz, (World Scientific), 171-185 (2001).
[21] H. Rösner, A.V. Shelyakov, A.M. Glezer, K. Feit, P. Schloßmacher, Mat Sci Eng A **273-275**, 733-737 (1999).
[22] R. Santamarta, D. Schryvers, Scripta Mater **50**, 1423-1427 (2004).

Received: 3 November 2004.

A R C H I V E S O F M E T A L L U R G Y A N D M A T E R I A L S
Volume 49 2004 Issue 4

T. GORYCZKA*, P. OCHIN**, H. MORAWIEC*

TEXTURE AND THE SHAPE MEMORY EFFECT IN Ni-Ti-Cu STRIPS CASTED BY TWIN ROLL TECHNIQUE

TEKSTURA I EFEKT PAMIĘCI KSZTAŁTU W STOPACH Ni-Ti-Co ODLEWANYCH TECHNIKĄ SZYBKIEGO SCHŁADZANIA Z FAZY CIEKŁEJ W UKŁADZIE PODWÓJNEGO BĘBNA CHŁODZĄCEGO

Strips of $Ni_{25}Ti_{50}Cu_{25}$ shape memory alloys produced by the twin roll casting technique were solidified from two melt temperature: 1400°C and 1450°C. It results in completely different orientation of grains across the strip forming fibre and sheet texture components. Especially presence of (001)[110] texture orientation improves shape recovery with maximal elongation up to 5%.

Taśmy stopu $Ni_{25}Ti_{50}Cu_{25}$ z pamięcią kształtu zostały wytworzone metodą szybkiego schładzania z fazy ciekłej w układzie podwójnego bębna chłodzącego. Krzepnięcie taśm prowadzono dla dwóch różnych temperatur ciekłego metalu: 1400°C i 1450°C, co przyczyniło się do powstania różnej tekstury ziarn na przekroju taśmy. Zwłaszcza obecność składowej tekstury (001)[110] wpłynęła korzystnie na odzysk pamięci kształtu dzięki czemu uzyskano ponad 5% wydłużenia względnego taśmy.

1. Introduction

It is well known that the shape memory effect which is correlated with a reversible martensitic transformation strictly depends on crystallographic orientation. Therefore, the orientation of grains in polycrystalline materials is one of the most important factors for controlling shape memory behaviour. M o n a s h e v i c h [1] studied the texture influence on shape memory effect and has found that the presence of a {112}< 110 > component in hot- rolled TiNi sheet increases the possibility of deformation by torsion. Such textural components as {110}< 110 > and {111}< 110 > were also observed in hot-rolled and cold-rolled TiNi sheets and affected the shape memory effect [2, 3].

* UNIVERSITY OF SILESIA, INSTITUTE OF MATERIALS SCIENCE, BANKOWA 12, 40-007 KATOWICE, POLAND
** CECM-CNRS, 15 RUE G. URBAIN, 94407 VITRY-SUR SEINE, FRANCE

Apart from mechanical deformation, preferred orientation of the grains can be induced by technologies, which provide rapid solidification from molten state, such as melt-spinning or twin-roll casting technique. Dependently on a cooling rate, columnar grains are formed under "frozen" small grains zone. Directional heat outflow causes the texture forming, also at the first stage of solidification in the "frozen" zone.

In the present work $Ni_{25}Ti_{50}Cu_{25}$ alloy was manufactured by twin roll casting technique. The main purpose was to study the distribution of grains orientation across the strip in respect of the shape memory recovery.

2. Experimental procedure

Thin strips were prepared in vertical twin roll caster. The bulk alloys with a nominal composition of Ni 25 at.%, Ti 50 at.% and Cu 25 at.% were inductionally melted under helium gas atmosphere. Ingot was placed to the quartz crucible fixed directly over a gap between two wheels (400 mm in diameter each). After induction melting, the melt was vertically ejected with argon pressure between two wheels rotated in opposite directions. Thin metal layers solidified on the surface of the wheels simultaneously, when the remaining liquid was spread from central part of the gap to its outer side forming the strip. Two strips were obtained with different melt temperature: 1400°C (strip A) and 1450°C (strip B) – for details see table 1. Obtained strips revealed smooth surface without cracks.

TABLE 1

Processing parameters and thickness of the studied alloys

Material	Melting temp. [°C]	Wheel material	Wheel speed [m/s]	Ejection pressure [MPa]	roller- gap [μm]	Thickness [μm]	Width [mm]
Strip A	1400	Cu	0.6	0.025	200	352	45
Strip B	1450	Cu	0.6	0.025	100	305	45

In order to study grains distribution on the cross-section of the strip samples were chemically thinned by etching in 500 ml H_2O + 62 ml HF + 125 ml HNO_3 solution simultaneously from both sides up to thickness of 150 μm every 50 μm (figure 1).

Microstructure of strips was observed using an optical microscope NEOPHOT equipped with a digital camera for image storing. The samples were polished following by etching in a solution which consist of: 50 ml H_2O_2 + 12 ml HNO_3 + 3 ml HF.

Transformation temperatures were determined from measurement carried out using Perkin-Elmer differential scanning calorimeter (DSC). Samples were preliminary heated to 100°C and after that cooled 40 degrees below temperature where martensitic transformation was completed (M_f) and after that again heated 40 degrees over reverse martensitic transformation finish temperature (A_f) with cooling/heating rate of 10 deg/min. Transformation temperatures were determined from thermal peaks using a slope line extension method.

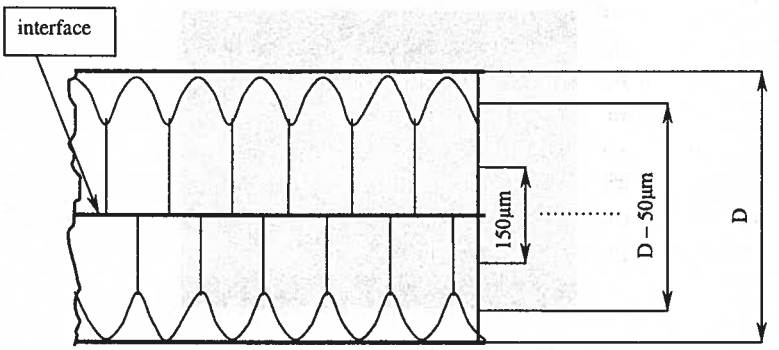

Fig. 1. Scheme of a sample preparation; D – thickness of the strip

Sequence of martensitic transformation was studied by X-ray diffraction patterns obtained on the INEL diffractometer, equipped with a curved position-sensitive detector CPS120, a flat Ge monochromator and a temperature attachment. The temperature device gives the possibility to record X-ray diffraction patterns from –100°C to +120°C [5]. X- ray diffraction patterns were recorded with a temperature step of 4 degrees.

The pole figures were recorded on Philips PW1130 diffractometer with texture goniometer only by reflection mode to the maximum tilting angle 80°. Shulz formula was applied for correction of the pole figure intensity.

Shape recovery was studied by means of elongation versus temperature changes under constant load.

3. Results and discussion

3.1. Microstructure of the strip

The typical microstructure of the twin roll cast strip is shown in figure 2. As the crystallization front proceeds from both wheels the columnar grain microstructure is developed. Due to the two-sides solidification an interface between solidified shells was formed. The interface on the cross-section, remains straight line separating two joined symmetrical parts of the strip. In the strip A (figure 2a) solidification on wheel surface caused frozen grain's zone formation under which columnar grains are shaped. As a result of higher cooling rate, which is realized in the strip B, additional layer of shorter column of grain is crystallized.

3.2. Transformation behavior

DSC cooling/heating curves registered for the strip A and B are shown in figure 3. In general, both strips A and B reveal presence of thermal peaks correlated to martensitic and reverse martensitic transformation with transformation temperatures given in table 2.

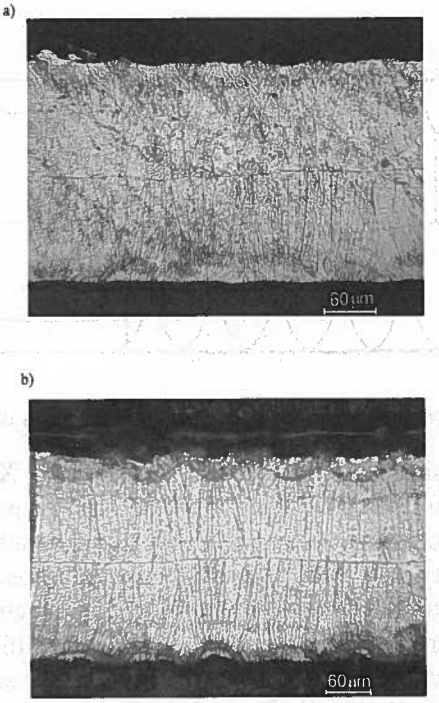

Fig. 2. Cross-section of the twin rolled strip: A (a) and B (b)

TABLE 2

Transformation temperatures of the studied strips

Specimen	Thickness D [μm]	M_s [°C]	M_f [°C]	A_s [°C]	A_f [°C]
Strip A as-cast	352	52.1	29.3	37.9	60.2
Strip A thinned	150	50.6	43.2	52.3	57.9
Strip B as-cast	305	29.2	21.1	29.2	38.5
Strip B thinned	150	26.2	19.5	28.5	36.0

As-cast strip A reveals two overlapping thermal peaks on cooling and heating curves. Both of these peaks are related to B2↔B19 transformation. The low temperature peak may be caused by the presence of outside layer with different chemical composition due to the segregation which occurs during crystallization.

The ribbon, with the same chemical composition but manufactured by the melt-spinning, shows also a thin layer on the surface which consists of monoclinic martensite B19' [6]. In order to find a reason of peak splitting, another sample of strip A was cut off from its central part and thinned to 150 μm by chemical etching. First part of the thinned sample was measured with DSC and second part conveyed to the X-ray diffraction analysis. Obtained DSC cooling/heating curves, for as-cast and thinned strip A, are compared each to the other in figure 3a.

a)

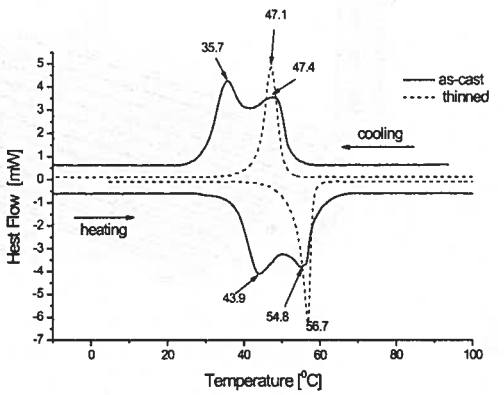

b)

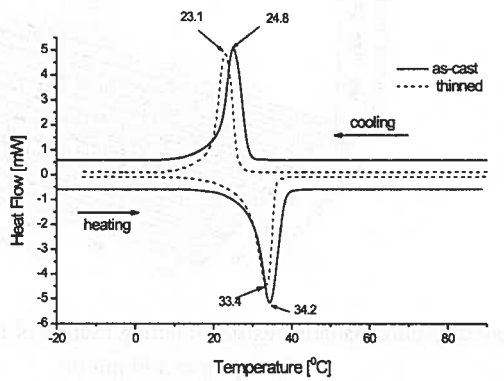

Fig. 3. DSC cooling/heating curves registered for: strip A (a) and strip B (b)

It has been seen that the lower temperature thermal peak completely vanished after surface removing. Moreover, transformation temperatures of thinned sample are in a good agreement with the higher thermal peak registered for the as-cast sample. On the other hand, X-ray diffraction pattern stored on heating (figure 4) for both samples: as-cast and thinned one shows that only orthorhombic martensite B19 was transformed directly to the parent phase B2. On the contrary, the parent phase B2 was transformed to orthorhombic martensite on cooling. However, for the as-cast strip A some amount of B19 martensite was still present despite of sample cooling more than 50 degrees over the A_f temperature. Also some non- transformable parent phase B2 was detected at the X-ray diffraction pattern taken 40 degrees below M_f temperature. This may confirm the suggestion that the outside thin layer of the strip has different chemical composition caused by the segregation process. For thinned sample all amount of martensitic phase and parent phase was completely transformed on cooling and heating, respectively.

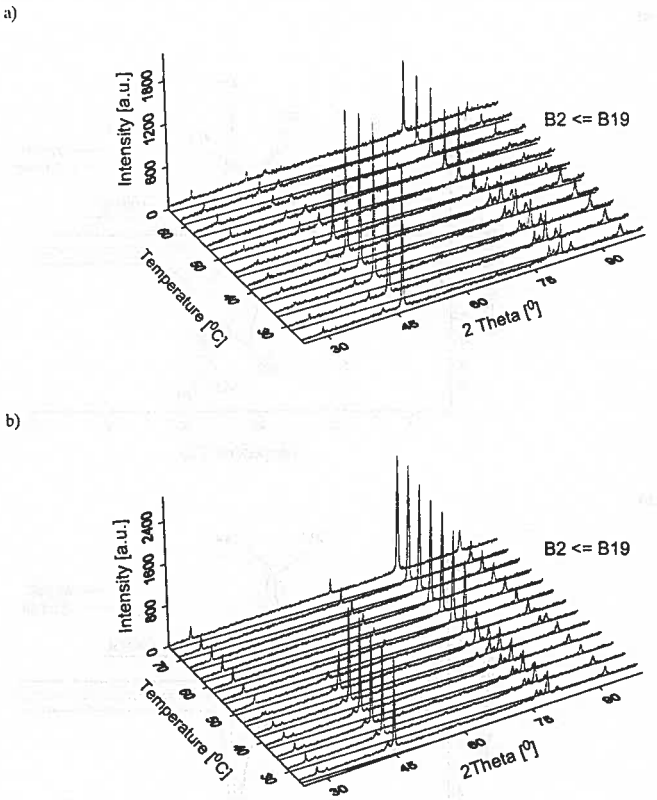

Fig. 4. Set of X-ray diffraction patterns registered during heating of the strip A: as- cast (a) and After etching up to 150 μm (b)

In case of as-cast strip *B*, only one thermal peak appeared on cooling and heating DSC curve, respectively. Also, DSC curves (figure 3b) registered for thinned strip B (150μm) reveal one stage transformation, however, transformation temperatures are shifted in direction of lower temperature region about 2 degrees. Analysis of X-ray diffraction patterns confirmed that both studied samples of strip B: as-cast and thinned, transform with sequence B2↔B19.

Comparing DSC curves for as-cast strip A and B it has been clearly shown that higher temperature of melt (1450°C in case of strip B) results in higher cooling rates, what in consequence leads to defects increasing and finally shifts transformation temperature to the lower region.

3.3. Texture

The measurement of the preferred orientations were carried out at room temperature on a circular sample 2 cm in diameter. In order to study grains orientation across the strip thickness, pole figures were registered after thinning of sample for every 50 μm

up to thickness of 150 μm. Pole figures for the strip A were determined starting from the as-cast thickness 352 μm up to 150 μm, whereas for strip B – 305 μm (as-cast), 300 μm, 250 μm, 200 μm and 150 μm. The indexes of pole figures were given in the B2 structure description based on the crystallographic correlation between the lattices of the B2 and B19 phases.

Thus, for texture analysis, the pole figures for {100}, {110} and {112} planes, referring to indexes of the parent phase B2, were registered. Samples for pole figure measurement were fixed in a holder in such a way that an RD direction at the pole figure corresponds to the wheel rotation direction. The orientation distribution function (ODF) was calculated from obtained pole figure data.

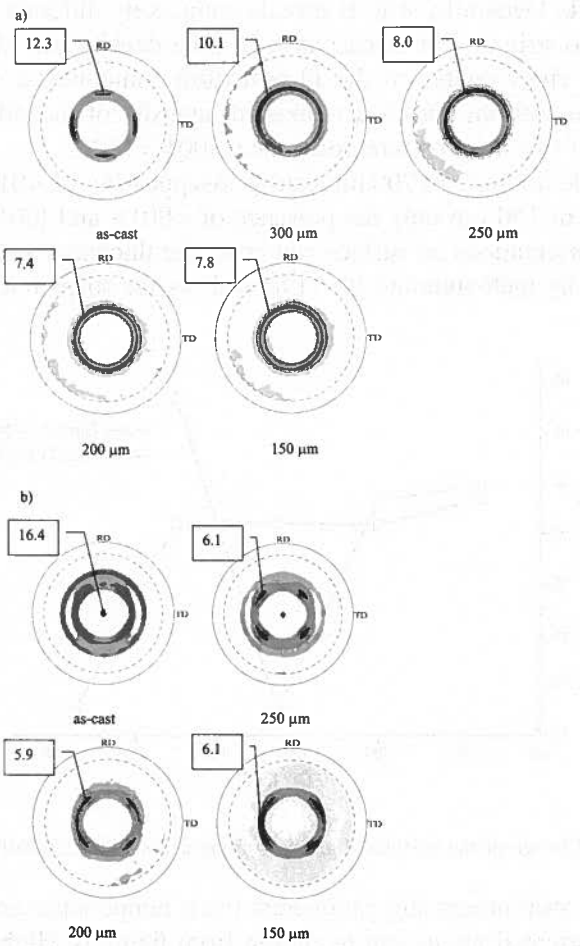

Fig. 5. Set of the $\{011\}_{B2}$ pole figures determined for strip A (a) and B (b)

Figure 5a shows a set of the $\{011\}_{B2}$ pole figures collected for strip A versus thickness changes. The pole figure for as-cast strip reveals pole density concentration around of <001> axis as well as clustering around orientation of the {001}<100> sheet texture component. The texture of studied strip is relatively strong. Maximum of the pole density achieves twelve levels for {011} pole figures whereas for {001} pole figure exceed 169 levels.

After sample thinning to 300 μm the sheet texture component vanishs and for sample 200 μm thick only < 001 > fibre components exists. The volume fraction of grains oriented with the fibre < 001 > component varies from 51% (150 μm) to 57% for as-cast strip. Considering the sum of total volume of oriented grains along both textural component – only 27,4% volume of grains is randomly oriented. This fact indicates that the volume of preferentially oriented grains decreases from the surface to the middle of the strip. A set of the {011} pole figures for thinned strip B is shown in figure 5b. Generally, strip B reveals completely different texture orientations when compared to strip A. For as-cast strip B, pole density was clustered around two centre-symmetric rings related to the fibre texture components: <011> and <001>. Sample thinned to 250 μm reveals a weakened intensity of the <011> orientation but strong intensity of the sheet texture component {001}<110>.

Farther sample thinning to 200 μm causes disappearing of <011> fibre orientation and for thickness of 150 μm only the presence of <001> and {001}<011> was stated. The determined orientations on surface and cross the thickness are quit different to the ribbons obtained by melt-spinning [6, 7] as well as for strips hot and cold rolled [8, 9].

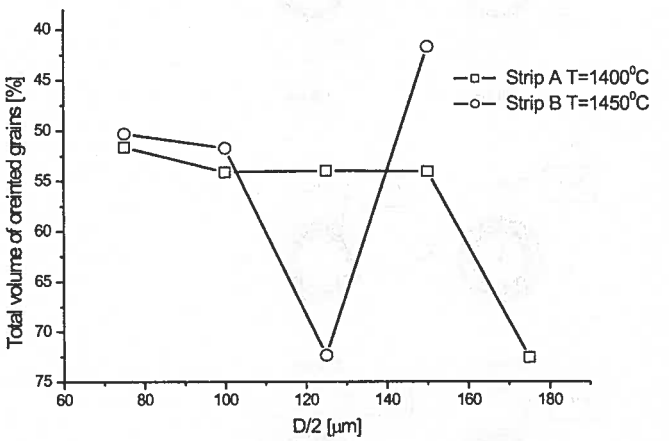

Fig. 6. Change of the orientated grains volume across the strip half thickness

The effect of strip processing parameters (melt temperature and roller-gap) on the total volume of oriented grains can be driven from figure 6. Higher melt temperature (strip B) causes higher cooling rate as well as smaller roller-gap limits time contact, what in consequence leads to melt "freezing" on the wheel surface and only 40% of

grains volume is preferentially oriented. Below the surface of the strip B only less than 28% of grains are randomly oriented. At the opposition to that, for the strip A the lower melt temperature causes the highest grains orientation just on the surface. Approaching to the half of strip thickness, in the case of both strips A and B, volume of the preferentially oriented grains decreases and finally reaching more than 54%.

3.4. Shape recovery

The shape recovery of the strip was determined by measuring the change of elongation during reversible martensitic transformation under constant tensile load. Samples were cut off along the strip and mounted in such a manner that applied load was parallel to the wheel rotation direction. Completed hysteresis of the shape recovery was registered in temperature range between M_f–40° and A_f+40° (figure 7). From the loop, the maximal elongation was determined as the highest point of the hysteresis. In order to find material response for the stress, after cycle finishing, applied stress was increased of 10 MPa comparing to the previous cycle.

a)

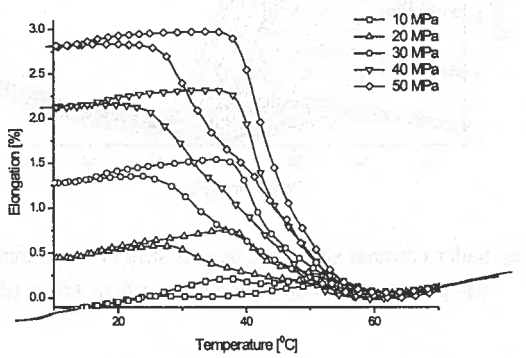

b)

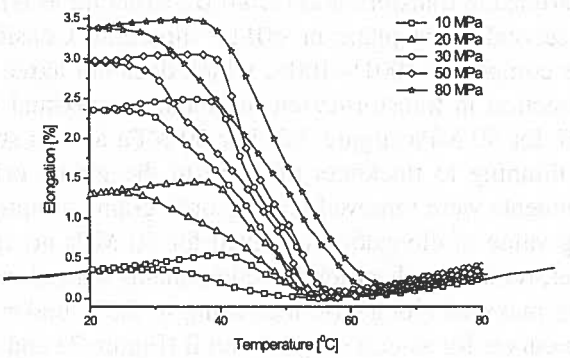

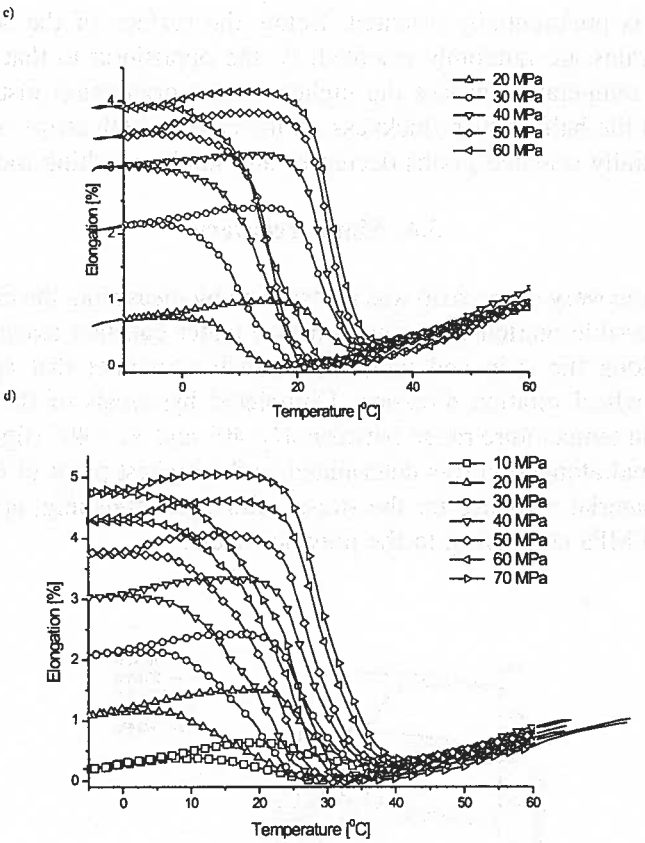

Fig. 7. Shape recovery under constant stress for: as-cast strip A (a), thinned strip A to 150 μm (b), as-cast strip B (c) and thinned strip B to 150 μ (d)

As-cast strip A shows two steps of the shape recovery with the transformation temperature correlated to the results determined from DSC curves. It has been very well known that martensitic transformation from B2 structure to B19 proceeds by atom shearing in every second {011} plane in <011> direction. Considering the presence of the sheet texture component {001}<100>, which does not agree with the privileged crystallographic direction in transformation mechanism, maximal value of elongation does not exceed 3% for 50 MPa (figure 7a). For 60 MPa as-cast stripe A broke down.

After strip A thinning to thickness of 150 μm the grains oriented according to sheet texture components were removed leaving only grains oriented with fibre texture <001>. Comparing value of elongation obtained for 50 MPa no significant difference was stated. However, removing sheet texture components caused increasing of durability, which results in maximal elongation increasing to 3.5% under 80MPa (figure 7b).

Comparing the curves for as-cast strips A and B (Figure 7a and 7c) for 50 MPa load – the increase of elongation for strip B is visible. The strip B (thinned up to 150 μm),

which consists of the grain mostly oriented along the {001}<110> component texture, shows increase of maximal elongation up to 5% thanks to the privileged direction [110] (figure 7d).

4. Conclusions

The obtained results can be summarized as follows:

- Both of the studied strips of ternary Ni-Ti-Cu alloys reveal following sequence of the martensitic transformation: B2↔B19.
- The lower cooling rate realizing during solidification of the strip A (lower temperature of the liquid metal) causes grains forming and their concentration around < 001 > crystallographic orientation.
- Presence of the sheet texture component {001} < 110 > in strip B improves the degree of shape memory recovery measured by elongation changes.

REFERENCES

[1] L.A. Monasevich, Yu.I. Paskal, V.E. Prib, G.D. Timonin, D.B. Chernov, Metalloved. i Term. Obrab. Met. **9**, 62 (1979).
[2] S. Eucken, J. Hirsch, Matter. Sci. Forum **56-58**, 487 (1990).
[3] D.Y. Li, X.F. Wu, T. Ko, Acta metal. mater. **38**, 19 (1990).
[4] P. Ochin, A. Dezellus, Ph. Plaindoux, Ph. Vermaut, F. Dalle, R. Portier, Materials Science and Engineering **A346** 320 (2003).
[5] H. Morawiec, T. Goryczka, A. Chrobak, Mater. Sci. Forum **166-169**, 147 (1994).
[6] T. Goryczka, M. Karolus, P. Ochin, H. Morawiec, J. Phys. IV France **11**, Pr8-345 (2001).
[7] T. Goryczka, H. Morawiec, P. Ochin, Proc. of the XIX Int. Conf. on Appl. Cyst. 138 (2003).
[8] S.H. Chang, S.K. Wu, Scripta Mat. **50**, 937 (2004).
[9] H. Inoue, N. Miwa, N. Inakazu, Acta Mater. **44**, 4825 (1996).

Received: 3 November 2004

A R C H I V E S O F M E T A L L U R G Y A N D M A T E R I A L S
Volume 49 2004 Issue 4

G.P. VASSILEV*

PHASE EQUILIBRIA IN THE Zn-RICH REGIONS OF THE Cu-Ni-Zn AND Co-Ni-Zn SYSTEMS

RÓWNOWAGI FAZOWE W BOGATEJ W Zn CZĘŚCI UKŁADÓW Cu-Ni-Zn i Co- Ni-Zn

Cu-Ni-Zn and Co-Ni-Zn alloys were prepared in quartz tubes using pure components. The specimens were polished and their phase compositions were determined by electron probe microanalyses.

The phase boundaries in the zinc-rich corners of the Cu-Ni-Zn and Co-Ni-Zn systems have been investigated at 868 K. The phase relations at higher temperatures (1178 and 1080 K) are verified as well. Ternary compounds non-related with the binary systems have not been found. The ternary extension of the Cu-Zn ε-phase contains up to 4 at.% Ni. The location of the phase boundaries of the ternary liquid and γ-phases have been precised for both ternary systems.

Isothermal sections of the phase diagrams Cu-Ni-Zn (at 868 K) and Co-Ni-Zn (at 868 K and 1083 K) have been constructed using the experimental data obtained in this work and literature data about the end binary systems.

Badane stopy Cu-Ni-Zn i Co-Ni-Zn przygotowanio z czystych metali przez stopienie w ampułach kwarcowych po próżnią. Skład fazowy polerowanych próbek tych stopów okkreślono za pomoca mikroanalizy elektronowej.

Dla bogatych w Zn części ukladów fazowych Cu-Ni-Zn i Co-Ni-Zn określono granice fazowe dla temoeratury 868 K. Relacje fazowe zweryfikowano także dla wyższych temperatur: 1083 i 1178 K. Nie stwierdzono występowania niezwiązanych z fazami dwuskładnikowymi, osobnych faz trójskładnikowych. Określono maksymalną rozpuszczalność Ni w fazie Cu-Zn-ε na ok. 4%at.

Sprecyzowano położenie granic fazowych pomiędzy roztworem ciekłym, a fazą γ w obu układach trójskładnikowych.

Wykorzystując dane własne i dane literaturowe dla układów dwuskładnikowych skonstruowano izotermiczne przekroje układów fazowych Cu-Ni-Zn dla temperatury 868 K i Co-Ni-Zn dla 868 i 1083 K.

* UNIVERSITY OF SOFIA, FACULTY OF CHEMISTRY, 1 J. BOURCHIER AV., 1164 SOFIA, BULGARIA

1. Introduction

The iron-group metals, copper and the zinc are largely used as pure elements or alloys. Moreover, some materials based on the iron or cobalt are interesting because of their attractive magnetic properties. The development of multicomponent high-temperature solders including these ternary systems might be foreseen too. It has also been found that third element additions (for example Ni) to the galvanizing bathes improve coatings quality. Thus, phase equilibria in ternary systems involving these metals (in this case the systems Cu-Ni-Zn and Co-Ni-Zn) are technologically interesting.

Nevertheless, there is lack of phase diagram data concerning the zinc-rich corners of both ternary systems. Thus, the purpose of the present work is to obtain experimental data about the zinc-rich region and to verify the phase boundaries of the solid phases.

1a. Cu-Ni-Zn System

The Cu-Ni-Zn phase diagram is of fundamental interest for the design of multicomponent copper-nickel alloys such as materials with high electric or corrosion resistance and some types of brass and bronze. The studies of Cu-Ni-X systems (where X is a low melting metal) are prospective for the development of high temperature solders as well because both copper and nickel are often used substrates. For these reasons numerous phase equilibria investigations have been done [1-2]. The Cu-Ni-Zn phase diagram has been evaluated by Chang et al. [3]. Due to the latter work a liquidus projection and an isothermal section at 1084 K have been presented.

Recently, new thermodynamic descriptions of the Cu-Ni-Zn system [4, 5] appeared, both essentially accepting the assessments done by Mey [6] for the Cu-Ni system, by Kowalski and Spencer [7] for the Cu-Zn system, and by Vassilev et al. [8] for the Ni-Zn system. We would like to notice that some binary phases in both Cu-Zn and Ni-Zn systems have been remodelled for the sake of simplicity, when the optimisations of the ternary Cu-Ni-Zn phase diagram were done. No ternary phase have been revealed in this system, but continuous solutions regions for the face centred cubic and γ- brass type phases are observed.

1b. Co-Ni-Zn System

Zinc binary and ternary phase diagrams with Co and Ni have been subject of experimental studies by the authors [9-13]. Thermochemical studies of the Ni-Zn, Co-Zn and Co-Ni-Zn systems have been published [14-17] as well as thermodynamic assessments of the Ni-Zn [18-20] and Co-Zn systems [20, 21]. No ternary phases have been found in the Co-Ni-Zn system, but continuous solutions regions for the face centred cubic and γ-brass type phases are observed. The crystal structures descriptions of the phases of the end-member systems (Co-Ni, Co-Zn and Ni-Zn) are compiled in Table 1.

TABLE 1

Crystal Structures of phases of the systems Co-Ni, Cu-Ni, Co-Zn and Ni-Zn [1, 2, 8, 21]

Phase and system	Homog. Interval or formula	Pearson symbol	Space group	Prototype
α, (αCo,Ni)*	0-100 at.%Ni	cF4	$Fm\bar{3}m$	Cu
α,(αCo,Zn)*	0-37.5 at.%Zn	cF4	$Fm\bar{3}m$	Cu
α,(αCu,Ni)	0-100 at.%Ni	cF4	$Fm\bar{3}m$	Cu
α,(αCu,Zn)	0-40 at.%Zn	cF4	$Fm\bar{3}m$	Cu
α,(αNi,Zn)	0-39.5 at.% Zn	cF4	$Fm\bar{3}m$	Cu
β′(CoZn)***	50 at.%Zn	cP20	$Pm\bar{3}m$	CsCl
β_1(CoZn)*	48.0-55.0	CP20	$P4_132$	βMn
β(CuZn)*** disordered	36-54 at.% Zn	Cl2	$Im\bar{3}m$	W
β′(CuZn) ordered	36-54 at.% Zn	cP2	$Pm\bar{3}m$	CsCl
β (NiZn)***	47.5-58.5 at.% Zn	cP2	$Pm\bar{3}m$	CsCl
β_1(NiZn)*	45.5-52 at.% Zn	tP2	$P4/mmm$	AuCu
γ(Ni_5Zn_{12})	70-85 at.% Zn	cI52	$I\bar{4}3m$	Cu_5Zn_8
γ(Co_5Zn_{21})	69-85 at.% Zn	cI52	$I\bar{4}3m$	Cu_5Zn_8
γ(Cu_5Zn_8)	57-70 at.% Zn	cI52	$I\bar{4}3m$	Cu_5Zn_8
γ_1($CoZn_7$)	$CoZn_7$	****	cubic	γ-brass related
γ_2(Co-Zn)	$CoZn_{13}$	mC28	$C2/m$	$CoZn_{13}$
δ (Ni-Zn)	NiZn8	mC28	$C2/m$	$CoZn_{13}$
δ′ (Cu-Zn)***	$CuZn_3$	hP3	$P\bar{6}$	$CuZn_3$
δ′(Co-Zn)***	Co_2Zn_{15}	****	****	****
ε(εCo,Ni)**	0-35 at.% Ni	hP2	$P6_3/mmc$	Mg
ε,(εCo,Zn)**	0-2.5 at.% Ni	hP2	$P6_3/mmc$	Mg
ε(Cu-Zn)	78-88 at.% Zn	hP2	$P6_3/mmc$	Mg
η, (zn)	100 at% Zn	hP2	$P6_3/mmc$	Mg

*Phases where magnetic transformation takes place; ** ferromagnetic phase;

*** high temperature phase; **** no data

2. Experimental

The Cu-Ni-Zn and Co-Ni-Zn alloys (Table 2) were prepared using pure components (at least 99.99%) weighed and sealed in quartz tubes, under argon pressure of around 1 Pa. All specimens were gradually heated and annealed at 1178 K (i.e. just below the zinc boiling point). After annealing, the ampoules were broken and the alloys were grinded in agate mortar, resealed, annealed furthermore at 750 K and finally at 868 K (Table 2).

Some of the Co-Ni-Zn specimens were annealed at 1083 K (Table 2).All experiments have been done in sealed ampoules. The mass of the specimens has been

TABLE 2

Overall chemical composition and heat treatment of the Cu-Ni-Zn and Co-Ni-Zn alloys. No — numbers and labels of the specimens, Xi — initial mole fractions of the respective constituents

No	X_{Ni}	X_{Cu}	X_{Zn}	Notes
CNZ1	0.1162	0.1110	0.7728	Annealed 21 d. at 1178 K; grinded and heated 5 d. at 1023 K; annealed 180 d. at 868 K
CNZ2	0.0848	0.0783	0.8369	
CNZ3	0.0564	0.0622	0.8814	
CNZ4	0.0239	0.0906	0.8855	Annealed 4 d. at 1178 K; grinded and heated 5 d. at 1023 K; annealed 180 d. at 868 K
CNZ5	0.0446	0.0172	0.9382	Annealed 18 d. at 1178 K; grinded and heated 5 d. at 650 K; annealed 180 d. at 868 K
No	X_{Ni}	X_{Zn}	X_{Co}	Notes
CoNZ1	0.0666	0.8966	0.0368	Annealed 18 d. at 1178 K; grinded and heated 5 d. at 1023 K; annealed 210 d. at 868 K
CoNZ2	0.0424	0.8943	0.0633	
CoNZ3	0.0175	0.8722	0.1103	
CoNZ4	0.0579	0.92	0.0221	
CoNZ5	0.0575	0.32	0.6225	Annealed 60 d. at 1178 K; grinded and heated 5 d. at 1023 K; annealed 210 d. at 868 K
CoNZ6	0.315	0.32	0.365	
CoNZ7	0.6081	0.3199	0.072	
CoNZ8	0.2292	0.4271	0.3437	
CoNZ9	0.1782	0.5884	0.2334	
CoNZ10	0.29091	0.54545	0.1636	
CoNZ11	0.0252	0.8583	0.1165	
CoNZ12	0.0942	0.8555	0.0503	

controlled before and after annealing, and the mass lost has been found to be in the limits of the experimental error (fourth digit after the decimal point). After quenching in water, the specimens were polished and their phase compositions were determined by electron probe microanalyses (EPMA) using the wave dispersion system (WDS) method.

3. Results and discussion

3a. Cu-Ni-Zn phase diagram

In Fig. 1a calculated isothermal section at 1178 K (using a recent [4] thermodynamic optimisation of the Cu-Ni-Zn phase diagram) is represented. As one could see, at 1178 K all specimens should have been liquid. Figs. 2 and 3 show the microstructures of the specimens CNZ1, CNZ2 and CNZ3, respectively, as quenched from 1178 K. Namely, in specimen CNZ1 (Fig. 2) no dendrites are seen. The information that can be deducted by this micrograph (combined with EPMA data, Table 2) is that

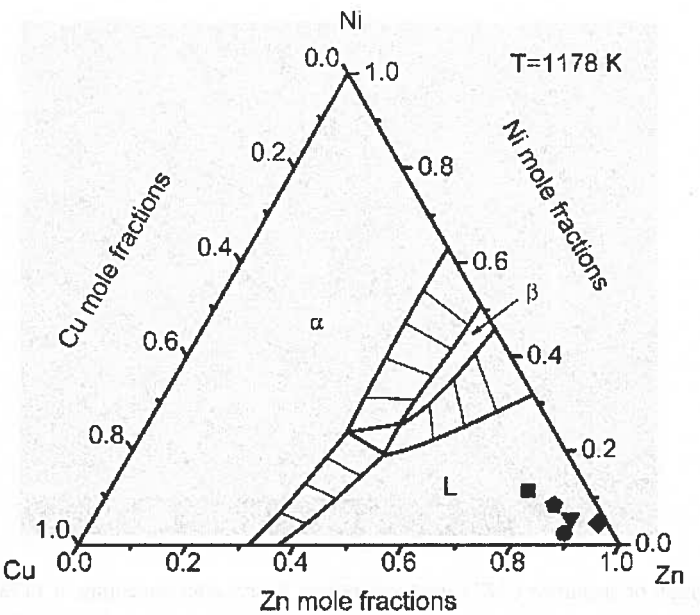

Fig. 1. Isothermal section at 1178 K of the Cu-Ni-Zn phase diagram, calculated using optimized adjustable coefficients. The overall composition of the specimens used in this work are also represented: ■ – CNZ1, ⬟ – CNZ2, ▼ – CNZ3, ● – CNZ4, ◆ – CNZ5. Three phases are stable at the working temperature: face centered solid solutions (α), intermetallic compound (β) and liquid solutions (L). The thin solid lines symbolize the tie-lines in the two-phase areas

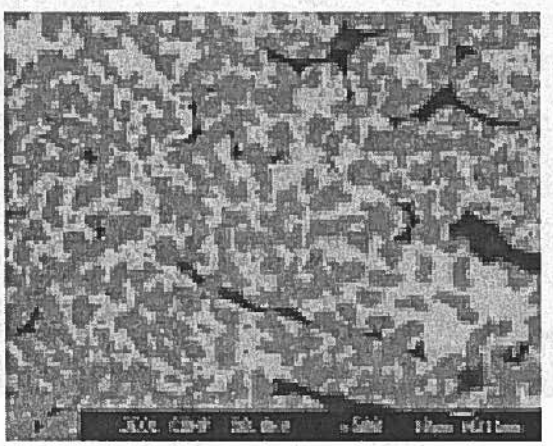

Fig. 2. Micrograph of specimen CNZ1 in characteristic X-rays after annealing at 1178 K. Both, light and dark areas pertain to the γ-phase. The dark are richer in Ni, while the light – richer in Cu

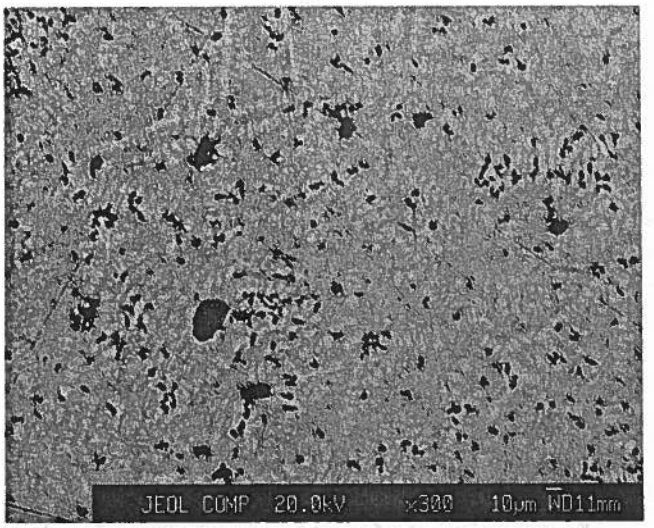

Fig. 3. Micrograph of specimen CNZ3 in characteristic X-rays after annealing at 1178 K. Dendrites of γ-phase (dark areas) have formed thus indicating large difference between the liquidus and the solidus temperatures. The black areas are voids

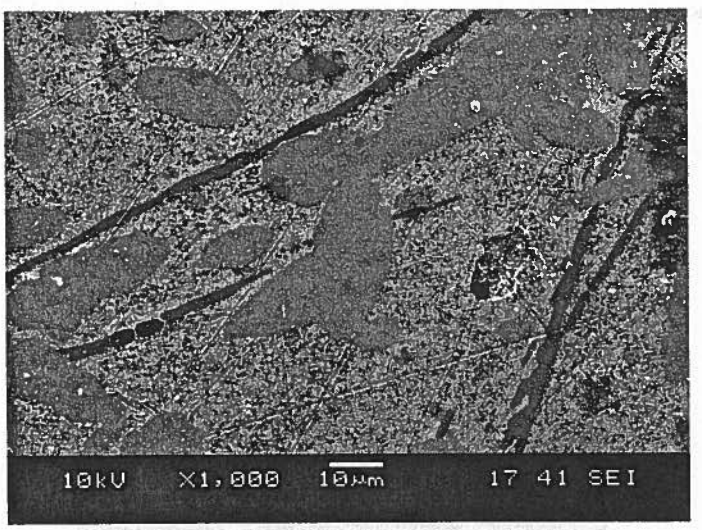

Fig. 4. Micrograph of specimen CNZ3 in back scattered electrons, after annealing at 1178 K. The dark-gray areas are of γ – phase the light areas correspond to the liquide phase (L). Needle-like zinc dendrites have formed during the cooling. The small black areas are voids, probably

the melting temperature of the ternary γ-phase is near to the working temperature 1178 K. Besides, it seems that some liquation occurs during the cooling, due to the non-equilibrium crystallization, thus areas with different chemical compositions have formed. Nevertheless, they all are situated in the γ-phase homogeneity range (Table 2).

Contrary, dendrites at quenching from 1178 K are observed in specimens whose composition is located out of a monophase field. Such an observation indicates large difference between the liquidus and the solidus temperatures. This is also in agreement with the almost vertical phase boundaries know in the pertinent binary systems. For example, in Fig. 3 and Fig. 4 are shown microstructures of the specimen No. CNZ3 quenched after annealing at 1178 K (i.e. liquid state) and at 868 K, respectively. The primary crystallizing phases are: the zinc (Zn) (at the quenching from at 868 K) and the γ-phase (at quenching from 1178 K). This behaviour is an agreement with the expected from the pertinent binary phase diagrams and indicates the lack of new phases in the studied region.

TABLE 3

Phase composition of the ternary Cu-Ni-Zn specimens, determined by electron microprobe analyses. The predominant phase is placed first

No.	Phases	Note
CNZ1	(a) Ni-rich γ-CuNiZn (light areas) (b) Cu-rich γ–CuNiZn (dark areas)	After annealing at 1178 K: The alloy is melted at the annealing temperature. γ-CuNiZn with different composition formed in some parts of the specimen during the cooling due to the non-equilibrium crystallization. (a) $X_{Cu} = 0.11 \pm 0.02$, $X_{Ni} = 0.12 \pm 0.01$, $X_{Zn} = 0.77 \pm 0.02$; (b) $X_{Cu} = 0.13 \pm 0.02$, $X_{Ni} = 0.10 \pm 0.01$, $X_{Zn} = 0.77 \pm 0.02$
CNZ1	(a) γ-CuNiZn ((light areas))	Annealed at 868 K. Inclusions of dark phase with similar compositions are seen. (a) $X_{Cu} = 0.12 \pm 0.01$, $X_{Ni} = 0.12 \pm 0.01$, $X_{Zn} = 0.76 \pm 0.02$
CNZ2	(a) Liquid phase (light areas); (b) γ-CuNiZn (dark areas)	After quenching from 1178 K: (a) $X_{Cu} = 0.04 \pm 0.02$, $X_{Ni} = 0.03 \pm 0.02$, $X_{Zn} = 0.93 \pm 0.02$; (b) $X_{Cu} = 0.06 \pm 0.01$, $X_{Ni} = 0.08 \pm 0.01$, $X_{Zn} = 0.86 \pm 0.01$
CNZ2	(a) γ-CuNiZn (b) Liquid phase	Annealed at 868 K: (a) $X_{Cu} = 0.09 \pm 0.02$, $X_{Ni} = 0.10 \pm 0.01$, $X_{Zn} = 0.81 \pm 0.03$ (b) $X_{Cu} = 0.03 \pm 0.01$, $X_{Ni} = 0.02 \pm 0.01$, $X_{Zn} = 0.95 \pm 0.01$
CNZ3	(a) γ-CuNiZn (light areas); (b) Liquid phase	Annealed at 868 K: (a) $X_{Cu} = 0.09 \pm 0.02$, $X_{Ni} = 0.09 \pm 0.01$, $X_{Zn} = 0.82 \pm 0.02$ (b) $X_{Cu} = 0.05 \pm 0.03$, $X_{Ni} = 0.02 \pm 0.01$, $X_{Zn} = 0.93 \pm 0.03$
CNZ4	(a) ε-CuNiZn (b) Liquid phase	Annealed at 868 K,, ε-CuNiZn is formed. (a) $X_{Cu} = 0.12 \pm 0.01$, $X_{Ni} = 0.03 \pm 0.01$, $X_{Zn} = 0.85 \pm 0.01$ (b) $X_{Cu} = 0.05 \pm 0.01$, $X_{Ni} = 0.01 \pm 0.01$, $X_{Zn} = 0.94 \pm 0.02$
CNZ5	(a) γ-CuNiZn (b) Liquid phase	Annealed at 868 K: (a) $X_{Cu} = 0.02 \pm 0.01$, $X_{Ni} = 0.15 \pm 0.01$, $X_{Zn} = 0.83 \pm 0.01$ (b) $X_{Cu} = 0.02 \pm 0.01$, $X_{Ni} = 0.02 \pm 0.01$, $X_{Zn} = 0.96 \pm 0.01$

Voids are seen in Figs 3 and 4. One might suggest that these voids are due to zinc evaporation Nevertheless, at the working temeperatures the zinc vapour pressure is less than 10^5 Pa (even at 1178 K), thus negligible quantities of zinc are needed to saturate the gas phase. Thus we conclude that the voids are formed during the crystallization of the formed liquid, and are due to the differences of the specific volumes of the phases.

The chemical compositions of the phases of the Cu-Ni-Zn specimens, determined by EPMA are compiled in Table 3. Five measurements at least (point or area analyses) have been done for every phase and the 95% confidence intervals are calculated.

Using the experimental data found in this work and optimised literature data about the binary end – systems [8, 21] we constructed a section at 868 K, of the region containing more than 70 at.% Zn (fig. 5). The ternary extension of the Cu-Zn ε-phase contains up to 4 at % Ni. The location of the phase boundaries of the ternary liquid and γ-phases have been précised.

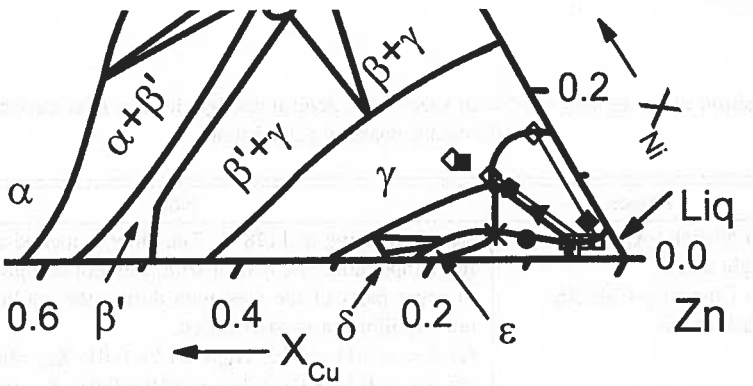

Fig. 5. Details of the constructed in this work zinc-rich region (at 868 K) of the Cu-Ni-Zn phase diagram – the phase boundaries of the γ-phase with ε and liquid phases. The overall composition of the specimens are represented as follows: ■ – CNZ1, ⬟ – CNZ2, ▼ – CNZ3, ● – CNZ4, ◆ – CNZ5. The compositions of the phases, obtained by electron microprobe analyses are shown: ◇ – γ-phase; ✳ – ε–phase; □ – Liquid phase(liq). The thin solid lines symbolize the experimental tie-lines of the specimens CNZ2 and CNZ5. The tie-lines of the specimens CNZ3 and CNZ4 practically coincide with the phase boundaries limiting the two-phase regions γ + Liq and ε + Liq, respectively. The phase boundaries of the α and β_1 phases are calculated with coefficients optimized by Jiang et al. [4]. The mole fractions of the zinc and the copper (X_{Zn} and X_{Cu}) are plotted along the respective axis

3b. Co-Ni-Zn phase diagram

An isothermal section of the Co-Ni-Zn phase diagram at 1083 K, is drawn in Fig. 6 representing the results obtained in this work. Details of the phase compositions are shown in Table 4.

Five measurements at least (point or area analyses) have been done for each phase and the 95% confidence intervals are calculated. The results of previous authors' in-

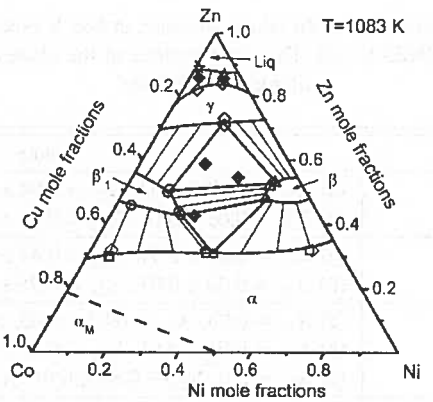

Fig. 6. Isothermal section at 1083 K,of the Cu-Ni-Zn phase diagram, constructed using the experimental data found in this work and literature data about the end binary systems. The overall compositions of the specimens are represented by the symbol (◆). The numbers 1 to 8 correspond to the specimens with labels CoNZ5 to CoNZ12 in Table 4. The compositions of the equilibrium phases, obtained by electron microprobe analyses are shown as follows: ◇ – γ-phase; □ – α-phase (solid f.c.c. solutions); ☆ – Liquid phase; ∘ – β'_1-phase (ternary extension of the Co-Zn β_1-phase); △ – β_1-phase (ternary extension of the Ni-Zn β_1-phase). The dashed line indicates the transition between paramagnetic (α) and ferromagnetic (α_M) state. The thin solid lines symbolize the experimental tie – lines of the respective two-phase specimens (1, 2, 7 and 8)

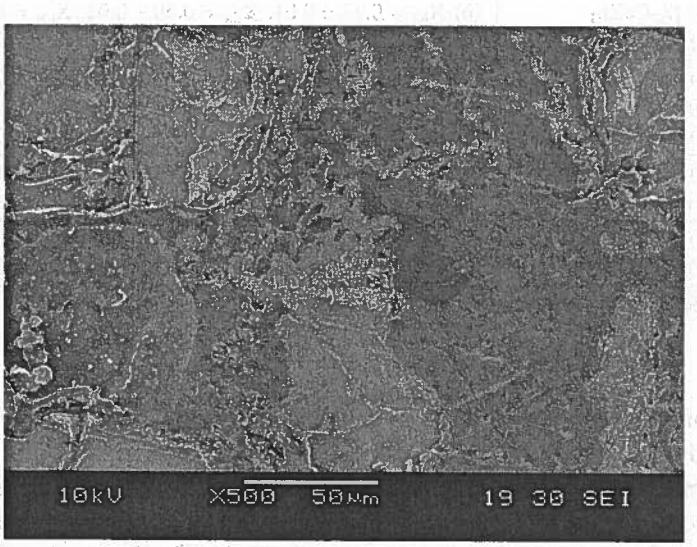

Fig. 7. Micrograph of specimen CoNZ3 in back scattered electrons. The specimen is annealed at 868 K. The light-gray fields correspond to the zinc-rich liquid phase (Liq), while the dark-gray – to the ternary γ-phase (γ–CoNiZn). The darkest area corresponds to the Co-Zn γ_1-phase ($CoZn_7$)

TABLE 4

Results obtained with equilibrated Co-Ni-Zn alloys annealed at 868 K (specimens nos. CONZ1 to 4) and 1083 K (specimens nos. CONZ5 to 12). The compositions of the phases are determined by electron microprobe analyses

No.	Phases	Note
CoNZ1	(a) γ-CoNiZn (b) Liquid	(a) $X_{Ni} = 0.10 \pm 0.02$, $X_{Zn} = 0.84 \pm 0.02$, $X_{Co} = 0.06 \pm 0.01$; (b) $X_{Ni} = 0.02 \pm 0.01$, $X_{Zn} = 0.96 \pm 0.02$, $X_{Co} = 0.02 \pm 0.01$;
CoNZ2	(a) γ-CoNiZn (b) Liquid	(a) $X_{Ni} = 0.05 \pm 0.01$, $X_{Zn} = 0.84 \pm 0.03$,$X_{Co} = 0.11 \pm 0.02$; (b) $X_{Ni} = 0.03 \pm 0.01$, $X_{Zn} = 0.95 \pm 0.03$, $X_{Co} = 0.02 \pm 0.01$;
CoNZ3	(a) γ-CoNiZn (b) Liquid (c) γ_1-$CoZn_7$	(a) $X_{Ni} = 0.03$, $X_{Zn} = 0.81 \pm 0.03$, $X_{Co} = 0.16 \pm 0.02$; (b) $X_{Ni} = 0.01 \pm 0.01$, $X_{Zn} = 0.96 \pm 0.04$, $X_{Co} = 0.03 \pm 0.01$; (c) $X_{Ni} = 0.0$, $X_{Zn} = 0.88 \pm 0.01$, $X_{Co} = 0.12 \pm 0.01$;
CoNZ4	(a) γ-CoNiZn (b) Liquid	(a) $X_{Ni} = 0.12 \pm 0.03$, $X_{Zn} = 0.86 \pm 0.02$, $X_{Co} = 0.04 \pm 0.01$; (b) $X_{Ni} = 0.04 \pm 0.01$, $X_{Zn} = 0.95 \pm 0.03$, $X_{Co} = 0.01 \pm 0.03$;
CoNZ5	(a) (αCo) (b) β_1'-$CoZn_1$	(a) $X_{Ni} = 0.06 \pm 0.02$, $X_{Zn} = 0.30 \pm 0.03$, $X_{Co} = 0.64 \pm 0.02$; (b) $X_{Ni} = 0.04 \pm 0.02$, $X_{Zn} = 0.49 \pm 0.03$, $X_{Co} = 0.47 \pm 0.03$;
CoNZ6	(a) (αCo) (b) β_1'-$CoZn_1$	(a) $X_{Ni} = 0.32 \pm 0.01$, $X_{Zn} = 0.31 \pm 0.02$, $X_{Co} = 0.37 \pm 0.03$; (b) $X_{Ni} = 0.18 \pm 0.03$, $X_{Zn} = 0.44 \pm 0.03$, $X_{Co} = 0.38 \pm 0.02$;
CoNZ7	(a) (αCo)	(a) $X_{Ni} = 0.60 \pm 0.03$, $X_{Zn} = 0.32 \pm 0.02$, $X_{Co} = 0.08 \pm 0.01$;
CoNZ8	(a) (αCo) (b) β_1'-$CoZn_1$ (c) β_1-NiZn	(a) $X_{Ni} = 0.34 \pm 0.03$, $X_{Zn} = 0.31 \pm 0.02$, $X_{Co} = 0.35 \pm 0.03$; (b) $X_{Ni} = 0.19 \pm 0.02$, $X_{Zn} = 0.43 \pm 0.03$, $X_{Co} = 0.38 \pm 0.03$; (c) $X_{Ni} = 0.40 \pm 0.03$, $X_{Zn} = 0.48 \pm 0.03$, $X_{Co} = 0.12 \pm 0.03$
CoNZ9	(a) γ-CoNiZn (b) β_1'-$CoZn_1$ (c) β1-NiZn	(a) $X_{Ni} = 0.17 \pm 0.02$, $X_{Zn} = 0.71 \pm 0.03$, $X_{Co} = 0.12 \pm 0.03$; (b) $X_{Ni} = 0.12 \pm 0.01$, $X_{Zn} = 0.50 \pm 0.02$, $X_{Co} = 0.38 \pm 0.02$; (c) $X_{Ni} = 0.39 \pm 0.01$, $X_{Zn} = 0.52 \pm 0.02$, $X_{Co} = 0.09 \pm 0.03$
CoNZ10	(a) γ-CoNiZn (b) β_1'-$CoZn_1$ (c) β_1-NiZn	(a) $X_{Ni} = 0.16 \pm 0.01$, $X_{Zn} = 0.73 \pm 0.02$, $X_{Co} = 0.11 \pm 0.01$; (b) $X_{Ni} = 0.12 \pm 0.01$, $X_{Zn} = 0.51 \pm 0.03$, $X_{Co} = 0.37 \pm 0.03$; (c) $X_{Ni} = 0.40 \pm 0.03$, $X_{Zn} = 0.53 \pm 0.03$, $X_{Co} = 0.07 \pm 0.01$
CoNZ11	(a) γ-CoNiZn (b) Liquid	(a) $X_{Ni} = 0.04 \pm 0.02$, $X_{Zn} = 0.82 \pm 0.03$, $X_{Co} = 0.14 \pm 0.02$; (b) $X_{Ni} = 0.01 \pm 0.01$, $X_{Zn} = 0.89 \pm 0.03$, $X_{Co} = 0.10 \pm 0.03$;
CoNZ12	(a) γ-CoNiZn (b) Liquid	(a) $X_{Ni} = 0.10 \pm 0.01$, $X_{Zn} = 0.84 \pm 0.02$, $X_{Co} = 0.06 \pm 0.02$; (b) $X_{Ni} = 0.09 \pm 0.02$, $X_{Zn} = 0.87 \pm 0.03$, $X_{Co} = 0.04 \pm 0.01$

[1] – β_1'-CoZn designates the ternary extension of the Co-Zn β_1-phase.

vestigations of this ternary system [11, 12] and thermodynamic optimisations of the respective end binary systems [8, 21] are taken into account as well. Fig. 7 and Fig. 8 are micrographs of the alloys nos. CoNZ3 and CoNZ2, respectively. The light-grey fields correspond to the zinc-rich liquid phase, while the dark-grey – to the ternary γ-phase. The darkest area in Fig. 8 corresponds to the Co-Zn γ_1-phase (approximate formula $CoZn_7$).

In Fig. 9 an isothermal section of the zinc-rich side of the Co-Ni-Zn phase diagram at 868 K is plotted, with the experimental data obtained in this work. The data allow to precise the phase boundaries shapes for the ternary liquid and γ-phases.

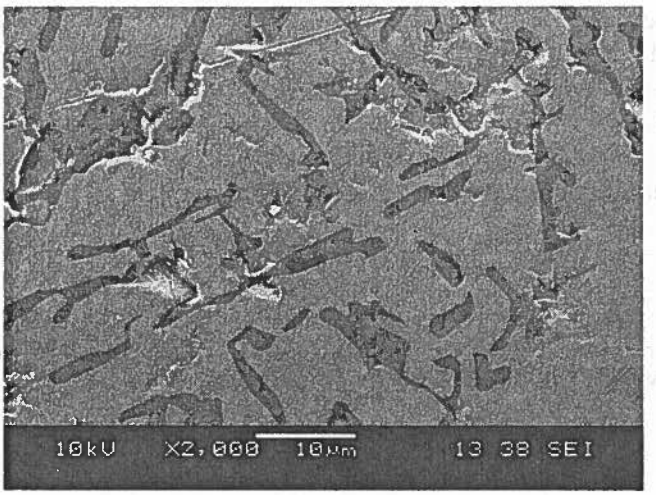

Fig. 8. Micrograph of specimen CoNZ2 in back scattered electrons. The specimen is annealed at 868 K. The light-gray fields correspond to the zinc-rich liquid phase (Liq), while the dark-gray – to the ternary γ-phase (γ–CoNiZn)

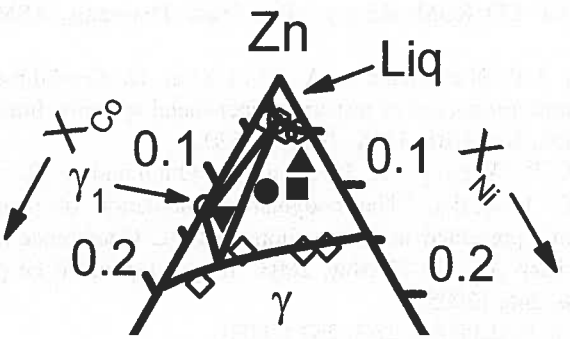

Fig. 9. Isothermal section at 868 K, of the zinc-rich side of the Co-Ni-Zn phase diagram constructed using the experimental data acquired in this work. The overall compositions of the specimens are represented as follows: ■ – CoNZ1, ● – CoNZ2, ▼ – CoNZ3, ▲ – CoNZ4. The compositions of the phases, obtained by electron microprobe analyses are: ◇ – γ-phase; ○ – γ_1-phase; ⬡ – Liquid phase. The mole fractions of the zinc and the nickel (X_{Zn} and X_{Ni}) are plotted along the respective axis

4. Conclusion

The phase boundaries in the zinc-rich corners of the Cu-Ni-Zn and Co-Ni-Zn systems have been investigated at 868 K. The phase relations at higher temperatures (1178 and 1083 K) are verified as well. Ternary compounds non-related with the binary systems have not been found. Data about the phase compositions of the Cu-Ni-Zn and

Co-Ni-Zn phases have been obtained. The existence of continuous γ-phase regions has been confirmed for both ternary systems. The nickel solubility in the ternary extension of the Cu-Zn ε-phase has been found for the first time.

Isothermal sections of the Cu-Ni-Zn (at 868 K) and of the Co-Ni-Zn (at 868 K and 1083 K) phase diagrams have been constructed using the experimental data obtained in this work and literature data about the end binary systems.

Acknowledgements

This work is related to the European Concerted Action COST 531. Thanks are due to Prof.K. Ishida (Tohoku University, Sendai, Japan) for helping and encouraging the author.

REFERENCES

[1] M. Hansen, K. Anderko, Constitution of Binary Alloys, Second ed., McGraw-Hill, New York, p. 1488, 1958.
[2] T. Massalski, CD ROM: Binary Alloy Phase Diagrams, ASM Intern., OH, USA, 1996.
[3] Y.A. Chang, J.P. Neumann, A. Mikula, D. Goldberg, Phase diagrams and thermodynamic properties of ternary copper-metal systems, International Copper Research Association, Inc. NBS, USA, 1979, p. 620.
[4] M. Jiang, C.P. Wang, X.J. Liu, I. Ohnuma, R. Kainuma, G.P. Vassilev, K. Ishida, "Thermodynamic calculation of phase equilibria in the Cu-Ni-Zn system", presented in "International IUPAC Conference on High Temperature Materials Chemistry–XI", 19-23 May, 2003, Tokyo, Japan, To be published in J. Phys. Chem. Solids **66**, 246, (2005).
[5] J. Miettinen, CALPHAD **27**/3, 263 (2003).
[6] S.A. Mey, CALPHAD **16**, 255 (1992).
[7] M. Kowalski, P.J. Spencer, J. Phase Equilibria **14**, 432 (1993).
[8] G.P. Vassilev, T. Gomez-Acebo, J.C. Tedenac, J. Phase Equilibria **21**, 287 (2000).
[9] S. Budurov, G.P. Vassilev, N. Nentchev, Z. Metallkunde **65**/11, 683 (1974).
[10] S. Budurov, G.P. Vassilev, Z. Metallkunde **67**, 170 (1976).
[11] G.P. Vassilev, S. Budurov, Annual of the Univeristy of Sofia, Faculty of Chemistry **73**/1, 73 (1979).
[12] G.P. Vassilev, S. Budurov, Izvestia AN USSR "Metally" **2**, 229 (1980).
[13] G.P. Vassilev, S. Budurov, J. Alloys and Compounds **199**, 197 (1993).
[14] S. Budurov, G.P. Vassilev, L. Mandadjieva, Z. Metallkunde **67**, 307 (1976).
[15] S. Budurov, G.P. Vassilev, Z. Metallkunde **68**, 795 (1977).
[16] G.P. Vassilev, J. of Alloys and Compounds **176**, 295 (1991).

[17] G. P. Vassilev, J. of Alloys and Compounds **186**, 99 (1992).
[18] G. P. Vassilev, Cryst. Res. and Techn. **27**/4, 523 (1992).
[19] G. P. Vassilev, J. of Alloys and Compounds **190**, 107 (1992).
[20] G. P. Vassilev, Cryst. Res. Technol. **28**/1, 57 (1993).
[21] G. P. Vassilev, M. Jiang, J. Phase Equilibria and Diffusion **25**, 3 259 (2004).

Received: 10 June 2004.

A R C H I V E S O F M E T A L L U R G Y A N D M A T E R I A L S
Volume 49 2004 Issue 4

G. WNUK*, J. ROMANOWSKA*

INFLUENCE OF Cu ON THE ACTIVITY OF Zn IN Sn-Zn-Cu LIQUID SOLUTIONS

WPŁYW Cu NA WSPÓŁCZYNNIK AKTYWNOŚCI Zn W CIEKŁYCH ROZTWORACH Sn-Zn-Cu

The activity of Zn in low – melting Sn-Zn-Cu alloys has been determined by the method of equilibrium saturation with metal vapour at T = 873K. The total mole fraction of Zn and Cu was less than 0.25. As the method of equilibrium saturation is a comparative one it is necessary to have an appropriate reference mixture. The Sn-Zn alloy was accepted as the reference mixture. The interaction parameter ε_{Zn}^{Cu} was determined by the least squares method. The experimental value of ε_{Zn}^{Cu} was compared with the value calculated on the basis of model of relative difference of ionic volumes.

Keywords: activity, interaction parameter; multicomponent alloys

Aktywność cynku w stopach Sn-Zn-Cu o niskiej temperaturze topnienia została wyznaczona metodą równowagowego nasycania parą metalu w temperaturze 873 K. Sumaryczny udział cynku i miedzi nie przekraczał 0.25 (w ułamkach molowych). Ponieważ metoda równowagowego nasycania jest porównawcza, niezbędne jest posiadanie odpowiedniego stopu odniesienia. W pracy rolę tę pełnił roztwór Sn-Zn. Z wyników pomiarów wyznaczono przy pomocy metody najmniejszych kwadratów wartość parametru oddziaływania ε_{Zn}^{Cu}. Wartość tę porównano z wynikiem obliczeń przy pomocy modelu opartego na względnych różnicach promieni jonowych.

1. Introduction

Thermodynamic properties of diluted multicomponent alloys are useful in processes of refinement of metals and for designing new alloys. Interaction parameters, introduced by W a g n e r [1], enable the determination of influence of one component on the thermodynamic properties of another component in a multicomponent system. Interaction parameters are calculated on the basis of experimental results, such as activity data of a given component in a multicomponent system. However, experiments

* POLITECHNIKA RZESZOWSKA, 35-959 RZESZÓW, UL. W. POLA 2

are difficult to carry out, it is useful to calculate or to predict the values of interaction parameters from other physico- chemical properties.

This paper presents results of experimental investigation of Sn-Zn-Cu alloys at the temperature 873K carried out by means of the method of equilibrium saturation with metal vapour using Sn-Zn alloy as the reference mixture. This method can be used for determining the activity of the volatile component in any multicomponent system. In the studied system zinc is a volatile component. The Sn-Zn-Cu system has been investigated by Tefelske and Chang [2] using the torsion-effusion technique at the temperature 803K for the zinc concentration from $x_{Zn} = 0.03$ to $x_{Zn} = 0.05$ and copper concentration from $x_{Cu} = 0.01$ to $x_{Cu} = 0.05$ and by Nguyen-Duy and Rigaud [3] using the electrochemical method in the temperature range from 723 to 923 K (x_{Zn} and x_{Cu} from 0.01 to 0.05).

The experimental value of the interaction parameter has been compared with the value calculated on the basis of the model of relative difference of ionic volumes [4, 5] and the values obtained in references 2 and 3.

2. Experimental

The analyzed alloys show considerable differences between the vapour pressures of their elements at T=873K: $p^*_{Sn} = 7.8 * 10^{-4}$ Pa p^*_{Zn}=120 Pa, $p^*_{Cu} = 3.98 * 10^{-3}$Pa [6]. Since the vapour pressure of Zn is much higher than that of the other elements, the activity measurements of Zn were carried out by the comparative method of equilibrium vapour saturation. This method has been successfully applied for alloys with one volatile component [7–10]. The studied Sn-Zn-Cu mixture and the reference mixture Sn- Zn have been placed inside a closed crucible under a reduced argon pressure and saturated with the vapour of zinc until equilibrium was reached. At equilibrium the activity of Zn is the same in all mixtures inside a closed system. If the activity of Zn in reference Sn-Zn (l) is known, it is possible to calculate the activity of Zn in the Sn-Zn-Cu (l):

$$a_{Zn(Sn-Zn-Cu)} = a_{Zn(Sn-Zn)} \tag{1}$$

$$\gamma_{Zn(Sn-Zn-Cu)} = x_{Zn(Sn-Zn)} * \gamma_{Zn(Sn-Zn)}/x_{Zn(Sn-Zn-Cu)}, \tag{2}$$

where $x_{Zn(Sn-Zn)}$ and $x_{Zn(Sn-Zn-Cu)}$ denote the equilibrium mole fraction of Zn in Sn-Zn and Sn-Zn-Cu, respectively, and $\gamma_{Zn(Sn-Zn)}$ and $\gamma_{Zn(Sn-Zn-Cu)}$ are the corresponding activity coefficients of Zn.

This method, has enabled simultaneous measurements of up to a dozen mixtures. All the studied mixtures had exactly the same conditions of saturation. The number of mixtures was limited only by the lenght of the isothermal zone in the furnace. The essential part of the apparatus (see figure 1) consisted of a set of graphite blocks with grooves for alloys and orifices which allowed free evaporation and migration of the vapour of zinc inside the system. The set of blocks was placed inside a tube made

of extra-fine, creep-resistant steel, which served as a vacuum chamber, placed inside a resistance furnace. The blocks with alloys were placed exactly in the isothermal zone of the furnace. The temperature was measured with a {Ni-(Ni-Cr)} thermocouple. The accuracy of temperature measurements was ±5K. The pressure in the furnace was measured with a vacuum meter APG-010 manufactured by Balzers. The accuracy of pressure measurements was ±10 Pa. Alloys were prepared from elements of purity at least 0.9998 mass fraction purchased from Aldrich. Graphite elements were made of EK-412 type graphite purchased from Ringsdorf. The reference and the studied mixtures of appropriate compositions were prepared by melting carefully weighed masses of metals at an argon pressure of 0.1Pa. The equilibrium compositions of the alloys were determined by the weighing method. The accuracy of weighing was $\pm 10^{-5}$g.

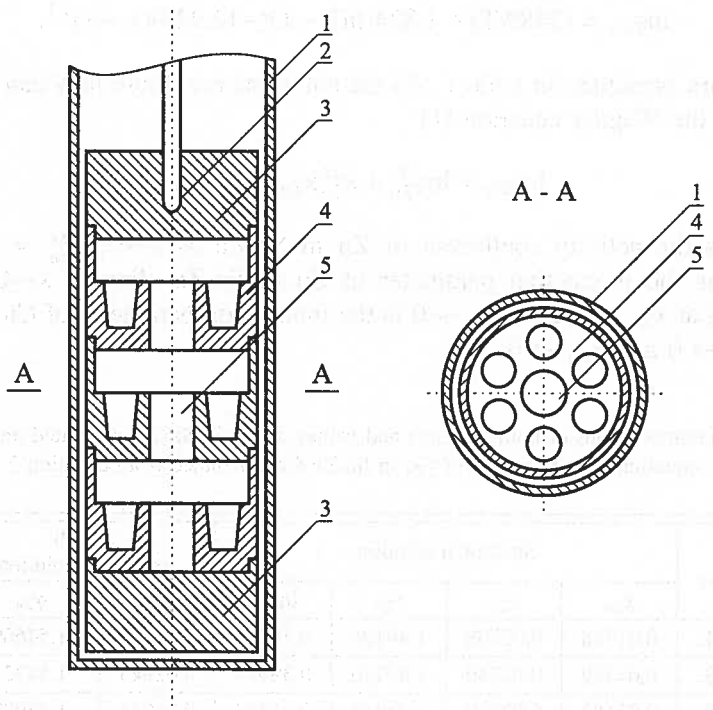

Fig. 1. Apparatus for equilibrium saturation with metal vapour.1, – vacuum chamber; 2, – [Ni-(Ni-Cr)] thermocouple and alundum sheath for thermocouple; 3, – graphite cover; 4, – graphite blocks with grooves for alloys; 5, – orifices and a channel which enables free evaporation and migration of vapour

The quantities determined experimentally, i.e. the argon pressure and the equilibration time were meant to ensure the attainment of equilibrium between Zn(g) in the reference and the studied mixture. In preliminary tests all the mixtures in the grooves were Sn and Zn alloys. The equilibrium state was attained when the mole fraction of Zn was the same in all mixtures. The argon pressure was specially chosen to be higher than the vapour pressure of zinc and to limit the evaporation process to that of zinc

only with a sufficient rate. It was established, that for the temperature 873K the time necessary to reach equilibrium was 2.5 hours with an argon pressure of 2.8 kPa.

3. Results

The activity of zinc in Sn-Zn-Cu at T=873K has been determined by the equilibrium saturation method. The activity coefficient of zinc, γ_{Zn} in this alloy was calculated from equation (2). For describing the activity coefficient of zinc γ_{Zn} in the reference mixture Sn-Zn the equation proposed by P t a k [11] and veryfied by the further investigation [12] has been used:

$$\ln\gamma_{Zn} = (2489/T) + 1.824(\ln T - 1)(-12.929)(1 - x)^{1.1}. \quad (3)$$

The results are presented in table 1. As the solutions are dilute they can be described by means of the Wagner equation [1]:

$$\ln\gamma_{Zn} = \ln\gamma^0_{Zn} + \varepsilon^{Zn}_{Zn}x_{Zn} + \varepsilon^{Cu}_{Zn}x_{Cu}, \quad (4)$$

where γ^0_{Zn} is the activity coefficient of Zn in Sn-Zn as $x\to 0$, $\varepsilon^{Zn}_{Zn} = (\partial \ln f_{Zn}/\partial x_{Zn})$ as $x_{Zn} \to 0$ is the interaction parameter of Zn in Sn-Zn alloy as $x\to 0$, and $\varepsilon^{Cu}_{Zn} = (\partial \ln f_{Zn}/\partial x_{Cu})$ at $x_{Zn} \to 0$ and $x_{Cu} \to 0$ is the interaction parameter of Cu in Sn-Zn-Cu alloy at $x_{Zn} \to 0$ and $x_{Cu} \to 0$.

TABLE

Equilibrium compositions of both mixtures and values of γ_{Zn} in Sn-Zn calculated on the basis of equation (3) and values of γ_{Zn} in Sn-Zn-Cu calculated from equation 2

Nr	Sn-Zn-Cu solution				Sn-Zn reference solution	
	x_{Cu}	x_{Zn}	γ_{Zn}	$\ln\gamma_{Zn}$	x_{Zn}	γ_{Zn}
1.	0,01388	0,02808	1,49196	0,40009	0,02911	1,54669
2.	0,01389	0,02740	1,49140	0,39971	0,02843	1,54721
3.	0,02182	0,03810	1,45446	0,37464	0,04031	1,53907
4.	0,02195	0,03291	1,47202	0,38664	0,03450	1,54301
5.	0,02233	0,01708	1,51494	0,41537	0,01754	1,55512
6.	0,03034	0,02774	1,42904	0,35700	0,03003	1,54695
7.	0,03034	0,02808	1,44630	0,36901	0,03003	1,54669
8.	0,03038	0,02740	1,46560	0,38226	0,02893	1,54721
9.	0,03093	0,01065	1,47084	0,38583	0,01130	1,56007
10.	0,03542	0,04000	1,44138	0,36560	0,04267	1,53763
11.	0,03659	0,01053	1,47931	0,39158	0,01111	1,56016
12.	0,03670	0,00744	1,45930	0,37796	0,00797	1,56255
13.	0,04709	0,02740	1,37844	0,32095	0,03076	1,54721

14.	0,04768	0,01681	1,40117	0,33731	0,01866	1,55533
15.	0,07794	0,02774	1,35664	0,30501	0,03163	1,54695
16.	0,07794	0,02808	1,37302	0,31702	0,03163	1,54669
17.	0,07808	0,02740	1,42091	0,35130	0,02984	1,54721
18.	0,07898	0,01610	1,34003	0,29269	0,01869	1,55588
19.	0,07898	0,01681	1,39893	0,33571	0,01869	1,55533
20.	0,07947	0,01065	1,31776	0,27594	0,01261	1,56007
21.	0,07985	0,00652	1,29348	0,25733	0,00788	1,56326
22.	0,08926	0,02774	1,34346	0,29525	0,03194	1,54695
23.	0,08926	0,02808	1,35969	0,30725	0,03194	1,54669
24.	0,08941	0,02740	1,39436	0,33244	0,03041	1,54721
25.	0,09045	0,01610	1,31076	0,27061	0,01911	1,55588
26.	0,09045	0,01681	1,36838	0,31363	0,01911	1,55533
27.	0,09101	0,01065	1,27833	0,24555	0,01300	1,56007
28.	0,09146	0,00652	1,25908	0,23038	0,00809	1,56326
29.	0,09401	0,03810	1,26451	0,23468	0,04637	1,53907
30.	0,09401	0,04000	1,32633	0,28241	0,04637	1,53763
31.	0,09498	0,03291	1,38996	0,32928	0,03654	1,54301
32.	0,09668	0,01708	1,38142	0,32311	0,01923	1,55512
33.	0,09732	0,01053	1,28361	0,24967	0,01280	1,56016
34.	0,09765	0,00744	1,23247	0,20902	0,00944	1,56255
35.	0,14223	0,03810	1,24537	0,21943	0,04708	1,53907
36.	0,14223	0,04000	1,30625	0,26716	0,04708	1,53763
37.	0,14637	0,01441	1,16050	0,14885	0,01934	1,55717
38.	0,14739	0,01053	1,31519	0,27398	0,01249	1,56016
39.	0,14806	0,00617	1,20439	0,18598	0,00801	1,56353
40.	0,00025	0,00587	1,56567	0,44831	0,00215	0,57382
41.	0,00390	0,01053	1,53570	0,42899	0,02357	3,43727
42.	0,00031	0,03291	1,56635	0,44875	0,00153	0,07268
43.	0,00618	0,01708	1,53363	0,42764	0,02378	2,13493
44.	0,00332	0,00587	1,54638	0,43592	0,01124	2,96243
45.	0,01339	0,01065	1,50006	0,40550	0,03615	5,09186
46.	0,00655	0,04000	1,53985	0,43169	0,01938	0,74600
47.	0,02032	0,01053	1,50271	0,40727	0,03223	4,59934
48.	0,02625	0,03291	1,49011	0,39885	0,03215	1,45541

The interaction parameter $\ln f^{0}_{Zn(Sn-Zn-Cu)}$ is the boundary value of $\ln f_{Zn(Sn-Zn-Cu)}$ function and its value depends on the direction of achieving the boundary value, which is ilustrated in the figure 2.

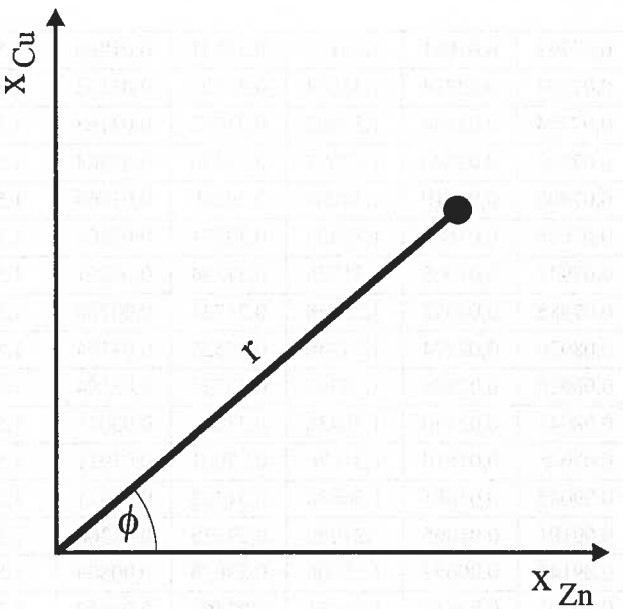

Fig. 2. The dependence of the $\ln \gamma_{Zn(Sn-Zn-Cu)^0}$ value on the direction of achieving the limiting value

It is necessary to determine the influence of two variables: $tg\phi = x_{Cu}/x_{Zn}ir = \sqrt{x_{Cu}^2 + xZn^2}$ on the $\ln\gamma^0_{Zn(Sn-Zn-Cu)}$ value. The small number of experimental points on one direction made it impossible to determine the activity coefficient for low element's concentrations. Therefore its value has been accepted from the binary alloy Sn-Zn. Subsequently, using the dependences $x_{Zn} = r\cos\phi$ and $x_{Cu} = r\sin\phi$ the Wagner equation bas been transformed and the following form has been obtained:

$$\frac{\ln \gamma_{Zn(Sn-Zn-Cu)} - \ln \gamma^0_{Zn(Sn-Zn)}}{r} = \varepsilon^{Zn}_{Zn} \cos\phi + \varepsilon^{Cu}_{Zn} \sin\phi, \tag{5}$$

The left side of the equation (5) has been calculated for each experimental point and the interaction parameters ε^{Zn}_{Zn} and ε^{Cu}_{Zn} have been calculated by means of the least-squares method. On the basis of the experimental results of the studied mixture the following equation was obtained:

$$ln\gamma_{Zn} = -0.45 - 0.5x_{Zn} - 1.70x_{Cu}, \tag{6}$$

4. Discussion

The value of interaction parameter $\varepsilon^{Cu}_{Zn} = -1.7$, obtained experimentally was compared with the value calculated on the basis of the relative difference of ionic volumes

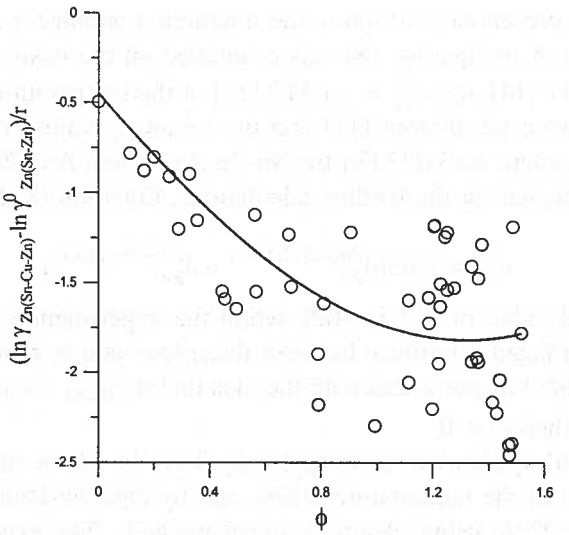

Fig. 3. Experimental points and equation (5)

model, widely described in references 4, 5 and 8. This model is based on the assumption, that alloys with predominating metallic bonds can be considered as a ionic system without valence electrons. The valence electrons can be regarded as free electrons, because the mean free path of electrons is long [13]. Therefore, Pomianek [4, 5, 8] has made an assumption, that the ionic radius should be regarded as a measure of the geometry of metallic solutions. On the basis on the ionic radius, or rather the relative difference of ionic volumes as well as the electron density and electronegativity, thermodynamic properties of binary and ternary metallic solutions can be calculated. A distinct linear correlation between the interaction parameter ε_j^i and the relative difference of ionic volumes $d_i^{i(+n)-j(+p)}$ has been found. The relative difference of ionic volumes in ternary solutions $d_i^{i(+n)-j(+p)}$ is defined as follows:

$$d_i^{i(+n)-j(+p)} = (r_{i(+n)}^3 - r_{(j+p)}^3)/0.5(r_{i(+n)}^3 + r_{(j+p)}^3), \tag{7}$$

where $r_{i(+n)}$, $r_{j(+p)}$, are ionic radii of metals i and j respectively and n, p, are the numbers of valence electrons of metal i and j respectively. Moreover, it has been stated with high probability, that $\varepsilon_i^i > 0$ if the ionic radius r_{1+m} of the solvent is bigger than the ionic radius r_{j+p} of metal j, while $\varepsilon_j^i < 0$ if $r_{1(+m)} < r_{j(+p)}$. The proposed regularity occurs at least in 56 solutions, among 66 systems analyzed. Both described regularities are expressed by the equation:

$$\varepsilon_j^i = A(d_i^{i(+n)-j(+m)} - d_i^{i(+n)-1(+m)}), \tag{8}$$

where A is a constant.

Basing on the presented conception the interaction parameter ε_{Zn}^{Cu} has been calculated. The constant A in equation (8) was calculated on the basis of the experimental values $\varepsilon_{Zn}^{Bi} = -0.041$ [14] and $\varepsilon_{Zn}^{Ag} = -1.519$ [12] at the temperature 773K. The appropriate ionic radii were taken from [15] and the following values of A were obtained: For the Sn-Zn-Bi system A=3.002 For the Sn-Zn-Ag system A=2.26 The average value of A=2.63 was accepted for the further calculations. Equation (8) for the ε_{Zn}^{Cu} becomes then:

$$\varepsilon_{Zn}^{Cu} = 2.63(d_{Zn}^{Zn(+2)-Cu(+1)} - d_{Zn}^{Zn(+2)-Sn(+4)}) \qquad (9)$$

The calculated value of ε_{Zn}^{Cu} is –0.8, while the experimental one is $\varepsilon_{Zn}^{Cu} = -1.7$. There is not a significant difference between these two values, moreover both of them are negative, and that fact correlates with the idea that if $r_{1(+m)} < r_{j(+p)}$($r_{Sn(+4)} = 0.71$ Å, $r_{Cu(+1)} = 0.96$ Å), then $\varepsilon_i^j < 0$.

The (Sn-Zn-Cu) system was investigated by Tefelske [2] by means of the torsion--effusion technique at the temperature 804K. and by Nguyen-Duy [3], at the temperature from 723 to 923K using electrochemical method.. The experimental values of interaction parameter are $\varepsilon_{Zn}^{Cu} = -1.5$ and -0.82 respectively. The value of interaction parameter obtained by the authors of this paper is almost the same as the value obtained by Tefelske [2] and differs from the value obtained by Nguyen-Duy [3]. In this case the experimental results obtained by means of the e.m.f. method, as usually, differ from the results obtained by vapour pressure measurements (or similar ones like torsion- effusion technique or equilibrium vapour saturation) as these both methods are based on different principles.

The calculated value of interaction parameter $\varepsilon_{Zn}^{Cu} = -0.8$, whereas the value calculated by Tefelske [2] using the respective binary activity coefficients of the three components in ternary alloys equals $\varepsilon_{Zn}^{Cu} = -3,0$. Although these values differ significantly, both of them are negative.

5. Conclusions

Using the vapour saturation method the activity of Zn in Sn-Zn-Cu dilute solutions at the temperature 873K was measured. The interaction parameter was calculated on the basis of the experimental results and by the use of the method of relative difference of ionic volumes. This method allows the calculation of the interaction parameter ε_{Zn}^{j} as a function of the ionic radii in any Sn-Zn-j if the number of valence electrons passing over to the common electron cloud in the system has been properly determined.

REFERENCES

[1] K. Wagner, Thermodynamics of alloys Addison-Wesley Reading, Mass. 1952.
[2] T. Tefalske, Y.A. Chang, Materials Science and Engineering. **14**, 211-216 (1974).

[3] P. Nguyen-Duy, M. Rigaud, J.Chem. Thermodynamics. **6**, 999-1004 (1974).
[4] T. Pomianek, Zeszyty Naukowe Politechniki Rzeszowskiej. **32**, 1 (1986).
[5] T. Pomianek, M. Rychlewski, Journal the Chimie Phisique. **85**, 3, 425-432 (1988).
[6] O. Kubaschewski, C.B. Alcock, Metallic Thermochemistry. Pergamon Press, Oxford 1972.
[7] T. Pomianek, J.J. Golonka, Met. Technol. **6**, 433-442 (1979).
[8] T. Pomianek, Trans of the Japan Institute of Metals. **29**, 3, 223-234 (1988).
[9] J. Midura, T. Pomianek, J. Chem. Thermodynamics. **26**, 507-512 (1994).
[10] G. Wnuk, T. Pomianek, J. Romanowska, M. Rychlewski, J. Chem. Thermodynamics. **29**, 931-937 (1997).
[11] W. Ptak, Arch. Hutn. **5**, 169-178 (1960).
[12] G. Wnuk, Doctor's Thesis. Kraków, 1998.
[13] N.F. Mott, E.A. Davis, Electron in Non-Crystaline Materials. Clarendon Press 1979.
[14] V.N.S. Mathur, J.F. Elliot, Metal Science. **8**, 298-309 (1974).
[15] M. Winter, Webelements Periodic Table; The University of Sheffild, UK, Professional edition. Htmp// www.webelements.com.

Received: 10 June 2004

A R C H I V E S O F M E T A L L U R G Y A N D M A T E R I A L S
Volume 49 2004 Issue 4

W. MYDLARCZYK*, S. POLAK*

INTERNAL STATE CONSTITUTIVE MODELS DESCRIBING THE FLOW STRESS OF METALLIC MATERIALS

RÓWNANIA KONSTYTUTYWNE OPISUJĄCE NAPRĘŻENIE UPLASTYCZNIAJĄCE UWZGLĘDNIAJĄCE STAN WEWNĘTRZNY MATERIAŁU

The main aim of the paper is to give a review of different constitutive models with the internal state of the material as a base parameter for the computation of the changes in the flow stress-strain relationship. Some models are so complicated that on the basis of the nowadays knowledge of phenomena taking place during the deformation processes of metals and alloys, their application is in practice very difficult or even impossible.

Several typical models have been presented. They differ in their treatment of the factors that influence on the course of the flow stress curves. Each of them allows determining the dependence of the flow stress on the internal state and the deformation conditions. All the presented models differ in their range of applications. Also, the accuracy reached in the description of the real flow stress curve is different in each of them. Some models have been described in detail. Moreover, one of them was used for calculation of the flow stress strain relationship. Owing the introduction of the conception of the internal state, that model could take into account the strain hardening, dynamic and static kinetics of softening, slow and sudden changes of the strain rate and temperature, as well as the influence of the interruption in the deformation. Some models can be applied to the large plastic strains in a wide range of the deformation conditions and not only for hot and warm deformation temperatures, but also for the low temperature, where the softening processes do not hold.

So far no model has been built which would incorporate all the thermo-mechanical and structural processes that occur during and after the deformation. Therefore, the researches aimed at improving the existing models, which describe the reactions of the material to complex deformation conditions, are still very attractive.

Zasadniczym celem pracy jest przedstawienie różnych modeli konstytutywnych opisujących zależności pomiędzy naprężeniem uplastyczniającym a odkształceniem uwzględniające stan wewnętrzny materiału jako główny parametr. Niektóre modele są tak złożone, że ich praktyczne zastosowanie jest bardzo trudne a nawet niemożliwe przy obecnej wiedzy o zjawiskach i ich wzajemnym oddziaływaniu podczas odkształcania metali i stopów.

* WROCŁAW UNIVERSITY OF TECHNOLOGY, WYBRZEŻE WYSPIAŃSKIEGO 27, 50-370 WROCŁAW, POLAND

Typowe modele różniące się w ujęciu czynników określających przebieg naprężenia uplastyczniającego zostały przedstawione. Każdy z nich umożliwia określenie naprężenia uplastyczniającego w zależności od stanu wewnętrznego i warunków odkształcania. Modele różnią się w zakresie ich zastosowania i dokładności opisu rzeczywistych przebiegów naprężenia uplastyczniającego. Kilka modeli zostało dokładniej opisane i jeden z nich został użyty do obliczenia zależności pomiędzy naprężeniem uplastyczniającym a odkształceniem. Modele poprzez uwzględnienie stanu wewnętrznego umożliwiają określenie umocnienia, kinetyki dynamicznego i statycznego osłabienia, powolnych i szybkich zmian prędkości odkształcania i temperatury, przerw w procesie odkształcania. Niektóre modele mogą być zastosowane do dużych odkształceń plastycznych w szerokim zakresie warunków odkształcania, zarówno w procesach kształtowania na ciepło jak i gorąco jak również na zimno po wyeliminowaniu procesów osłabienia.

Dotychczas uniwersalny model, zawierający pełne termo-mechaniczne i strukturalne procesy zachodzące podczas i po odkształceniu nie został jeszcze w pełni opracowany, dlatego należy kontynuować badania prowadzące do udoskonalenia istniejących modeli, szczególnie w przypadkach opisu zachowania się materiałów złożonych procesach odkształcania.

1. Introduction

The progress in computing techniques has made it possible to design and analyze plastic working processes by means of modern numerical methods such as the finite and the boundary element method. This way of plastic forming processes simulation is no longer limited by the memory capacity of computers or data processing capabilities. The main difficulties are usually connected with lack of a precise mathematical model of the material behaviour, the knowledge of the boundary conditions including friction law and transfer of heat between workpiece and the surroundings, and the accurate description of the finite element mesh evolution at large deformation.

The model describing the material behaviour is the most important element in simulating the metal forming processes. The mathematical form of the functions in such models should take into account the physical phenomena that occur in the material depending on its kind, the conditions of forming and the history of deformation prior to the current conditions of the material. The fundamental criterion for the selection of the flow stress curve functions is to reflect phenomena essential for the computer simulation of forming processes such as structural phenomena, the strain evolution and a change in the orientation of the principal axes of the strain.

The equations, which describe changes in the flow stress or limit strain, can be divided into two groups [1]. The first group comprises models that describe changes in the flow stress and the limit strain of materials by expressions involving explicitly the deformation conditions mainly such as the temperature, the strain and strain rate. These models usually do not take into account the deformation history [2-5]. They correctly describe the flow stress, when the strain hardening is a dominant factor determining the state of the material. However, when the thermally activated softening becomes essential and the deformation history starts to play a role in the strengthening

processes, the above models lead to erroneous results. In such cases, the models of the other group should be employed [6-10].

The second group embraces models in which the effect of the deformation history on the internal state of the material, determined primarily by its structure is considered. In such models, the material behaviour is analysed taking into account two separate factors:

— the evolution of the material internal state caused by a continuous deformation;

— the response of the material being in a particular internal state to a sudden change in the deformation conditions.

There is a large number of the known constitutive equations. Taking as a criterion which parameters are used for the description of the flow stress, the constitutive equations can be divided into several groups. Such a division into the following six subgroups was proposed by Grosman [11]:

1. The flow stress σ_p is a function of the current strain ε and eventually of the initial values of the stress σ_0 and the strain ε_0:

$$\sigma_p = f(\varepsilon, \varepsilon_0, \sigma_0) \tag{1}$$

2. The flow stress σ_p is a function of the current strain rate $\dot{\varepsilon}$ and ε_0, σ_0:

$$\sigma_p = f(\dot{\varepsilon}, \varepsilon_0, \sigma_0) \tag{2}$$

3. The flow stress σ_p is a function of the current temperature T and $\dot{\varepsilon}$, ε, σ_0, ε_0:

$$\sigma_p = f(\dot{\varepsilon}, \varepsilon, \varepsilon_0, \sigma_0, T) \tag{3}$$

4. As an additional parameter, the time t is taken. This allows to describe phenomena which take place not only during the deformation process but also within its interruptions:

$$\sigma_p = f(\dot{\varepsilon}, \varepsilon, \varepsilon_0, \sigma_0, T, t) \tag{4}$$

5. The flow stress σ_p is a function of the internal state of the material σ_w and $\dot{\varepsilon}$, ε, T, σ_0 and ε_0:

$$\sigma_p = f(\dot{\varepsilon}, \varepsilon, \varepsilon_0, \sigma_0, T, \sigma_w) \tag{5}$$

6. The equations in the last group apart from $\dot{\varepsilon}$, ε, T, take into account a change in the orientation of the principal strain components η during the deformation or in its successive stages:

$$\sigma_p = f(\varepsilon, \dot{\varepsilon}, T, \eta) \tag{6}$$

The functions belonging to the first three groups can be easily implemented in programs of the computer simulation of the cold and hot forming. Then the temperatures are not very high and the softening process is usually absent. The other functions mainly used at warm temperatures should describe the changes in the flow stress in the whole range of strains, where strengthening, softening and the steady state flow can occur. Therefore, in such a case the best solution is to take into account the

deformation history. This can be done by introducing a new parameter describing the current internal state of the material into the constitutive equations [7]. It is typically related to such structural parameters as the dislocation density, the grain size, the degree of recovery and the fraction of recrystallization. Numerous papers have been devoted to the investigations of the structural changes that occur during the deformation proceeded under different conditions [12-16]. Those studies can be very helpful for the formulation of constitutive equations, starting with discrete phenomena and ending with their description in terms of the mechanics of continuous media.

The main aim of the paper is to present the most popular models that take into account the deformation history described by the evolution of the internal state of the material and to modified one of them.

2. Models with internal state of materials

The primary goal of a theory of work hardening is a prediction of the stress-strain curve. This is linked to the development of dislocation substructure. A fundamental fact, however, is that even a simple description of the substructure requires many parameters, whereas a description of work hardening requires only few. Thus, any model of work hardening that starts with observed substructures must involve a substantial contraction of information as a basic part of the model, conversely any theory that begins with the stress-strain curve can only hope to be in accord with a very coarse approximation to substructural features. The theory of work hardening, even of pure FCC metal, is today as hopeless as before; but a model of work hardening can be consider now virtually available [17].

A formulation of a precise definition of the material internal state is a very difficult task. In a general conception, the models with internal state of materials usually have the following two characteristic features: they take into account some initial parameters very important for application of the model and the flow stress σ_p is described by a function depending on the internal state parameters and conditions of the deformation. Moreover, each of the internal state parameter should be described by an appropriate evolution equation

$$\dot{\sigma}_w = \dot{\sigma}_w(T, \varepsilon, \dot{\varepsilon}, \sigma_w). \tag{7}$$

Though the internal state parameters can be determined arbitrarily, it seems that it is best to use the theory of micromechanics of the plastic deformation. From the point of view of metal physics and metallurgy the following internal state parameters: the dislocation density, the size and shape of grains, the surface of the grain boundary, the distribution of subgrains, the stored energy, the texture and degree of deformation play the most important role in the technology. The strain-hardening behavior for different FCC metals does not follow a sequence based on melting temperature or diffusion coefficient, but of normalized stacking- fault energy. The microstructure that developed become more heterogeneous the larger the strain, the higher the temperature, the lower the strain rate. The thermal activation, with a stress-dependent activation energy, play a

central role, as evidenced by the fact that the temperature and strain-rate dependencies can be unified. The decrease of hardening rate with strain is strongly dependent on temperature and weakly on strain rate–indicating a need for a stress-dependent activation energy. They also have an essential influence on the useful properties of metals [15, 16]. However, so far they were very rarely included in constitutive equations having practical application.

To obtain such an equation useful in practice, the phenomenological theory has to be combined with the theory of micromechanics of the plastic deformation.

According to the Hart model [18], the internal state parameters are determined by two factors. The first describes the internal stress caused by the deformation stored by pile-up of the dislocations. The second is equal to the critical internal stress and it is a function of the history of the deformation. Furthermore, it also describes the isotropic hardening. This model confines only to processes with the pile-up of dislocations, whereas in deformation processes there hold also other mechanisms of dislocation movement, as well as various thermally activated processes. Application of this model is practically impossible, because it needs some functions of the internal state parameters and deformation conditions, which are very difficult for determining.

The Anand model of the internal state of the material [19] is based on an equation similar to the Garofalo equation, which comes from the theory of creep, if only one internal state parameter σ_w is considered

$$\dot{\varepsilon} = A\left[\exp\left(-\frac{Q}{RT}\right)\right]\left(\frac{\sigma_p}{\sigma_w}\right)^n. \tag{8}$$

.where: Q is activation energy of deformation and n is material constant.

Zhou and Clode [20] followed a similar way introducing the same parameter directly into the Garofalo equation. Thus they obtained the relationship

$$\dot{\varepsilon} = A\left[\sinh\left(\frac{\sigma_p}{\sigma_w}\right)\right]^n \exp\left(-\frac{Q}{RT}\right). \tag{9}$$

where: R is gas constant.

In this model, the evolution of the internal state parameter is given by the following relationship

$$\dot{\sigma}_w = \frac{h_0}{\sigma_{wn}}(\sigma_{wn} - \sigma_w)\,\dot{\varepsilon} = h_0\dot{\varepsilon} - h_0\dot{\varepsilon}\sigma_w/\sigma_{wn}, \tag{10}$$

where: σ_{wn} is the internal state saturation stress, h_0 is material constant, the first term $h_0\dot{\varepsilon}$ corresponds to the linear hardening, and the second one $h_0\dot{\varepsilon}\sigma_w/\sigma_{wn}$ corresponds to the softening caused by the dynamical recovery.

Constitutive equations (9) and (10) relate to the maximum and steady state values of internal state parameters and they take into account neither the static recovery nor static and dynamic recrystallizations.

A very complicated model based on the physical background of the plastic flow dislocation model and the Perzyna and Sawczuk law [21] was elaborated by

Sandström and Langeborg [22]. Unfortunately, its mathematical form is so very complicated that its practical applications are very difficult.

A phenomenological model of plastic deformation was proposed by Estrin and Mecking [23], which makes possible to describe in a unified way the plastic flow of a material both in metal forming processes and in creep. The model based on the assumption that kinetics of plastic flow is determined by a single structure parameter S representing the current structure. The dependence of the flow stress σ_p on the plastic strain rate $\dot{\varepsilon}$ and the absolute temperature T at a given structure of the material is given by the kinetic equation

$$\sigma_p = \sigma_p(S, \dot{\varepsilon}, T). \tag{11}$$

For the complete description of plastic behavior the kinetic equation is complemented with an evolution equation which describes the variation of the structure parameters S with strain ε at given rate and temperature

$$dS/d\varepsilon = f(S, \dot{\varepsilon}, T). \tag{12}$$

As the deformation progress, the structure parameter S evolves towards a saturation value S_s and flow stress as determined by equation (1) will tend to saturation or steady state, value σ_s, defined by a dynamic equilibrium of athermal work hardening associated with the storage of dislocations and work softening associated with the annihilation of dislocation. Mecking and Kocks [24] on the basis of various experimental observation in pure FCC mono- and polycrystals found the correlation between the kinetics of glide at constant structure and kinetics of structure evolution. It is a fundamental tenet of materials science that the current properties of material depend entirely on its current structure, and that changes in properties result from changes in structure. They found two identified regimes of behavior, in the initial regime, the Cotrell-Stokes law is satisfied, hardening is athermal, and a single internal structure parameter is adequate. With increasing importance of dynamic recovery, at large strains or at high temperature, all of these simple assumptions break down. However, the proportionality between the flow stress and the square-root of the dislocation density holds, to a good approximation, over the entire regime. On these assumptions the phenomenological model was proposed, which incorporate the rate of dynamic recovery into the flow kinetics.

The mechanistic interpretation and the developed model elaborated by [17, 25] is restricted to monotonous deformation at low enough temperature where dynamic recovery is governed by conservative glide of dislocations, rather than by time recovery in conjunction with self diffusion and dislocation climb. It is still an open question where exactly the control of diffusion begins. In literature the discussion on the transition to the diffusion regime several times were presented. Based on the analysis of data on single-crystal [26] the transition was assumed to occur at some value of stress exponent determined by temperature and strain rate.

The models describes the many experimental data quantitatively, but none above described models [17] and [23-25] take into consideration course of the flow stress

behind the saturation or steady state flow. However, it can be stated that these works as well as work [22] were used in elaboration of many constitutive models with internal state parameters, for example the works [8-10].

Another model was built on the base of the reciprocal interaction of mobile dislocation with near-range barrier of stress fields [27]. In that model, two components of the flow stress: the thermal σ_{pT} and the athermal σ_{pE} are considered. The thermal component depends explicitly on the temperature T and it is given by the relationship

$$\sigma_{pT} = \sigma_{pT}^{0}\left[1 - \left(\frac{T}{T_0}\right)^{n}\right]^{m}, \tag{13}$$

where: σ_{pT}^{0} is thermal component of flow stress at temperature T_0, n and m are material constants.

The athermal term is a function of the Young modulus. Since the latter varies with temperature, σ_{pE} also depends on the temperature in an implicit way. The final expression for the flow stress takes the form

$$\sigma_p = \sigma_{pT} + \sigma_{pE} = \sigma_{pT}^{0}\left[1 - \left(\frac{T}{T_0}\right)^{n}\right]^{m} + \sigma_{pE}. \tag{14}$$

The model has been created under assumption that the hardening caused by decrease of the temperature in the range from T to T_0 is connected with a reduction of the dislocation mobility by the near-range barrier. It is very simple but it does not take into account a few important factors.

Starting from the concept of the internal state of a material, Marciniak and Konieczny [7] developed a model, which incorporates the history of the deformation through the introduction of the internal state parameter σ_w. It has been assumed that the flow stress σ_p of a material depends on the internal state σ_w and the deformation conditions such as the strain, the strain rate and the temperature. Changes of the flow stress at the constant temperature can be presented in a general form:

$$\dot{\sigma}_p = \frac{\partial \sigma_p}{\partial \dot{\varepsilon}}\ddot{\varepsilon} + \frac{\partial \sigma_p}{\partial \sigma_w}F_1\dot{\varepsilon} + \frac{\partial \sigma_p}{\partial \sigma_w}F_o, \tag{15}$$

where the functions F_o and F_1 describe the internal state parameters depending on the deformation conditions.

The first term on the right-hand side of the equation (15) describes the material reaction on the sudden change in the strain rate, the second one determines the shape of the flow stress curve by taking into account the hardening or the softening, and the third one defines the change of the internal state of the material during the deformation interruption.

The functions and the state parameters in this model are described by equations that have rather a complex mathematical form and no physical meaning. The model describes with a sufficient accuracy the behaviour of low-carbon steel containing up

to 0.1 %C in a wide range of temperatures and deformation rates. However, it does not take into account the dynamic recrystallization that at higher temperatures starts already at a very small deformation. This is a source difficulty when the model is to be used for description of the material behaviour at higher temperature and under large plastic strains.

An original method for calculating the flow stress was proposed by P i e t r z y k and H o d g s o n [8-10]. Those models base on the structural description of the flow stress, which is determined on the basis of the dislocation development. Here, a dislocation density ρ is a main parameter. Assuming that the mechanic resistance for the dislocation mobility depends on the dislocation density, the stress-strain relationship:

$$\sigma_p = A\mu b\rho^{0,5}, \tag{16}$$

where: μ is a shear modulus, b is Burgers vectors and A is material constant. Starting from these assumptions, a few versions of various dislocation functions describing the material internal state are considered.

In the first P i e t r z y k model, the dislocation density distribution function $G(\rho, t)$ has been used [8, 9]. This function, suggested by Sandström and Lagneborg [22], is defined as a volume fraction with the dislocation density in the range $\langle \rho, \rho + d\rho \rangle$. In consequence, the differential equation that describes the dislocation evolution is obtained

$$\frac{dG(\rho,t)}{dt} = \frac{\dot{\varepsilon}}{bl} - g(\varepsilon) - \kappa\rho G(\rho,t), \tag{17}$$

where $\frac{\dot{\varepsilon}}{bl}$ is the athermal hardening, $g(\varepsilon)$ is the thermally activated recovery and $\kappa\rho G(\rho,t)$ is the thermally activated recrystallization.

Determination of the coefficients that occur in that model is a basic difficulty in its applications. Therefore a simplified version of the above model has been suggested, where for the change of the average dislocation density, a differential equation

$$\frac{d\rho(t)}{dt} = A_1\dot{\varepsilon} - A_2\rho t^2 - A_3\rho(t - E_d), \tag{18}$$

where: E_d is dislocation energy, A_1, A_2, A_3 are material constants,
was proposed [28]. The first term in (18) describes the athermal hardening. The second term is responsible for the recovery and it may depend on the dislocation density depending on the recovery mechanism. The last one corresponds to the softening caused by the dynamic recrystallization that starts at the critical time t. Needed values of the material constants can be determined by the inverse method [29] using the Comp_axi program [30].

In another more simplify version of the P i e t r z y k model the first two terms in (18) (reflecting the strain hardening and dynamic recovery) are exchanged by σ_p given by the following expression

$$\sigma_p = A_1\varepsilon^{n_1}\sinh^{-1}(A_2Z)^{n_2} \tag{19}$$

where: A_1, A_2, n_1, n_2 are material constants, Z is Zener-Hollomon parameter.

The dynamic recrystallization is represented by an additional term that includes the integral of the dislocation density over a time. The integral term represents the accumulation of lattice defects, which is a driving force for dynamic recrystallization.

Great difficulties arising when the described models are to be implemented into the finite element codes were a reason that Pietrzyk has proposed some simplifications relying on using the averaged dislocation density and determining the needed coefficients empirically. The conception of this model and the way in which the coefficients can be determined, have been presented in the paper [31]. The basic assumption taken in this model is that the flow stress in metal forming processes is a function of the dislocation density. A quantitative relationship between the stress and the averaged dislocation density is given by the expression

$$\sigma_p = \sigma_0 b \mu \sqrt{\rho}. \tag{20}$$

The main advantage of the model above is that it can be easily implemented into the finite element codes. The proposed model was experimentally verified with good results.

Another Pietrzyk model of the material internal state bases on the evolution of the dislocation density. It assumes that the work hardening is caused by increase of dislocations, whereas the softening is an effect of the dynamical recovery, where the movement of dislocations is caused both by cross slip and by development of the cell structure.

The separation of the inner and outer surfaces of the cell structure as well as an application of the tensile test behind the instability limit by using the Bridgman-Spiridonova equation are original ideas applied in that model.

Modern investigations to build the model for the flow stress and strain on the base of behaviour of the individual grain by using MES have been also proceeded. Such relationships are built by using the phenomenological description of the work hardening by dislocation density changes. Very modern models are built for the single crystal of the FCC structure and the policrystals created from the single layer of grains either with precise oriented boundaries or with the diameter below a few micrometers [32].

Another model taking into account the material internal state and structural processes was elaborated by Gronostajski [6, 33, 34]. That model can be applied to large plastic strains. To render properly the influence of the strain rate history on the flow stress, it was assumed that the material response caused by a change of the viscous properties occurs simultaneously with the change of the strain rate, whereas the change in the material internal state is somewhat delayed. The latter change is defined by introducing the concept of the evolution rate of the material internal strain $\dot{\varepsilon}_w$.

In this model, the flow stress has the following form

$$\sigma_p = M(T)P(\dot{\varepsilon}, T)\sigma_w(\varepsilon, \dot{\varepsilon}_w, T), \tag{21}$$

where: $\sigma_w(\varepsilon, \dot{\varepsilon}_w, T)$ is the material internal state, $M(T)$ is a function describing an influence of changes of the elastic material properties varying with temperature on the flow stress, $P(\dot{\varepsilon}, T)$ is a function describing the effect of sudden changes of the strain rate on the flow stress.

Each material is described by its basic internal state-strain curve. Such a curve allows to determine both the $\sigma_w - \varepsilon$ and $\sigma_p - \varepsilon$ curves at various temperatures and strain rates.

The change of the material internal state caused by structural processes is described by the following differential equation

$$\left(\frac{\partial \sigma_w}{\partial \varepsilon}\right)_{\varepsilon,\dot{\varepsilon},T} = \left(\frac{\partial \sigma_{wB}}{\partial \varepsilon}\right)_{\varepsilon,\dot{\varepsilon}_B,T_B} - \left(\frac{\partial \sigma_{wZ}}{\partial \varepsilon}\right)_{\varepsilon,\dot{\varepsilon},T} - \left(\frac{\partial \sigma_{wR}}{\partial \varepsilon}\right)_{\varepsilon,\dot{\varepsilon},T} + \left(\frac{\partial \sigma_{wD}}{\partial \varepsilon}\right)_{\varepsilon,\dot{\varepsilon},T}, \tag{22}$$

where: the last three terms on the right-hand side are the change rates of: the material internal state which reflect the dynamical recovery, the dynamical recrystallization and ageing processes, respectively. The first term on the right-hand side is the basic change rate of the material internal state when all the left terms on the right-hand side of (22) are equal to zero. The term on the left-hand side in (22) is the change rate of the internal state determined by ε, $\dot{\varepsilon}$ and T.

The basic material internal state curve σ_{wB} is defined separately for the strains over the range $0 < \varepsilon < \varepsilon_n$ and for the strains $\varepsilon_n \leqslant \varepsilon$. The ε_n is the strain at the point of saturation. The first piece of the curve is given by

$$\sigma_{wB} = A(\varepsilon + \varepsilon_n)^n \tag{23}$$

and the second one by

$$\sigma_{wB} = A_1 \varepsilon. \tag{24}$$

All the parameters are so chosen that the resulting curve is continuous.

It is postulated that the change rate of the material internal state σ_{wZ} caused by the dynamic recovery should be of the form

$$\left(\frac{\partial \sigma_{wZ}}{\partial \varepsilon}\right)_{\varepsilon,\dot{\varepsilon},T} = (b - a\varepsilon)\left(\frac{\partial \sigma_{wB}}{\partial \varepsilon}\right)_{\varepsilon,\dot{\varepsilon}_B,T_B}, \tag{25}$$

where a and b are material constants depending on the temperature and the strain rate.

For description of the change rate of the material internal state caused by the dynamic recrystallization σ_{wR}, the following function is taken

$$\left(\frac{\partial \sigma_{wR}}{\partial \varepsilon}\right)_{\varepsilon,\dot{\varepsilon},T} = \frac{2(\sigma_{wm} - \sigma_{ws})}{\varepsilon_s - \varepsilon_c} \frac{1}{\cosh^2\left(\frac{4}{\varepsilon_s - \varepsilon_c}\left(\frac{\varepsilon_c + \varepsilon_s}{2} - \varepsilon\right)\right)} + \left(\frac{\partial \sigma_{wB}}{\partial \varepsilon}\right)_{\varepsilon,\dot{\varepsilon},T}$$
$$+ \left(\frac{\partial \sigma_{wD}}{\partial \varepsilon}\right)_{\varepsilon,\dot{\varepsilon},T} - \left(\frac{\partial \sigma_{wZ}}{\partial \varepsilon}\right)_{\varepsilon,\dot{\varepsilon},T} + \left(\frac{\partial \sigma_{wB}}{\partial \varepsilon}\right)_{\varepsilon,\dot{\varepsilon},T} + \left(\frac{\partial \sigma_{wD}}{\partial \varepsilon}\right)_{\varepsilon,\dot{\varepsilon},T} - \left(\frac{\partial \sigma_{wZ}}{\partial \varepsilon}\right)_{\varepsilon,\dot{\varepsilon},T}, \tag{26}$$

where: σ_{wm} is the material internal state at the critical strain, σ_{ws} is the material internal state in the range of the steady state flow, ε_c is the critical strain corresponding to the maximum flow stress, and ε_s is the strain at the outset of the steady state flow.

The values of σ_{wm} and σ_{ws} can be obtained from the equation (19) as follows

$$\sigma_{wm} = \frac{\sigma_{pm}}{M(T)P(\dot{\varepsilon}, T)}, \tag{27}$$

$$\sigma_{ws} = \frac{\sigma_{ps}}{M(T)P(\dot{\varepsilon}, T)}, \tag{28}$$

where: σ_{pm} is the maximum flow stress and σ_{ps} is the stress level in the range of the steady state flow.

The quantities σ_{pm} and σ_{ps} are connected with the temperature and the strain rate by the Arrhenius equation [35]

$$Z = A[\sinh(\alpha\sigma_p)]^n \tag{29}$$

where: B, α, u are material constants and the flow stress σ_p is equal to either σ_{pm} or σ_{ps}.

The Zener-Hollomon parameter is also used for description of the dependences of the critical strain ε_c and the strain ε_s at the outset of the steady state flow. These dependences can be expressed as follows

$$\varepsilon_{cr} = M_m Z_m^{l_m} = k_m D^p Z_m^{l_m}, \tag{30}$$

$$\varepsilon_s = M_s Z_s^{l_s} = k_s D^p Z_s^{l_s}, \tag{31}$$

where M_s, l_s M_m, p, l_m, k_m and k_s are material constants and D is the initial grain size in μm.

The function $M(T)$ in (27) is defined as the ratio

$$M(T) = \frac{E_T}{E_{T_0}} \tag{32}$$

of the Young modulus E_T at the particular temperature T to the Young modulus E_{T_o} at the ambient temperature T_0 ($T_0 = 293$) (both are taken at the same constant strain rate).

It has been assumed that the function $P(\dot{\varepsilon}, T)$ can be defined as follows

$$P(\dot{\varepsilon}, T) = \dot{\varepsilon}^m \tag{33}$$

where m is the strain rate sensitivity coefficient dependent on temperature.

To render properly the influence of the strain rate history on the flow stress, it is assumed that the response of the material on the changes in its viscous properties described by the function $P(\dot{\varepsilon}, T)$ occurs simultaneously with the strain rate changes, whereas the change in the material internal state appears with some delay.

The change in the strain rate $\dot{\varepsilon}$ has an effect on the evolution rate of the internal state $\dot{\varepsilon}_w$ and it is given by the following differential equation

$$\frac{\dot{\varepsilon} d_w}{dt} = L_T \left[\dot{\varepsilon}(t) - \dot{\varepsilon}_w(t)\right], \tag{34}$$

where L_T is a coefficient depending on the temperature. Thus, it also influences on the change of the material internal state σ_w and the flow stress σ_p.

The material internal state σ_w has two different forms, depending on the strain range. For strains less than the critical strain $\varepsilon \leqslant \varepsilon_c$, the internal state of materials is given by

$$\sigma_w = (1 - b + a\varepsilon)(\sigma_{wB})_{\varepsilon,\dot{\varepsilon}_B,T_B}. \tag{35}$$

For the strain greater than ε_c, the material internal state can be written as follows

$$\sigma_w = \frac{\sigma_{wm} - \sigma_{ws}}{2} \operatorname{tgh}\left[\frac{4}{\varepsilon_s - \varepsilon_c}\left(\frac{\varepsilon_c + \varepsilon_s}{2} - \varepsilon\right)\right] + \frac{0,96\sigma_{ws} + 1,04\sigma_{wm}}{2}. \tag{36}$$

Substituting the expressions (36) and (37) into (21) successively allows to obtain the following two forms for the flow stress

$$\sigma_p = M(T) P(\dot{\varepsilon}, T) \sigma_w = M(T) P(\dot{\varepsilon}, T)(1 - b + a\varepsilon)(\sigma_{wB})_{\varepsilon,\dot{\varepsilon}_B,T_B}, \tag{37}$$

in case of $\varepsilon \leqslant \varepsilon_c$ and

$$\begin{aligned}\sigma_p &= M(T) P(\dot{\varepsilon}, T)\sigma_w \\ &= M(T) P(\dot{\varepsilon}, T) \frac{\sigma_{wm} - \sigma_{ps}}{2} \operatorname{tgh}\left[\frac{4}{\varepsilon_s - \varepsilon_c}\left(\frac{\varepsilon_c + \varepsilon_s}{2} - \varepsilon\right)\right] + \frac{0,96\sigma_{ws} + 1,04\sigma_{wm}}{2}\end{aligned} \tag{38}$$

in case of $\varepsilon > \varepsilon_c$.

Before any application of the model, the basic curves of the material internal state, the functions $P(\dot{\varepsilon}, T)$, $M(T)$, a and b, and the parameters σ_{wm}, σ_{ws}, ε_c, ε_s have to be determined.

The basic curves are usually constructed on the basis of simple compression, tension or torsion tests. Each of these tests has its advantages and disadvantages. It seems that the most suitable one is the torsion test, because it allows considering large plastic strains at high strain rates not causing the geometric instability. Thus, the conditions of the test are comparable with those occurring in industrial metal forming processes. Owing this, the results obtained from torsion tests can be used for describing continuous and discontinuous industrial processes such as: die forging, extrusion, rolling and so on. On the other hand, the difficulties arising in proper calculating the flow stress and strain caused by the heterogeneous deformation in a cross section of twisted samples are their main disadvantage. There are a few various methods for calculating the flow stress and strain in the torsion test, both simple ones based on the Huber-Mises

hypothesis [36-39] and more complicated ones giving a more accuracy based on FEM [40-42].

The model shortly presented above allows not only to determine the flow stress over wide ranges of the strain rate (0.01-10 s^{-1}) and the temperature (293-1073 K), but also to include the deformation rate history. The model is used for the design optimisation of the metal forming processes of non-iron alloys to gain their high efficiency and a good quality of products. Unfortunately, this model does not take into account the static and dynamic softening kinetics and the sudden changes of temperature during deformation.

A newer improved model [43] includes all the factors mentioned above. It is based on a differential equation that joins the changes in the internal state intensity and in the deformation conditions with quantities characterising the different interrelations between homogeneously distributed hardening and softening processes [44, 45].

The conception of this model is based on the following six assumptions:

a) The flow stress σ_p of the material in the equilibrium conditions and the material internal state $\sigma_w(\varepsilon, \dot{\varepsilon}, T)$ are related as follows

$$\sigma_p(\varepsilon, \dot{\varepsilon}, T) = P'(\dot{\varepsilon}, T)\sigma_w(\varepsilon, \dot{\varepsilon}, T), \tag{39}$$

In the model [43] the function

$$P'(\dot{\varepsilon}, T) = \frac{\sigma_p + \Delta\sigma_{p\dot{\varepsilon}}}{\sigma_w} \cdot \frac{\sigma_p + \Delta\sigma_{pT}}{\sigma_w}, \tag{40}$$

where: $\Delta\sigma_{p\dot{\varepsilon}}$ is increase of flow stress caused by change of strain rate,
$\Delta\sigma_{pT}$ is increase of flow stress caused by change of temperature.

is introduced instead of function (33) used in models [6, 29, 30]. The function (40) should describe the immediate jumped change in the flow stress $\sigma_p^u(\varepsilon, \dot{\varepsilon}_2, T_2)$ given by the following equality

$$\sigma_p^u(\varepsilon, \dot{\varepsilon}_2, T_2) = P'(\dot{\varepsilon}_2, T_2)\sigma_w(\varepsilon, \dot{\varepsilon}_1, T_1), \tag{41}$$

caused by sudden change of the strain rate and temperature.

The function (40) in the model [43] takes into account the reciprocal effect of changes of temperature and strain rate, which in normal metal forming processes does not exist, therefore the authors of the paper change the equation (40) by the following

$$P'(\dot{\varepsilon}_2, T_2) = \left.\frac{\sigma_p + \Delta\sigma_{pE} + \Delta\sigma_{pT}}{\sigma_w}\right|_{\varepsilon_1, T_1}. \tag{42}$$

Since the changes in the material internal state σ_w are caused by the changes in the structure, it evolves and affects the flow stress. In consequence, the instable flow stress σ_p^u evolves with the time to the stable level given by equation (41) at $\dot{\varepsilon} = \dot{\varepsilon}_2$ and $T = T_2$.

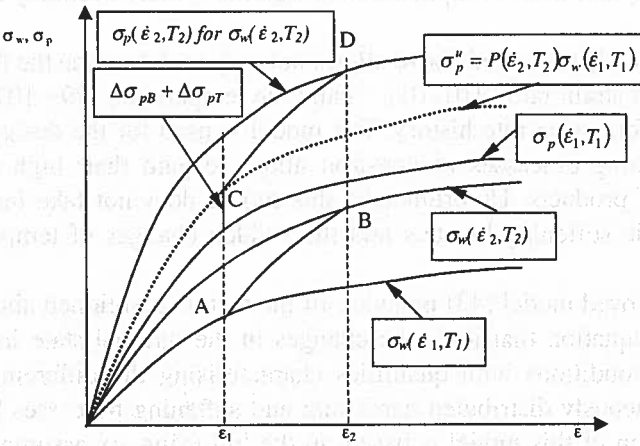

Fig. 1. Relationship between flow stress σ_p and internal state of material σ_w and stable and unstable deformation conditions. The sudden change in the strain rate from $\dot{\varepsilon}_1$ to $\dot{\varepsilon}_2$ and temperature from T_1 to T_2 takes place at ε_1 and evolution of internal state reaches stable deformation at ε_2. The change of internal state of material σ_w from point A to B is caused by change of strain rate and temperature, and that caused the increase of flow stress σ_p from point C to D

The mechanism described above is illustrated in figure 1.

b) The material is characterised by base internal state curves. Under real deformation conditions, they must be modified to include changes in the temperature and the strain rate, as well as the interruption time in the deformation process. The part of the base curve representing the state before attaining saturation is a monotonically increasing function of the internal stress. At lower temperatures, the curves usually have no part representing the saturation state, because a fracture takes place early enough. The characteristic levels of the material internal state are described by the modified Garofalo equation [46], and characteristic values of the critical strains can be determined by the Zener-Hollomon parameter [4].

c) The following factors: the strain hardening processes and the opposite processes associated with a reconstruction of the deformed structure and the interruption time in the deformation process affect on the internal state. The dynamic softening kinetics can be determined from the flow stress-strain curves, whereas the static softening kinetics can be determined from the relaxation stress curves [47].

d) If the deformation process consists of a few operations, during the interruption between any two consecutive operations or after the whole deformation, only the static softening process can hold.

e) If the deformation process is in progress, besides the strain hardening the softening caused by the dynamic recrystallization can hold. It is assumed that both processes are homogeneously distributed in the material. This means that in a very small region around each point both processes affect simultaneously the material internal state.

Since the hardening and softening processes are time dependent, the average value of the internal state in each point is varying in the time. The internal state of such material can be calculated as follows $\sigma_{wn}(t) = a\sigma_{wr}(t) + b\sigma_{wa}(t)$, where a is a fraction of the strain hardening and b is the fraction of the softening of material.

f) The model assumes that the final decrease in the internal state caused by the softening, reaches its initial value and then during the further deformation it increases again due to the strain hardening. During the deformation the material can undergo strain hardening and softening many times. When the deformation is stopped, the static or metadynamic softening processes can take place.

In order that the model above could be applied, the basic curve of the internal state, the kinetics of the softening and the critical strain for the recrystallization has to be known. For the model to construct, a programme in Turbo Pascal was prepared.

In the model, for description of the base relationship between the internal state of the metal and the true strain, a differential equation for the changes in the internal state intensity is used. The internal state intensity contains two terms, one describes an increase in internal state intensity and another one, built on the basis of the recovery theory describes a decrease in that intensity. Each material was characterised by a σ_{wb}/σ_{wn} ratio, the characteristic strain ε_r, and the strain-hardening coefficient n. The differential equation presented below is the most suitable for the description of the base curves $\sigma_w b$

$$\frac{d\sigma_{wb}}{d\varepsilon} = \frac{n}{\varepsilon_r}\frac{\sigma_{wn}^2}{\sigma_{wb}}\left[1 - \left(\frac{\sigma_{wb}}{\sigma_{wn}}\right)^{1/n}\right]\left(\frac{\sigma_{wb}}{\sigma_{wn}}\right)^{2-\frac{1}{n}} \tag{43}$$

which after integration at the boundary condition $\varepsilon = 0$, $\sigma_w b = 0$ takes the following form

$$\sigma_{wb}(t; t_1) = \sigma_{wn}\left[1 - \exp\left(-\frac{t}{\varepsilon_r}\right)\right]^n. \tag{44}$$

The study of the kinetics of the dynamic softening is based on an analysis of the flow stress-strain curves. The dynamic softening begins at the critical strain ε_c and ends at the outset of the steady stable flow ε_s. The kinetics equation of the dynamic softening X_{red} is given by:

$$X_{red} = 1 - \exp\left[-K_d(\varepsilon - \varepsilon_c)^{N_d}\right], \tag{45}$$

where: N_d, K_d are material constants,

The kinetics of the static softening is determined by analysing the relaxation stress when the deformation of the material ceased at the strain greater than the critical one and at the flow stress during reloading with the same strain rate. The material softening X_{res} for a given relaxation time is calculated from the formula

$$X_{res} = \frac{(\sigma_{prs} - \sigma_{prb})(\sigma_{pr} - \sigma'_{p0})}{(\sigma_{pr} - \sigma_{p0})(\sigma_{prs} - \sigma_{prf})}, \tag{46}$$

where σ_{prb} is the current relaxation stress, σ_{prs} is the initial relaxation stress, which is a result of the decrease of the stress σ_{pr} due to the viscoplastic properties of the

material, σ_{prf} is the final relaxation stress, σ_{p0} is the initial yield stress, σ'_{p0} is the yield stress under reloading and σ_{pr} is the flow stress prior to the deformation is ceased (Fig. 2) [47].

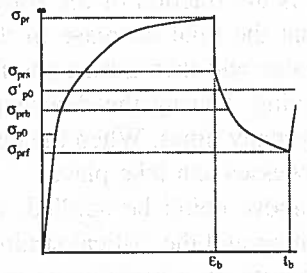

Fig. 2. Flow relaxation method

In the case of a sudden change of the strain rate or temperature, the material does not reach the flow stress level, which would be attained if the material were deformed continuously at a constant strain rate or the temperature corresponding to the values obtained after the sudden change.

For the proper analysis of the effect of the sudden change on the deformation temperature, it is assumed that the material response is initially associated with changes in the atom vibration kinetic energy, which cause immediate changes in the resistance of the dislocation movement and in consequence, in the flow stress. Such an influence of the temperature conditions is described by the function $P'(T, \dot{\varepsilon})$. The variation of the deformation temperature T influences also indirectly on the evolution of the internal state by the internal temperature T_w related to T by the following differential equation

$$\frac{dT_w}{dt} = L_{\dot{\varepsilon}} \left[T(t) - T_w(t) \right], \tag{47}$$

where: $L_{\dot{\varepsilon}}$ is the strain rate dependent coefficient.

To sum up, it can be stated that if there is a sudden change in the strain rate, for example, from $\dot{\varepsilon}_1$ to $\dot{\varepsilon}_2$, then the flow stress evolves as follows

$$\sigma_p(\varepsilon, \dot{\varepsilon}_2, T_1) = P'_{\varepsilon_2, T_1} \sigma_p(\varepsilon, \dot{\varepsilon}_2, T_1), \tag{48}$$

whereas for a sudden change in the temperature from T_1 to T_2, the flow stress changes as follows

$$\sigma_p(\varepsilon, \dot{\varepsilon}_1, T_2) = P'_{\varepsilon_1, T_2} \sigma_p(\varepsilon, \dot{\varepsilon}_1, T_2). \tag{49}$$

The proposed method makes it possible to analyse the effect of optional strain rate and temperature deformation changes on the flow stress. In such a case, the differential equations (34) and (47) can be approximately solved, for example by the Runge-Kutta method.

The model describing continuous courses of the internal state for various deformation conditions needs some characteristic points on the internal state-strain curves.

Such points are defined by four parameters: σ_{wn}, ε_{wn}, σ_{ws} and ε_s. The parameter σ_{wn} is the internal saturation state, ε_{wn} is the strain saturation corresponding to σ_{wn}, σ_{ws} is the level of the steady internal state and ε_s is the strain observed when σ_{ws} begins. On the basis of the performed investigations [4, 6, 33, 48] it can be stated that for the silicon and aluminium bronzes and brasses in the wide range of the temperature and the strain rate changes, the characteristic levels of the flow stress can be described with a sufficient accuracy by the Garofalo equation. The characteristic values of the strain can be also easily determined, because they are known functions of the Zener-Hollomon parameters.

The algorithm of determining the flow stress curves based on the above model can be divided into a few steps. At the beginning, the basic curves of the material internal state are determined by the formula (44) taking into account only the recovery process and the deformation conditions including the temperature and the strain rate. The obtained curves are modified by superimposing the given dynamic softening kinetics (DSK) which results in new curves, on which the values of the maximum and the steady state flow stress are distinct. The curves are further modified by superimposing the static softening kinetics (SSK), which occurs during breaks in the deformation or at the end of the deformation process. Finally, the curves are modified to include sudden changes in the deformation conditions (SDCC). This algorithm is shown in Fig. 3.

It seems that the above general model can be used for determining the flow stress curves, as they are functions of only such parameters as: ε_c, ε_r, σ_{wn}, n, K_d,, N_d, $\dot{\varepsilon}$, T. These parameters can be easily determined in the basic tests such as: the torsion test [36-42], the dynamic and static kinetics tests [47] and the test of the reaction on the sudden change of the strain rate and temperature [43].

The model above was used for the theoretical description of the flow stress-strain curve of aluminium bronze containing Al 8 % (mass fraction) subjected to the continuous deformation at temperature of 923 K and at the strain rate of 0.1 s^{-1}. The result of the comparison of the flow stress - true strain curve calculated by using the described model with an experimental one obtained in the torsion test is shown in Fig. 4.

The correlation between both curves is high. At such low strain rate the effect of plastic work on the increase of deformed sample temperature is very small, because the heat transfers between sample and the surroundings and small plastic work at high temperature. In that case the increase of temperature was below few degrees Celsius and that effect on flow stress was negligible. The model usually gives the confidence interval ±5% at significance level of 0.05.

It is worth to mention that the internal state of the material deformed in a complex way differs from the internal state of the same specimen deformed in another way even if the initial and final states in both deformation processes are the same. These differences could be explained as an effect of the crystallographic texture, which develops during the deformation process, as it is a function of the strain path. This effect of the texture is visible on the stress-strain curve whose shape essentially depends on the texture nature [45].

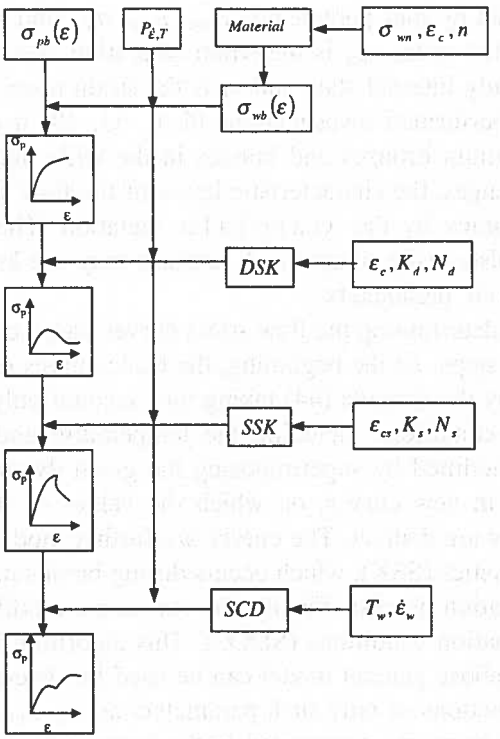

Fig. 3. Algorithm for calculation of constitutive equations

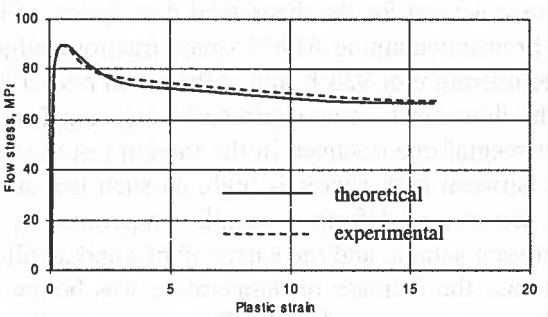

Fig. 4. Theoretical and experimental flow stress-strain curves for aluminium bronze containing 8 % of Al at 923 K and strain rate of 0.1 s^{-1}

3. Conclusions

As it can be seen from the review given above, there are a few models which describe the internal state of the material subjected the deformation. Some of them are so complicated that their practical application is in practice very difficult or even

impossible, on the basis of the nowadays knowledge of phenomena taking place during the deformation processes of metals and alloys.

Several typical models have been presented. They differs in their treatment of the factors that influence on the course of the flow stress curves. Each of them allows to determine the dependence of the flow stress on the internal state and the deformation conditions. All the presented models differ in their range of applications. Also, the accuracy reached in the description of the real course of the flow stress is different in each of them. Some models were described in more detail. Moreover, one of them was little modified and used for calculation of the flow stress strain relationship. Owing introducing the conception of the internal state that model could take into account the strain hardening, the dynamic and static kinetics of softening, slow and sudden changes of the strain rate and temperature, the interruption of the deformation. Some models can be applied to the large plastic strains in a wide range of the deformation conditions and not only for hot and warm deformation temperatures, but also for the low temperature after elimination of the softening process.

A few models can be easily implemented into FEM of design and optimization procedures of the metal forming processes, for reducing process energy consumption and obtaining the products of the desired properties.

A crucial requirement for models in materials science is that they must be based on the structure/properties connection. In phenomenological terms, this means that they can only involve state parameters; history variable such as strain and time can only appear differentially. Thus, strain-hardening behavior must be expressed by differential equations; the integral over a specific path gives the stress-strain curve. Now it is commonly known that changes of direction of straining, not only reversal, cause significant transients of the hardening coefficient, sometimes even initially negative values i.e. work softening.

So far no model has been built which would incorporate all the thermo-mechanical and structural processes that occur during and after deformation. Therefore, the researches aimed at improving the existing models, which describe the reactions of materials to complex deformation conditions, are still very attractive.

REFERENCES

[1] Z. Gronostajski, Constitutive equations applied in sheet metal forming processes, Proc. of Int. Conf. Advances in Materials and Processing Technologies, AMPT'95, 919-925 Guimaräes, Portugal, (1997) .

[2] Z. Gronostajski, Model describing the flow stress of silicon bronzes below critical strain, J. of Mater. Proc. Technol. **64**, 157-168 (1997).

[3] Z. Gronostajski, Constitutive model of silicon bronzes for finite element analysis, Proc. of the 4th Int. Conf. Sheet Metal 1996, 229-238 Twente (1996).

[4] Z. Gronostajski, Model describing the characteristic values of flow stress and strain of brass M63 and aluminium bronze BA93, J. of Mater. Proc. Technol. **78**, 84-89 (1998).

[5] Z. Gronostajski, Równania konstytutywne stosowane w warunkach obróbki plastycznej na zimno blach, Obróbka Plastyczna Metali **8** 19-23 (1997).
[6] Z. Gronostajski, Z. Misiołek, Model describing flow stress by means of structural processes and internal state of materials, Archive of Metallurgy **40**, 399-418 (1995).
[7] Z. Marciniak, A. Konieczny, Modelling the variation of the yield stress within the temperature range typical for cold and warm metal forming, J. Mech. Work. Technol. **15**, 15-37 (1987).
[8] M. Pietrzyk, Propozycja modelu opisującego umocnienie metali w procesach plastycznej przeróbki na gorąco i uwzględniającego historię odkształcenia, Mat. Międz. Konf. Plast'96 1-10 Ustroń (1996).
[9] M. Pietrzyk, Zastosowanie modelu konstytutywnego wykorzystującego zmienną wewnętrzną do symulacji metodą elementów skończonych procesów plastycznej przeróbki na gorąco. Proc. Int. Conf. Forming'2000 1 Ustroń (2000).
[10] M. Pietrzyk, P.D. Hodgson, Internal variable model applied to the prediction of grain size during thermomechanical processing of C-Mn steel, Inżynieria Materiałowa, **19**, 645-650 (1998).
[11] F. Grosman, The characteristics of materials technological plasticity, rozdział w monografii pt. Plasticity of Metallic Materials, Deformation Behaviour, Structure Development, Testing, Modeling. Red. E. Hadasik i I. Schindler, Wydawnictwo Politechniki Śląskiej, 11-40 Gliwice (2004).
[12] A. K. Miller, Unified constitutive equations for creep and plasticity, Elsevier, London (1987).
[13] Z. Gronostajski, Selected Models Descrbing Flow Stress in Conditions of Plastic Working Processes, Proc. of 14th Int. Sc. Conf. Advanced Materials and Technologies, AMT'95, 141-148 Zakopane (1995).
[14] Z. Gronostajski, Modelling of the Flow Stress of Copper Silicon Alloys, Proc. of Int. Conf. Advances in Materials and Processing Technologies, AMPT'95, Dublin 765-774 (1995) .
[15] C. M. Sellars, Role of computer modelling in thermomechanical processing, Inżynieria Materiałowa **19**, 100-107 (1998).
[16] C. M. Sellars, J. A. Whiteman, Recrystallization and grain growth in hot rolling, Metal. Sci, **13**, 187-194 (1979).
[17] U. F. Kocks, H. Mecking, Physics and phenomenology of strain hardening: the FCC case, Progress In Mat. Sci. **48**, 171-273 (2003).
[18] E. W. Hart, Micromechanical basis for constitutive equations with internal state variables, Trans. of ASME **106**, 322-325 (1984).
[19] L. Anand, Constitutive equations for the rate-dependent deformation of metals at elevated temperatures, Trans. of ASME **104**, 12-17 (1982).
[20] M. Zhou, M. P. Clode, Modeling of high temperature viscoplastic flow of aluminium alloys by hot torsion testing, Mat. Science and Technol. **13**, 818-824 (1997) .
[21] P. Perzyna, A. Sawczuk, Problems of thermoplasticity, Nuclear Eng. Design, **24**,1-6 (1973).
[22] R. Sandström, R. Langeborg, A model for hot working occurring by recrystallizatin, Acta Met. **23**, 387-398 (1975).
[23] Y. Estrin, H. Mecking, A unified phenomenological description of work hardening and creep base on one-parameter models, Acta Metall. **32**, 57-70 (1984).

[24] H. Mecking, U.F. Kocks, Kinetics of flow and strain hardening, Acta Metall. 29 (1981) 1865-1875.
[25] Y. Estrin, Dislocation density related constitutive modelling, In Unified Constitutive Laws of Plastic Deformation, Eds. Krausz A.S. and Krausz K., Academic Press, 1996.
[26] H. Mecking, B. Nicklas, N. Zarubova, U.F. Kocks, A "universal" temperature scale for plastic flow, Acta Metall. **34**, 527-530 (1986).
[27] E.S. Palma, O. Voehringer, Modelagem da tensão de escoamento de materiais metálicos em função da temperatura e velocidade de deformação, J. of the Braz. Soc. Mechanical Sciences **17**, 77-88 (1995).
[28] C.H.J. Davies, Dynamics of the evolution of dislocation populations. Scr. Met. Mater. **30**, 349-353 (1994).
[29] J. Kusiak, R. Kawalla, M. Pietrzyk, H. Pircher, Inverse analysis applied to the evaluation of material parameters in the history dependent flow stress equation in hot forming of metals, J. Mat. Proc. Technol. **60**, 455-461 (1996).
[30] M. Pietrzyk, J. Kusiak, Nowa wersja programu Comp-axi pozwalająca na automatyczne wyznaczanie krzywych umocnienia metali i stopów odkształcanych plastycznie na gorąco. Mat. Konf. Zastosowanie Komputerów w Zakładach Przetwórstwa Metali. Koninki 49-54 (1996).
[31] J. Ordon, R. Kuziak, M. Pietrzyk, History dependent constitutive law for austenitic steel. Proc. Int. Conf. Metal Forming'2000, Kraków.
[32] L. Tabourot, M.C. Fivel, E.F. Rauch, Physically based constitutive equations for fcc single crystals, Proc. of Int. Conf. Plasticity'99, 1-4 Mexico, (1998).
[33] Z. Gronostajski, Development of constitutive equations of copper- silicon alloys, J. of Mat. Proc. Techn. **60**, 621-627 (1996).
[34] Z. Gronostajski, Z. Misiołek, Constitutive equations of silicon bronzes, J. of Mat. Proc. Techn. **62**, 133-139 (1996).
[35] L. Błaż, A. Korbel, Wysokotemperaturowe odkształcanie miedzi i mosiądzu (34.4%Zn), Archiwum Hutnictwa **27**, 285-312 (1982).
[36] Z. Gronostajski, Wyznaczanie naprężenia uplastyczniającego w próbie skręcania z uwzględnieniem osłabienia materiału, Mat. Konferencji Projekty Badawcze z Zakresu Przeróbki Plastycznej, Metaloznawstwa i Technologii Spiekowych, Szklarska Poręba 51-55 (1997).
[37] Z. Gronostajski, Analiza wyznaczania naprężenia uplastyczniającego w próbie skręcania, Rudy i Metale Nieżelazne, **44**, 236-242 (1999).
[38] E. Hadasik, A. Płachta, I. Schindler, Z. Gronostajski, Analysis of methodology for determination of the flow stress in hot torsion test, Proc. of 11th Int. Metallurgical and Materials Conf., Metal'2002, Hradec and Moravici, (2002) 1-8.
[39] E. Hadasik, A. Płachta, Z. Gronostajski, Analiza sposobów wyznaczania naprężenia uplastyczniającego w próbie skręcania na gorąco, Rudy i Metale Nieżelazne **46**, 504-507 (2001).
[40] Z. Gronostajski, E. Hadasik, I. Schindler, Analiza próby skręcania na gorąco metodą elementów skończonych, Mat. 9 Konf KomPlasTech'2002, Szczawnica, 103-109 (2002).
[41] Z. Gronostajski, Analiza metodą elementów skończonych plastometrycznej próby skręcania, Informatyka w Technologii Materiałów **2**, 64-54 (2002).
[42] Z. Gronostajski, Symulacja MES rozkładu temperatury w skręcanych próbkach,

Mat. 7 Konf. Zastosowanie Komputerów w Zakładach Przetwórstwa Metali, KomPlas-Tech'2000 247-254 Krynica (2000).

[43] Z. Gronostajski, A general model describing flow stress of copper alloys in different deformation conditions, J. Mat. Proc. Technol. **142** 684-691 (2003).

[44] Z. Gronostajski, Model opisujący zmiany naprężenia uplastyczniającego uwzględniający osłabienie materiału, Przegląd Mechaniczny **60** 9-12 (2001).

[45] Z. Gronostajski, Modele konstytutywne opisujące zachowanie się wybranych stopów miedzi w zakresie dużych odkształceń plastycznych, Monograph, Ed. Oficyna Wydawnicza of Wroclaw University of Technology, (2000).

[46] S. Garofalo, An empirical relation defining the stress dependence of minimum creep rate in metals, Trans. AIME **227**, 351-355 (1963) .

[47] Z. Gronostajski, Metody badania kinetyki osłabienia statycznego i dynamicznego, Rudy i Metale Nieżelazne **47**, (2002) 11-16.

[48] Z. Gronostajski, Badania stosowane w zaawansowanych procesach kształtowania plastycznego, Ed. Oficyna Wydawnicza of Wroclaw University of Technology, Wrocław (2003) 1-207.

Received: 10 May 2004.

A R C H I V E S O F M E T A L L U R G Y A N D M A T E R I A L S
Volume 49 2004 Issue 4

Z. OKSIUTA*, J.R. DĄBROWSKI*, W. RATUSZEK**

STRUCTURE OF POROUS SAMPLES OF Co-Cr-Mo ALLOY

STRUKTURA POROWATYCH PRÓBEK ZE STOPU Co-Cr-Mo

This paper presents the results of structural examination of porous Co-Cr-Mo alloy for bio-implants samples received after different stages of technological powder metallurgy (PM) process. The material tests were conducted on the powder obtained using the water atomization process and subsequent annealing in hydrogen, followed by green compacts sintering, rotary cold repressing (on PXW100A press), as well as the final heat treatment.

The powder particles of the Co-Cr-Mo alloy, after water atomisation, have a dendritic α-Co phase structure with a small volume of the hexagonal phase. The annealing in hydrogen atmosphere develops the isothermal ε-martensite transformation (fcc $\rightarrow$ hcp). The process of the green compacts sintering at the temperature of 1150°C shows a homogenous α-Co fine-grained structure, but the mechanical properties of samples are not satisfactory. The rotary cold repressing process causes an increase in the density and a rise in the strength parameter and hardness of samples, but the volume of the hcp-phase structure increases to 90%. The volume of the hcp-phase structure consistently increases together with the number of the repressing rotations.

The temperature of the final heat treatment exerts favourable changes on the phase structure and the mechanical properties of samples. The samples after solution treatment at the temperatures ranging from 1150°C to 1250°C obtained a homogenous α-Co structure, good ductility and the highest mechanical properties.

W pracy przedstawiono wyniki badań strukturalnych próbek otrzymanych ze stopu Co-Cr-Mo na bio-implanty, metodą metalurgii proszków (MP), po różnych etapach procesu technologicznego. Badaniom poddano materiał wyjściowy – proszek po rozpylaniu wodą i wyżarzaniu w wodorze, następnie badano próbki po spiekaniu, doprasowaniu obwiedniowym na zimno (na prasie z wahającą matrycą PXW100A) oraz końcowej obróbce cieplnej.

Bezpośrednio po rozpylaniu wodą cząstki proszku stopu Co-Cr-Mo mają dendrytyczną strukturę roztworu stałego α-Co (RSC) oraz niewielkie ilości fazy ε-Co. Proces wyżarzania proszku w wodorze w temperaturze 1000°C powoduje, na skutek izotermicznej przemiany martenzytycznej, zwiększenie udziału objętościowego fazy heksagonalnej. Po

* POLITECHNIKA BIAŁOSTOCKA, WYDZIAŁ MECHANICZNY, 15-351 BIAŁYSTOK, UL. WIEJSKA 45C

** WYDZIAŁ METALURGII I INŻYNIERII MATERIAŁOWEJ, AKADEMIA GÓRNICZO-HUTNICZA, 30-059 KRAKÓW, AL. MICKIEWICZA 30

spiekaniu w temperaturze 1150°C i wolnym chłodzeniu wraz z piecem próbki, o porowatości około 30%, posiadają jednorodną strukturę α-Co, drobne ziarno oraz stosunkowo słabe właściwości mechaniczne. Proces doprasowania spowodował znaczące zwiększenie gęstości (18÷22%), podwyższenie wartości umownej granicy plastyczności oraz mikrotwardości, przy czym udział fazy heksagonalnej zwiększył się wraz ze zwiększeniem stopnia odkształcenia próbek.

Temperatura obróbki cieplnej wpłynęła na strukturę, a tym samym na właściwości próbek. Korzystne zmiany, w postaci zwiększenia gęstości jak i uzyskanie jednorodnej pod względem fazowym struktury, otrzymano po obróbce cieplnej próbek w temperaturze 1150÷1250°C.

1. Introduction

Among modern materials used in surgery, cobalt-based alloys occupy a very important position. Co-Cr-Mo alloys of the Vitalium type have been in use for over 60 years. Due to their excellent biocompatibility, significant mechanical properties, corrosion and wear resistance they have been used as long-term implantation materials. The main advantage of these alloys is a possibility of further enhancing their properties by applying a proper production technology and heat treatment [1÷5].

The common properties of the Vitalium alloy are connected with the chemical composition of the material, its crystallographic structure and intrinsic microstructural features, such as stacking faults and twins. The matrix of this Co-Cr-Mo alloy is the metastable solid solution α–Co (fcc). The exact temperature of fcc $\rightarrow$ hcp phase transformations is not established and it is the function of the chemical composition of the alloy, the grain size, and the parameters of the annealing process (temperature and cooling rate).

The Co-Cr-Mo alloys may exhibit an fcc $\rightarrow$ hcp ($\alpha \rightarrow \varepsilon$) martensitic phase change under athermal, isothermal or strain induced transformations [3, 4]. The mechanisms of the transformation were described in numerous publications [3÷14] in which it was confirmed that quenching the Vitalium alloy from the temperature above 1100°C in water or iced brine leads to a two-phase structure ($\alpha + \varepsilon$) at the room temperature. However, this effect vanishes when a less drastic cooling rate is used. It is possible to receive the same effect through the cold plastic deformation process. In this case, together with the increase of the plastic strain, the fraction of hcp ε-phase rises. It was also indicated that the increase of the grain sizes results in hcp phase formation. This phenomenon is explained as a decrease in the temperature of the martensite start (MS), which causes a decrease in the number of ε-martensite nuclei initiating this transformation. This $\alpha \rightarrow \varepsilon$ transformation is undesirable, as the ductility of alloy diminishes drastically, mainly due to the presence of ε-phase.

According to the ISO and ASTM standards concerning implantation materials, cobalt- based alloys should be characterized by a fine-grain size, chemically homogeneous and paramagnetic structure of the solid solution of the cobalt α-phase. Moreover, according to no. 1 or 2 in ASTM standard specification, it is permitted that the matrix

of the alloy contains fine-dispersed, equally spread carbide precipitates or other non-metallic inclusions.

This paper presents the results of structural examination of porous samples received from Co-Cr-Mo implantation alloy after different stages of technological powder metallurgy (PM) process. The material tests were conducted on the powder having undergone the water atomization process and subsequent annealing in hydrogen, followed by green compacts sintering, rotary cold repressing (on PXW100A press), as well as the final heat treatment.

2. Material and experimental procedure

Two water atomized powders of Co-Cr-Mo alloy with the particle size of 20÷200 μm and different contents of carbon were examined. The chemical composition of powders is given in Table 1. The carbon and oxygen contents were determined by

TABLE 1

The chemical analysis of both Co-Cr-Mo powders after water atomization and annealing in the argon atmosphere at the temperature of 1000°C in hydrogen for 2 hours

Alloy	Chemical composition of alloy (wt.%)											
	C	O	Mo	Si	P	Ni	Fe	S	Mn	Cr	W	Co
I	0.12	0.69	4.50	0.50	0.01	–	0.55	0.01	0.88	28.22	0.02	Ball.
II	0.31	0.57	5.40	0.50	0.01	0.02	1.37	0.01	0.49	29.29	0.01	Ball.

means of LECOCS-125 and TC-336 analysers. The powders, having undergone the process of annealing in the hydrogen atmosphere at the temperature of 1000°C for 2 hours, were single-action pressed under the pressure of 600 MPa, and sintered in the argon atmosphere at the temperature of 1150°C for 1 hour and then cooled naturally inside the furnace. The next stage of the PM process was a rotary cold repressing on PXW100A press of cylindrical specimens (⌀20 × 15 mm) under the pressure of 600 MPa, with the number of rotations $i = 12$ and the conical upper die angle $\gamma_n = 2°$, with spinning tool movements (Fig. 1). The final heat treatment was carried out on the samples ⌀20 × 10 mm in size at the temperature range of 950÷1250°C in the argon atmosphere for 1 hour. Cooling of the samples was carried out in the cold area of furnace at an average speed of 45°C/min.

An X-ray research of the powders on non-mechanically treated samples after each of the stages of the PM process was conducted by means of TuR M62 diffractometer, using CoKα radiation ($\lambda_{K\alpha}$ = 1.79 A). On the basis of the obtained diffraction patterns, the phase analysis was conducted.

The compressing test was performed with the use of INSTRON 8502 Plus testing machine, equipped with a static type extensometer 2620-6D1, of ±5.0 mm in gauge length. Cylindrical samples of ⌀7.0 × 10.5 mm in dimension were prepared for the examination. During the test, a crosshead speed of 0.5 mm min^{-1} was applied. The

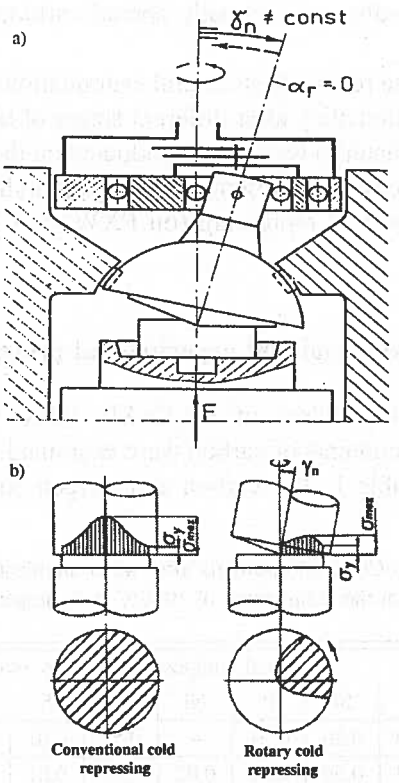

Fig. 1. Schematic view (a) of the PXW100A press, (b) principle of rotary repressing

yield strength (Ys), ultimate compressing strength (UCS) and the contraction (ε) were defined. The Vickers $HV_{0,1}$ method was applied to determine the hardness. Microstructure observations were performed using the optical microscope (Neophot 21) and the scanning electron microscope SEM (Hitachi 3000N with EDS microanalyser).

3. Results and discussion

The structure examination of the powders before and after the annealing shows that the particles of the powder after water atomization have a dendritic structure, typical for this kind of materials (Fig. 2), which results from rapid cooling [5, 6]. After annealing, both powders have a homogenous structure.

The results of the X-ray diffraction phase analysis after water atomization for both powders (Fig. 3) revealed the presence of the α-Co solid solution and the hexagonal phase ε identified as a martensitic one.

But in the case of the powder obtained from alloy II, in which the carbon contents is lower, a smaller participation of ε phase was found. The above corresponds to the

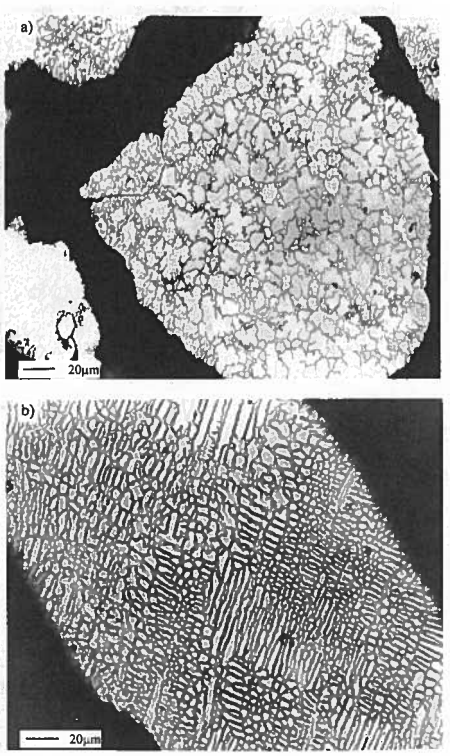

Fig. 2. Structures of the powders of cobalt alloys (a) after annealing at 1000°C/2h, (b) before annealing

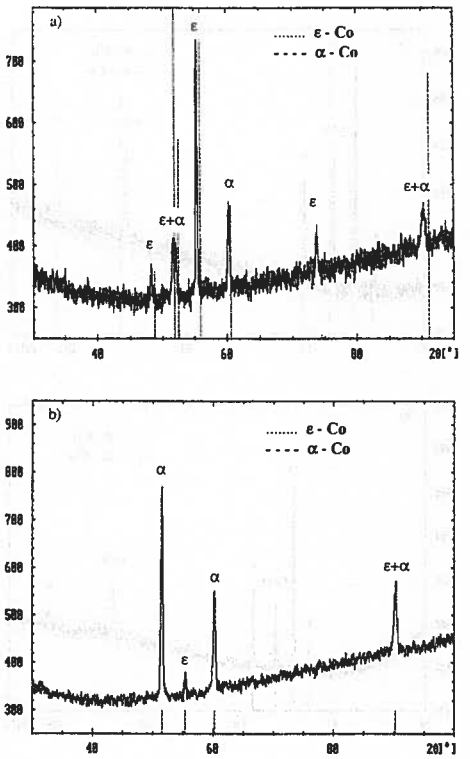

Fig. 3. Diffraction patterns of Vitalium powders after water atomisation (a) alloy I, (b) alloy II

literature data as an increase in the carbon contents results in lowering the temperature of the beginning of the martensitic transformation.

The process of annealing in the hydrogen atmosphere (Fig. 4) caused qualitative and quantitative changes of the phase contents. The increase in the ε-Co phase amount was the result of the athermal ε-martensite transformation.

Figure 5a presents examples of the specimen microstructure after sintering in the argon atmosphere at 1150°C. The structure of all sintered samples is one-phase and fine-grained (with the average grain size of 40 μm), consisting of solid solution of chromium, molybdenum and carbon in α-cobalt with small precipitation of carbons and non- metallic inclusions. This result has been confirmed by the X-ray phase analysis (Fig. 5b) and SEM with EDS microanalyser (Fig. 6a and 6b). The presence of oxygen reflexes may point at the existence of hard removable chromium and silicon oxides.

The results of the phase analysis of specimens after sintering, irrespective of the kind of powder, reveal only the presence of α-cobalt solid solution [15]. A slight

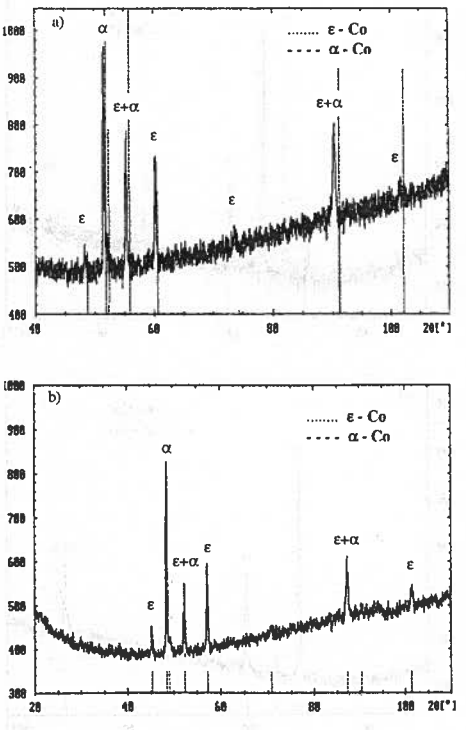

Fig. 4. Diffraction patterns of Vitalium powders after annealing in hydrogen (a) alloy I, (b) alloy II

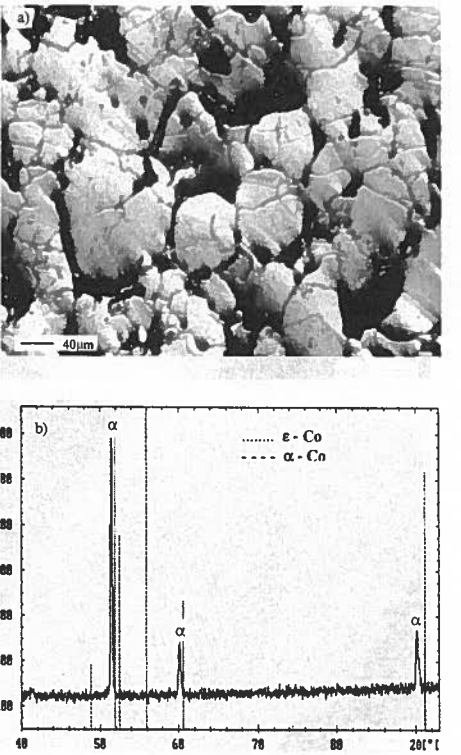

Fig. 5. Microstructure of alloy I (a) sample after sintering in argon, (b) diffraction pattern

displacement of diffraction peaks to the left of the centre layers as compared to those of standard cobalt element testify to changes of the lattice parameters, connected with the presence of alloy additions solved in the solid solution.

The rotary cold repressing of the sintered samples resulted in increasing the material density and phase changes (two-phase structure α-Co and ε-Co), caused by plastic deformation at room temperature (Fig. 7). The microstructure on the cross-section of the samples after repressing is shown in Fig. 8. The characteristic texture of matrix (elongated grains) was not observed, as in the case of the cast Vitalium alloy having undergone plastic deformation. It might indicate that the increase in the specimen density resulted from the porosity changes of the material [16, 17].

The number of upper die rotations is a very important parameter, causing differences in the material structure and properties. The X-ray diffraction method revealed that when the number of rotation cycles increases, the value of ε-Co phase increases to approximately 90% (Table 2).

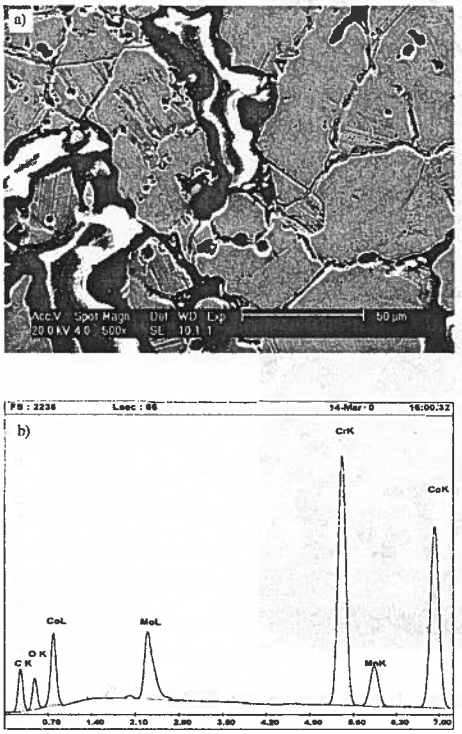

Fig. 6. SEM examination of sintered sample (a) microstructure of alloy II, (b) EDS microanalysis

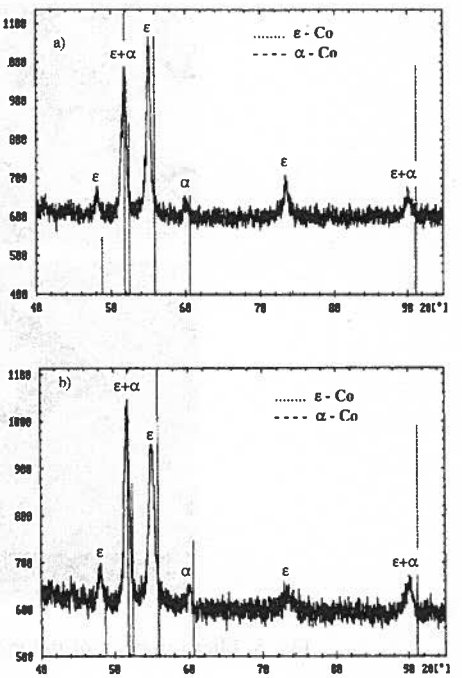

Fig. 7. X-ray diffraction patterns of specimens after repressing (a) alloy I, (b) alloy II

TABLE 2

XRD results of alloy I

Kind of phase	Phase volume (wt.%)			
	After repressing	After heat treatment		
	600 MPa, $i = 7 \div 22$	950°C	1150°C	1250°C
α-Co	22...8	17	100	100
ε-Co	78...92	83	0	0

However, it was also found that in the case of increased carbon content in the alloy, the value of ε-Co phase and the hardness of the repressed samples rise (Fig. 9). The calculated values of true plastic deformation ($\varepsilon = \ln H_0/H$) with a different number of rotations applied (7÷22) were equal to: 0.25; 0.28; 0,31; 0.32 respectively.

The above facts indicate that the plastic strain of Co-based alloys can result in hardening, due to the number of twins and fcc-hcp phase transformation [3, 5], owing to the low stacking fault energy of Co-Cr-Mo alloys.

Fig. 8. Microstructure of the samples (a) after repressing, (b) SEM

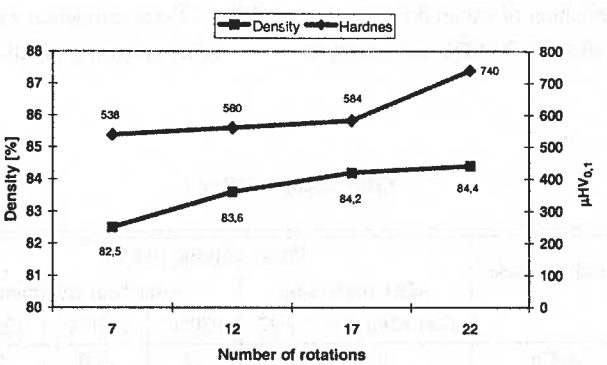

Fig. 9. The influence of the number of repressing cycles on the hardness and density of the samples

The microhardness and density investigation confirms that when the number of cycles increases, the density and strain hardening of samples also rise, until the number of 17 die rotations is reached. After that, the samples density slightly increases but the microhardness of the specimens grows. This strength effect is caused by permanent increasing of the number of dislocations (crystal defects), which block plastic deformation of the sample matrices. Also the progressive fraction of the ε-Co structure, due to its lower number of slip systems and due to the interaction of the dislocations with

TABLE 3

Properties of samples produced with powder alloy I obtained after sintering, repressing and heat treatment

Material	UCS Mpa	Ys Mpa	ε %	$\mu HV_{0,1}$	Phase	Density %
Sinters 1150°C	270±44.1	150±28.6	6.0	325	fcc	68.0
After repressing	575±35.7	460±14.1	4.1	520	hcp	86.0
Heat treated 950°C	602±57.3	320±39.3	5.5	425	hcp	85.6
Heat treated 1150°C	1310±55.4	380±29.6	24.7	311	fcc	85.9
Heat treated 1250°C	1290±76.5	410±44.9	28.0	283	fcc	86.3

* Average value of 5 samples

the stacking faults, causes a decrease in the plastic strain of samples. Hence, there is a need to use the final heat treatment (HT).

From the works of Huang [3, 4] it results that in the case of the cast Vitalium alloy, slow cooling in the furnace at the annealing temperatures ranging from 1150°C to 1250°C does not lead to the development of the $\alpha \rightarrow \varepsilon$ phase changes. However, it causes an increase in the number of carbide precipitation [5÷7]. This effect in not observed when less drastic cooling rate is applied. Hence, to conduct effectively the process of the Vitalium alloy structure homogenisation, an intermediate rate of cooling, from the solid solution temperature, might be applied. Thus, in this work the sample cooling was carried out at the speed of 45°/min.

In the case of the porous samples based on Co-Cr-Mo alloy, the heat treatment should ensure an increase of specimen density, rebuilding and homogenizing of the structure destroyed in the process of repressing, as well as improvement of mechanical properties.

X-ray diffraction patterns provided some information on the influence of the heat treatment temperature on the quantitative changes in the ε-Co phase volume (Table 2). The density, the mechanical properties of the samples and the type of the phase structure obtained in the following stages of the technological process are given in Table 3.

The temperature of the heat treatment has a slight influence on the specimen density. At the temperature of 950°C, all the samples reveal unbeneficial dimension changes (bulking), a decrease in the mechanical properties and further developing of ε-martensite transformation. At this temperature, the recrystallization of the specimens having undergone repressing caused a decrease in hardening and an increase of ductility. The results shown in Table 3 confirm the data obtained by Bojar [5] and Clemow [7], namely the fact that annealing at temperatures ranging from 500 to 1000°C causes development of the isothermal ε-martensite transformation and further second phase precipitation.

A small increase of the density occurs at the temperature of 1150°C, in comparison with the density of the samples annealed at 950°C. At this temperature, the specimens

show slight shrinkage in the horizontal direction and slight bulking in the vertical one. We assume that this temperature of heat treatment is not high enough for favourable changes to occur in the density of the materials. The phase analysis of all the samples having undergone the heat treatment at the temperature range of 1150÷1250°C revealed homogenous cobalt α-phase structure.

The most significant shrinkage of samples, in the case of both examined materials, as well as the highest density, were obtained after the process of heat treatment at the temperature of 1250°C. It is worth mentioning that, although increasing the temperature of annealing caused reduction of the oxygen contents, it did not promote significant grain growth (Fig. 10).

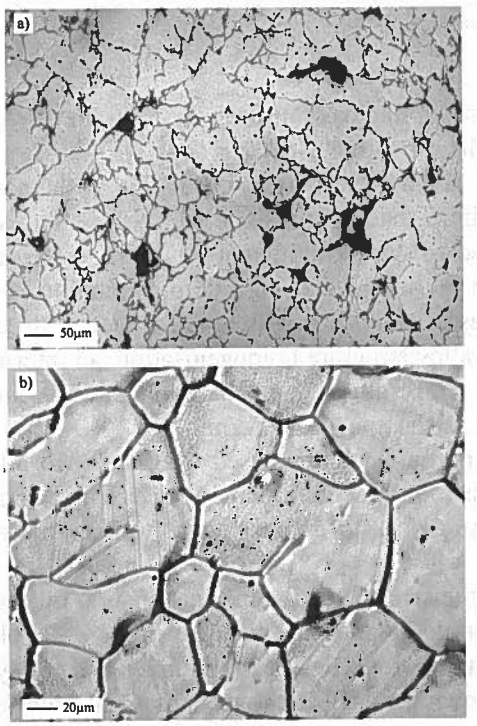

Fig. 10. Microstructure of the samples after heat treatment (a) at 950°C, (b) at 1250°C

The equiaxed grain structure, with grain size measured by means of the secant random distribution method, proved to range from 20 to 120 μm. Notice the presence of the annealing twins and the carbon precipitations (Fig. 10b).

The properties of the samples, presented in table 3, confirm that the phase structure of Co- Cr-Mo specimens influences their mechanical and physical properties. The samples having undergone repressing show low ductility and the ultimate compressing strength (UCS) values but the hardness of the material has increased. The solution heat treatment at the temperature of 950°C did not cause any significant changes. The recrystallization process at this temperature slightly decreased the alloy hardness and increased the ductility as well as the UCS of the samples. Increasing the temperature

of the heat treatment to 1150°C caused the sintering process activation and a visible increase of the mechanical properties of the specimens, but it did not indicate any significant changes of the grain size. The samples made of this powder, having smaller carbon contents, show lower (by about 20%) values of their mechanical properties (UCS, Ys) in comparison to the samples obtained from powder alloy II.

4. Summary

Summing up the results of the present paper, we may conclude that the powder particles of the Co-Cr-Mo alloy, after the water atomisation, have a homogenous α-Co one-phase structure, independent of the kind of the materials used. The annealing in the hydrogen atmosphere develops the isothermal ε-martensite transformation (fcc $\rightarrow$ hcp). The process of the green compacts sintering at the temperature of 1150°C shows a homogenous α-Co fine-grained structure, but the mechanical properties of samples are not satisfactory with reference to the requirements concerning implantation materials. The rotary cold repressing process causes an increase in the density and a rise in the strength parameter and hardness of samples, but the volume of the hcp-phase structure increases to 90%. The volume of the hcp- phase structure consistently increases together with the number of the repressing rotations.

The temperature of the final heat treatment exerts favourable changes on the phase structure and the mechanical properties of samples. The samples after solution at the temperatures ranging from 1150°C to 1250°C obtained a homogenous α-Co structure, good ductility and the highest mechanical property values. The highest ultimate strength was obtained in the case of the samples made of powder alloy II, with larger carbon contents.

The following general conclusions can be drawn from the above:

1. Higher carbon contents of samples causes, on one hand, better mechanical properties, but on the other hand higher volume of the hcp ε-phase structure.

2. Rotary cold repressing is an effective method of increasing the density of sintered samples, but the presence of strain induced fcc $\rightarrow$ hcp martensite transformation demands the application of the final heat treatment.

3. The temperature of the heat treatment has a significant influence on the phase structure and the mechanical properties of the repressed samples. Significantly better mechanical properties and a homogenous α-Co one-phase structure were obtained after solution at the temperature range of 1150÷1250°C.

This work was supported by the Polish Committee of Scientific (KBN) No. 7 T08D 030 21

REFERENCES

[1] S. H. Teoh, Fatigue of biomaterials: a review, International Journal of Fatigue **22** 825-837 (2000).

[2] B. S. Becker, J. D. Bolton, M. Youseffi, Production of porous sintered Co-Cr-Mo alloys for possible surgical implants application. Part 1: Compaction, sintering behaviour and properties, Powder Met. **3** 201-208 (1995).

[3] P. Huang, H. F. López, Effects of grain size on development of athermal and strain induced ε martensite in Co-Cr-Mo implant alloy, Mat. Sci. Techn. **15** 157-163 (1999).

[4] P. Huang, H. F. López, Athermal ε-martensite in Co-Cr-Mo alloy: grain size effects. Mat. Letters **39** 249-253 (1999).

[5] Z. Bojar, Analiza wpływu struktury na odporność korozyjną i mechanizm pękania stopów kobaltu typu Vitalium. Rozprawa habilitacyjna WAT, Warszawa (1992).

[6] L. Z. Zhuang, E. W. Langer, Effects of cooling rate control during the solidification process on the microstructure and mechanical properties of cast Co-Cr-Mo alloy used for surgical implants. J. Mat. Sci. **24** 381-388, 4324-4330 (1989) .

[7] A. T. Clemow, B. L. Daniell, Solution treatment behaviour of Co-Cr-Mo alloy, Journal of Biomed. Mat. Research **2** 265-279 (1979).

[8] T. Kilner, M. R. Pilliar, G. C. Weatherly, C. Allibert, Phase identification and incipient melting in a cast Co-Cr surgical implant alloy, J Biomed. Mat. Res, **16** 63-79 (1982).

[9] L. Z. Zhuang, E. W. Langer, Effects of range the stress intensity factor on the appearence of localized fatigue fracture in cast Co-Cr-Mo alloy used for surgical implants. Materials Science and Engineering A **1029-12** (1988).

[10] W. Ratuszek, Przemiany fazowe w kobalcie i jego stopach, Materiały niepublikowane, AGH, Kraków, 2000.

[11] W. B. Pearson, Handbook of lattice spacing and structures of metals, Pergamon Press **2** (1967).

[12] K. Rajan, B. Vander Sande, Room temperature strengthening mechanisms Co-Cr-Mo-C alloy. J Mat. Scie. **17** 769-778 (1982).

[13] P. Huang, H. F. López, Strain induced ε-martensite in Co-Cr- Mo alloy: grain size effects. Mat. Letters, **39** (1999) 244-248 (1999).

[14] N. Cong Dahn, D. Morphy, K. Rajan, Kinetics of the martensitic fcc-hcp transformation in Co-Cr-Mo alloy powders, Acta Metall. **32**, 9 1317-1322 (1984).

[15] J. R. Dąbrowski, J. Frydrych, H. Frydrych, W. Ratuszek, Effect of sintering on structure and properties of Vitalium type sintered materials, Archives of Metallurgy **46** 1 81-92 (2001) .

[16] L. Wojnar, J. R. Dąbrowski, Z. Oksiuta, Porosity structure and mechanical properties of vitalium-type alloy for implants, Materials Characterization **46** 221-225 (2001).

[17] Z. Oksiuta, J. R. Dąbrowski, Rotary cold repressing and heat treatment of sintered materials from Co-Cr-Mo alloy powder, Powder Metallurgy **45**, 1 63-66 (2002).

Received: 20 April 2004.

A R C H I V E S O F M E T A L L U R G Y A N D M A T E R I A L S
Volume 49 2004 Issue 4

T. SKOWRONEK*, W. RATUSZEK*, K. CHRUŚCIEL*, A. CZARSKI*, K. SATORA*, K. WIENCEK*

SPHEROIDIZATION OF CEMENTITE IN PEARLITE

SFEROIDYZACJA CEMENTU W PERLICIE STALI EUTEKTOIDALNEJ

Spheroidization of cementite in an eutectoid carbon steel, whose pearlite phases (ferrite and cementite) possess crystallographic texture, has been investigated by light microscopy and X-ray diffraction. During spheroidization the microstructural changes are accompanied by the ones of cementite texture. In particular, the ideal orientations (010)[201] and $(0\bar{1}0)$[100] describe the main texture component of cementite in pearlite and spheroidized cementite, respectively.

Przedmiotem pracy jest izotermiczna sferoidyzacja cementu w grubopłytkowym perlicie stali węglowej eutektoidalnej. W wyniku badań metalograficznych i rentgenograficznych zostało wykazane, że z jakościowymi (morfologicznymi) i ilościowymi zmianami mikrostruktury cementu są związane określone zmiany krystalograficznej tekstury faz: ferrytu i cementytu.

1. Introduction

The microstructure of an eutectoid carbon steel may appear in two quite different morphological forms, as the pearlite and as the spheroidized cementite. The pearlite has a lamellar structure, which is formed by alternate cementite and ferrite plates, with ferrite as the continuous phase [1]. The spheroidized cementite consists of cementite spheroids which are randomly dispersed in the continuous ferrite matrix [2].

It is well known, that the structure of pearlite is unstable and by annealing for a sufficient long time just below the eutectoid temperature it transforms from lamellar to spheroidal form. The thermodynamic driving force of spheroidization is the change of the interphase surface free energy while the spheroidization kinetics is determined by diffusion-controlled processes [2, 3]. Consequently,

* WYDZIAŁ METALURGII I INŻYNIERII MATERIAŁOWEJ, AKADEMIA GÓRNICZO-HUTNICZA, 30-059 KRAKÓW, AL. MICKIEWICZA 30

the spheroidization of cementite in pearlite can be regarded as a diffusional grain coarsening process, which is due to morphological changes of the microstructure [2].

For the analysis of the cementite spheroidization mechanism one can distinguish four partial structural processes [4]: (i) the partitioning of cementite plates into smaller segments (the so-called fragmentation); (ii) rounding off small plate segments into spherical particles; (iii) particle coarsening (Ostwald ripening [2]); and (iv) recrystallization and growth of ferrite grains.

The spheroidization of cementite was a subject of many theoretical and experimental investigations. The most of the theoretical approaches has resulted in some simple models for destabilization of the plates [5]. The subject of experimental works was mainly due to the fragmentations of cementite plates and the global spheroidization kinetics, both analysed metallographically by using light or electron microscopy methods [4, 6-8]. Unfortunately, the structural processes concerning the substructure of ferrite during the spheroidization of cementite were investigated rarely. In accordance to the present knowledge, the spheroidization mechanism is closely connected to the migration of local faults of the interphase boundary imperfections of a large curvature [6]. Although at present the understanding of the spheroidization process is fairly advanced, the molecular mechanism and its kinetics are still not sufficiently elucidated. In such a situation additional investigations occurred necessary. Microstructural changes which proceed during the spheroidization (caused by coarsening of cementite and recrystallization of ferrite) are connected with local changes in crystal orientations of both phases and can influence their crystallographic textures. The texture data obtained by X-ray diffraction may contain the information – referring to the spheroidization - which is not available by metallography. According to the knowledge of the authors, in the literature there is no information related to the texture with regard to the spheroidization.

The aim of the present work was to perform experimental studies of the spheroidization of cementite in pearlite by taking into account the microstructure and crystallographic texture of the phases: ferrite and cementite.

2. Material and heat treatements

The material to be analysed [9], in a form of speciments cut from an 1.5 kg eutectoid steel ingot (the chemical composition of the material is given in Table 1.), which was melted in Balcers vacuum furnace, was prepared as follows:

1) diffusion annealing (1300°C/10h in vacuum);
2) plastic deformation (forging and subsequent cold-rolling with 50 deformation) which resulted in pre-specimens of dimensions $5,5 \times 15 \times 120$mm;
3) normalizing annealing (900°C/0.5h).

In order to produce a coarse lamellar pearlite, the material was subjected to the following heat treatment:

1) austenitizing (900°C/0.5h) with subsequent transfer to a lead bath at temperature 700°C;
2) isothermal holding in the bath (700°C/3h).

TABLE 1

Chemical composition of the steel under examination

Element	C	Mn	Si	P	S	Cr	Ni	Cu	Al.	N
%	0.75	0.05	0.01	0.002	0.012	0.03	0.03	0.01	0.01	0.009

Obtained material were cut into the proper specimens of dimensions $5.5 \times 15 \times 10$ (mm) perpendicularly to the rolling direction. For spheroidization, the specimens were annealed at the temperature 700 ± 2°C for the duration times (t in hours): $t = 0$ (pearlite), $t = 50$, $t = 100$, $t = 200$, $t = 400$ and $t = 600$ in vacuum (10^{-2}Tr).

For the subsequent investigation (by metallography and X-ray diffraction) a planar surface of specimens (perpendicularly to the rolling direction of the pre-specimen) was selected and polished. Figure 1 shows a scheme of the specimen with the selected polished surface together with a rectangular Cartesian coordinate system with axes: x_1, x_2, x_3 (x_1 is parallel to the rolling direction, x_2 is perpendicular to the rolling surface and x_3 is perpendicular to x_1 and x_2).

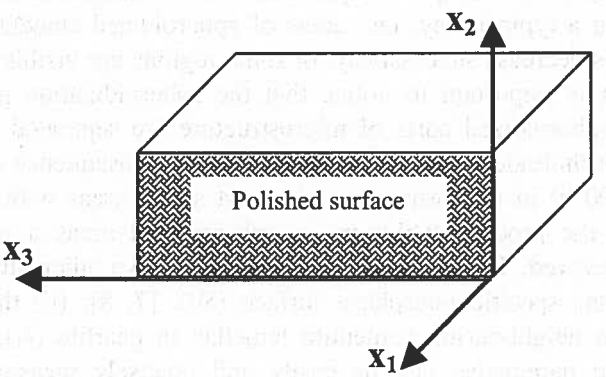

Fig. 1. Scheme of the specimen with the selected polished surface together with a rectangular Cartesian coordinate system with axes: x_1, x_2, x_3

3. Metallography

The qualitative and quantitative metallographic studies were performed by means of light microscopy, using the NU2-Zeiss microscope. Figure 2 shows the microstructure after isothermal annealing (700°C/3h).

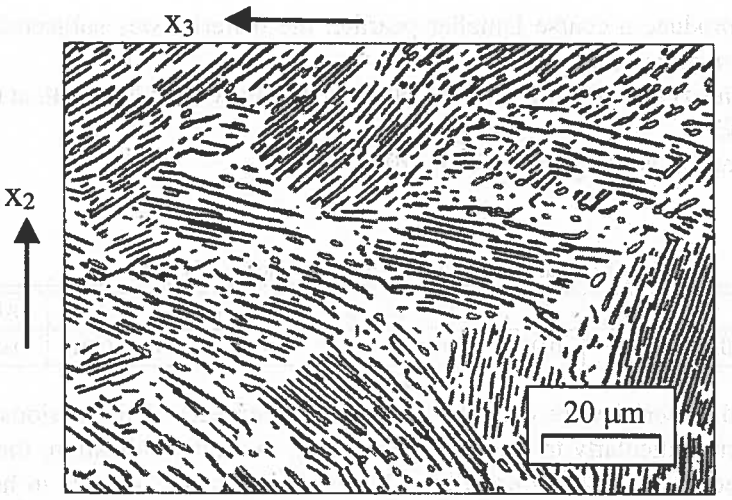

Fig. 2. Microstructure with coarse lamellar pearlite after isothermal annealing of the Fe- 0.75%C steel (etched in picral)

The microstructure consists mainly of coarse lamellar pearlite accompanied by only small fraction of spheroidized cementite. Figure 3 shows typical microstructures for the respective spheroidization times compared to the initial pearlite (t = 0, Fig. 3a). A detailed microscopic analysis shows that changes in microstructure morphology occur in a typical way: i.e., areas of spheroidized cementite increase while lamellar fractions decrease successively. In some regions are visible partitioned lamellae, (Fig. 3c). It is important to notice that the spheroidization process occurs not uniformly, i.e., spheroidized parts of microstructure are separated by lamellar areas, while mixed morphologies appear occasionally. As a consequence for the longest annealing time (600 h) in microstructure still exist stable areas with lamellar structure (Fig. 3e). With the process evolution, in spheroidized areas a particle coarsening (ripening) is observed. For quantitative description, two microstructure parameters are chosen: (i) the specific interphase surface (S_V), [7, 8]; (ii) the harmonic mean distance between neighbouring cementite lamellae in pearlite (l_3), which is defined in [10, 11]. The parameters can be easily and precisely measured by stereological methods [10, 11, 12]. Microstructure parameter (S_V, l_3) as a function of time (t) describes the kinetics of spheroidization. The functions $S_V(t)$ and $l_3(t)$, i.e., the so-called kinetics equations, describe the spheroidization kinetics from global and local point of view, respectively. In particular, $l_3(t)$ describes the process in relation to the lamellar fraction in microstructure. Table 2 presents the empirical functions $S_V(t)$ and $l_3(t)$ in a numeric form (obtained by measurements made on specimen section micrographs at 2500× magnification). The relative statistical limit error γ_g of the function values in Table 2 does not exceed 4%. Then, Figure 4 shows the graphs of the empirical $S_V(t)$ and $l_3(t)$ functions (with the 95% confidence intervals). The $S_V(t)$ function decreases, while the $l_3(t)$ function increases monotonically. The

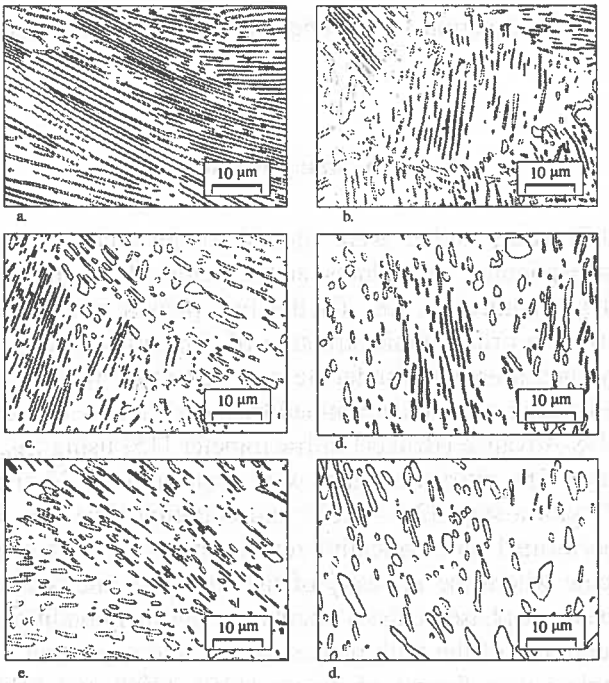

Fig. 3. Microstructures of the Fe-0.75%C steel during spheroidization at 700°C for times (t in hours): a./ t = 0, b./ t = 50, c./ t = 100, d./ t = 200, e./ t = 400, f./ t = 600 (etched in picral)

TABLE 2

Empirical kinetics functions $S_V(t)$ and $l_3(t)$ in numeric form

Parameter \ Time t, h	0	5	50	100	200	400	600
$S_v(t)$, mm^{-1}	2031.8	1784.3	1239.7	1079.5	931.4	745.5	580.7
$l_3(t) \times 10^3$mm	0.493	0.541	0.592	0.649	–	0.663	–

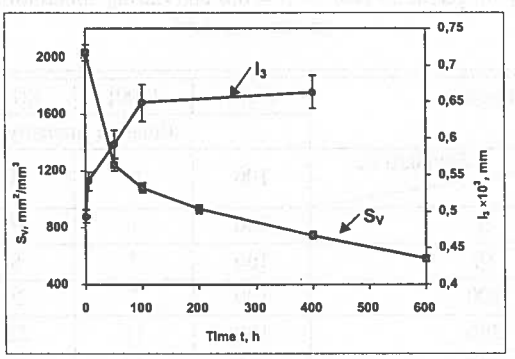

Fig. 4. Plots of the empirical $S_V(t)$ and $l_3(t)$ functions (with the 95% confidence intervals)

greatest changes of the function values occur for the annealing periods less than 100 hours.

4. X-ray structure analysis

The X-ray diffraction studies were limited to the qualitative phase and texture analysis. The corresponding procedures are determined by the crystal structure of the material under examination, i.e., (i) the two phases microstructure (ferrite and cementite) [13]; (ii) the orthorombic structure of cementite [14].

The intensity measurements for ferrite and cementite were carried out from the specimen polished planar section determined by the x_2 and x_1 coordinate axes (Fig. 2) by means of the D8-Advance (Bruker) diffractometer [15] using $\lambda_{K\alpha}$ = 1.79 Å filtered cobalt anode X-rays. The diffraction lines were registered for 2θ angles for the region from 20° to 140° with a step $\Delta 2\theta$ = 0.02° and counting time τ = 5s. The qualitative phase analyse (performed automatically) results in relative intensities of diffraction lines (with the scale where the intensity of the strongest line is assumed to be equal to 100). On the basis of phase analysis results the optimal conditions were chosen for pole figure measurement of the both phases: ferrite and cementite.

Three incomplete pole figures of planes {110}, {200} and {211} were measured for the ferrite, five incomplete pole figures of planes (002), (102), (211), (112) and (131) for the cementite. On the basis of the incomplete pole figures, the complete pole figure were calculated by means of the orientation distribution function (ODF). The measurement of pole figures for the cementite was performed according to the procedure described in [16].

4.1. Phase analysis

TABLE 3

Diffraction peak intensity for ferrite in pearlite (t = 0h) and during spheroidization compared to the Fe_α powder standard

Planes	{110}	{200}	{211}	{220}
	Relative intensity, %			
Standard Fe_α / Time t, h	100	20	30	10
0	100	1	10	8
50	100	7	8	6
100	100	7	29	11
200	100	11	55	8
400	100	13	31	8
600	100	4	17	8

The results of intensity measurement as a function of the 2θ angle are given in Table 3 (for ferrite) and in Table 4 (for cementite). The Tables also contain the appropriate intensities for the Fe_α and Fe_3C powder standards [17].

TABLE 4

Diffraction peak intensity for cementite in pearlite (t = 0h) and during spheroidization compared to the Fe_3C powder standard

Planes	(121)	(002)	(201)	(211)	(102)	(112)	(131)	(221)	(122)
	Relative intensity, %								
Standard Fe_3C / Time t, h	25	40	35	80	100	65	20	45	14
0	26	17	15	100	41	36	44	40	21
50	30	21	11	100	29	33	17	20	19
100	54	92	37	59	96	100	32	38	40
200	69	28	23	95	100	51	35	50	24
400	77	50	18	31	100	81	64	62	25
600	25	39	21	48	71	100	100	54	48

From Tables 3 and 4 it results that for the planes {200}, {211}, {220} of ferrite and the planes (121), (002), (211), (131), (122) of cementite, the relative intensities depend on spheroidizing time and differ significantly from the powder standard intensities. It indicates on crystallographic texture of the analysed phases, i.e., ferrite and cementite in pearlite as well as during the spheroidization.

4.2. Texture analysis

The ferrite texture is described by the {110} pole figure while the cementite texture is described by the (002) pole figure. The main texture components corresponding in the pole figure to the largest intensities are characterized by ideal orientations [14, 18].

Figure 5 shows the calculated {110} pole figures of ferrite in pearlite and during spheroidization together with ideal orientations which describe the main texture components. The orientations $\{110\} < 112 >$ dominates in the ferrite texture (Fig. 5a and Fig. $5a_1$). The Figure 5 and Table 3 indicate that during spheroidization a change of the ferrite texture is rather meaningless. The texture index is small, $s_t \cong 2$, it means, the ferrite texture is weak.

Figure 6 shows the calculated (002) pole figures of cementite in pearlite and during the spheroidization together with ideal orientations for describing the main texture components. The orientation (010)[201] describes the main cementite texture component in pearlite (Fig. 6a and Fig. $6a_1$). Figure 6 and Table 3 present the texture evolution during spheroidization. Table 5 gives the main texture components together with the maximum radiation intensity.

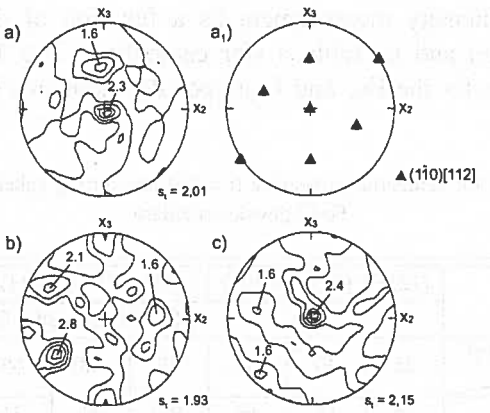

Fig. 5. {100} pole figures of ferrite in pearlite (a) t = 0h) and during spheroidization (b) t = 50h, (c) t = 600h) together with ideal orientations which describe the main texture components (a_1./)

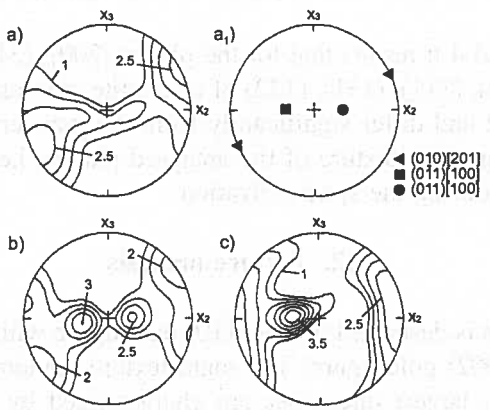

Fig. 6. (002) pole figures of cementite in pearlite (a) t = 0h) and during spheroidization (b) t = 50h, (c) t = 600h) together with ideal orientations which describe the main texure components (a_1)

Beside the orientation (010)[201], which is characteristic for pearlite, two other orientations: (0$\bar{1}$1)[100] and (011)[100] describe the main cementite texture components. At shorter spheroidizing periods times (< 100h, Fig. 6b), both orientations (010)[100] and (011) [100] exist together, however for longer times (>50h, Fig. 6c and Table 5) (010)[100] the orientation tends to dominate the texture. It should be noted that during spheroidization the texture of cementite is distinctly stronger that the one of ferrite.

TABLE 5

Main cementite texture components and the maximum radiation intensity

Spheroidization time t, h	Maximum intensity	Orientation
0	2.81	(010)[201]
50	3.02	$(0\bar{1}1)[100]$, (011)[100]
100	3.71	~ $(0\bar{1}1)[100]$
200	4.74	~ $(0\bar{1}1)[100]$
400	4.90	~ $(0\bar{2}1)[100]$
600	3.87	~ $(0\bar{1}1)[100]$

5. Discussion of results

The initial coarse lamellar pearlite (of interlamellar spacing $l_3(0) = 4.93\times10^{-4}$ mm, Table 2) is characterised by isometric microstructure and crystallographic texture of the phases. The texture of cementite is stronger than the one of ferrite.

During spheroidization, the microstructural changes are described by empirical kinetics equations, $S_V(t)$ and $l_3(t)$, which are of a monotonic type as it should be expected. Namely, multiplying of $S_V(t)$ by the specific surface free energy results in a form of interphase surface free energy as a function of time, which decreases monotonically during spheroidization, i.e., according to the general condition of spheroidization. Next, the form of the empirical $l_3(t)$ – function describes an obvious fact that when the interlamellar spacing are small, the pearlite is more susceptible to spheroidize.

The main texture components of the phases in pearlite are described by the orientations: {110} <112> in ferrite and (010)[201] in cementite. During spheriodization the texture of ferrite is similar to the one of pearlite and is dominated by the orientation {110} <112>. The small change of the texture may be connected with structural processes leading to ferrite grain growth.

During spheroidization the main texture components of cementite are described by the orientations: (010)[201], (011)[100] and $(0\bar{1}1)[100]$. In particular, in (010)[201] the (010) plane is parallel to the plane which includes the x_2 and x_3 axes, (Fig. 2), and the direction [201] is parallel to the x_3 axis; in (011)[100] the (011) plane is parallel to the plane which includes the x_2 and x_3 axes, and the direction [100] is parallel to the x_3 axis; and in $(0\bar{1}1)[100]$ the $(0\bar{1}1)$ plane is parallel to the plane which includes the x_2 and x_3 axes, and the direction [100] is parallel to the x_3 axis.

The orientations (010)[201] and $(0\bar{1}1)[100]$ dominate in cementite texture of pearlite and spheroidized cementite, respectively, one can conclude that during spheroidization the orientation (010)[201] evolves at the expense of the $(0\bar{1}1)[100]$.

It should be noted that the largest change of the cementite texture, as well as its microstructure, occurs for spheroidizing times less than 100 hours.

The main result of this investigation could be formulate as follows. When the spheroidized cementite is formed from pearlite, in which the orientation (010)[201]

describes the main cementite texture component, the orientation $(0\bar{1}1)[100]$ describes its main cementite texture component. Presumably, it is possible to formulate this statement in a more general form, namely, when the cementite in pearlite is textured, the spheroidization process preserves the texture however its components are different.

It could be assumed that the changes of the cementite texture during spheriodization are related to the coarsening (Ostwald ripening) of cementite particles by diffusion-controlled processes, which occur for not random orientation difference between dissolving and growing particles.

6. Conclusions

1. Microstructure of the coarse lamellar pearlite is isometric but the phases (ferrite and cementite) reveal crystallographic texture.
2. The ideal orientation (010)[201] describes the main texture component of cementite in pearlite.
3. During spheroidization the geometric parameters of microstructure and the texture of phases are changing. The largest changes occur at spheroidizing times shorter than 100 hours and indicate at a correlation between texture and microstructural changes.
4. The ideal orientation $(0\bar{1}1)[100]$ describes the main texture component of cementite in spheroidized cementite.
5. During spheroidization there occurs a change of the main texture components of cementite, from the orientation (010)[201] in pearlite to the orientation $(0\bar{1}1)[100]$ in spheroidized cementite.

Acknowledgements

Financial support from the Polish Committee for Scientific Research (KBN), Contract No. 10.10.110.497, is gratefully acknowledged.

REFERENCES

[1] A. Czarski, J. Ryś, Morfologia perlitu. Arch. of Metallurgy **32**, 453-464 (1987).
[2] J. Ryś, K. Wiencek, Koagulacja faz w stopach. Wyd. Śląsk, Katowice 1979.
[3] J.W. Martin, R.D. Doherty, Stability of Microstructure in Metallic Systems. Cambridge University Press 1976.
[4] S. Chattopadhyay, C.M. Sellars, Quantitative Measurements of Pearlite Spheroidization. Metallography **10**, 89-105 1977.
[5] F.A. Nichols, W.W. Mullins, Surface- (interface-) and Volume-Diffusion Contributions to Morphological Changes Driven by Capillarity. Trans. TMS AIME **233**, 1840-1848 (1965).
[6] Y.L. Tian, R.W. Kraft, Mechanism of Pearlite Spheroidization Met. Trans. A **18A**, 1403-1413 (1987).

[7] Y.L. Tian, R.W. Kraft, Kinetics of Pearlite Spheroidization. Met. Trans. A, **18A**, 1359-1369 (1987).
[8] T. Skowronek, A. Czarski, K. Satora, Kinetyka sferoidyzacji perlitu. Mat. XXX Szkoły Inżynierii Materiałowej, 205-209, Kraków-Ustroń Jaszowiec 2002.
[9] A. Czarski., T. Skowronek, K. Satora, Sferoidyzacja struktury płytkowej. Sprawozdanie z grantu KBN nr 7T08A02508, AGH, Kraków 1998.
[10] A. Czarski, J. Ryś, Stereological relationships for lamellar structure. Acta Stereol. **6/III**, 567-572 (1987).
[11] T. Skowronek, A. Czarski, K. Satora, Stabilność struktury płytkowej. Mat. XXXI Szkoły Inżynierii Materiałowej, 137-141, Kraków-Krynica 2003.
[12] J. Ryś, Stereologia materiałów. Fotobit, Kraków 1995.
[13] H.J. Bunge, Texture in Multiphase Alloys. Zeitschrift für Metallkunde **76** 92-101 (1985).
[14] B.D. Cullity, S.R. Stock, Elements of X-Ray Diffraction (Ed.III). Prentice Haal, Upper Saddle River, New Jersey 2001.
[15] PDF maint is the DIFFRACplus Powder Diffraction Data base manager. BRUKER D8-Advance. Bruker AXS GmbH, Karlsruhe 2000.
[16] W. Ratuszek, K. Chruściel, T. Skowronek, Pomiar figur biegunowych dla cementytu w perlicie. (in preparation)
[17] Powder Diffraction File. J.C.P.D.S., 1976, 1601 Park Lane, Swarthmore, Pensylvania 19081.
[18] F.J. Humphreys, M. Hatherly, Recrystallization and Related Annealing Phenomena. Pergamon, Oxford 1996.

Received: 10 February 2004

A R C H I V E S O F M E T A L L U R G Y A N D M A T E R I A L S
Volume 49 2004 Issue 4

H. FRYDRYCH*, A. ROMAŃSKI*, J. KONSTANTY*

THE INFLUENCE OF IRON CONTENT AND POWDER METALLURGY PROCESSING ROUTE ON MICROSTRUCTURE AND MECHANICAL PROPERTIES OF COBALT-IRON MATERIALS

WPŁYW ZAWARTOŚCI ŻELAZA I TECHNOLOGII WYTWARZANIA NA MIKROSKTRUKTURĘ I WŁASNOŚCI MECHANICZNE SPIEKÓW KOBALT- ŻELAZO

The effects of iron content and Powder Metallurgy (PM) processing conditions on microstructure and mechanical properties of cobalt-iron materials were investigated. The specimens were manufactured from commercial powders by both the conventional single cold press/sinter and hot press routes. The iron content was varied between 3 and 15 wt.%. The specimens were subjected to density measurements, Rockwell hardness, tensile and impact tests, metallographic and fractographic examinations by optical microscopy and scanning electron microscopy, respectively.

The investigations indicated that higher mechanical properties were obtained in the hot pressed specimens as compared with their furnace sintered counterparts. This was attributed to the higher densities and additional reinforcement by the presence of the oxide phase in the as-hot-pressed material. Moderate iron additions, of between 6 and 10 wt.%, were found to have a strong positive effect on the ductility of the material notwithstanding its processing route.

W artykule przedstawiono wpływ zawartości żelaza oraz procesów wytwarzania na mikrostrukturę i własności mechaniczne spieków kobalt-żelazo. Spieki zawierające od 3 do 15% żelaza wykonano z komercyjnych proszków metodą konwencjonalnego prasowania i spiekania oraz prasowania na gorąco. Materiały poddano badaniom gęstości, twardości, wytrzymałości, strukturalnym oraz fraktograficznym z wykorzystaniem mikroskopii optycznej i skaningowej.

Przeprowadzone badania wykazały wyższe własności mechaniczne materiałów uzyskanych technologią prasowania na gorąco w porównianiu z materiałami spiekanymi. Wynikają one z większej gęstości spieków oraz umocnieniem wywołanym obecnością tlenków. Wykazano także, że zawartość żelaza w zakresie od 6 do 10% ma bardzo korzystny wpływ na plastyczność spieków niezależnie od sposobu ich wytwarzania.

* WYDZIAŁ METALURGII I INŻYNIERII MATERIAŁOWEJ, AKADEMIA GÓRNICZO-HUTNICZA, 30-059 KRAKÓW, AL. MICKIEWICZA 30

1. Introduction

Cobalt-iron alloys have long been used as the matrix for diamonds in diamond impregnated tools [1]. A typical fabrication process utilises PM technology whereby a mixture of diamond grits and bonding powders is consolidated to form diverse cutting tool components such as diamond segments for grinding wheels, circular sawblades, gang sawblades and core drills, as well as diamond beads for wire saws. Although hot pressing to net shape has become widespread [1], the powders can also be densified by means of pressure-less furnace sintering [2], hot isostatic pressing [3], or a combination of these two methods [4].

The tool manufacturing process determines the ability of the matrix to hold the diamonds firmly, keeping them exposed for maximum cutting efficiency, and the degree of diamond degradation. Therefore the application performance of diamond impregnated tools greatly depends on the PM processing time, temperature and atmosphere, and chemical composition of the matrix. Metals showing appreciable solubility for carbon, such as iron or cobalt, increase the possibility of severe surface attack and subsequent failure of diamond before it can be utilised [1]. Therefore, in the case of furnace sintering, which normally requires relatively long thermal treating times, of around an hour, it is of critical importance that the matrix is less *reactive-with-diamond* and that it achieves near-full density after sintering at moderate temperatures.

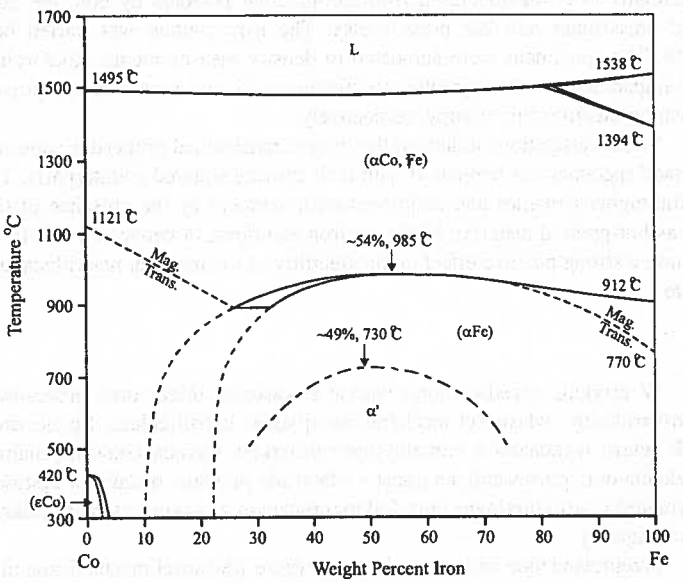

Fig. 1. Phase diagram of the iron-cobalt system [6, 7]

Cobalt exists in two allotropic forms, a closed-packed hexagonal (ϵ) stable at temperatures below about 421°C, and a face-centred cubic (α) stable at higher temperatures [5]. As shown by the phase diagram of Figure 1, additions of up to 10

wt.% Fe have a strong ability to stabilise the cubic phase thus imparting ductility to the material, which factor has been found beneficial to the matrix with regard to its diamond retention capacity [1].

Figure 1 shows that at room temperature the (αCo, γFe) phase exists all alone in Co-(5 ÷ 10 wt.%) Fe alloys and coexists with the (αFe) phase over a range between 10 ÷ 22 wt.% Fe. Further additions of iron to cobalt may lead to formation of a brittle, ordered α' phase which is stable at room temperature in alloys containing between 25 ÷ 75 wt.% Fe.

2. Experimental

The specimens were prepared from mixtures containing various proportions of iron powder to cobalt powder by both the conventional cold pressing/furnace sintering process and by hot pressing in a graphite mould. The starting powders are shown in Figure 2.

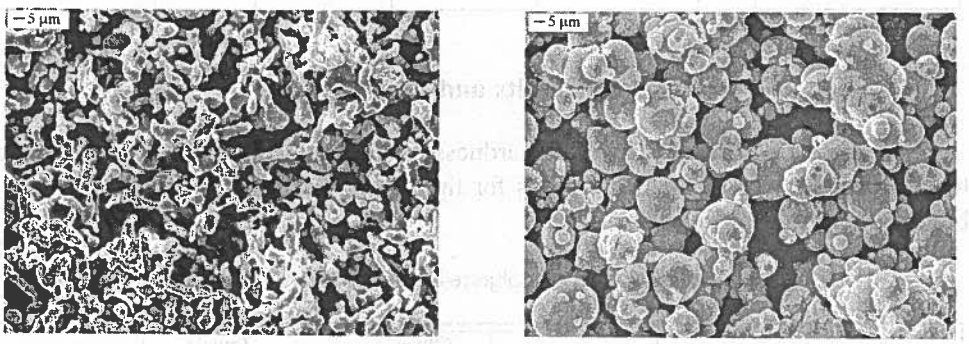

Fig. 2. SEM micrographs of experimental powders; (a) *extrafine* cobalt; (b) *carbonyl* iron

After mixing for 1 hour in the *Turbula T2C* mixer, the powders were consolidated by either cold pressing in a rigid die followed by furnace sintering in hydrogen or by hot pressing in a graphite mould. The latter operation was accomplished using resistance heating equipment. The hot-stage processing temperature, being 950°C in both cases, was selected in order to facilitate solid state diffusion in the cobalt-iron system, to assure adequate as-sintered densities of the furnace treated specimens and, also, to avoid potential degradation of diamond grits [1] if any of the procedures proved suitable for industrial application. The batch designation system and the remaining powder processing conditions are detailed in Table 1. After densification, all specimens were subjected to density measurements and hardness tests. The water displacement technique and Rockwell B method were used, respectively. The materials were also tested for tensile properties, such as the offset yield strength, tensile strength

and elongation. The surfaces of fractured specimens were examined with a scanning electron microscope. The microstructures were also observed on polished and etched transverse sections.

TABLE 1

Material designation and procesing conditions

Material designation	Iron content, wt.%	Pressure, MPa		Time at temperature, min	
		Cold press	Hot press	Sinter	Hot press
Co3Fe(S)	3	400	–	60	–
Co6Fe(S)	6	400	–	60	–
Co10Fe(S)	10	400	–	60	–
Co15Fe(S)	15	400	–	60	–
Co3Fe(HP)	3	–	35	–	2
Co6Fe(HP)	6	–	35	–	2
Co10Fe(HP)	10	–	35	–	2
Co15Fe(HP)	15	–	35	–	2

3. Results and discussion

The mean densities, Rockwell B hardness numbers, and 0.2% offset yield strength, tensile strength and elongation figures for the tested materials are summarised in Table 2.

TABLE 2

Properties of materials subjected to different PM treatments

Designation	Density, g/cm^3	Hardness, RB	Offset Yield Strength, MPa	Tensile Strength, MPa	Elongation, %
Co3Fe(S)	8.36	84	412	658	24
Co6Fe(S)	8.15	68	297	535	40
Co10Fe(S)	7.88	51	264	394	20
Co15Fe(S)	7.60	41	251	357	13
Co3Fe(HP)	8.51	91	473	686	4
Co6Fe(HP)	8.46	88	447	640	15
Co10Fe(HP)	8.42	81	437	604	37
Co15Fe(HP)	8.44	87	450	567	30

Selected stress-strain curves, typical for each material, are presented in Figure 3.

From the density measurements it is evident that the variation in the iron content has a marked influence on the ultimate density of the sintered material, but in contrast the hot pressed specimens are negligibly affected since the small difference in their densities should mostly be attributed to the variation in chemical composition.

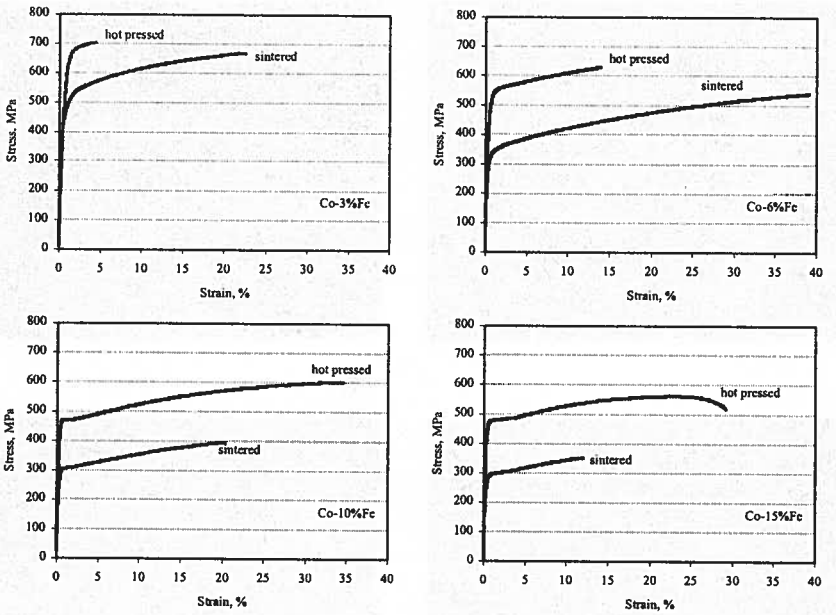

Fig. 3. Stress-strain curves obtained from a tensile test

The tensile test data indicates that moderate iron additions to cobalt have a pronounced positive effect on the ductility of the material. The maximum % elongation is observed at 6 and 10 wt.% iron for the sintered and hot pressed material, respectively. The relatively high porosity of the sintered specimens containing more than 6 wt.% iron should apparently account for the sharp drop in their ductility.

As documented in Table 2, the yield strength, and hardness as well, of the hot pressed material is only a week function of iron content although the tensile strength appears to be markedly affected. Comparison of the stress-strain curves given in Figure 3 indicates that iron weakens the response of the material to strain-hardening thus yielding lower tensile strength figures.

Contrary to the hot pressed material, its sintered equivalent displays strong dependence of the yield strength, tensile strength and hardness on iron content. Such an effect of iron on mechanical strength is apparently augmented by the porosity present in the iron-rich materials.

By comparing microstructures of the tested specimens it may be inferred that oxide particles and, to some extent, porosity play an important role in grain refinement of the hot pressed and sintered material, respectively. As presented in Figure 4, the examined specimens retained relatively fine-grained microstructure even after an hour hold at 950°C in hydrogen.

The fracture surfaces illustrated in Figure 5 indicate that all specimens failed in a ductile manner producing dimpled fracture surface. In the sintered specimens the dimples are markedly coarser than in their hot pressed counterparts. In the former case the

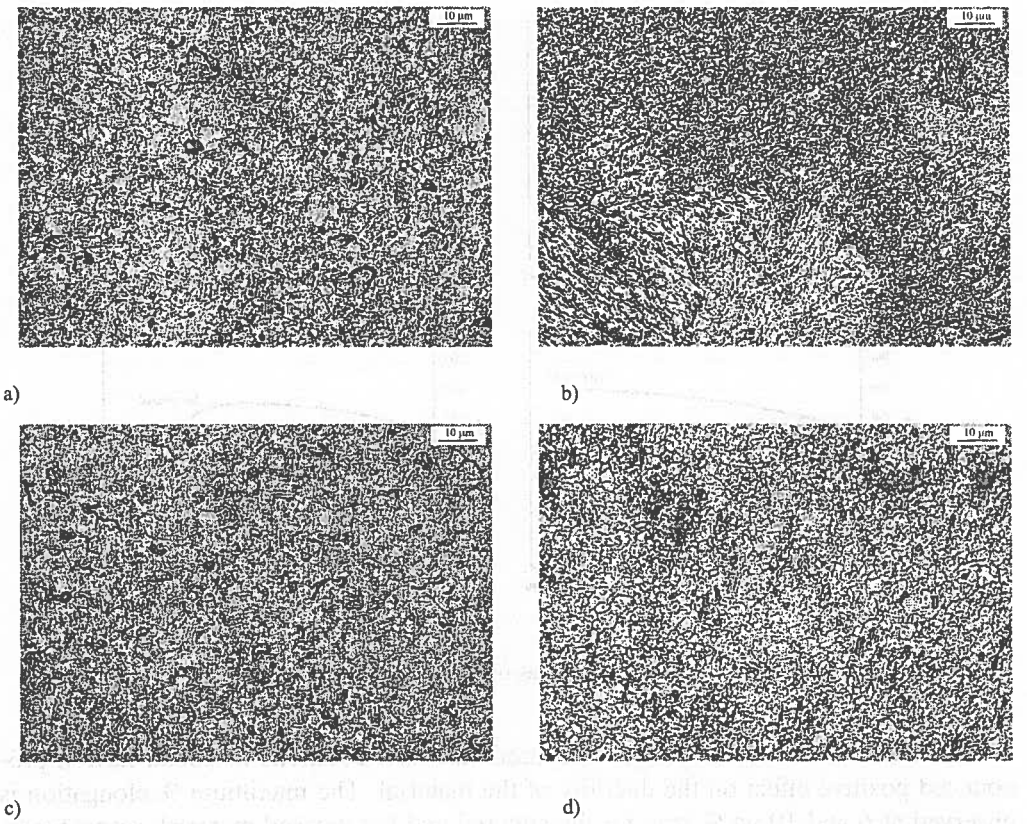

Fig. 4. Typical microstructures of cobalt-iron materials; (a) Co3Fe(S); (b) Co3Fe(HP); (c) Co10Fe(S); (d) Co10Fe(HP)

nucleation of fracture voids must have been facilitated by the existing porosity, whereas in the hot pressed specimens the voids appear to be nucleated on particles retained in the dimples, which were identified with the EDX detector as oxides (Figures 5b and 5d).

4. Conclusion

The experimental work has shown that by PM processing of fine cobalt and iron powders it is possible to obtain a material suitable for a matrix in diamond impregnated tools. It has been found that an adequately consolidated powder mix, containing from 3 to 15 wt.% iron, yields a material characterised by an excellent combination of high mechanical strength and ductility.

The hot press route, which has hitherto been extensively used in the tool-making practice, yields a fine-grained material having virtually theoretical density and high mechanical strength, notwithstanding its chemical composition. The excellent strength

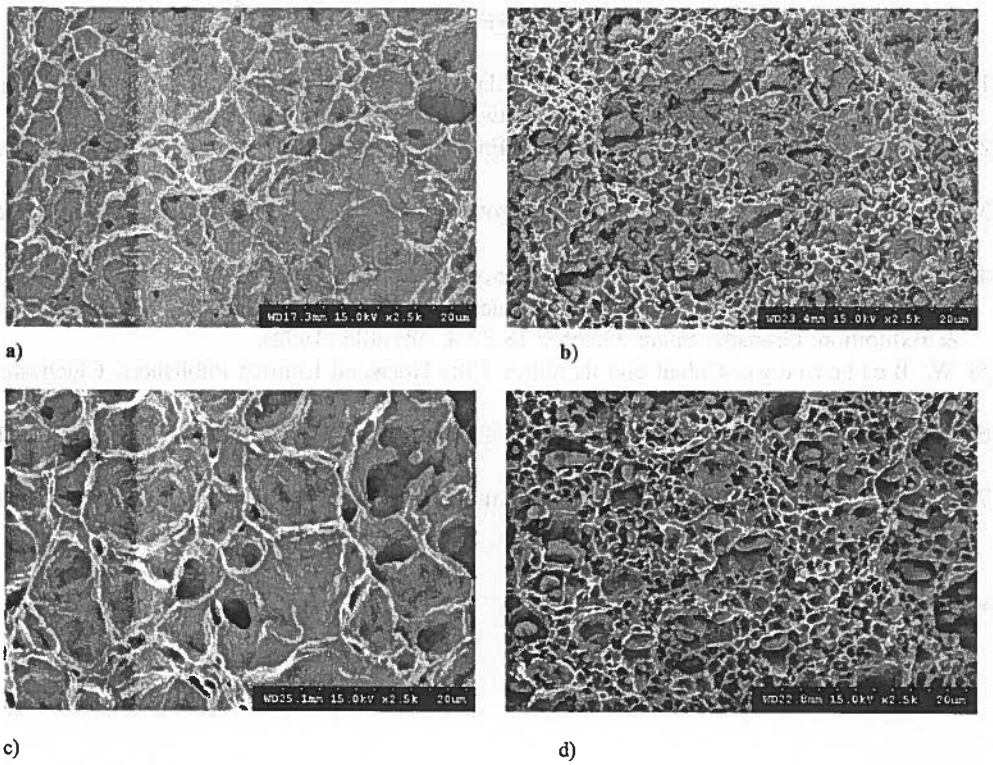

Fig. 5. Typical SEM fractographs of cobalt-iron materials; (a) Co3Fe(S); (b) Co3Fe(HP); (c) Co10Fe(S); (d) Co10Fe(HP)

of the hot pressed material should obviously be associated with finely dispersed oxide particles, which impede recrystallisation and grain growth [1]. Consequently, the material is able to resist higher stress without any signs of plastic yielding. Among other advantages of hot pressing is the avoidance of shape distortion and manufacturing restrictions as regards tool components of comparatively complex geometry.

On the other hand, the cold press/sinter route has been found useful for consolidation of the powder mix containing 3 wt.% iron. This specific composition can be successfully sintered to near-full density in hydrogen, at 950°C, which results in high yield strength and six-fold increase in the pressed material. It is therefore assumed that the conventional cold press/sinter process, being markedly cheaper than hot pressing, has a great potential for the cost-effective production of diamond impregnated wire saw beads containing low-iron, cobalt-base matrix.

Acknowledgements

The work was supported by the State Committee for Scientific Research (KBN) through contract 11.11.110.491.

REFERENCES

[1] J. Konstanty, Cobalt as a Matrix in Diamond Impregnated Tools for Stone Sawing Applications. AGH Uczelniane Wydawnictwa Naukowo-Dydaktyczne, Krakow (2002).
[2] O. Cai, Sintering Without Pressure, or Free Sintering, Diamante Applicazioni & Technologia **3**, 11, 106-122 (1997).
[3] A.S.D. Crum, Hot isostatic pressing, Proc. Seminar on PM Diamond Tools, Lausanne, Switzerland, November 2-3, 1995.
[4] R.G. Ojeda, M. del Villar, P. Muro, I. Iturriza, F. Castro, Densification of diamond tools with Co, Ni, and Fe based metallic binders, Proc. 1998 PM World Congress & Exhibition, Granada, Spain, October 18-22 **4**, 481-486 (1998).
[5] W. Betteridge, Cobalt and its alloys. Ellis Horwood Limited Publishers, Chichester, 14-15 (1982).
[6] T.B. Massalski (Ed.), Binary Alloy Phase Diagrams. ASM International Materials Park, Ohio **2**, 1186-1187 (1990).
[7] Cobalt Monograph. Centre D'Information du Cobalt, Brussels, Belgium, 179-180 (1960).

Received: 12 March 2004

A R C H I V E S O F M E T A L L U R G Y A N D M A T E R I A L S
Volume 49 2004 Issue 4

G. MICHTA*, J. PIETRZYK*, W. OSUCH*, A. KRUK*

DETERMINATION OF M_s TEMPERATURE AND THE DECOMPOSITION OF RETAINED AUSTENITE IN LOW-CARBON 0.2C/1.5Mn/1.5 Si STEEL

OKREŚLANIE TEMPERATURY M_S I ROZPADU AUSTENITU RESZTKOWEGO W STALI NISKOWĘGLOWEJ 0,2C/1,5Mn/1,5 Si

The paper presents magnetometric measurements of the decomposition of retained austenite brought about by low-temperature bainite transformation, and also the structure obtained and mechanical properties. The data included herein indicates that the bainite transformation- taking place at low temperatures, or at higher temperatures over shorter periods, produces two types of austenite with varying stabilities. The less stable austenite disintegrates when cooled to –196°C, while the second – only when heated up to 560°C. The first type is present in the form of large grains, while the second is more scattered and locates between the bainite areas. Their stability during plastic strain also differs; the former disintegrates already at small strain, without making a contribution to the TRIP effect.

W pracy przedstawiono magnetometryczne pomiary rozpadu austenitu resztkowego powstałego w wyniku niskotemperaturowej przemiany bainitycznej, oraz otrzymaną strukturę i własności mechaniczne. Przedstawione dane wskazują, że przemiana bainityczna przebiegająca przy niskich temperaturach, lub przy temperaturach wyższych ale krótkich czasach, wytwarza dwa rodzaje austenitu o różnej stabilności. Mniej stabilny rozpada się podczas chłodzenia do –196°C, drugi dopiero podczas nagrzewania do 560°C. Pierwszy występuje wpostaci dużych ziaren, drugi jest bardziej rozdrobniony znajduje się pomiędzy obszarami bainitu. Różna jest też ich stabilność podczas odkształcania próbki. Pierwszy rozpada się już przy małych odkształceniach, nie wnosząc swego wkładu w efekt TRIP.

1. Introduction

Over the past 20 years, a considerable number of works has been devoted to low-carbon steels (0.2 pct C, 1.5 pct Mn, 1.5 pct Si, chemical composition in weight

* WYDZIAŁ METALURGII I INŻYNIERII MATERIAŁOWEJ, AKADEMIA GÓRNICZO-HUTNICZA, 30-059 KRAKÓW, AL. MICKIEWICZA 30

percent) utilizing the TRIP (TRansformation Induced Plasticity) effect. Their production technology, which consists in annealing within a two-phase region, rapid cooling and bainite transformation process, creates a structure made up of ferrite (60–70 pct), bainite (15–30 pct) and retained austenite γ_r (5–15 pct) [1].

The good plastic properties of these steels, combined with their high strength, are decisively determined by the mechanical stability and quantity of retained austenite γ_r – under the influence of strains, this austenite undergoes transformation into martensite (M). The magnitude of plastic strains at which this transformation takes place, significantly influences the plasticity of the steel. Ideal for the attainment of maximum plasticity would be a transformation under a strain corresponding to the loss of strain stability. This corresponds to the initial appearance of a neck during the tensile test (maximum uniform elongation U.El.), or of a contraction during a cupping test. The occurrence – under these strains at the point of stability loss – of martensite coming from the $\gamma_r \rightarrow M$ transformation, considerably increases the plastic strainability of steel.

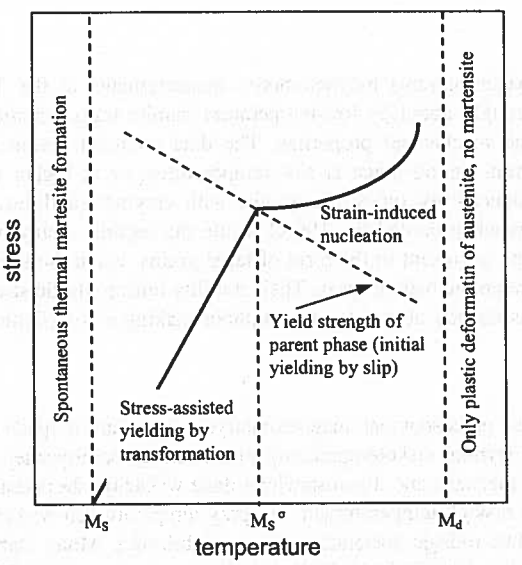

Fig. 1. Diagrammatic presentations of the dependence between M_s, M_s^σ, M_d

The stability of γ_r determines of sensitivity to the $\gamma_r \rightarrow M$ transformation taking place under the influence of stresses, strains or temperature. The γ_r stability may be assessed quantitatively through material parameters such as M_s, M_s^σ, M_d (Fig. 1) and the $d\gamma_r/d\epsilon$ vs. ϵ dependence, where:

M_s is the temperature below which there occurs the spontaneous $\gamma \rightarrow M$ transformation during a fall in temperature, M_s^σ – the maximum temperature at which elastic stresses are able to initiate the $\gamma_r \rightarrow M$ transformation, above M_s^σ only plastic strains are able to bring about the $\gamma_r \rightarrow M$ transformation.

M_d – the temperature above, which no plastic strains, are able to initiate the transformation.

M_s is conditioned by the free energy connected with the chemical composition of austenite and its morphology (scattering, shape, dislocation density), while the remaining parameters are additionally connected with the energy coming from stresses and strains.

The $d\gamma_r/d\epsilon$ vs. ϵ dependence is described by the Ludwigson and Berger relation [2].

$$1/V_{\gamma r} - 1/V_{0\gamma r} = A/V_{0\gamma r})\epsilon^B \tag{1}$$

or its modification [3]

$$1/V_{\gamma r} - 1/V_{0\gamma r} = (k_p/p)\epsilon^p \tag{2}$$

where: $V\gamma r$ – volume fraction occupied by retained austenite following strain ϵ, $V_{0\gamma r}$ – volume fraction occupied by retained austenite at $\epsilon = 0$; the possibility of stress-initiated transformation is not taken into consideration here; A, k_p – empirical constants determining the stability of austenite; B, p – empirical constants (for TRIP steel $p = 1$).

The equations (1, 2) assume a gradual modification of γ_r under the influence of strain, and the majority of experimental data confirm this type of dependence [3, 4]. Of the above mentioned characteristics, the $\gamma_r(\epsilon)$ dependence is the one most frequently determined.

The γ_{r0} stability is attested to, among others, by temperature M_s; however, the available papers do not contain any direct measurements thereof for low-carbon steels utilizing the TRIP effect – even though references thereto are quite common [Fig. 1]. For the assessment of M_s, with chemical composition (carbon content) we used well-known empirical formula (Andrews' et al.), obtained for cooled steels from the austenitic range (100 pct austenite). In some works [5] this formula was used either for steel rapid cooled from dual- phase region, were beside austenite existing ferrite grains.

$$M_s(^\circ C) = 539 - 423C_\gamma - 30.4Mn - 7.5Si + 30Al. \tag{3}$$

Acquaintance of M_s and chemical composition of steel allows determining of carbon concentration in austenite C_γ. With assumption that carbon concentration in ferrite $C_\alpha = 0.02\%$, volume fraction of austenite V_γ can be determined from relation:

$$C = V_\alpha * C_\alpha + V_\gamma * C_\gamma; \qquad V_\alpha + V_\gamma = 1, \tag{4}$$

where: C – average carbon concentration in steel.

For steels after partial bainite transformation in which retained austenite γ_{r0} accounts for only 5–15 pct of volume and is considerably scattered, such an assessment carries a significant error. Therefore purposely is direct measurement of M_s and retained austenite fraction V_γ.

2. Test material and methodology

The initial test material for the present investigations was cold-rolled 1.25 mm thick steel, containing 0.2 pct C, 1.5 pct Mn, 1.5 pct Si, 0.002 pct S, 0.016 pct P, 0.036 pct Al. Samples for magnetic and strength tests were cut laterally with respect to the direction of rolling. The heat treatment and measurements of austenite decomposition were executed in two salt bath furnaces, the first of which was used for annealing within a temperature range of A_1–A_3 (usually, this was a temperature of 760°C). The second furnace was utilized for isothermal bainite transformation at temperatures ranging from 250 to 380°C.

The decomposition of austenite during entire cycle of heat treatment was measured on the small-dimensional samples (1.25*3*35mm^3) with welded thermocouple Cu-Constantan by means of a torsional magnetometer, making use of the fact that the torsional moment of a sample placed in a strong (3.5T) magnetic field is dependent on its magnetization of saturation J_s.

The J_s dependencies on torsional moment (M_s) was a subject of our earlier consideration presented in [6], where ascertain that under certain condition this is directly proportional relation. Deflection of this condition strongly deforms this relation. This method (Fig. 2a) allow on the qualitatively determination of J_s in whole range of heat treatment cycle.

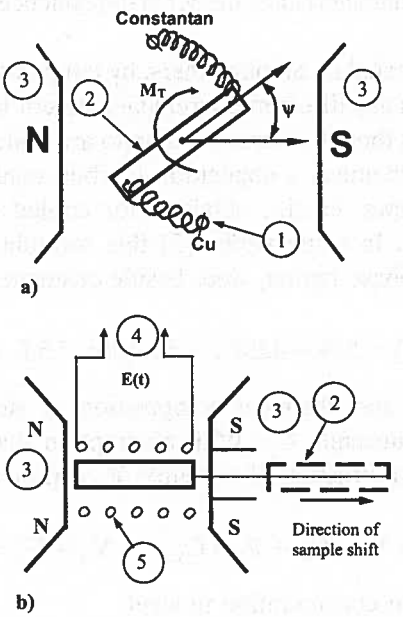

Fig. 2. Diagram of the measuring systems. a) torsional magnetometer, b) differential magnetometer, where: 1-thermocuple Cu-Constantan, 2-samples, 3-pole pieces, 4-electromotive force E(t), 5-measurement coil, Ψ-angle between magnetic field and sample axis

Differential magnetometer was used for precise determination of J_s (Fig. 2b). The J_s measurements were performed on the samples with dimension of 1.25 * 8 * 35 mm, after heat treatment or on the samples cut from deformed tensile test samples. Measurements of J_s during cooling to –196°C and heating up to 560°C were either performed on this samples. The mean disadvantage of differential magnetometer is only possibility of taking measurements at room temperatures. This method gives information from whole volume of sample and was many times verified [7, 8]. dependence, where:
Magnetization saturation is strictly combined with amount of ferromagnetic phase V_α:

$$J_s = J_{s\alpha} * V_\alpha + J_{s\gamma} * V_\gamma, \tag{5}$$

where: V_α, V_γ volume fractions of ferromagnetic phase (ferrite, bainitic ferrite and martensite) and paramagnetic phase (austenite), $J_{s\alpha}$, $J_{s\alpha}$ adequate magnetization saturation of ferromagnetic and paramagnetic phases.

For calculations, the previously tested sample annealed at 560°C was used as the $V_\gamma = 0$ pct master ($V_\alpha \cong 1, J_s \cong J_{s\alpha}$) In consequence, measurement of J_s permits to determine the quantity of the γ phase, using the following equation:

$$V_\gamma(T) = [J_{s\alpha} - J_s]/J_{s\alpha}. \tag{6}$$

Tests of the structure on thin foils were carried out using a JEM 100C transmission electron microscope. Measurements of the mechanical properties were made using an MTS 810 universal testing machine on samples with a section of 1.25*8 mm^2 and measurement length of 90 mm.

3. Test results

A. Measurements under rapid cooling from the two-phase range

Small-dimensional samples (1.25*3*35 mm^3), with a thermocouple welded thereto, were fixed in the measuring device and heated in the furnace at a temperature of 760°C for 10 minutes, and subsequently cooled in liquid nitrogen, thereby ensuring a cooling rate of 40 [deg/sec.]. Following cooling to the temperature of liquid nitrogen, the samples were gradually heated up to a temperature of 560°C in order to bring about decomposition of austenite retained after cooling into ferrite and carbides, and to receive the reference sample, for which $V_\gamma(T) = 0$.

Typical changes of torsional moment vs. temperature changes has been presented in Fig. 3. During cooling from a temperature of 760°C (two-phase area), which practically coincides with the Curie temperature of the ferritic phase, one can observe a smooth increase in the torsional moment, this being connected with the increase in magnetization saturation due to the ferrite created within the two-phase range.

At a temperature of +124°C, the increase in the torsional moment, connected with the beginning of the martensitic transformation (M_s), becomes evident. Starting from this temperature, the increase in moment observed during cooling, is conditioned both by the increase in the quantity of martensite (decrease in γ), and the increase of magnetization saturation of ferrite and martensite.

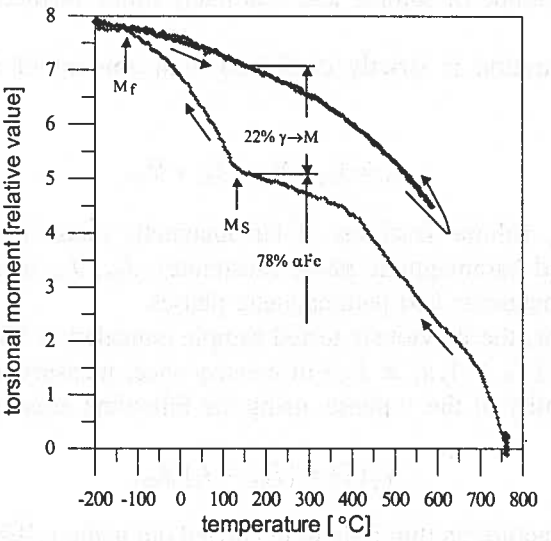

Fig. 3. Change in the torsional moment (magnetization saturation) during rapid – approximately 40 deg/s – cooling from 760°C / 600 seconds down to – 196°C, heating up to 560°C and repeated cooling down to –196°C

Following cooling to a temperature of –196°C, the sample was heated up to 560°C, in order to ensure the decomposition of the retained austenite that was not transformed into martensite, and subsequently cooled again to –196°C. As one can observe, this operations does not lead to changes in magnetization, while the heating and cooling curves coincide, and this clearly attests to the full decomposition of the austenite created at 760°C into martensite during the first cooling down to –196°C.

On the basis of the presented curves it is possible to determine M_s and M_f temperatures. For determination of retained austenite volume fraction which transform to martensite we can use measured values of M_s temperature (mean value from five measurements is +130°C) and (3) and (4) relations. Obtained values are $C_\gamma = 0.84\%$ and $V_\gamma = 22\%$. These values not conform to equilibrium at 760°C, what gives evidence that during cooling (devolving of samples between furnace and dish with liquid nitrogen – time about 3 sec.) ensued decomposition of austenite to ferrite and carbon enriching of austenite.

B. Measurements of the decomposition of austenite during the isothermal transformation into bainite and further cooling to the temperature of liquid nitrogen

The typical curve for such a measurement has been presented in Fig. 4. Following submersion in salt with a temperature of 300°C, the austenite (approximately 30 pct with a content of 0.6 pct C) present at the temperature of 760°C (two-phase range) disintegrates into bainite, causing the carbon enrichment of the remaining retained austenite γ_{r0}.

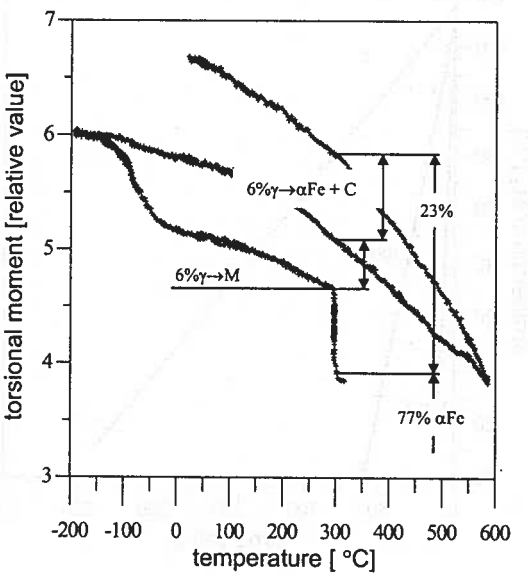

Fig. 4. Change in the torsional moment (magnetization saturation) during rapid cooling from 760°C / 600 seconds down to 300°C, isothermal transformation over 60 minutes, heating up to 560°C and repeated cooling

During this process, which lasts 60 minutes, the γ_{r0} stability increases so that its M_s observed during further cooling totals approximately –40°C, and decreases in comparison with samples cooled directly by approximately 160°C (M_s = +124°C in Fig. 3).

Cooling to –196°C does not lead to the full decomposition of austenite γ, as was observed in Fig. 3. The thermal decomposition of the retained austenite following cooling to –196°C takes place only during heating up to 560°C, and the cooling curve from this temperature runs above the heating curve. Using data from differential magnetometer, is one may calculate that after isothermal transformation the tested sample contained approximately 12 pct of γ (austenite), of which approximately 6 pct disintegrated into martensite during cooling from M_s to –196°C, while the remaining 6 pct disintegrated into ferrite and carbides during heating up to 560°C.

Increasing the period of isothermal transformation to 90 minutes at 300°C results in greater stabilization γ, so that when cooling to –196°C we do not observe trans-

formation into martensite (M_s point); the austenite remaining after isothermal transformation disintegrated only during heating up to 560°C.

Measurements, similar to those presented in Fig. 4, were carried out for various periods of isothermal transformation at 250, 300 and 350°C. These data, in the form of the dependence of Ms on the isothermal transformation period at varying temperatures, have been compiled in Fig. 5. As one could have expected, an increase in temperature leads to the more rapid stabilization of the γ_{r0} retained austenite obtained.

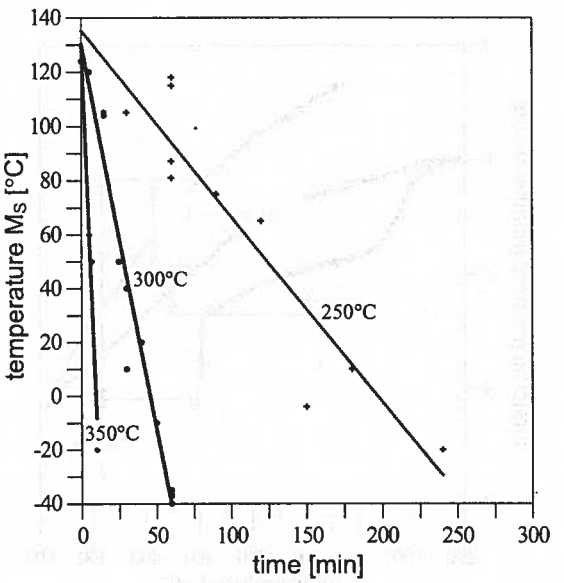

Fig. 5. Dependence of M_s on the duration of isothermal transformation at temperatures of 250, 300 and 350°C, for samples annealed at 760°C over a period of 600 seconds

The lengthening of the bainite transformation period leads, for each temperature, to both a decrease in γ_{r0} and M_s, and a decrease in the proportion of austenite undergoing transformation into martensite (during cooling to –196°C) in relation to austenite disintegrating into ferrite and carbides during heating up to 560°C. This results in difficulties in determining M_s when this temperature falls below –80°C.

C. Influence of M_s on mechanical properties has been traced for transformation temperatures of 300°C and 380°C

At a temperature of 300°C, it is easy to change M_s by changing of isothermal transformation period. Periods of 30, 60 and 90 minutes were selected, these giving M_s temperatures of approximately +30, -40 and lower than –196°C, respectively. Typical stress-strain curves have been presented in Fig. 6a, while average mechanical properties in Table 1.

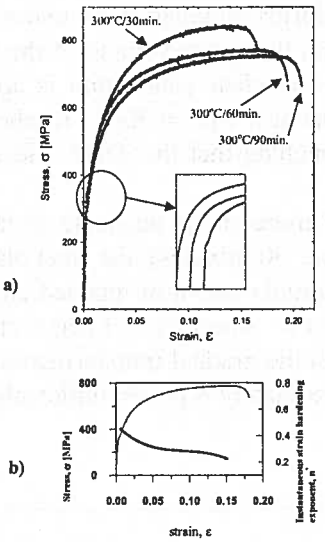

Fig. 6. The stress-strain curves for samples annealed at 760°C / 600 seconds following their isothermal transformation at 300°C over 30 minutes (M_s = +30°C), 60 min (M_s = −40°C), 90 min (M_s < −196°C) a), and strain dependencies of instantaneous strain hardening exponent n^* for sample after isothermal transformation at 300°C for 30 minutes b)

TABLE

Mean mechanical properties for the samples annealed at 760°C/600 seconds following their isothermal transformation at 300°C over 30, 60 and 90 minutes

Heat treatment	YS MPa	TS MPa	U.EL. pct	T.E L. pct	TS*U.EL. Mpa*pct
300°C/30 min.	358.6	824.6	13.7	19.9	11297.02
300°C/60 min.	353.3	771.9	14.9	21.7	11547.62
300°C/90 min.	361.6	760.3	14.4	21.5	10948.32

Additionally, measurements were made on temperature function of the quantity of austenite remaining in the sample for samples with M_s = −40°C (transformation period of 60 minutes, see Fig. 4) following their plastic strain to 1 and 18 pct. In both cases, no transformations into martensite were observed during the cooling of the samples from 20°C down to −196°C.

Further heating to 560°C and repeated cooling allowed us to determine that the strained samples contained 6 pct and 3 pct of austenite, respectively. This indicates that even a small (1 pct) plastic strain leads to the transformation into martensite of approximately 14 pct of austenite – the entire of the less stable austenite (8 pct, disintegrating into martensite during cooling down to −196°C) and half (6 pct) of the more stable austenite form. Further plastic straining (from 1 pct to 15 pct) results in the decomposition of only 3 pct of retained austenite.

The austenite, which transforms into martensite under small strains, homogeneously initiates slip processes within the entire volume of the sample, as a result of which Lüders' lines do not appear – no clear yield point is apparent (Fig.6a). The instantaneous strain hardening exponent $n*$ ($\sigma = K\epsilon^{n*}$) reaches maximum values at small strains (Fig. 6b). One may conclude that the TRIP effect does not occur at all or is small in these samples.

Following the creation of more stable austenite in the samples, generated under higher temperatures (380°C over 30 minutes), the steel plasticity visibly increases (see Fig. 7). In these samples, the initial content of retained austenite totaled approximately γ_{r0} = 18 pct, following L ü d e r s ' strain (e_L = 3 pct) it changed slightly (γ_r = 15 pct), while only greater strains led to the gradual transformation $\gamma \rightarrow M$, so that in ruptured samples its quantity was approximately 8 pct on uniformly strained sections (U.El.=20 pct).

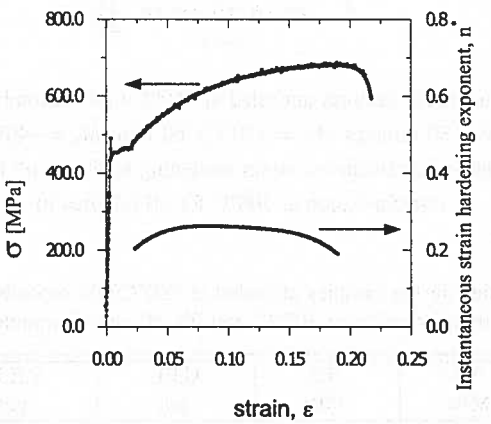

Fig. 7. The stress-strain curve and strain dependencies of instantaneous strain hardening exponent $n*$ for samples annealed at 760°C / 600 seconds following their isothermal transformation at 380°C over 30 minutes (TS= 671MPa, YS = 455MPa, U.El. = 19.6 pct, TEl. = 40 pct)

Since the M_s temperature of this sample was –40°C, no martensite was observed in its structure. Cooling of the sample to the temperature of liquid nitrogen in transmission electron microscope and reheating to ambient temperature resulted in the appearance of martensite at certain points (Fig. 11). Martensite appeared in areas previously occupied by the large austenite grains. However, austenite was still observed in both the above-mentioned morphological forms.

As one can observe, the austenite obtained under these conditions transforms into martensite at greater strains, moving the $n*$ maximum to higher strains, and L ü d e r s ' strain is evident. The TRIP effect occurring in these circumstances clearly improves plasticity.

D. Microscopic observations

Observations were made on a sample following annealing at 760°C / 600 seconds and bainite transformation at 300°C/60 minutes; changes in the quantities of austenite during cooling and heating have been presented in Fig. 4. The data presented indicates that of the total quantity of austenite (12 pct), 6 pct was characterized by a low stability and transformed into martensite during cooling to a temperature of – 196°C.

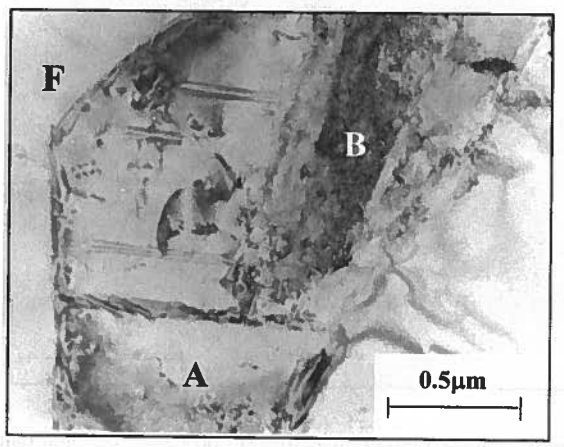

Fig. 8. Microstructure of sample follows annealing at 760°C/600 sec. and bainite transformation at 300°C/60 minutes and cooling down to room temperature. TEM. A- retained austenite, F-ferrite and B-bainitic ferrite

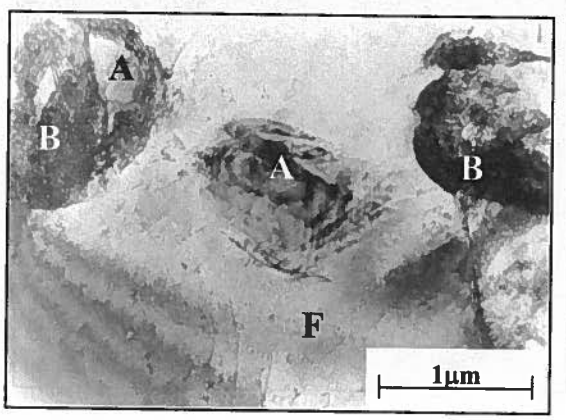

Fig. 9. Microstructure of sample follows annealing at 760°C/600 sec. and bainite transformation at 300°C/60 minutes and cooling down to room temperature. TEM. A- retained austenite, F-ferrite and B-bainitic ferrite

Ferrite, bainite and austenite were observed in the structure of the sample (Fig. 8, 9). The morphology of austenite varied; it was either large-grained or present as a considerable number of small areas closed in on all sides by bainite. The large austenite grains shown in Figs. 8 and 9 ranged in size from 2 to 3 μm, while the areas closed in by bainite were decidedly smaller (Figs. 9 and 10). The strip of austenite (see Fig. 10) proceeding through the bainite was only 0.07 μm.

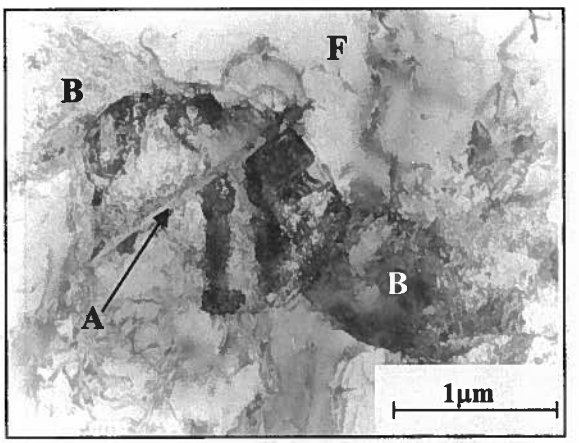

Fig. 10. Microstructure of sample follows annealing at 760°C/600 sec. and bainite transformation at 300°C/60 minutes and cooling down to room temperature. TEM. A- retained austenite, B-bainitic ferrite, F-ferrite

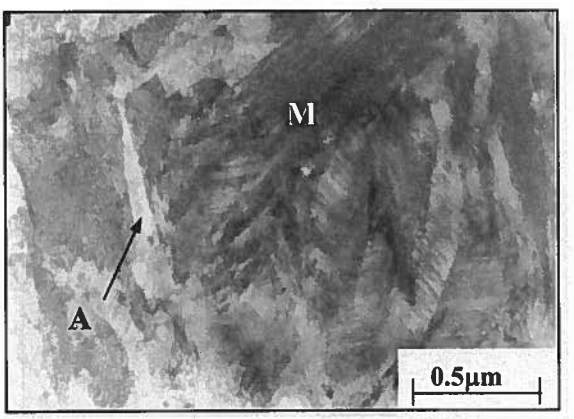

Fig. 11. Microstructure of sample follows annealing at 760°C/600 sec. and bainite transformation at 300°C/60 minutes and addition cooling to –196°C. TEM. A- retained austenite, M-martesite

4. Discussion of results

During annealing within the two-phase range (760°C/10 minutes) there is created a structure made up of ferrite (approximately 70 pct) and austenite (30 pct) containing approximately 0.66 pct of carbon. During cooling, the austenite separated by ferrite areas starts to transform into martensite at approximately 130°C (Fig. 3).

The bainite transformation of the austenite thus obtained under low temperatures or at higher temperatures over shorter periods, led to the creation of two types of austenite with different stabilities. The less stable austenite transformed into martensite during cooling down to – 196°C, while the second – into αFe and carbides during heating up to 560°C.

The first variety occurs in the form of large grains, while the second is more scattered and locates between the bainite areas.

Their stability during sample straining also differs. The first type disintegrates at even small strains. The nucleation of plastic strains occurs at numerous points, and as a result the static stretching curve is even, without a clear yield point (Fig. 6). Inferring from the low plastic properties, one may assume that in this instance the $\gamma_r \rightarrow M$ transformation under the influence of stain, does not contribute to the TRIP effect.

The creation of a more stable austenite (e.g. 760°C/10 minutes, 380°C/30 minutes) with an M_s temperature below –196°C leads during straining to gradual decomposition at greater strains; also, Lüders' strain and a clear yield point both appear (Fig. 7). At greater strains, the austenite starts to gradually transform into martensite; if this transformation takes place under strains corresponding to the conditions of strain stability loss for a given cold work diagram, one can observe the TRIP (TRansformation Induced Plasticity) effect. This makes it possible to obtain good plastic properties while maintaining high strength properties.

The results presented indicate that there is no simple correlation between the quantity of mechanically metastable retained austenite and mechanical properties. One should take into consideration its structural diversification and the varying stability of austenite connected therewith.

5. Conclusions

1. M_s temperature was determined for austenite created within the two-phase range and for retained austenite following bainite transformation.

2. Depending on the temperature and bainite transformation period, we obtain retained austenite that is varyingly diversified in terms of morphology and stability.

3. Low bainite transformation temperatures and short transformation periods under higher temperatures result in a less stable retained austenite with an M_s temperature above – 196°C.

4. Retained austenite with low stabilities disintegrates into martensite even under small strains, and this changes the straining mechanism typical for low-carbon steels; Lüders' strain is not present. This decomposition does not contribute to the TRIP effect.

The present paper has been co-financed by the KBN (Polish Scientific Research Committee) under research project AGH nr 11.11.110.499.

REFERENCES

[1] W. Bleck, International Conference on TRIP–Aided High Strength Ferrous Alloys, Gent, Belgium, 13-23 June 19–21, 2002.
[2] D.C. Ludwigson, J.A. Berger, JISI 192, 63–69 (1969).
[3] Suzelotte Kruijver et al.. International Conference on TRIP–Aided High Strength Ferrous Alloys, Gent, Belgium, pp. 25-29 June 19–21, 2002.
[4] A. Kruk, L.B. Magalas, W. Osuch, J. Pietrzyk, G. Rigaut, S. Gorczyca, Proceedings of the 14th International Scientific Conference ADVANCED MATERIALS & TECHNOLOGIES, Zakopane, Poland, 255-258 May 17 –21, 1995.
[5] M. De Meyer, J. Mahieu, B.C. De Cooman, Mater.Sci. Technol. **18**, 1121-1132 (2002).
[6] J. Pietrzyk, A. Maksymowicz, G. Michta, Metallurgy and Foun- dry Engineering **23**, 3, 341 –347 (1997).
[7] W. Osuch et all, IX Conference on Electron Microscopy in Solids, 263- 266 Kraków, Poland, 1996.
[8] E. Wirthl et.all: International Conference on TRIP-Aided High Strenght Fer- rous Alloys, Gent Belgium, 61-64 June 19-21, 2002.

Received: 10 March 2004